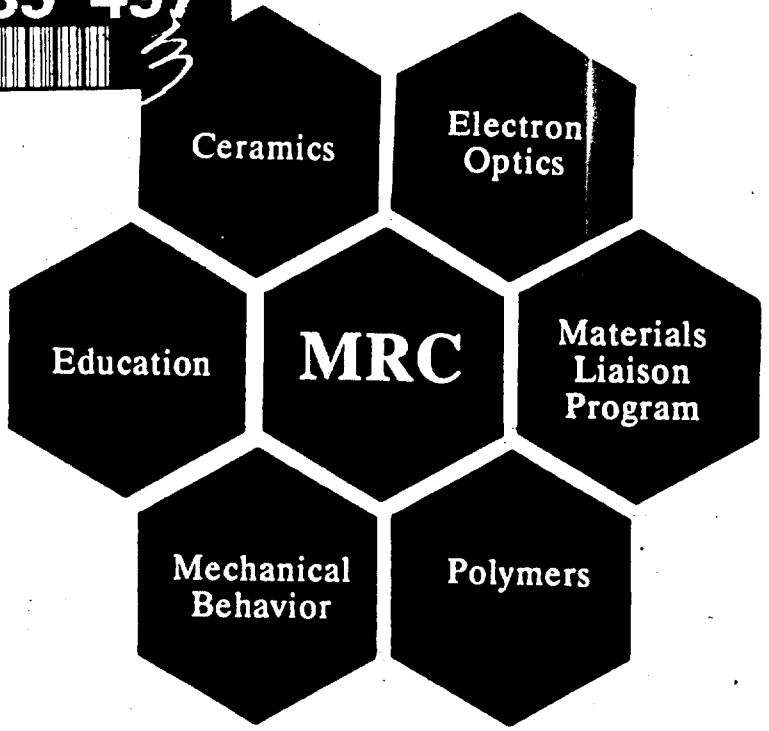

FINAL REPORT

MULTIPHASE CERAMICS FOR MECHANICAL AND STRUCTURAL RELIABILITY AT LOW AND ELEVATED TEMPERATURES

Professors M. P. Harmer (P.I.), H. M. Chan (Co-P.I.),
G. A. Miller (Co-P.I.), and Research Assistants/Associates
A. M. Thompson, J. Zhao, J. Fang, J. D. French, A. Khan, C. J. Russo

Sponsored by

U.S. Air Force - Office of Scientific Research

Contract No. AFOSR 91-0126

Report Period: 15 December 1990 - 30 June 1994

Materials Research Center, MRC
Lehigh University

[redacted] Dist: A

REPORT DOCUMENTATION PAGE

Form Approved
OMB No. 0704-0188

1. AGENCY USE ONLY (Leave blank)	2. REPORT DATE	3. REPORT TYPE AND DATES COVERED
	8/10/94	Final Report - 12/14/92 - 06/14/94

4. TITLE AND SUBTITLE

MULTIPHASE CERAMICS FOR MECHANICAL AND STRUCTURAL RELIABILITY AT LOW AND ELEVATED TEMPERATURES

5. FUNDING NUMBERS

AFOSR-91-0126
2306/A2

6. AUTHOR(S)

M. P. Harmer
H. M. Chan

7. PERFORMING ORGANIZATION NAME(S) AND ADDRESS(ES)

Materials Research Center
Whitaker Lab
Lehigh University
5 E. Packer Avenue
Bethlehem, PA 18015-3194

8. PERFORMING ORGANIZATION REPORT NUMBER

2

9. SPONSORING/MONITORING AGENCY NAME(S) AND ADDRESS(ES)

NC

Dr. Alexander Pechenik
AFOSR/NC
Department of the Air Force
110 Duncan Ave. - Suite B115
Bolling AFB, D.C. 20336-6448

10. SPONSORING/MONITORING AGENCY REPORT NUMBER

AFOSR-91-0126
2306/A2

11. SUPPLEMENTARY NOTES

12a. DISTRIBUTION/AVAILABILITY STATEMENT

Approved for public release,
distribution unlimited

A

12b. DISTRIBUTION CODE

13. ABSTRACT (Maximum 200 words)

(See next page)

94-31801

14. SUBJECT TERMS

Keywords: multiphase ceramics, creep, fracture

15. NUMBER OF PAGES

16. PRICE CODE

17. SECURITY CLASSIFICATION OF REPORT	18. SECURITY CLASSIFICATION OF THIS PAGE	19. SECURITY CLASSIFICATION OF ABSTRACT	20. LIMITATION OF ABSTRACT
Unclassified	Unclassified	Unclassified	Unlimited

ABSTRACT

AFOSR project 91-0126 was undertaken to develop a design approach for improving the high-temperature structural reliability (e.g., resistance to creep, fracture and grain growth) and room temperature mechanical reliability (e.g., flaw tolerance) of structural ceramics. Some of the major accomplishments of this work are highlighted below:

1. Engineering of the grain boundary chemistry in alumina resulted in a lowering of the creep rate by over two orders of magnitude by the addition of 1000ppm of Y_2O_3. It is conjectured that the presence of a highly segregated oversized (similarly charged) ion at the grain boundaries is responsible for inhibiting grain boundary difffusion and lowering the creep rate.

2. Duplex microstructures of Al_2O_3:YAG and Al_2O_3:ZrO_2 exhibited lower creep rates and higher fracture toughness values than their single phase constituents. The creep data was well described by a composite creep equation developed for isostrain behavior (i.e. the strain rates are the same for each phase). The higher fracture toughness was attributed to the contribution of low energy interphase boundaries to the overall composite toughness.

3. It has been found that "nanocomposites' of hot pressed Al_2O_3 containing 5 vol% of 0.15μm SiC have exceptionally high strength (>1GPa), confirming the findings of Japanese researchers (Niihara et al.). The strengthening was attributed to a combination of apparent toughening arising from machining-induced residual compressive stress and flaw size reduction via crack healing.

4. Dramatic improvements in flaw tolerance have been achieved by the designed incorporation of spray-dried agglomerates into two-phase ceramic matrices (such as Al_2O_3 agglomerates in an Al_2O_3:mullite matrix). The primary mechanism appears to be localized grain bridging, although stress induced microcracking has also been observed.

5. Ceramics with high strength and toughness over a wide range of flaw sizes have been produced using a novel laminar (trilaminate) design. The mechanical properties were modelled using a micro-mechanics model that incorporates R-curve behavior.

TABLE OF CONTENTS

1. PREVIOUS TECHNICAL REPORTS

1. PREVIOUS TECHNICAL REPORTS

Characterization and Mechanical Behavior of Alumina-Mullite Ceramics

Unique Opportunities for Microstructural Engineering with Duplex and Laminar Ceramic Composites

Mechanical Behavior of Al_2O_3-SiC "Nanocomposites"

Processing and Microstructure Development in Al_2O_3-SiC "Nanocomposites"

Mechanical Properties of Laminated Ceramic Composites in Alumina- and Zirconia-Based Systems

Design of a Laminated Ceramic Composite for Improved Strength and Toughness

Flaw Tolerant Alumina-Mullite Ceramics

Tensile Creep of Duplex Ceramic Microstructures

TEM Study on Creep Deformation in Yttrium Doped Alumina

High Temperature Deformation and Fracture Toughness of Duplex Ceramic Microstructures

2. CURRENT TECHNICAL REPORTS

DIRECT OBSERVATION OF Y AND La DISTRIBUTIONS IN POLYCRYSTALLINE Al_2O_3

Direct Observation of Y and La Distributions in Polycrystalline Al_2O_3

A. Mark Thompson, Helen M. Chan, Martin P. Harmer, and David B. Williams
Dept. of Materials Science and Materials Research Center.
Lehigh University

Kamal K. Soni, Jan M. Chabala, and Riccardo Levi-Setti
Enrico Fermi Institute and Dept. of Physics
University of Chicago

For the first time the distribution of yttrium and lanthanum dopants is mapped in a polycrystalline alumina. Using a novel scanning ion microprobe (SIM) in combination with a secondary ion mass spectrometer (SIMS), the dopants are found to segregate to grain boundaries and pore surfaces. In 1000 ppm Y-doped Al_2O_3, an abundance of YAG precipitates are also observed, shedding new light on yttrium's role in reducing the creep rate of Al_2O_3. The similarity in the segregation behavior of Y and La, highlights the potential of La-doped Al_2O_3 for improved creep properties.

I. Introduction

Yttrium can enhance the properties of both metals and ceramics. When added to NiCr or FeCrTiAl alloys, yttrium reduces the oxidation rate of the alloy[1,2]. At dopant levels of 500-1500 ppm in Al_2O_3, yttrium lowers the compressive and tensile creep rate of alumina[3-5], in one study by greater than 2 orders of magnitude[3]. In both cases, the yttrium's beneficial role is attributed to its segregation to α-Al_2O_3 grain boundaries. Current theories have proposed that either (i) yttrium reduces the rate of ion transport along the grain boundaries[1,2,6] (possibly through the formation of a continuous two-dimensional second phase[6]), or (ii) yttrium inhibits the interface reaction believed to be controlling the rate of ion transport along the grain boundaries.[3]

In support of these hypotheses, numerous investigators have examined the distribution of

yttrium in polycrystalline Al_2O_3. A variety of techniques have been employed including, X-ray Energy Dispersive Spectroscopy (EDS),[1,6-9] Extended X-ray Absorption Fine Structure (EXAFS),[9] Auger Electron Spectroscopy (AES),[10,11] and Secondary Ion Mass Spectrometry (SIMS).[2] All studies found yttrium segregating as an Y-rich, grain-boundary monolayer. A few also detected fine precipitates of YAG ($3Y_2O_3.5Al_2O_3$) scattered throughout the microstructure.[1,6,9,10] The degree of grain boundary enrichment depended on the dopant level, Al_2O_3 grain size, impurity content of Al_2O_3, and the spatial resolution of the analytical technique. For example, techniques with inadequate resolution that sampled large areas, failed to identify the YAG precipitates and generally overestimated the enrichment factors.

The primary objective of this work was to examine the Y-distribution within an 1000 ppm Y-doped polycrystalline Al_2O_3 that had previously exhibited favorable creep properties.[3] In addition, a 1000 ppm La-doped sample was examined, primarily, to compare the segregation behavior of the two isovalent rare earth elements, and partly to assess the potential of La-doped Al_2O_3 for improved creep properties..

Imaging microanalysis of doped polycrystalline Al_2O_3 was performed with the SIM developed at The University of Chicago (UC).[12] The UC SIM uses a finely-focused scanning Ga^+ beam to sputter atoms and molecules from the uppermost layers of the specimen surface. In the process, a fraction of the particles become ionized, creating "secondary ions". The yield of secondary ions is dependent on the atomic or molecular species, the bombardment conditions and, most importantly, the electronic character of the surface. Secondary ions are collected, energy-filtered and mass analyzed. The mass-resolved SIMS signal is recorded along with the associated scan coordinates, thereby, allowing two-dimensional SIMS maps to be constructed. This technique provides both the high spatial resolution and the analytical sensitivity necessary to characterize the distribution of trace dopants in ceramics.[13]

II. Experimental Procedure

Samples were prepared using an ultra-high purity (>99.995%) monosized α-alumina powder (Sumitomo AKP-53). The powder was wet-mixed with a suitable aliquot of either yttrium or lanthanum nitrate solution to yield a doping level of 1000 ppm (cation/aluminum ion). After

drying, the powders were crushed and calcined in air at 600°C for 10 h to remove carbon and sulphur contaminants. All powder processing was carried out using precleaned Teflon ware under clean-room conditions to minimize powder contamination.

Fully-dense samples were fabricated by hot-pressing calcined powder in a 3" diameter graphite die under vacuum for 30 mins at 50 MPa. The hot pressing temperature was 1475°C for the 1000 ppm Y-doped alumina, and 1450°C for the 1000 ppm La-doped alumina. After hot-pressing, the materials were typically >99% theoretical density. Two pieces of each sample were polished down to 1 μm diamond finish; one was thermally etched in air at 1400°C for 1 hour and imaged using a scanning electron microscope (SEM), the other was analyzed in the as-polished condition using the SIM/SIMS at U. Chicago.

In the UC SIM, the primary ion beam is extracted from a liquid Ga source, accelerated at 40 keV and focused to a spot approximately 50 nm in diameter. The probe is scanned over the surface using a 512x512 raster, spanning areas ranging from 10x10 to 80x80 μm^2. Secondary ions are collected normal to the specimen surface (to minimize edge effects) and are mass analyzed in a magnetic sector mass spectrometer. It is also possible to obtain topographic images of the scanned area by collecting the total ion-induced secondary ion (ISI) signal via a channeltron overlooking the target at a glancing angle. The ISI images are useful in locating areas of interest and identifying microstructural features such as pores. SIMS maps are acquired, stored and processed using a Kontron IBAS image processing work station. Typically a SIMS map can be acquired in 1-9 minutes, depending on the signal statistics. In order to enhance this signal, the secondary ion transport optics was recently redesigned. It is only through this continuous development, that the capabilities of UC SIM have improved to the stage at which trace elements can now be analyzed.

III. Results

The microstructure of the 1000 ppm Y-doped Al_2O_3 is shown in Fig. 1. A few isolated pores are observed in the SEM micrograph (Fig 1(A)) confirming that the sample was near theoretical density. Grains were equiaxed with an average size of 2.6 ± 0.5 μm.[3] The SIMS maps shown in Fig. 1(B) and 1(C) were taken from the same area of the unetched sample; (B)

represents the unresolved ISI signal displaying topographic contrast, and (C) the mass-resolved Y^+ signal. The polishing procedure left little surface topography and thus the only features visible in the ISI map (Fig. 1(B)) are residual pores and occasional polishing scratches. In the corresponding Y^+ map a bright network of yttrium is observed, clearly demonstrating the segregation of Y to the Al_2O_3 grain boundaries. The thickness of this grain-boundary layer is determined to be approximately 0.1 μm. The uniformity of the signal intensity along each boundary indicates that the yttrium segregated isotropically. Comparison of the ISI and the Y^+ maps reveals that the surfaces of the isolated pores were also enriched with yttrium, as indicated in Fig 1(B),(C).

From the series of images shown in Fig. 1, it could be concluded that yttrium was accommodated only as a grain-boundary and surface segregant. However, Y^+ maps taken from different areas of the polished section (see Fig. 2) reveal an abundance of discrete Y-rich second phases, presumably YAG, located predominantly at the grain boundaries. In the regions containing a high density of YAG precipitates, the Al_2O_3 grain size was refined. A striking example of this is shown in Fig. 3; The Al_2O_3 grain size increases as the density of precipitates decreases, resulting in a "cobweb" structure.

The 1000 ppm La-doped Al_2O_3 sample was nearly fully-dense with a grain structure that was more elongated than that of the Y-doped sample (see Fig. 4(A)). The La^+ map in Fig 4(C) reveals a strong segregation of La to the Al_2O_3 grain boundaries. Similar to the Y-doped Al_2O_3, the dopant appears to be distributed uniformly along the grain boundaries. In addition, pore surfaces are enriched with the lanthanum, and La-rich precipitates are observed.

IV. Discussion

This work represents the first time that the distribution of Y and La have been mapped in a polycrystalline Al_2O_3. Both dopants are found to segregate to grain boundaries and pore surfaces, consistent with previous work on Y-doped Al_2O_3.[1,2,6-11] In contrast to other dopants such as Ca, which segregate anisotropically in Al_2O_3,[14] the Y and La appear to be distributed uniformly along the grain boundaries. Excess dopant that is not accommodated within the Al_2O_3 grains, or at the grain boundaries, is concentrated in discrete second phases. The ability to

distinguish between dopant segregation at the grain boundaries, pore surfaces, and precipitates within a single map underscores the useful capabilities of this imaging-SIMS technique.

In the light of these observations, it is appropriate to reconsider the role of yttrium in lowering the tensile creep rate of alumina. In a previous creep study it was determined that the principal effect of yttrium was to reduce the interface reaction believed to be governing the rate of grain boundary transport.[3] This hypothesis was based on microstructural observations which indicated an absence of second phases. Certainly, there exists regions of the Y-doped Al_2O_3 in which the YAG precipitates are sparse. However, the present analysis has also revealed areas of the material that contain an abundance of YAG precipitates. It is quite possible that these precipitates may be controlling the creep behavior. For example, YAG precipitates at the grain boundaries could inhibit the grain-boundary sliding that must accompany deformation. Resolution of these two contrasting hypotheses will require further creep work.

The non-uniform distribution YAG precipitates across the sample section is attributed to incomplete mixing of the Y-doped powder. It is interesting to note, however, that this artefact did not appear to diminish either the beneficial effect of yttrium doping on the tensile creep behavior, or the reproducibility of creep results. Two possible explanations for this favorable result are: (i) the creep behavior was dominated by the Y-rich grain boundary layer, and insensitive to the YAG precipitates, or (ii) the scale of the non-uniform distribution of precipitates was sufficiently small to yield an average and reproducible creep behavior across the sample section. These observation have some interesting implications: If the precipitates play no role in the creep behavior, then a similar creep behavior can be achieved at lower doping levels. Conversely, if the precipitates play a significant role, then increasing the volume fraction of precipitates should further improve the tensile creep properties. Further creep studies in this topic should therefore prove fruitful.

The similarity in the segregation behavior of Y and La indicates the potential of La-doping for reducing the creep rate of Al_2O_3. If the creep behavior arises from an inherent property of the dopant-rich boundaries or the grain-boundary precipitates, then La-doped Al_2O_3 could also have improved creep properties. Indeed, preliminary work has shown that lanthanum also reduces the creep rate of alumina, although not to the same extent.[15]

V. Conclusions

(1) Yttrium and lanthanum segregate to the grain boundaries and pore surfaces of polycrystalline alumina. Excess dopant is incorporated as discrete dopant-rich precipitates located predominantly at the grain boundaries.

(2) The role of yttrium in the reduction of the creep rate of Al_2O_3 should be reconsidered to include the effects of YAG precipitates.

(3) Lanthanum doping shows great potential for improving the creep properties of Al_2O_3.

(4) The imaging-SIMS technique is a powerful tool in the microanalysis of doped ceramics.

Acknowledgement

Development and operation of the unique SIM at the University of Chicago was sponsored by the National Science Foundation under grant DMR 9015868.

References

(1) K. Przybylski, A. J. Garratt-Reed, B. A. Pint, E. P. Katz, and G. J. Yurek, "Segregation of Y to Grain Boundaries in the Al_2O_3 Scale Formed on an ODS Alloy," *J. Electrochem. Soc.*, 134 3207-3208 (1987).

(2) B. A. Pint, J. R. Martin and L. W. Hobbs, "^{18}O/SIMS Characterization of the Growth Mechanism of Doped and Undoped α-Al_2O_3," *Oxidation of Metals*, **39** [3-4] 167-195 (1993).

(3) J. D. French, "High Temperature Deformation and Fracture Toughness of Duplex Ceramic Microstructures," Ph.D. Thesis, Lehigh University, (1993).

(4) S. Lartigue, C. Carry, and L. Priester, "Grain Boundaries in High Temperature Deformation of Yttria and Magnesia Co-Doped Alumina," *Coll. Phys. C1*, **51** [1] 985-90 (1990).

(5) P. Gruffel, and C. Carry, "Strain Rate Plateau in Creep of Yttria Doped Fine Grained Alumina," pp305-311 in Proc. of the 11th RISO International Symposium on Metallurgy and Materials Science: *Structural Ceramics - Microstructure and Properties*. Ed. by J. J. Bentzen, J. B. Bilde-Sorensen, N. Christiansen, A. Horsewell, and B. Ralph, Riso National Lab. Roskilde, Denmark, 1990.

(6) P. Gruffel, and C. Carry, "Effect of Grain Size on Yttrium Grain Boundary Segregation in Fine Grained Alumina, " submitted to *J. Eur. Ceram. Soc.*, (1994).

(7) C-W. Li, and W. D. Kingery, "Solute Segregation at Grain Boundaries in Polycrystalline Al_2O_3," pp 368-378 in Advances in Ceramics Vol. 10, *Structure and Properties of MgO and Al_2O_3 Ceramics*. Ed. W. D. Kingery, American Ceramic Society, Columbus, OH (1984).

(8) B. Bender, D. B. Williams, and M. R. Notis, "Investigation of Grain-Boundary Segregation in Ceramic Oxides by Analytical Scanning Transmission Electron Microscopy," *J. Amer. Ceram. Soc.*, **63** [9-10] 542-546 (1980).

(9) M. K. Loudjani, J. Roy, and A. M. Huntz, "Study by Extended X-Ray Absorption Fine-Structure Technique and Microscopy of the Chemical State of Yttrium in α-Polycrystalline Alumina, " *J. Amer. Ceram. Soc.*, **68** [11] 559-562 (1985).

(10) R. C. McCune, W. T. Donlon, and R. C. Ku, "Yttrium Segregation and Yag Precipitation at Surfaces of Yttrium-Doped α-Al_2O_3," *J. Amer. Ceram. Soc.*, **69** [8] C196-C199, (1986).

(11) P. Nanni, C. T. H. Stoddart, and A. D. Hondros, "Grain Boundary Segregation and Sintering in Alumina," *Materials Chemistry*, **1** 297-320 (1976).

(12) R. Levi-Setti, J. M. Chabala, J. Li, K. L. Gavrilov, R. Mogilevsky, and K. K. Soni, "Imaging-SIMS (Secondary Ion Mass Spectroscopy) Studies of Advanced Materials," Scanning Microscopy, **7** [4] 1161-1172 (1994).

(13) K. K. Soni, J. M. Chabala, R. Mogilevsky, R. Levi-Setti, W. S. Wolbach, S. R. Bryan,"Imaging Microanalysisi of Ceramic Materials with Scanning Ion Microprobe," *Surface and Interface Analysis*, **21** 117-122 (1994).

(14) S. Baik, J. H. Moon, "Effects of Magnesium Oxide on the Grain-Boundary Segregation of Calcium During Sintering of Alumina," *J. Amer. Ceram. Soc.*, **74** 819-822 (1991).

(15) A. M. Thompson, unpublished work.

(A)

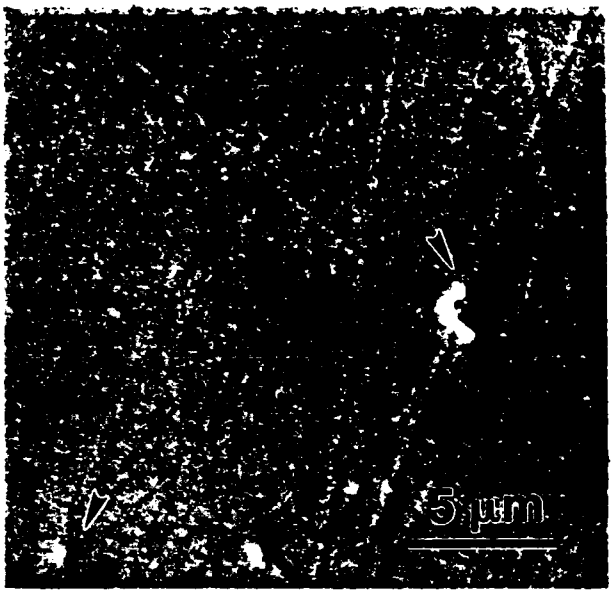

(B)

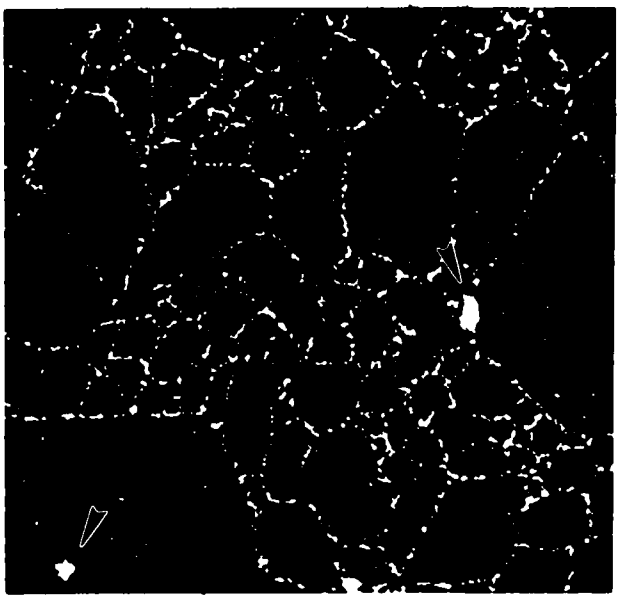

(C)

Figure 1: 1000 ppm Y-doped Al_2O_3; (A) SEM micrograph of a thermally etched polished section, (B) ISI SIMS map of an unetched polished section, (C) Y^+ SIMS map of same area clearly showing segregation of Y to pore surfaces and grain boundaries.

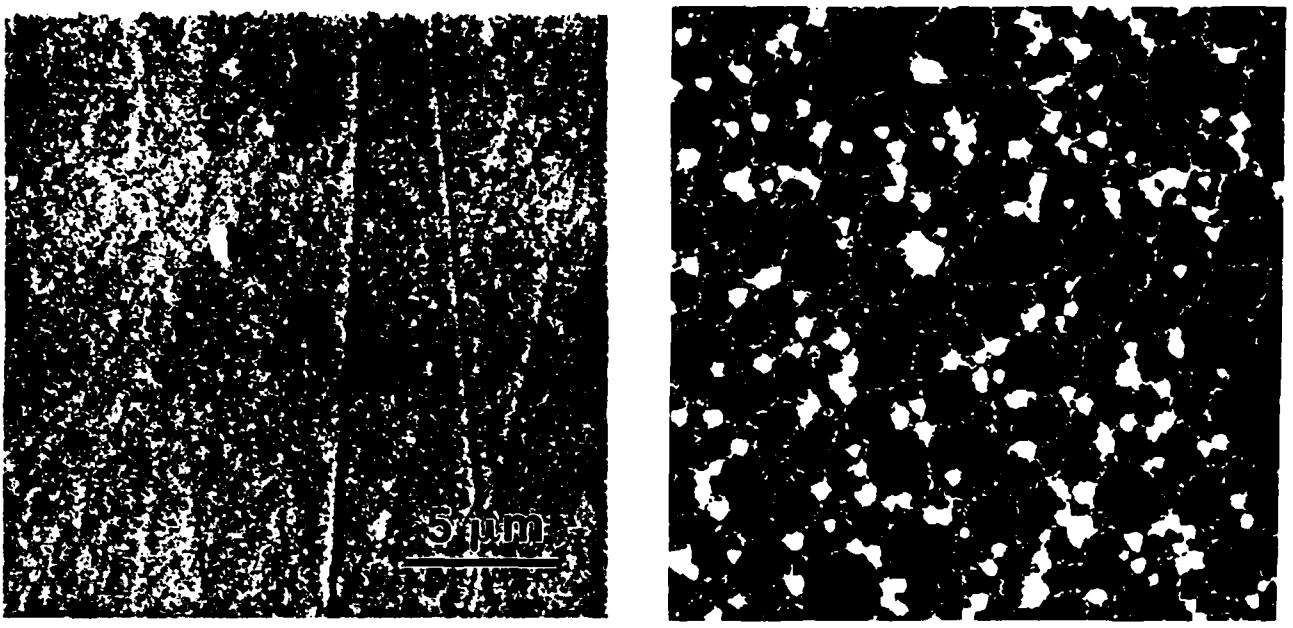

(A) (B)

Figure 2: 1000 ppm Y-doped Al_2O_3; (A) ISI SIMS map, (B) Y^+ SIMS map clearly showing Y-rich precipitates.

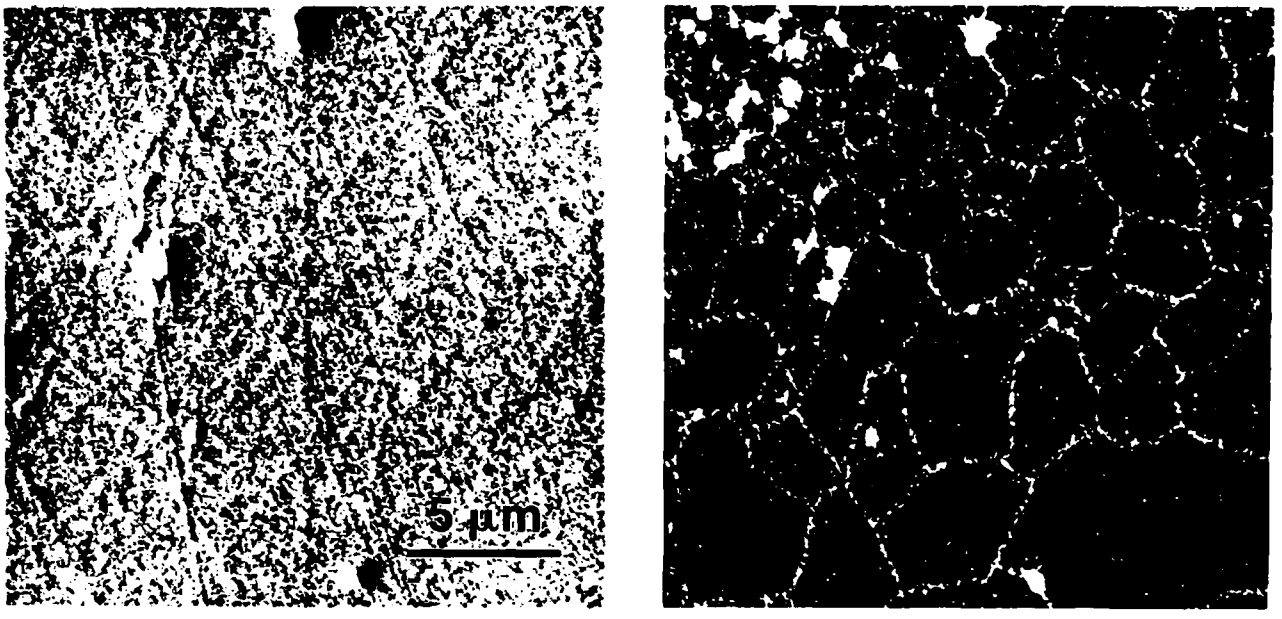

(A) (B)

Figure 3: 1000 ppm Y-doped Al_2O_3; (A) ISI SIMS map , (B) Y^+ SIMS map illustrating the "cobweb" structure resulting from the refinement of Al_2O_3 grains by the Y-rich precipitates.

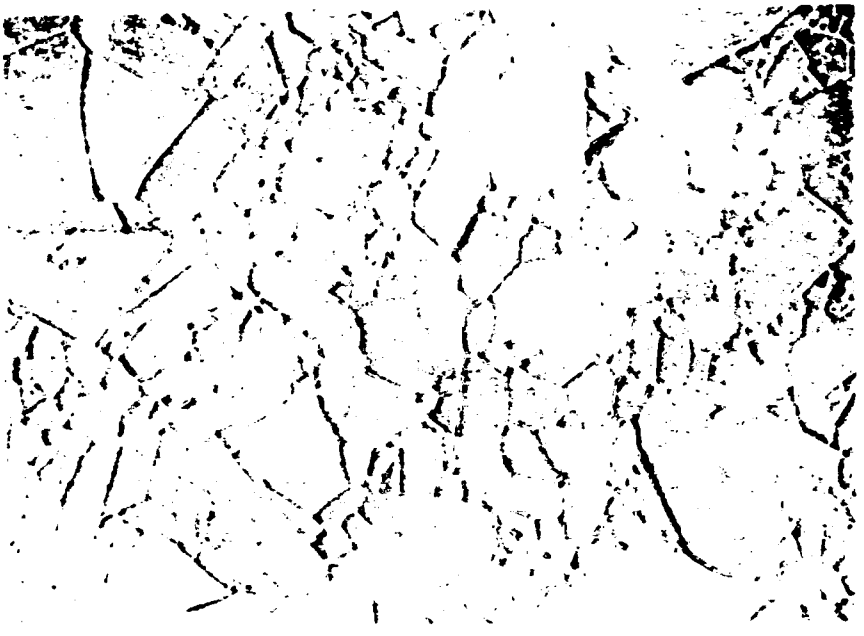

(A)

(B)

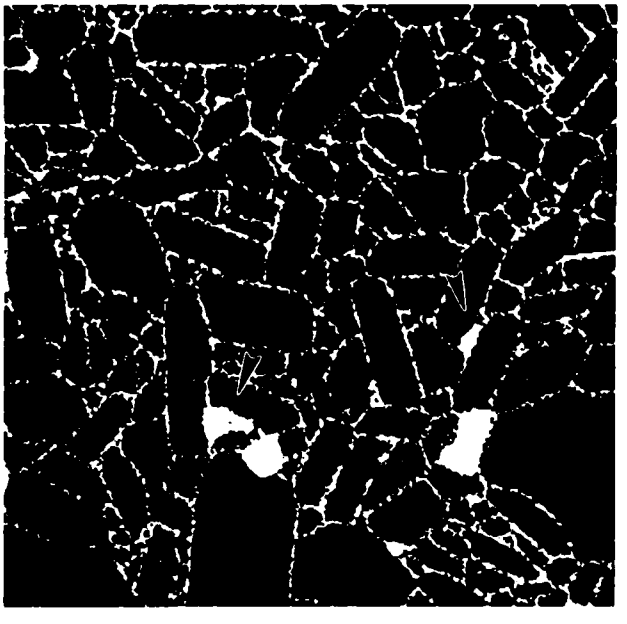

(C)

Figure 4: 1000 ppm La-doped Al_2O_3; (A) SEM micrograph of a thermally etched polished section, (B) ISI SIMS map of an unetched polished section, (C) La^+ SIMS map of same area clearly showing segregation of La to grain boundaries.

TOUGHENING MECHANISMS IN FLAW-TOLERANT ALUMINA-MULLITE CERAMICS

TOUGHENING MECHANISMS IN FLAW TOLERANT ALUMINA-MULLITE CERAMICS

A. Khan, H.M. Chan and M.P. Harmer

1. Introduction

In this study flaw tolerance is defined as an invariance in mechanical strength with flaw size. If obtainable, this is a desirable property in structural ceramics. Flaw tolerance of ceramics is known to improve if they display R-curve behavior during fracture [1], i.e. if resistance to crack propagation rises with increasing crack length. R-curve behavior is a consequence of crack tip shielding mechanisms that act to decrease the stress intensity at the crack tip as the crack grows. One type of shielding mechanism is known as the *bridged-interface*, in which the crack is bridged behind the crack tip, e.g. grain bridging, fiber bridging etc. [2]. This mechanism is now generally accepted as being responsible for R-curve behavior that is seen in nontransforming ceramics such as alumina and alumina-based ceramics, with grains acting as the bridges in the crack wake [1]. The most important variables affecting the amount of toughening achievable via this mechanism are, the internal stresses and the grain size [3,4,5,6]. The former variable controls the magnitude of frictional stresses between a bridging grain and the walls of the "sockets " in which it is situated, thus governing the amount of energy dissipated by a bridge during pull out and therefore its toughening contribution. The latter variable governs the critical crack opening displacement above which bridges disengage, thus affecting the area of bridging zone and therefore the toughening contribution.

Duplex alumina-mullite (AM) ceramics were chosen for study based on the "internal stresses" variable in mind. Significant internal stresses are expected to form in AM ceramics by virtue of a substantial mismatch in thermal expansion coefficient ($\alpha_A \approx 9 \times 10^{-6}$ K^{-1}, $\alpha_M \approx 5 \times 10^{-6}$ K^{-1}) which should lead to R-curve and hence flaw tolerant behavior. Other reasons for studying AM ceramics include the thermodynamic and morphological stability of AM mixtures, and the

potential for AM ceramics to exhibit attractive high temperature structural properties. The final reason derives from mullite's outstanding high temperature strength [7] and creep resistance [8].

Earlier work by Stuart [9] demonstrated that R-curve response is achievable in AM ceramics if the microstructure is coarsened to a grain size of about 7 μm; however the improvement in flaw tolerance was not significant. Moreover, the heat treatment time required to increase grain size further (and hence improve flaw tolerance) was too long to be practical. This led to the idea of deliberately introducing coarse-grained agglomerates of either alumina or mullite into the duplex AM matrix as potential bridging sites (the bridges being either, individual agglomerates or the large grains within them). This two-phase structure with a bimodal grain size distribution is termed a duplex-bimodal structure. A substantial improvement in flaw tolerance was demonstrated in this type of structure, the duplex-bimodal structure with the alumina agglomerates showing the best combination of strength and flaw tolerance. Although the alumina agglomerates were added with the intent that they individually, or the grains within them, act as bridges in the wake of a crack, this has not been substantiated. Also, other R-curve inducing mechanisms may be operative as well.

2. Objective

Firstly, the objective of this research was to elucidate the R-curve producing mechanisms that are responsible for improving flaw tolerance of duplex-bimodal AM ceramics. Secondly, variables affecting these mechanisms were to be manipulated with the intent of optimizing strength and flaw tolerance.

3. Approach

A series of experiments were conducted to identify the mechanism(s) responsible for R-curve behavior in duplex-bimodal AM ceramics. These included evaluating flaw tolerance as a

function of, (i) alumina agglomerate volume fraction (V_f) (agglomerate size fixed) and, (ii) alumina agglomerate size (agglomerate V_f fixed). These experiments combined with in-situ crack propagation experiments should reveal useful information regarding the operative R-curve mechanism(s). Once identified, variables affecting these mechanisms will be manipulated to optimize flaw tolerance.

4. Experimental Details

Batches of alumina+ 50 vol.% mullite (AM50) powder were mixed with ethanol and ball-milled into homogeneous slurries. Appropriate amounts of "sized" spherical spray-dried soft alumina agglomerates were gently stirred into these slurries to make the various duplex bimodal compositions required. The powder slurry mixtures were then dried under a heat lamp, while still stirring, to prevent settling of the agglomerates. In this manner a series of powder mixtures with 0, 0.15, 0.30 and 0.45 V_f medium sized alumina agglomerates were made. Two additional powder mixtures, one with 0.15 V_f small alumina agglomerates, and the other with 0.15 V_f large alumina agglomerates, were also made. The alumina agglomerate designations, "medium" and "large" refer to starting mean diameters of $\approx 69 \pm 6$ and 98 ± 7 μm respectively. The "small" designation corresponds to starting agglomerate diameters < 38 μm. Compositions are designated as AM50-$x(A_{ag})_y$ where AM50 corresponds to the 50/50 vol.% alumina+mullite matrix, A_{ag} corresponds to the alumina agglomerates, x to the volume fraction of agglomerates and y to their size designation (s=small, m=medium and L=large). Disc shaped samples for mechanical testing were first uniaxially pressed (30 MPa) and then isopressed (350 MPa) to remove density variations. The samples were then calcined in air at 1000°C for 4 hrs. to remove carbon and sulfur impurities, and pressureless sintered in air at 1650°C for 25 hours.

Flaw tolerance was evaluated using the so called identation-strength-in-bending testing technique. This is a method by which flaw tolerance and R-curve behavior can be qualitatively

assessed [10]. One can also extract quantitative R-curves from indentation-strength (P-σ) data using appropriate constitutive relations as done by Chantikul et al. for alumina [11], but this procedure was not carried out in this work. First, the tensile surfaces of disc shaped samples were indented with a Vickers indenter to introduce controlled flaws. Samples requiring the low-load indents were polished to a fine finish prior to indentation. Fracture strengths of the "flawed" samples were then measured in biaxial flexure. Fracture strength was measured for indentation loads in the range of 10 to 300 N. During loading, failures typically originated from one of the radial crack pairs emanating from an indent. Fractured sample surfaces were examined with an optical microscope to ensure failure originated from the indentation flaws. Any samples which did not fail from an indentation flaw were considered to have failed from an intrinsic flaw, therefore giving an intrinsic strength.

It should be noted that the biaxial flexure test geometry used in this study has been modified since previously reported work. Now thinner (2 mm thick vs. 3 mm), larger diameter discs (25 mm vs. 20 mm) are being tested on a larger support circle diameter (22 mm vs. 16 mm) and being loaded with a smaller loading flat diameter (3.2 mm vs 5.4 mm). With this geometry, the thin plate formulas used for determining fracture strengths are more accurate. Also, the failure yield from low load indent (small crack) samples is improved noticeably with this new testing geometry. This small flaw size data is very valuable and was often "lost" with the old testing geometry.

In-situ crack propagation experiments were conducted using a three point bending fixture which allowed qualitative observation of crack/microstructure interaction with either optical microscopy or SEM. Disc shaped samples with indentation cracks on a polished tensile surface were placed into this fixture and loaded by turning a screw against the compressive surface. Then the sample/fixture combination was placed under an optical microsope or into a SEM to image the crack path morphology with the sample under load.

4. Results and Discussion

Microstructure:

Sintered samples were nearly fully dense, all compositions sintering to densities in excess of 98.5 % theoretical. It is believed that the pressureless sintering processing route works in this case because the alumina agglomerates are initially *soft*, and sinter at a rate similar to the AM50 matrix, thereby preventing any differential sintering which would impede densification [12]. The resulting microstructures of the various AM50-$x(A_{ag})_y$ compositions had an AM50 grain size of ≈ 2 μm (measured) and an alumina agglomerate grain size of ≈ 10 μm (estimated). Final alumina agglomerate diameters were 78 ± 6, 55 ±5 and < 30 μm for the "large", "medium" and "small" designations respectively. An example of a typical microstructure at low and high magnification is shown in Figures 1a and 1b respectively (in this case that of an AM50-0.3$(A_{ag})_m$ sample). One can clearly see that the simple mixing procedure used to process the duplex-bimodal AM ceramics disperses the alumina agglomerates fairly well (Fig. 1a). At higher magnification it is apparent that the agglomerate grain size is at least an order of magnitude greater than that of the AM50 matrix (Fig. 1b).

Indentation-Strength Response:

Indentation-strength (P-σ) responses of the various duplex-bimodal AM compositions evaluated in this study are shown in Figures 2, 3 and 4. The shaded boxes indicate the range of intrinsic strength values of the various compositions, the majority of which are from 10 N indent load samples. The intrinsic strengths are taken to correspond to a range of indentation loads below the 10 N indentation load of those samples. Data points plotted with an error bar at a particular indentation load represent the mean and standard deviation of at least eight individual strength data

points. For cases with less strength data, individual points are plotted. In Figure 2 the P-σ response of AM50 is compared with AM50-0.15$(A_{ag})_m$. The addition of alumina agglomerates flattens the P-σ response indicating that the AM50-0.15$(A_{ag})_m$ composition is a more flaw tolerant than AM50. Further improvement in flaw tolerance is realized as alumina agglomerate volume fraction is increased as shown in Figure 3. There is a substantial improvement in strengths at high indent loads as $V_f(A_{ag})_m$ is increased from 0.15 to 0.3. This improvement appears to be saturated at 0.3 $(A_{ag})_m$, a minimal increase being seen from 0.3 to 0.45$(A_{ag})_m$. Although the high indentation load strengths increased with increasing $V_f(A_{ag})_m$, the P-σ response of all three compositions plateau at approximately the same intrinsic strength level.

The P-σ response of AM50-0.15$(A_{ag})_s$ at 10 and 300 N is shown compared with that of AM50-0.15$(A_{ag})_L$ in Figure 4. Since the alumina agglomerate volume fraction is kept constant, varying agglomerate size changes the number density of agglomerates. The AM50-0.15$(A_{ag})_s$ composition has approximately 17x more alumina agglomerates than the AM50-0.15$(A_{ag})_L$ composition as calculated assuming all agglomerates as spherical with a "small" diameter of 30 μm and "large" diameter of 78 μm. The 300 N strength of AM50-0.15$(A_{ag})_L$ is greater than that of AM50-0.15$(A_{ag})_s$, 162 ±4 vs. 145 ±6 MPa respectively. There doesn't appear to be a strength difference between the two compositions at the lower indentation load of 10 N. A difference may become apparent with more AM50-0.15$(A_{ag})_L$ 10 N data points, there currently being only four points to compare against AM50-0.15$(A_{ag})_s$. To test the R-curve mechanism of bridging grains within alumina agglomerates, assume that only one bridge per agglomerate forms (actually an overestimate based on what is observed). Variables that would affect toughening are, (i) the alumina agglomerate grain size, (ii) the alumina agglomerate's internal stress state, and (iii) the number density of alumina agglomerates. Considering that the alumina agglomerate grain size of

both compositions is the same, and that the alumina agglomerate's internal stress state is not a function of agglomerate diameter [14] (assuming no debonding), the number density of agglomerates is the only remaining variable that could potentially affect R-curve toughening. Since there are ≈ 17x more alumina agglomerates in AM50-0.15$(A_{ag})_S$ and hence that many more potential bridges, one would expect greater toughening and consequently, a higher 300 N strength for this composition than AM50-0.15$(A_{ag})_L$. This is the opposite of what is observed. It follows that the origin of the 300 N indent strength difference may be from a different mechanism, i.e. either from the formation of elastic bridges or microcracking as described in the next section. Another possible explanation for the 300 N indent strength increase with alumina agglomerate diameter may be that the AM50-0.15$(A_{ag})_L$ composition is more susceptible to lateral cracking, a phenomena that is known to increase strength of ceramics at high indent loads [13].

In-Situ Crack Propagation Experiments:

In-situ crack propagation experiments have identified several types of crack/microstructure interactions in AM50-0.15$(A_{ag})_m$ and AM50-0.3$(A_{ag})_m$ samples. From these observations various possible R-curve producing mechanisms can be postulated. For example, fracture appears to proceed both around and through alumina agglomerates as shown in Figure 5 for an AM50-0.15$(A_{ag})_m$ specimen. Crack deflection around an alumina agglomerate can be explained in terms of the local stress state that arises due to differential contraction from the sintering temperature. Since $\alpha_A > \alpha_{AM50}$, the local stress state is that of tangential compression and radial tension in the AM50 adjacent to an alumina agglomerate, a stress state that favors crack deflection [14]. Although crack deflection is a toughening process it does not give rise to R-curve behavior [15]. The case of fracture path preference through alumina agglomerates may be the result of agglomerate/agglomerate stress field interactions or of a fairly strong agglomerate/matrix interface

strength. Fracture through agglomerates is desirable in that it provides the potential for the coarser alumina grains within them to set up as bridges, a mechanism known to produce R-curve behavior.

Occasionally cracks which grow into agglomerates lead to grain bridge formation as shown in Figure 6 for an AM50-0.3$(A_{ag})_m$ sample. In this case a large alumina grain within an alumina agglomerate is bridging the crack behind the crack tip. However, qualitative observation shows this type of bridge formation not to occur very often. Another bridging mechanism which occurred with some fre ency is what is known as beam-like elastic bridge formation, examples of which are shown in Figure 7. These types of bridges are characterized by a discontinuity in the crack as observed in 2D, resulting in a nonfractured beam-like ligament behind the crack tip. This nonfractured ligament is effectively another type of bridge in the crack wake and can also contribute to R-curve behavior.

In-situ crack growth experiments in an AM50-0.3$(A_{ag})_m$ specimen have also identified microcracking as another type of fracture mechanism in duplex-bimodal AM ceramics as shown in Figure 8. Microcracks have opened ahead of the crack tip in an orientation approximately perpendicular to the loading direction. These microcracks appear to remain open along the wake of the crack. Prior to loading very few microcracks were visible in this sample. This observation along with the crack orientation/stress direction observation indicate the microcracks formed as a result of the applied stress. The locations of the microcracks seen in Figure 8 are consistent with the microstress state associated with the agglomerates. As mentioned earlier the AM50 matrix adjacent to the alumina agglomerates is in a state of tangential compression and radial tension, and the agglomerates themselves in a state of hydrostatic tension. This type of microstress state supports the types of microcracking seen, i.e. (i) microcracking at the agglomerate/matrix interface (almost circumferential in some cases), (ii) microcracking of the matrix in-between agglomerates and (iii) microcracking within agglomerates. Evans and Faber [16] have modeled crack growth resistance for the case of a brittle material in which microcracks are formed ahead of a macro-crack tip during loading and then remain open in the macro-crack's wake. In their model they showed

theoretically that this type of mechanism can result in R-curve behavior. Since the microcracking observations just described are consistent with what Evans and Faber modeled, microcracking in the AM50-$x(A_{ag})_y$ ceramics is also postulated as a potential R-curve producing mechanism.

5. Status

In-situ fracture experiments have identified several different fracture mechanisms that may account for R-curve behavior in duplex-bimodal AM ceramics. These mechanisms are most likely acting simultaneously to effect R-curve behavior in duplex-bimodal AM ceramics, thereby resulting in the improved flaw tolerance as seen using the P-σ technique. Currently the plan is to determine the relative contributions of each mechanism and to see if one dominates. Based on these findings, work will focus on optimizing R-curve toughening to further improve flaw tolerance.

References

1. S.J. Bennison, N.P. Padture, J.L. Runyan and B.R. Lawn, "Flaw-insensitive ceramics," *Philosophical Magazine Letters*, vol. 64, no. 4, 191-95 (1991).

2. B. Lawn, Fracture of Brittle Solids-Second Edition, Cambridge University Press, 1993, 209-10.

3. Y-W. Mai and B.R. Lawn, "Crack-Interface Bridging as a Fracture Resistance Mechanism in Ceramics: II, Theoretical Fracture Mechanics Model," *J. Am. Ceram. Soc.*, 70 [4] 289-94 (1987).

4. M.V. Swain, "R-Curve Behavior in a Polycrystalline Alumina Material," *J. Mater. Sci. Lett.*, 5 1313-15 (1986).

5. S.J. Bennison and B.R. Lawn, "Role of Interfacial Grain-Bridging Sliding Friction in the Crack-Resistance and Strength Properties of Nontransforming Ceramics," *Acta Metall.*, 37 [10] 2659-71 (1989).

6. G. Vekinis, M.F. Ashby and P.W.R. Beaumont, "R-Curve Behavior of Al_2O_3 Ceramics," *Acta Metall. et Mater.*, 38 [6] 1151-62 (1990).

7. M. Ismail, Z. Nakai and S. Somiya, "Microstructure and Mechanical Properties of Mullite Prepared by the Sol-Gel Method," *J. Am. Ceram. Soc.*, 70 [1] C7-8 (1987).

8. R.A. Penty and D.P.H. Hasselman, "Creep Kinetics of High Purity, Ultra Fine Grain Polycrystalline Mullite," *Mater. Res. Bull.*, 7 [10] 1117-23 (1972).

9. M. Stuart, "Characterization and Mechanical Behavior of Alumina-Mullite Ceramics", M.S. Thesis, Lehigh University, Bethlehem, PA, 1991.

10. C.J. Russo, M.P. Harmer, H.M. Chan and G.A. Miller, "Design of a Laminated Ceramic Composite for Improved Strength and Toughness," *J. Am. Ceram. Soc.*, 75 [12] 3396-400 (1992).

11. P. Chantikul, S.J. Bennison and B.R. Lawn, "Role of Grain Size in the Strength and R-Curve Properties of Alumina," *J. Am. Ceram. Soc.*, 73 [8] 2419-27 (1990).

12. F.W. Dynys and J.W. Halloran, "Influence of Aggregates on Sintering," *J. Am. Ceram. Soc.*, 67 [9] 596-601 (1984).

13. R.F. Cook, E.G. Liniger, R.W. Steinbrech and F. Deuerler, "Sigmoidal Indentation-Strength Characteristics of Polycrystalline Alumina," *J. Am. Ceram. Soc.*, 77 [2] 303-14 (1994).

14. R.W. Davidge and T.J. Green, "The Strength of Two-Phase Ceramic/Glass Materials," *J. Mater. Sci.*, 3 [6] 629-34 (1968).

15. P.L. Swanson, D.J. Fairbanks, B.R. Lawn, Y-W. Mai and B.J. Hockey, "Crack-Interface Grain Bridging as a Fracture Resistance Mechanism in Ceramics: I. Experimental Study on Alumina," *J. Am. Ceram. Soc.*, 70 [4] 279-89 (1987).

16. A.G. Evans and K.T. Faber, "Crack-Growth Resistance of Microcracking Brittle Materials," *J. Am. Ceram. Soc.*, 67 [4] 255-260 (1984).

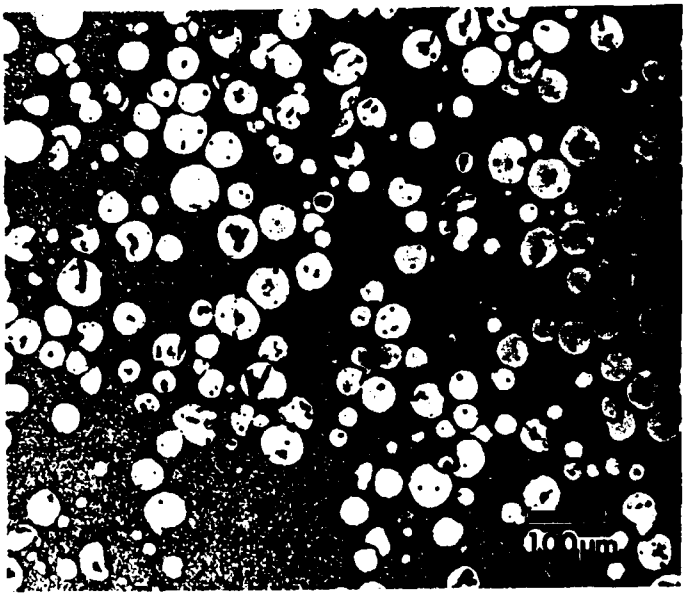

Figure 1a- Optical micrograph of AM50-0.3$(A_{ag})_m$ showing a typical duplex-bimodal AM microstructure. Note that most of the alumina agglomerates maintain their spherical shape and are fairly evenly dispersed within the AM50 matrix.

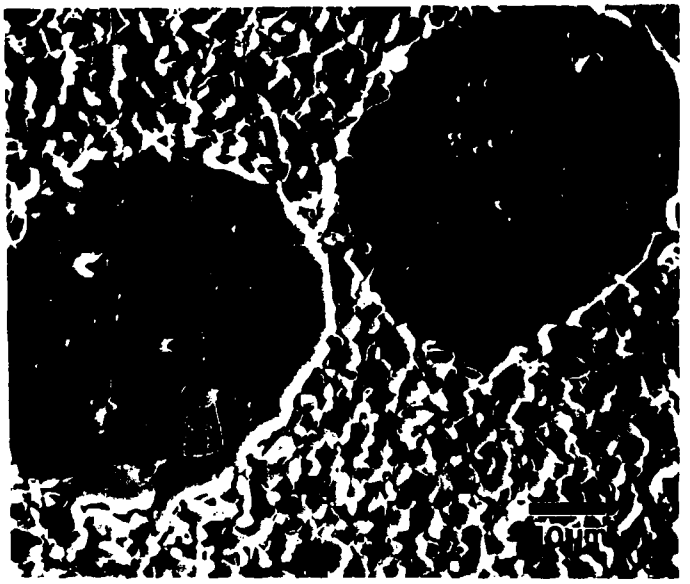

Figure 1b- SEM micrograph of AM50-0.3$(A_{ag})_m$ showing coarse grains within alumina agglomerates and a finer grained AM50 matrix. Sample thermally etched at 1575°C for 0.5 h.

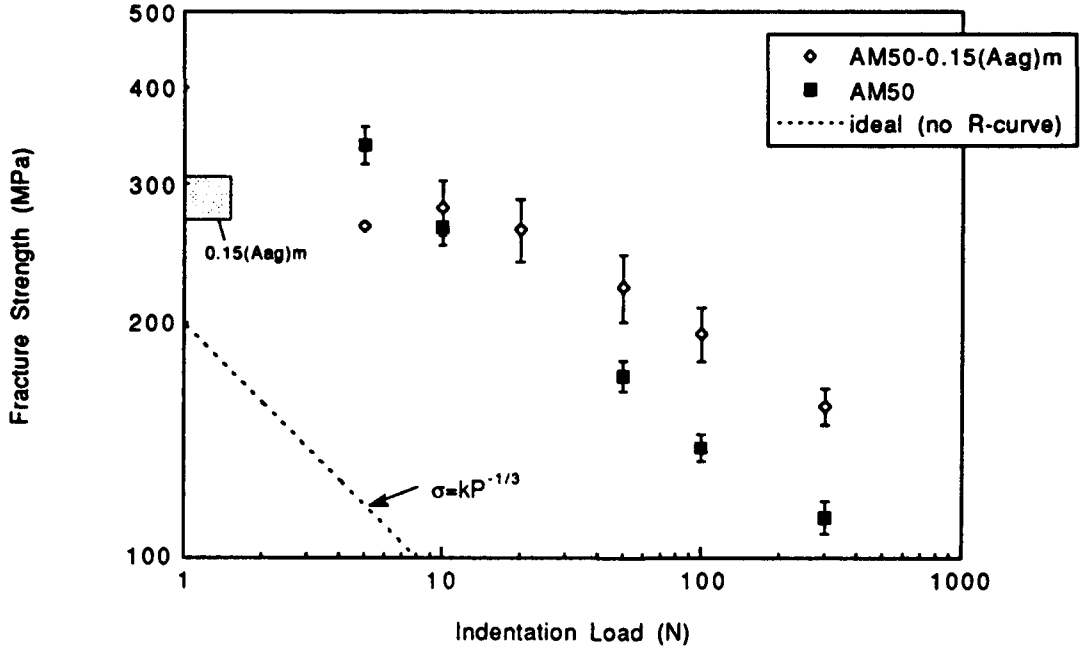

Figure 2- Comparison of the P-σ response of AM50 and AM50-0.15$(A_{ag})_m$.

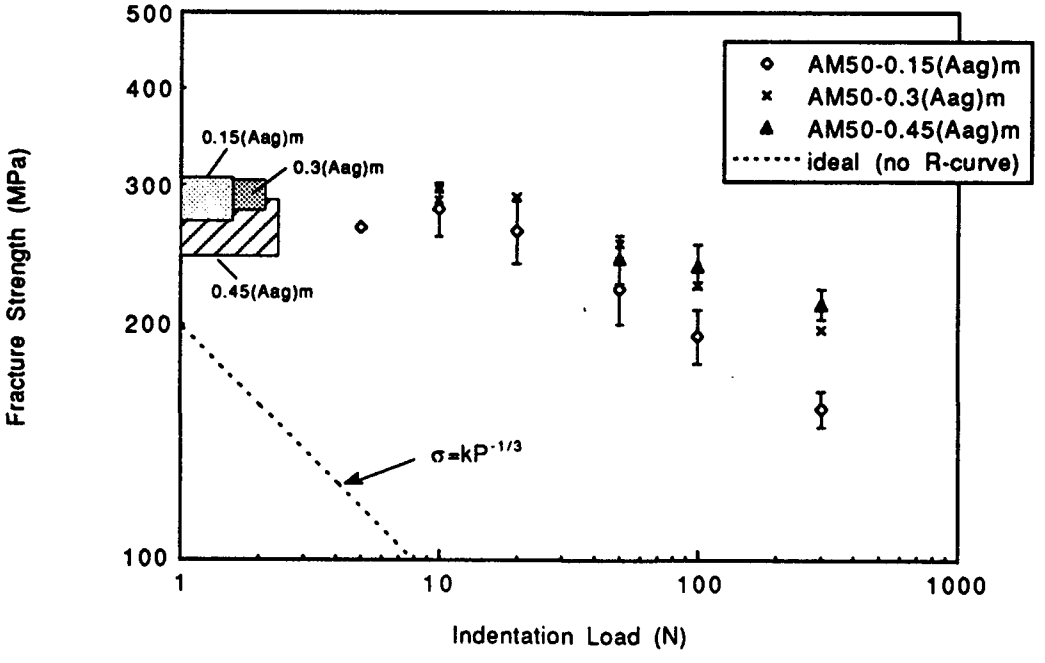

Figure 3- P-σ response as a function of agglomerate volume fraction (medium sized alumina agglomerates). Error bars for AM50-0.3$(A_{ag})_m$ removed for clarity.

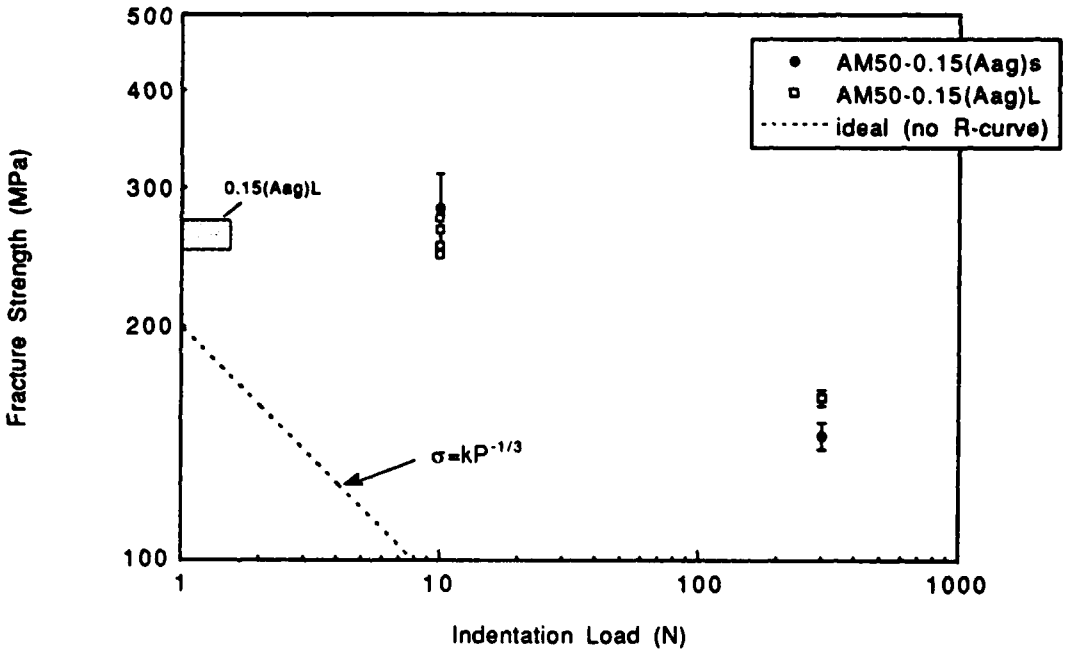

Figure 4- Comparison of P-σ response of AM50-0.15(A_{ag})$_s$ with AM50-0.15(A_{ag})$_L$, i.e. alumina agglomerate size effect.

Figure 5- In-situ fracture: Optical micrograph mosaic of fracture path in AM50-0.15$(A_{ag})_m$ showing how sometimes the fracture path, (a) is deflected around alumina agglomerates and (b) proceeds through agglomerates. Sample is under load.

Figure 6- In-situ fracture: Optical micrograph mosaic of crack path in AM50-0.3(A_{ag})$_m$ showing a bridging alumina grain within an alumina agglomerate. Sample is under load.

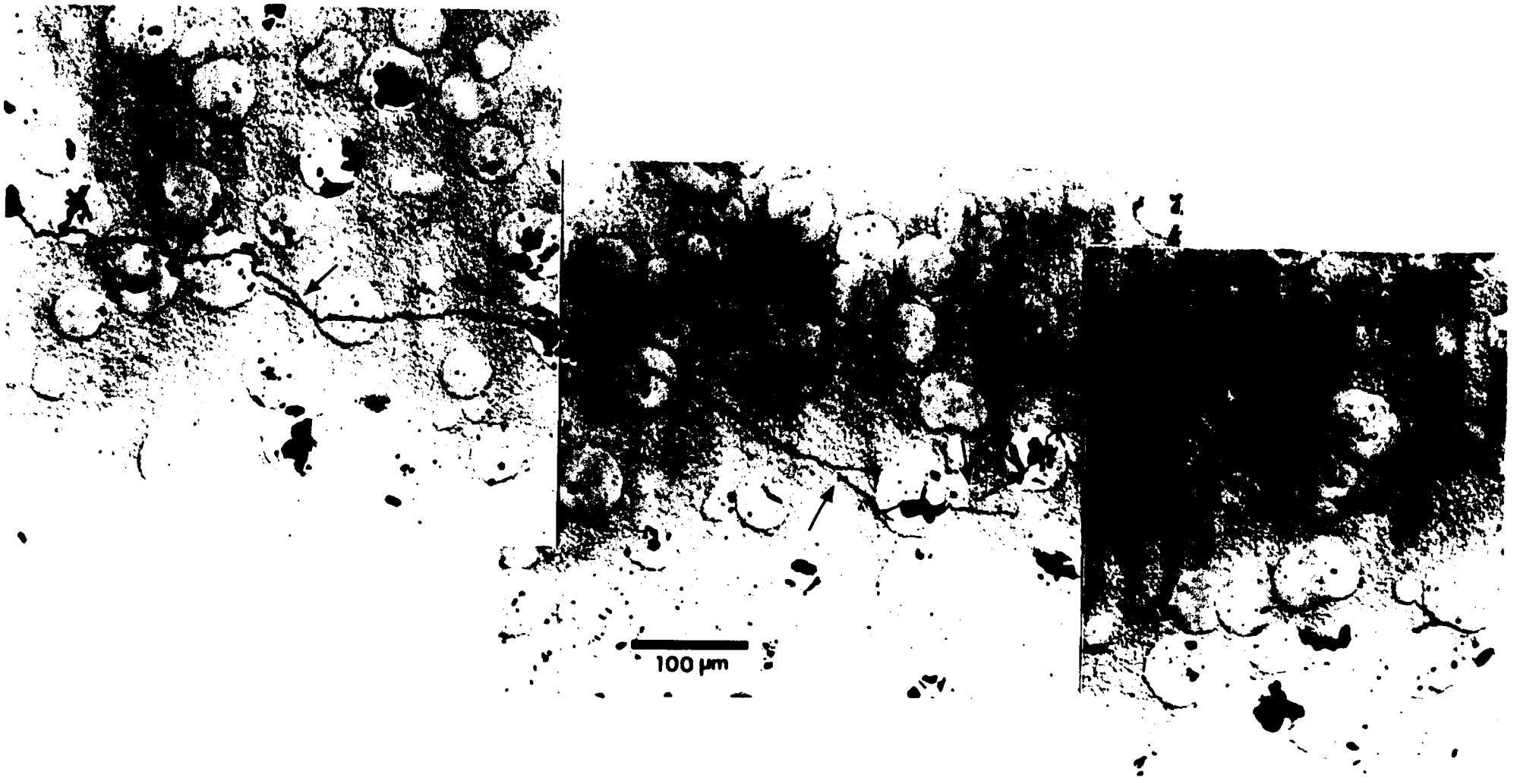

Figure 7- In-situ fracture: Optical micrograph mosaic showing formation of beam-like elastic bridges in AM50-0.3$(A_{sg})_m$. Sample is under load.

Figure 8- In-situ fracture: Scanning electron micrograph mosaic showing macrocrack and microcracks in AM50-0.3$(A_{ag})_m$. Note, (a) microcracking at the alumina agglomerate/AM50 matrix interface, (b) microcracking of the matrix in-between alumina agglomerates and (c) microcracking within alumina agglomerates.

HIGH TEMPERATURE FRACTURE TOUGHNESS OF DUPLEX MICROSTRUCTURES

HIGH TEMPERATURE FRACTURE TOUGHNESS OF DUPLEX MICROSTRUCTURES

Jonathan D. French[†,•], Helen M. Chan[•], Martin P. Harmer[•] and Gary A. Miller

Department of Materials Science and Engineering
and
Materials Research Center

Lehigh University, Bethlehem, PA 18015

Supported by the United Stated Office for Scientific Research under Contract Number 91-0126.

Based in part on the thesis submitted by J. D. French for the Ph. D. degree in Materials Science and Engineering, Lehigh University, Bethlehem, PA, 1993.

[†]Present address, Guest Scientist at the National Institute of Standards and Technology, Gaithersburg, MD 20899.

[•]Member of The American Ceramic Society.

Abstract

The temperature dependence of the fracture toughness of ceramics exhibiting duplex microstructures was studied relative to their single-phase constituents using two test methods: bend testing of chevron-notched beams, and the indentation technique. The two materials systems studied were Al_2O_3:c-ZrO_2(Y) and Al_2O_3:$Y_3Al_5O_{12}$ (YAG), and the testing temperature ranged from room temperature to 1200°C. The study showed that in both systems, the duplex materials showed higher toughness values than their single-phase constituents above 800°C. This result was attributed to the contribution of low energy interphase boundaries to the overall composite toughness. Indentation crack length measurements gave comparable toughness values and trends to those determined by the chevron-notched beam method. By comparing the results of the two test methods it was possible to demonstrate that the indentation calibration constant (ξ) shows no significant temperature or material dependence. For the zirconia containing materials, however, indentation at elevated temperatures is accompanied by significant localized plasticity, which suppressed the radial cracking. Under such conditions, some caution is warranted, since this can lead to an overestimation of the fracture toughness.

1. Introduction

Recent studies have shown that duplex microstructures offer several unique advantages for structural applications [1]. These include improved flaw tolerant behavior [2], and enhanced microstructural stability at high temperatures [3]. In many respects, Al_2O_3:c-ZrO_2(Y) and Al_2O_3:$Y_3Al_5O_{12}$(YAG) are ideal model duplex systems in that they form simple eutectics with no intermediate compounds, and exhibit limited solid-solid solubility between the end member

compositions. Previous studies have shown that relative to the single-phase constituents, grain growth is significantly retarded in both Al_2O_3:50 vol% c-ZrO_2 (AZ50) [3] and Al_2O_3:50 vol.% YAG (AY50) [4]. For composites in the Al_2O_3:c-ZrO_2 system, the room temperature strength and fracture toughness values were found to increase linearly with increasing alumina content [5]. Most recently, it was observed by French et al. [6] that the tensile creep behavior of both AZ50 and AY50 was superior to that of the constituent single phase materials, i.e. alumina, and either c-ZrO_2 or YAG respectively. However, when Y^{+3}-*doped* alumina was taken as the end-member composition, the behavior of both composites could be modelled according to a simple isostrain law of mixtures, which was derived assuming that the strain rate in both phases is uniform.

Despite the importance of high temperature fracture toughness from a design standpoint, pertinent data are relatively sparse [7-11]. Due its experimental simplicity, the indentation technique has found widespread use for room temperature testing, but has only been applied to the determination of high temperature fracture toughness in rare instances [12]. The objective of this work, therefore, was two-fold: to study the high temperature fracture toughness behavior of duplex microstructures using conventional chevron-notched bend testing, and to evaluate the direct indentation crack measurement method by comparing the results from both methods.

I. Chevron-Notched Beam Tests

1.1 Experimental

The experimental procedures for billet fabrication of the materials in this study have been discussed in detail elsewhere [6]. Briefly, composites of AZ50 and AY50 were processed by

mechanically mixing powders of Al_2O_3[1]+c-ZrO_2(Y)[2] and Al_2O_3+Y_2O_3[3] in the appropriate proportions. This was followed by uniaxial and isostatic pressing of the green pellets, and pressureless sintering to densities > 99% theoretical. In order to produce the corresponding single phase materials with similar average grain sizes (~2 μm) and sintered densities (>99% of theoretical) to the composites, alumina, c-ZrO_2 and YAG specimens were vacuum hot-pressed in graphite foil-lined graphite dies (3 *in. ID*).

Chevron-notched bend bars for mechanical testing were obtained by commercial machining[4]; the chevron geometry used is illustrated in Figure 1 [13]. The tests were carried out in air on a servo-hydraulic machine with attached high temperature furnace[5]. The specimens were tested in four-point-bending (inner and outer spans of 20 and 40 mm, respectively), at a crosshead speed of 0.050 mm/min. Under these conditions, the duration of each test was approximately 15 - 20 seconds. The test set-up was such that many samples could be broken in rapid succession. After fracture, the specimen halves dropped to the bottom of the furnace into catch-trays, and were immediately removed to minimize thermal etching of the fracture surface. Four or five valid tests were conducted at each temperature (R.T., 800°, 1000° and 1200°C). The validity of each test was determined by ensuring that the load-deflection (P-δ) curve bent over prior to failure, indicating stable crack growth [14]. Note that creep is not likely to contribute

---

[1]AKP-53, Sumitomo Corp.

[2]8 mol% Y_2O_3, Tosoh Inc.

[3]Molycorp

[4]Bomas Machine Specialties, Inc and Insaco Inc.

[5]MTS, Inc.

to the nonlinear P-δ curve for these materials for the crosshead speed used, even at 1200°C [6].

The fracture toughness from the chevron-notch tests, K_{ICV}, was calculated using the following relation [15]:

$$K_{ICV} = Y_m^*[P_{max}(S_1-S_2)/BW^{3/2}] \quad (1)$$

where W is the specimen height (6 mm), B is the width (3 mm), S_1 and S_2 are the outer and inner spans, respectively, P_{max} is the maximum load and Y_m^* is a calibration factor. The calibration constant was calculated using the Bluhm slice model [16,17] with the aid of a computer program [13]; a value of 4.356 was obtained for the chevron geometry used. A review of fracture toughness testing using chevron-notched specimens has been given by Newman [18].

1.2 Results

Fracture toughness, as a function of test temperature is plotted in Figure 2 for both composite systems. The room temperature values are within the range of values reported previously for similar materials [5,8-10,12,19,20]. The study showed that the fracture toughness decreased with increasing temperature for all materials except the YAG, in which it increased slightly. Interestingly, at temperatures above ~400°C, the composites of both systems exhibited higher fracture toughness values than their single phase constituents.

Fractography showed that the c-ZrO_2 and YAG materials experience a change in fracture mode with increasing temperature. At room temperature c-ZrO_2 and YAG both fracture transgranularly. At temperatures of 800°C and greater, however, these materials fracture intergranularly; see Figure 3. Conversely, the failure mode in Al_2O_3 was intergranular at all test temperatures. For the composite materials, the fracture surfaces exhibited a mixture of trans- and

intergranular failure at room temperature, and all intergranular fracture at high temperatures. No evidence of plasticity was observed on any of the fracture surfaces for any test temperature.

1.3 Discussion

a) Single phase materials

To rationalize the temperature dependence of the fracture toughness, consider the relation

$$K_{IC} = (2\gamma_{eff}E)^{1/2} \qquad (2)$$

where γ_{eff} is the effective fracture surface energy, and E is Young's modulus [21]. Clearly both terms will vary with temperature, and contribute to the overall temperature dependence of the fracture toughness. Taking into account the temperature dependence of the elastic modulus [22-26][6], we can plot the effective fracture surface energies ($2\gamma_{eff}$) for the materials tested in this study as a function of temperature (see Figure 4).

In the case of completely brittle fracture, since increased thermal vibration will facilitate bond breakage, one would expect γ_{eff} to decrease with increasing temperature, and this was indeed the case for all the materials studied. In the fracture of single crystal materials, the temperature dependence of γ_{eff} will be equivalent to that of the surface energy γ_s [7], however in polycrystalline materials there is the added consideration of fracture mode.

For the case of intergranular fracture, the energy (per unit area) required to separate two grains along the boundary is:

---

[6] In the case of c-ZrO_2, due to lack of data, values of elastic modulus for temperatures > 700°C were obtained by extrapolation [32]. For YAG, all values from room temperature and higher were obtained by extrapolation of data measured in the range 150 - 300 K [33]. For AZ50 and AY50, elastic moduli values were calculated using the averaging method by Hashin and Shtrikman [36].

$$G = 2\gamma_s - \gamma_{gb} \quad (3)$$

where γ_s is the surface energy and γ_{gb} is the grain boundary energy [28]. If one considers a mode I crack propagating perpendicular to the grain boundary, then in order for it to be deflected down the boundary, the value of γ_{gb} must be sufficiently large to make this path energetically favorable. A simple approximation for the criterion when this will occur is given by $\gamma_{gb} > \gamma_s$ [28-30]. A more rigorous approach was adopted by He and Hutchinson [31], who obtained the criterion for intergranular (or interfacial) fracture of $\gamma_{gb} > 1.5\gamma_s$.

The fact that the c-ZrO_2 and YAG materials undergo a transition in fracture mode from trans- to intergranular, clearly reflects a change in the relative temperature dependencies of the surface and grain boundary energies. Specifically, the results indicate that the ratio of the grain boundary energy to surface energy is increasing with temperature such that (using the He and Hutchinson criterion [31]), $\gamma_{gb}/\gamma_s < 1.5$ at low temperatures, and $\gamma_{gb}/\gamma_s > 1.5$ at high temperatures. No such transition can be inferred for the single phase Al_2O_3 material, since it intergranular fracture occurs over the entire range of temperatures tested.

Finally, it is perhaps worth mentioning that Ingle et al. using single edged notched beams observed a monotonic decrease in toughness up to 1000°C for c-ZrO_2 single-crystals, and a brittle-to-ductile transition in the range of 1000 - 1200°C [8]. However, no such evidence of a brittle-to-ductile transition was observed in the c-ZrO_2 (or AZ50) materials tested in the present work, most likely due to their polycrystalline nature, and hence different fracture mode.

b) AZ50 and AY50 Composites

As mentioned previously, at room temperature both AZ50 and AY50 exhibit a mixture

of intergranular and transgranular fracture. Given that single phase alumina fractures intergranularly at this temperature, and both c-ZrO_2 and YAG fracture transgranularly, the most straightforward explanation for this behavior is that the composites are behaving as simple mixtures of their constituent phases. Although attractive in its simplicity, it should be noted that this argument neglects several factors which could influence the toughness behavior of the duplex materials. Firstly, there is the possible role of residual stresses arising from thermal expansion mismatch between the two phases. This effect, if any, would be expected to be more pronounced in the case of AZ50 than AY50, due to the greater difference in thermal expansion coefficients (α_A = ~9.0x10^{-6}/°C [32], α_Z = ~10x10^{-6}/°C [33,34], α_{YAG} = ~8.9x10^{-6}/°C [35,36]). Secondly, in the duplex material there are added considerations due to the connectivity of the two phases, since this determines the extent to which the crack can follow the path of least resistance. To illustrate this point, consider for example the extreme case of a *laminar* composite, where it would be possible for the crack to propagate entirely within the weaker phase, or along the interphase boundary if it were more energetically favorable. Finally, one might expect some contribution of the interphase boundaries to the overall toughness behavior, but their influence at room temperature, if any, is unclear. Interestingly, in a previous study involving indentation cracks in AZ50 [5], fracture along AZ boundaries was rarely observed. The above considerations notwithstanding, it is believed that at room temperature, the law of mixtures is a reasonable approximation to the duplex behavior, given the toughness values of both AZ50 and AY50 fall almost exactly half-way between the single phase values.

At elevated temperatures, the behavior is markedly different in that the duplex composites exhibit toughness values which are higher than those of the single phase constituents. If we

consider first the case of AZ50, since the fracture path is purely intergranular (Figure 3), the expression for the composite fracture surface energy takes the form:

$$2\gamma_{C(eff)} = (2\gamma_A - \gamma_{AA})A_A + (2\gamma_Z - \gamma_{ZZ})A_Z + (\gamma_A + \gamma_Z - \gamma_{AZ})A_{AZ} \quad (4)$$

where A is now the area fraction, γ_{AA} and γ_{ZZ} are the alumina and zirconia grain boundary energies, and γ_{AZ} is the interphase boundary energy. For the single phase materials, the corresponding expressions are:

$$2\gamma_{A(eff)} = 2\gamma_A - \gamma_{AA} \quad (5a)$$

$$2\gamma_{Z(eff)} = 2\gamma_Z - \gamma_{ZZ} \quad (5b)$$

Clearly, the relative magnitude of the composite fracture surface energy compared to the single phase values will depend on the values of the area fractions, together with the relative magnitude of the interphase boundary term. As discussed previously, since a crack will invariably follow the path of least resistance, the area fractions of each type of fracture are not simple functions of the volume fraction. Instead, they will be dependent on the relative values of the interphase and grain boundary energies, as well as the distribution of the phases. Considering the microstructures of AZ50 and AY50, however, it would clearly be impossible for a crack propagating intergranularly to completely avoid all the interphase boundaries. Accordingly, in the case where the interphase boundary energy was *higher* than the grain boundary energies of the component phases, the composite would have a *lower* fracture surface energy than its single-phase constituents. Conversely, if the interphase boundary energy were *lower* than the grain boundary energies of either of the component phases, the fracture along the interfaces would add a toughening increment to the composite, thus increasing the toughness relative to the end-members. It is believed that this latter case applies to the alumina/zirconia and alumina/YAG

composite systems at high temperatures. As additional evidence to this, dihedral angle measurements [37] and microstructural observations of the Al_2O_3:c-ZrO_2(Y) system [3] indicate that the interphase boundary energy, γ_{AZ}, is indeed lower than either of the grain boundary energies of alumina and zirconia, i.e., $\gamma_{AA} > \gamma_{ZZ} > \gamma_{AZ}$. Unfortunately, corresponding data are not available for the alumina/YAG interphase boundary energies, although the higher composite fracture surface energy for AY50 relative to the single-phase components implies a similar trend to the alumina/zirconia system.

II. Indentation Testing

2.1 Experimental

Specimens for indentation testing (5 x 5 x 10 mm) were cut from the same billets of materials as used in the first part of the study. In each case, the prospective indentation surface was polished to a 1 μm diamond finish. The indentation tests were performed under vacuum (2 x 10^{-5} Torr) in a high temperature microhardness testing machine[7]; 5 - 8 indentations were measured for each temperature and indentation load condition. The range of temperatures tested was the same as that for the chevron notch bend tests, i.e., R.T. - 1200°C. A range of indentation loads (10, 5, 3 and 2 N) was used to test whether the materials exhibited R-curve behavior [19]. The crack lengths were measured as soon as possible after indentation (usually within 10 - 15 seconds) to minimize the effects of subcritical crack growth. The above values were then used to determine the temperature dependence of the fracture toughness K_{Ici} (see next section).

[7] Nikon, Model QM

2.2 Results

a) Effect of temperature on radial crack length and toughness

The temperature dependence of the radial crack length (5 N indentation load) for all the materials tested is shown in Figure 5. It can be seen that the different materials show markedly different behavior. For single phase Al_2O_3, the crack length increased linearly with increasing temperature; whereas in the case of YAG and AY50, the crack length was approximately invariant with temperature. For the zirconia containing materials AZ50 and c-ZrO_2, the radial crack size increased initially with increasing temperature, with a maximum at ~600°C. At even higher temperatures, however, cracking was no longer observed. Specifically, in AZ50, no cracks were seen above 700°C for 10 N loads, 600°C for 5 N loads, and 400°C for 3 and 2 N loads. In single-phase c-ZrO_2, radial cracking was not observed above 900°C for 10 N loads, 800°C for 5 N loads and 600°C for 3 and 2 N loads. In all cases, the decrease in radial crack length with increasing temperature above 600°C was accompanied by local plasticity around the indentation site in the form of material pile-up.

The fracture toughness corresponding to a given indentation temperature (θ) was calculated from the following expression:

$$K(\theta)_{Ici} = \xi\,[E(\theta)/H(\theta)]^{1/2}\,[P/c(\theta)^{3/2}] \qquad (6)$$

where ξ is the indentation calibration constant, E is Young's modulus, H is the hardness, c is the radial crack length, and P is the indentation load [19]. The temperature dependence of Young's modulus for the materials tested was determined from literature values as described previously (see Figure 6). The hardness values for the different indentation temperatures was determined experimentally from measurements of the impression size. The calculated modulus to hardness

ratio for all the materials studied was found to increase monotonically with increasing temperature, see Figure 7. The crack length data was analyzed in two ways. Firstly, a value of ξ taken from the literature was used to calculate fracture toughness values according to Eqn. (6), and the results are plotted in Figure 8. In the second case, the variation in ξ was investigated by calculating the following ratio,

$$\xi = K(\theta)_{ICV} / \{[E(\theta)/H(\theta)]^{1/2} [P/c(\theta)^{3/2}]\} \qquad (7)$$

where $K(\theta)_{ICV}$ is the fracture toughness value obtained previously by chevron notch testing.

Note that particularly at the higher indentation loads (5, 10 N), there was a tendency for pronounced lateral cracking in the c-ZrO_2, YAG and AY50 composite materials. In such cases, the value of radial crack length was not used in the calculation of fracture toughness, as these would tend to give artificially high values [38].

b) Effect of load on indentation behavior

Aside from the afore-mentioned lateral cracking at the higher loads, no significant effect of indentation load on the measured fracture toughness was observed. Specifically, at any given test temperature, the value ($P/c^{3/2}$) was relatively constant over the range of indentation loads tested. This result indicates that the materials' crack resistance behavior can be characterized by a single value of fracture toughness. The absence of room temperature R-curve behavior is in agreement with the results of a previous study, where the indentation strength in bending method [39] was used to study the mechanical behavior of Al_2O_3:c-ZrO_2 composites [5].

2.3 Discussion

a) Temperature Dependence of Indentation Crack Length

For Vickers indentation, the extent of radial cracking is determined by both the toughness, and the magnitude of the residual stress intensity resulting from the material's elastic accommodation of the plastically deformed impression zone. The explicit dependence of crack length on the above factors can be seen by rearranging Eqn. 6 to give:

$$c(\theta)^{3/2} \quad \alpha \quad [E(\theta)/H(\theta)]^{1/2} \cdot \; 1 / K_{IC}(\theta) \qquad (8)$$

The crack driving force term scales with the ratio of elastic modulus to hardness, both of which decrease with increasing temperature. Overall, however, the ratio $E(\theta)/H(\theta)$ *increases* (see Figure 7), since the hardness values fall off more rapidly. Thus the tendency will be for the radial crack length to increase with increasing temperature, unless there is a sufficiently large compensating increase in toughness. With this in mind, the invariance of crack length with temperature for the YAG and AY50 materials can be attributed to their relatively flat $(E/H)^{1/2}$ and toughness functions. In the case of alumina, c-ZrO_2 and AZ50, the sharply increasing crack driving force term, together with the decreasing toughness values give rise to the strong increase in crack length with increasing temperature.

At elevated indentation temperatures, the zirconia containing materials no longer exhibit radial cracking. Since this behavior is associated with substantial pile-up of material around the indentation site, it is postulated that at temperatures > 600°C, the permanent deformation can be accommodated by plastic flow up and around the indenter. Clearly this will result in a reduction of the residual stress intensity at the indentation site. The apparent increase in the measured indentation fracture toughness of AZ50 and c-ZrO_2 above 400 and 600°C (respectively) is an indication of this effect. Interestingly, our study also showed that the value of the transition temperature was load dependent. Thus for low indentation loads, the radial cracking behavior

did not extend to as high indentation temperatures as for high loads. This trend is consistent with the plastic flow model, since at lower loads, because the impression is smaller and more shallow, the displacement of a relatively smaller volume of material to the surface is facilitated.

The observation of suppressed radial cracking with increasing indentation temperature has been reported previously for single crystal c-ZrO_2 [12] and MgO [40], however the interpretation of such behavior is slightly different. *Unlike in the polycrystalline materials where brittle* intergranular fracture takes place, the single crystal materials are sufficiently ductile that the increased ease of dislocation movement at elevated temperatures gives rise to increased resistance to cracking and hence toughness.

b) Comparison Between Measurement Techniques

Figure 8 shows the temperature dependence of indentation fracture toughness values calculated from Eqn. 7, and using a value of $\xi = 0.016$ taken from the literature [19]. Comparison with the fracture toughness values measured by the chevron-notched beam (Figure 2) show that the general trends of the data with increasing temperature are in reasonable agreement between the two methods (aside from the data points in the zirconia-containing materials where the bulk plasticity led to erroneously high values).

An alternative method of analyzing the crack length results, is to calculate the value of the indentation calibration constant using the values of fracture toughness determined previously by chevron notch bend testing. Taking the average of the individual ξ values calculated for each material at each temperature, we obtain $\xi \sim 0.024 \pm 0.004$, which compares very favorably with the value of 0.016 ± 0.004 obtained by Anstis et al. [19]. The present results thus support the

contention that the calibration constant is material-independent. Further, the absence of any temperature dependence gives added confidence to the applicability of the indentation technique at high temperatures, at least to within the uncertainty of the measurement (~30%). The results of this study show, therefore, that provided the temperature dependence of the modulus and hardness are taken into account, in the absence of significant bulk plastic flow around the indenter, the indentation technique gives comparable toughness data to that of chevron notch beam at elevated temperatures for materials with flat R-curves.

Summary

i) The fracture mode and toughness behavior of Al_2O_3, c-ZrO_2, YAG, AZ50 and AY50 were studied using chevron notch bend testing and indentation. At room temperature, the fracture toughness of AZ50 and AY50 follows a simple rule of mixtures behavior with respect to their single phase constituents. At elevated temperatures, however, both duplex composites exhibit superior toughness; behavior which is attributed to the toughening contribution of the interphase boundaries.

ii) For the materials studied, both chevron notch bend testing and indentation gave comparable results for the temperature dependence of fracture toughness. The toughness decreases with increasing temperature for Al_2O_3, c-ZrO_2 and AZ50, whereas it is approximately constant for AY50. In the case of single phase YAG, the toughness first decreases with increasing temperature, and then increases very slightly.

iii) Calculated values of the indentation calibration constant (ξ) were essentially material and temperature invariant, and gave good agreement with previously reported values.

Acknowledgements

The authors would like to thank L. M. Braun at NIST for help with hot-pressing the single-phase materials, M. Roddy and W. R. Cannon at Rutgers for their help and use of the MTS high temperature testing machine, B. R. Lawn and E. R. Fuller for helpful discussions and W. E. Luecke for reviewing this manuscript.

References

1. M.P. Harmer, H.M. Chan and G.A. Miller, "Unique Opportunities for Microstructural Engineering with Duplex and Laminar Ceramic Composites", *J. Am. Ceram. Soc.*, 75[7] 1715-1728 (1992).

2. S.J. Bennison, N.P. Padture, J.L. Runyan and B.R. Lawn, "Flaw-Insensitive Ceramics", *Phil. Mag. Lett.*, 64[4] 191-195 (1991).

3. J. D. French, M. P. Harmer, H. M. Chan and G. A. Miller, "Coarsening-Resistant Dual-Phase Interpenetrating Microstructures", *J. Am. Ceram. Soc.*, 73[8] 2508-2510 (1990).

4. J.D. French, Unpublished Work.

5. J. D. French, H. M. Chan, M. P. Harmer and G. A. Miller, "Mechanical Properties of Interpenetrating Microstructures: The Al_2O3:c-ZrO_2 System", *J. Am. Ceram. Soc.*, 75[2] 418-423 (1992).

6. J. D. French, J. Zhao, M. P. Harmer, H. M. Chan and G. A. Miller, "Tensile Creep of Duplex Microstructures", *J. Am. Ceram. Soc.*, In Press (1994).

7. S. M. Wiederhorn, B. J. Hockey and D. E. Roberts, "Effect of Temperature on the Fracture

of Sapphire", *Phil. Mag.*, **28**[4] 783-796 (1973).

8. R. P. Ingle, D. Lewis, B. A. Bender and R. W Rice, "Temperature Dependence of Strength and Fracture Toughness of ZrO_2 Single Crystals", *J. Am. Ceram. Soc.*, **65**[7] C150-C152 (1982).

9. G. de With and J. E. D. Parren, "Translucent $Y_3Al_5O_{12}$ Ceramics: Mechanical Properties", *Solid State Ionics*, **16**, 87-94 (1985).

10. K. Keller, T. Mah and T. A. Parthasarathy, "Processing and Mechanical Properties of Polycrystalline $Y_3Al_5O_{12}$ (Yttrium Aluminum Garnet)", *Ceram. Eng. Sci. Proc.*, **11**[7-8] 1122-1133 (1990).

11. A. Ghosh, M. G. Jenkins, K. W. White, A. S. Kobayashi and R. C. Bradt, "Elevated-Temperature Fracture Resistance of a Sintered α-Silicon Carbide", *J. Am. Ceram. Soc.*, **72**[2] 242-247 (1989).

12. G. N. Morscher, P. Pirouz and A. H. Heuer, "Temperature Dependence of Hardness in Yttria-Stabilized Zirconia Single Crystals". *J. Am. Ceram. Soc.*, **74**[3] 491-500 (1991).

13. J. Salem, Private Communication (1991).

14. L. Chuck, E. R. Fuller Jr. and S. W. Freiman, "Chevron-Notch Bend Testing in Glass: Some Experimental Problems", pp. 167-175 in *Chevron-Notched Specimens: Testing and Stress Analysis, ASTM STP 855*, eds. J. H. Underwood, S. W. Freiman and F. I. Baratta, American Society for Testing and Materials, Philadelphia, (1984).

15. D. Munz, R. T. Bubsey and J, L. Shannon Jr., "Fracture Toughness Determination of alumina Using Four-Point-Bend Specimens with Straight-Through and Chevron Notches", *J. Am. Ceram. Soc.*, **63**[5-6] 300-305 (1980).

16. J. I. Bluhm, "Slice Synthesis of a Three Dimensional 'Work of Fracture' Specimen", *Eng.*

Fract. Mech., 7, 593-604 (1975).

17. J. I. Bluhm, "Stability Considerations in the Generalized Three Dimensional 'Work of Fracture' Specimen", pp. 409-417 in *Fracture 1977*, Vol. 3, ed. D. M. R. Taplin, University of Waterloo Press, Waterloo, Ontario, Canada (1977).

18. J. C. Newman Jr., "A Review of Chevron-Notched Fracture Specimens", pp. 5-31 in *Chevron-Notched Specimens: Testing and Stress Analysis, ASTM STP 855*, eds. J. H. Underwood, S. W. Freiman and F. I. Baratta, American Society for Testing and Materials, Philadelphia, (1984).

19. G. R. Anstis, P. Chantikul, B. R. Lawn D. B. Marshall, "Critical Evaluation of Indentation Techniques for Measuring Fracture Toughness: I, Direct Crack Measurements", *J. Am. Ceram. Soc.*, **64**[9] 533-539 (1981).

20. T. Nose and T. Fujii, "Evaluation of Fracture Toughness for Ceramic Materials by a Single-Edge-Precracked-Beam Method", *J. Am. Ceram. Soc.*, **71**[5] 328-333 (1988).

21. G. R. Irwin, "Fracture", pp. 551-590 in *Handbuch der Physik*, Vol. 6, ed. S. Flügge, Springer-Verlag, Berlin, FRG.

22. T. Goto, O. L. Anderson, I. Ohno and S. Yamamoto, "Elastic Constants of Corundum up to 1825 K", *J. Geophys. Res.*, **94**[B6] 7588-7602 (1989).

23. H. M. Kandil, J. D. Greiner and J. F. Smith, "Single Crystal Elastic Constants of Yttria-Stabilized Zirconia in the Range 20° to 700°C", *J. Am. Ceram. Soc.*, **67**[5] 341-346 (1984).

24. W. J. Alton and A. J. Barlow, "Temperature Dependence of the Elastic Constants of Yttrium Aluminum Garnet", *J. Appl. Phys.*, **38**[7] 3023-3024 (1967).

25. E. G. Spencer, R. T. Denton, T. B. Bateman, W. B. Snow and L. G. Van Uitert, "Microwave Elastic Properties of Nonmagnetic Garnets", *J. Appl. Phys.*, **34**[10] 3059-3060 (1963).

26. Z. Hashin and S. Shtrikman, "A Variational Approach to the Theory of Elastic Behavior of Polycrystals", *J. Mech. Phys. Solids*, **10**, 343-352 (1962).

27. Z. Hashin and S. Shtrikman, :A Variational Approach to the Theory of Elastic Behavior of Multiphase Materials", *J. Mech. Phys. Solids*, **11**, 127-140 (1963).

28. B. R. Lawn, *Fracture of Brittle Solids-Second Edition*, Cambridge Solid State Science Series, Cambridge University Press, Cambridge, 1993.

29. K. T. Faber and A. G. Evans, "Crack Deflection Processes - I. Theory", *Acta Metall.* **31**[4] 565-576 (1983).

30. K. T. Faber and A. G. Evans, "Crack Deflection Processes - II. Experiment", *Acta Metall.* **31**[4] 577-584 (1983).

31. M. Y. He and J. W. Hutchinson, "Crack Deflection at an Interface Between Dissimilar Elastic Materials", *Int. J. Solids Structures*, **25**[9] 1053-1067 (1989).

32. G. Bayer, "Thermal Expansion Anisotropy of Oxide Compounds", *Proc. Brit. Ceram. Soc.*, **22**, 39 (1973).

33. K. S. Mazdiyasni, C. T. Lynch and J. S. Smith II, "Cubic Phase Stabilization of Translucent Yttria-Zirconia at Very Low Temperatures", *J. Am. Ceram. Soc.*, **50**[10] 532-537 (1967).

34. V. B. Glushkova, V. V. Osiko, L. G. Shcherbakova, V. I. Aleksandrov, Y. N. Paputskii and V. M. Tatarintsev, "Characteristics of Monocrystalline Solid Solutions in the System ZrO_2-Y_2O_3", *Inorg. Mater. (USSR)*, **13**[12] 1751-1754 (1977).

35. P.H. Klein and W. J. Kroft, "Thermal Conductivity, Diffusivity and Thermal Expansion of Y_2O_3, $Y_3Al_5O_{12}$ and LaF_3 in the Range 77°-300°K", *J. Appl. Phys.*, **38**[4] 1603-1607 (1967).

36. T. K. Gupta and J. Valentich, "Thermal Expansion of Yttrium Aluminum Garnet", *J. Am.*

Ceram. Soc., **54**[7] 355-356 (1971).

37. I-W. Chen and L. A. Xue, "Development of Superplastic Ceramics", *J. Am. Ceram. Soc.*, **73**[9] 2585-2609 (1990).

38. R. F. Cook, M. R. Pascucci and W. H. Rhodes, "Lateral Cracks and Microstructural Effects in the Indentation Fracture of Yttria", *J. Am. Ceram. Soc.*, **73**[7] 1873-1878 (1990).

39. P. Chantikul, G. R. Anstis, B. R. Lawn and D. B. Marshall, "A Critical Evaluation of Indentation Techniques for Measuring Fracture Toughness: II, Strength Method", *J. Am. Ceram. Soc.*, **64**[9] 539-543.

40. N. Khasgiwale and H.M. Chan, "High Temperature Indentation Studies on the {110} Plane of Single Crystal MgO", *J. Am. Ceram. Soc.*, **75**[6] 1924-1928 (1992).

Figure Captions

Figure 1. Chevron geometry used. The beam length was 55 mm.

Figure 2. Fracture toughness, measured by chevron-notched beam, as a function of temperature for the Al_2O_3:c-ZrO_2 (top) and Al_2O_3:YAG (bottom) systems.

Figure 3. Fracture surfaces of Al_2O_3, AZ50, c-ZrO_2, AY50 and YAG at room temperature and 1200°C. Note the change in behavior to intergranular fracture at high temperatures in the c-ZrO2 and YAG containing materials. c-ZrO_2 specimen fractured at 1000°C.

Figure 4. Effective fracture surface energy, $2\gamma_{eff}$, for the Al_2O_3:c-ZrO_2 (top) and Al_2O_3:YAG (bottom) systems. Values are calculated from the chevron-notched beam results.

Figure 5. Indentation radial crack length as a function of temperature for the Al_2O_3:c-ZrO_2 (top) and Al_2O_3:YAG (bottom) systems (5 N load). Error bars are left off the AY50 and YAG data for clarity, the uncertainty is comparable to the Al_2O_3 data.

Figure 6. Temperature dependence of Young's modulus for both systems. The YAG data are extrapolated above room temperature from low temperature data, and the c-ZrO_2 data are extrapolated above 700°C.

Figure 7. Temperature dependence of the indentation crack driving force, $(E/H)^{1/2}$ for both systems.

Figure 8. Indentation fracture toughness, K_{Ici}, as a function of temperature for the Al_2O_3:c-ZrO_2 (top) and Al_2O_3:YAG (bottom) systems.

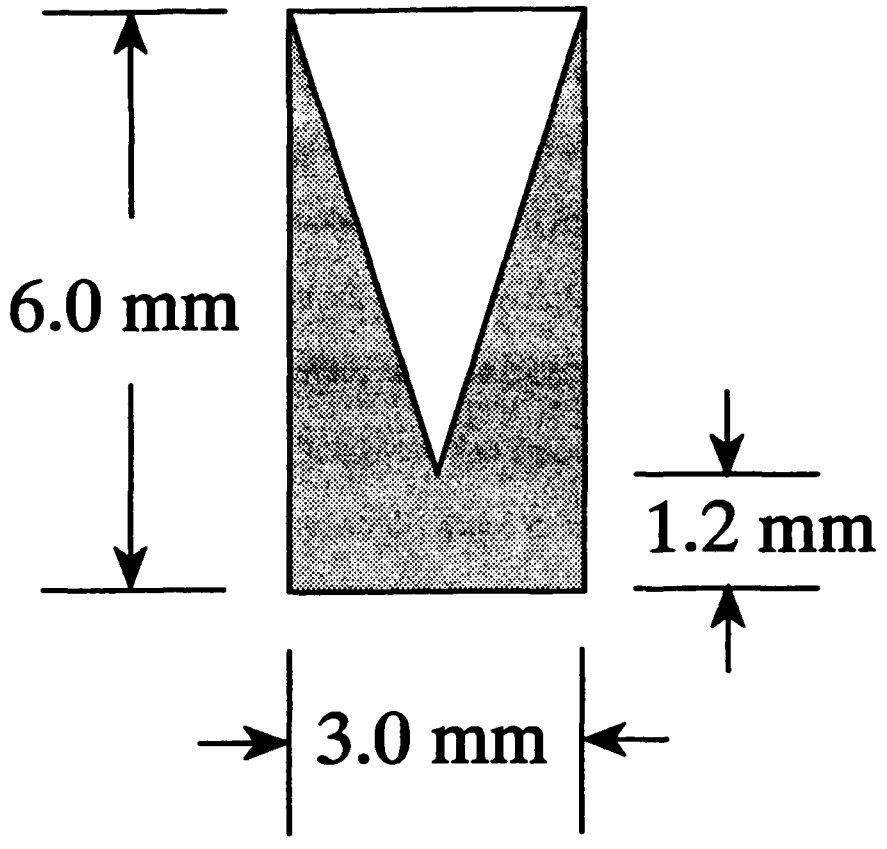

FIGURE 1

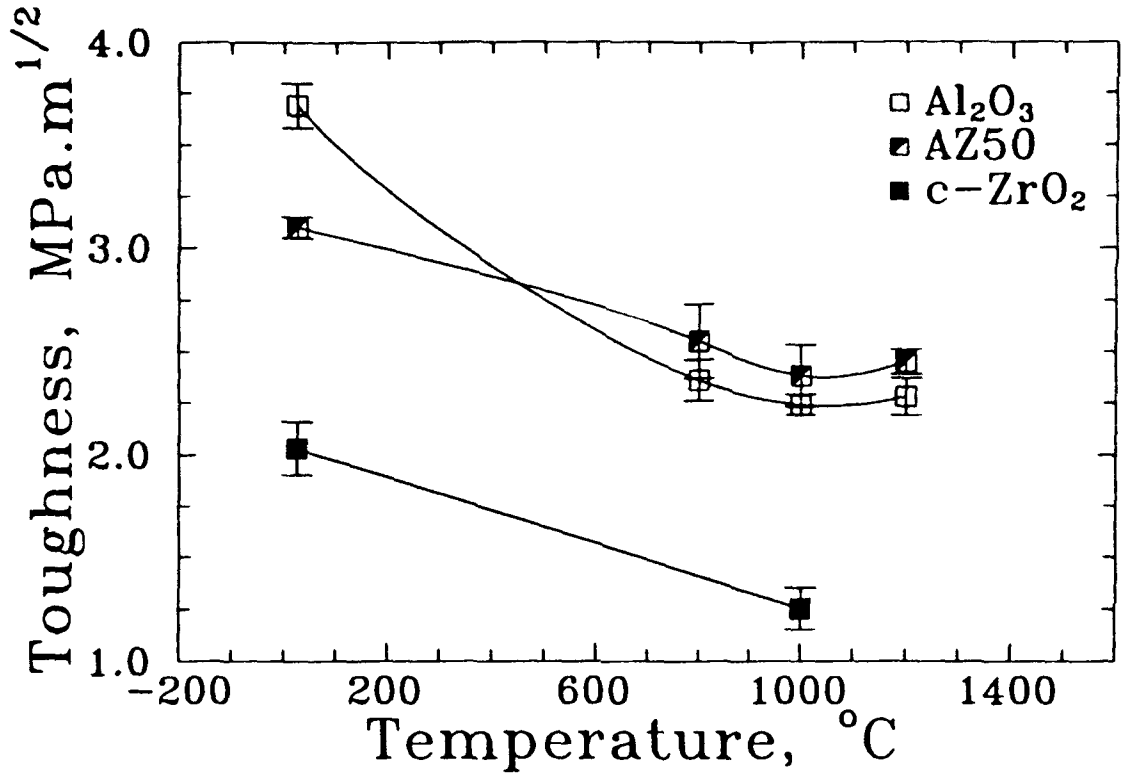
Toughness, MPa.m$^{1/2}$
4.0
3.0
2.0
1.0
−200
200
600
1000
1400
Temperature, °C
Al_2O_3
AZ50
c−ZrO_2

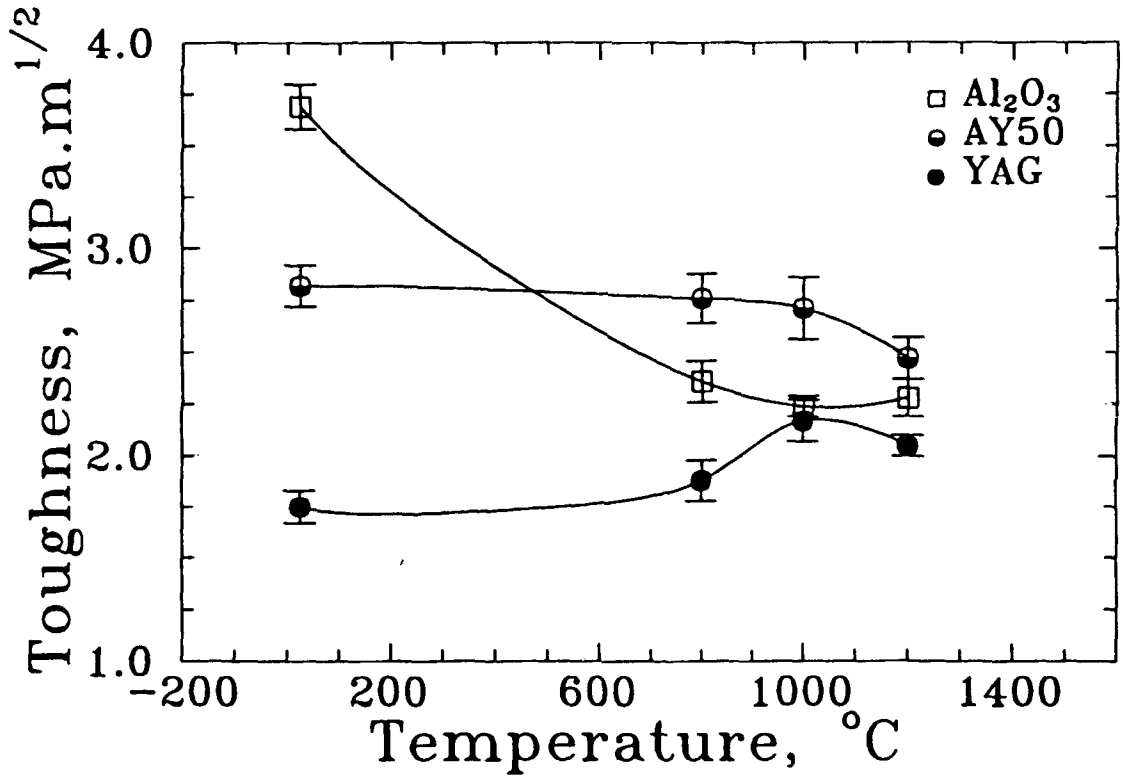
Toughness, MPa.m$^{1/2}$
4.0
3.0
2.0
1.0
−200
200
600
1000
1400
Temperature, °C
Al_2O_3
AY50
YAG

FIGURE 2.

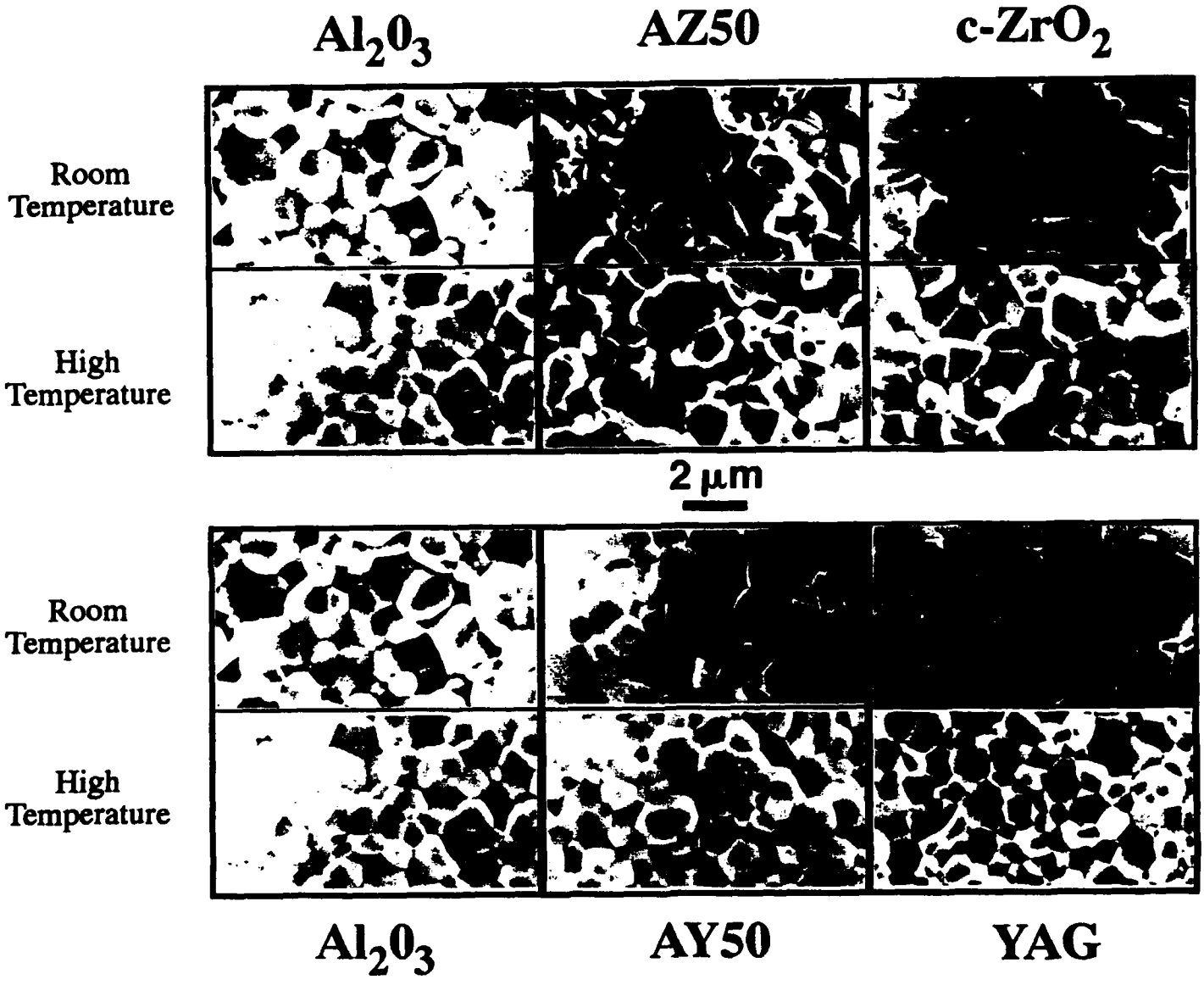
Al_2O_3
AZ50
c-ZrO_2
Room Temperature
High Temperature
2 μm
Room Temperature
High Temperature
Al_2O_3
AY50
YAG

FIGURE 3.

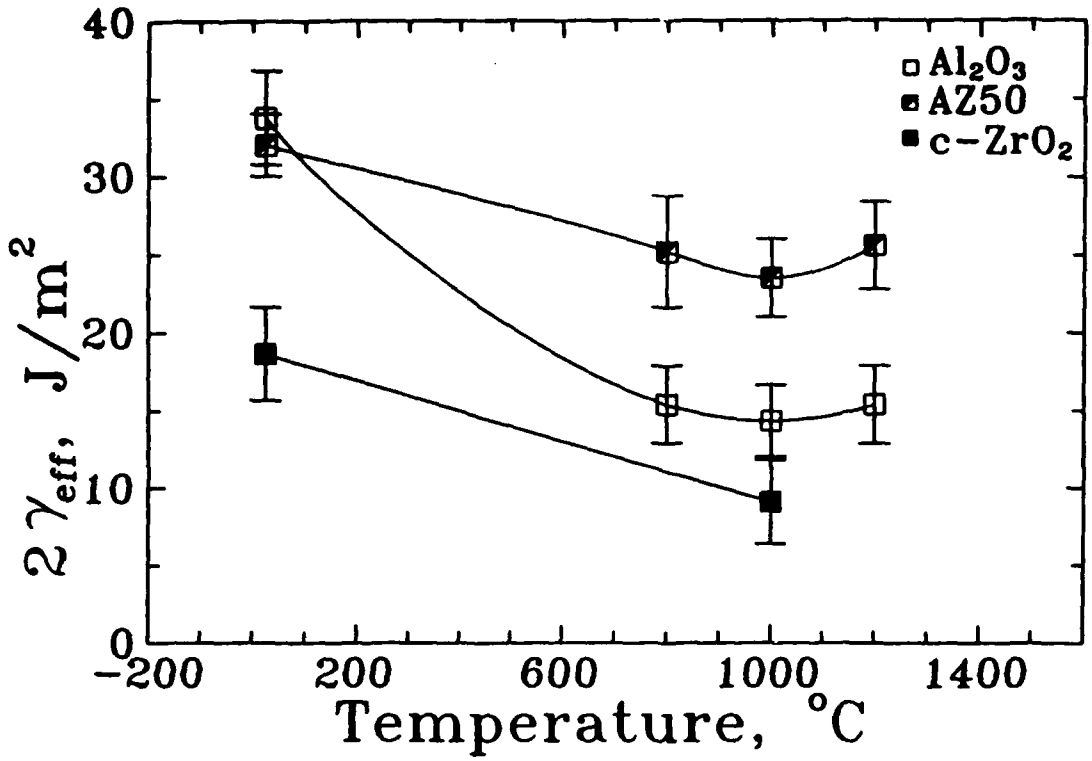
40
30
20
10
0
$2\gamma_{eff}$, J/m^2
Al_2O_3
AZ50
c-ZrO_2
−200
200
600
1000
1400
Temperature, °C

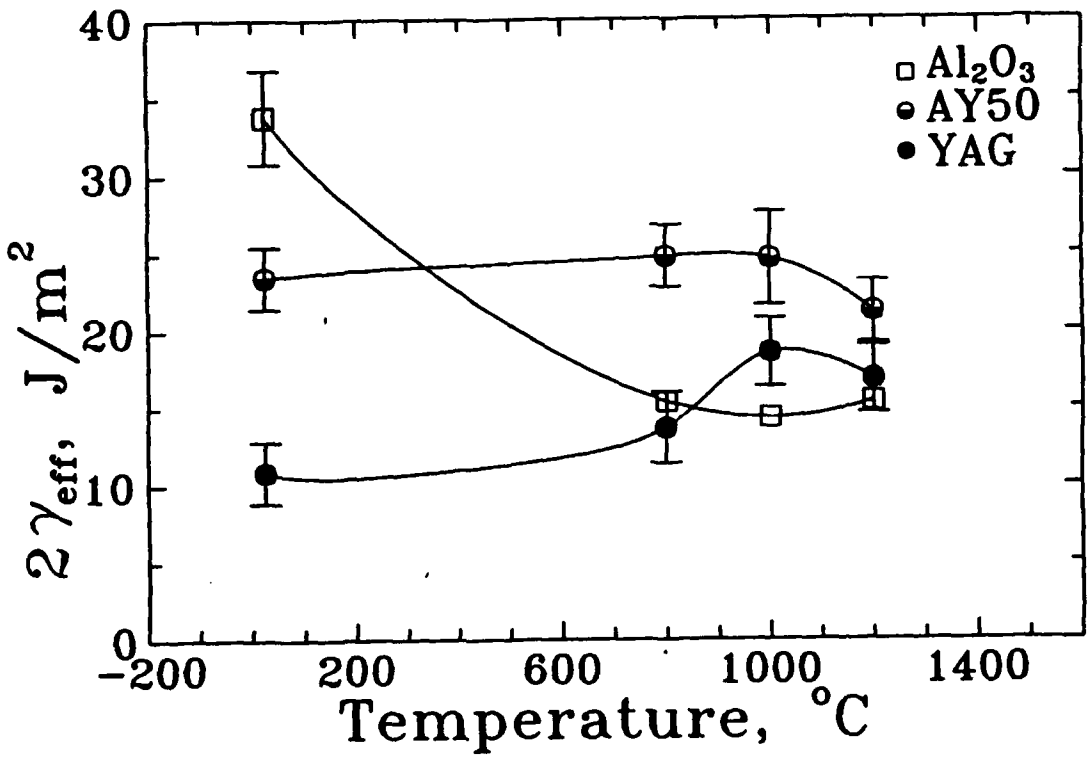
40
30
20
10
0
$2\gamma_{eff}$, J/m^2
Al_2O_3
AY50
YAG
−200
200
600
1000
1400
Temperature, °C

FIGURE 4.

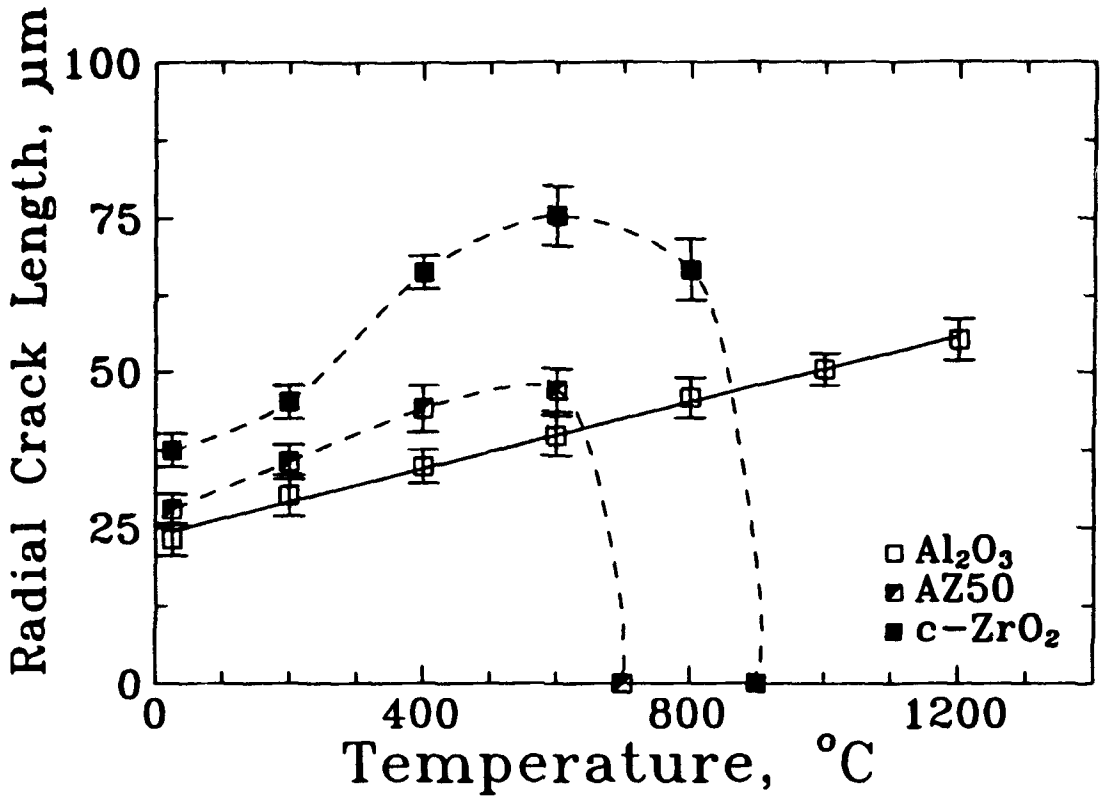
Radial Crack Length, μm
100
75
50
25
0
0
400
800
1200
Temperature, °C
Al2O3
AZ50
c-ZrO2

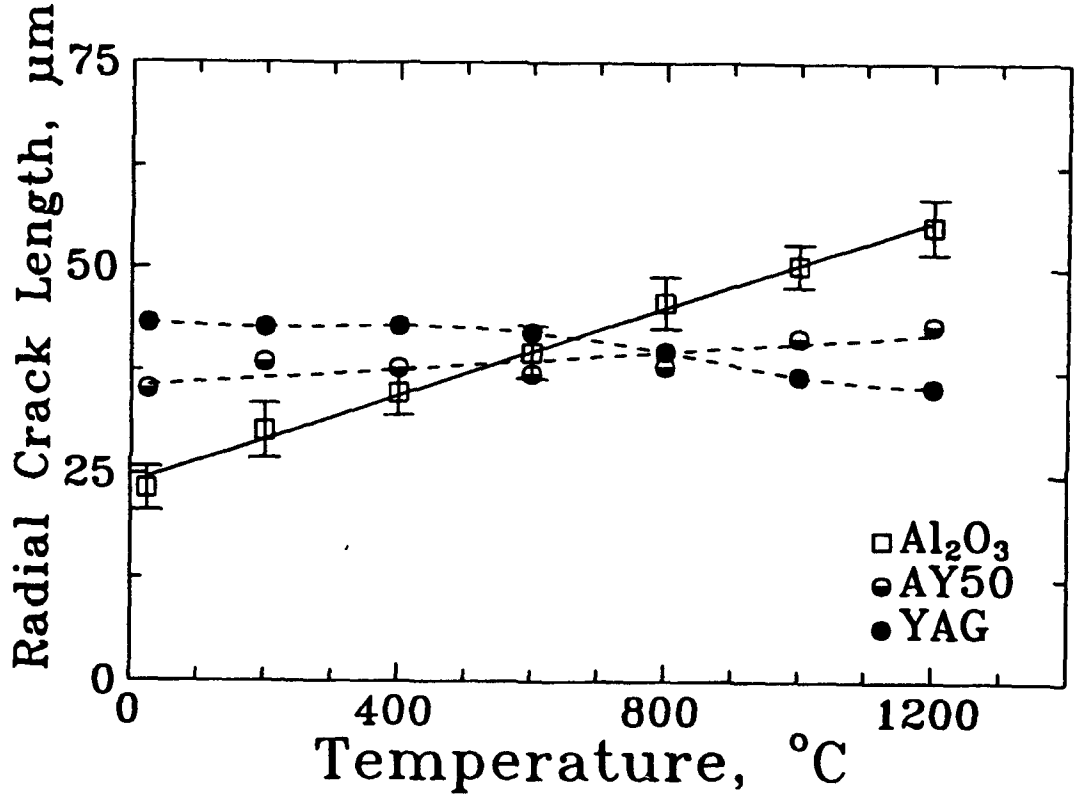
Radial Crack Length, μm
75
50
25
0
0
400
800
1200
Temperature, °C
Al2O3
AY50
YAG

FIGURE 5.

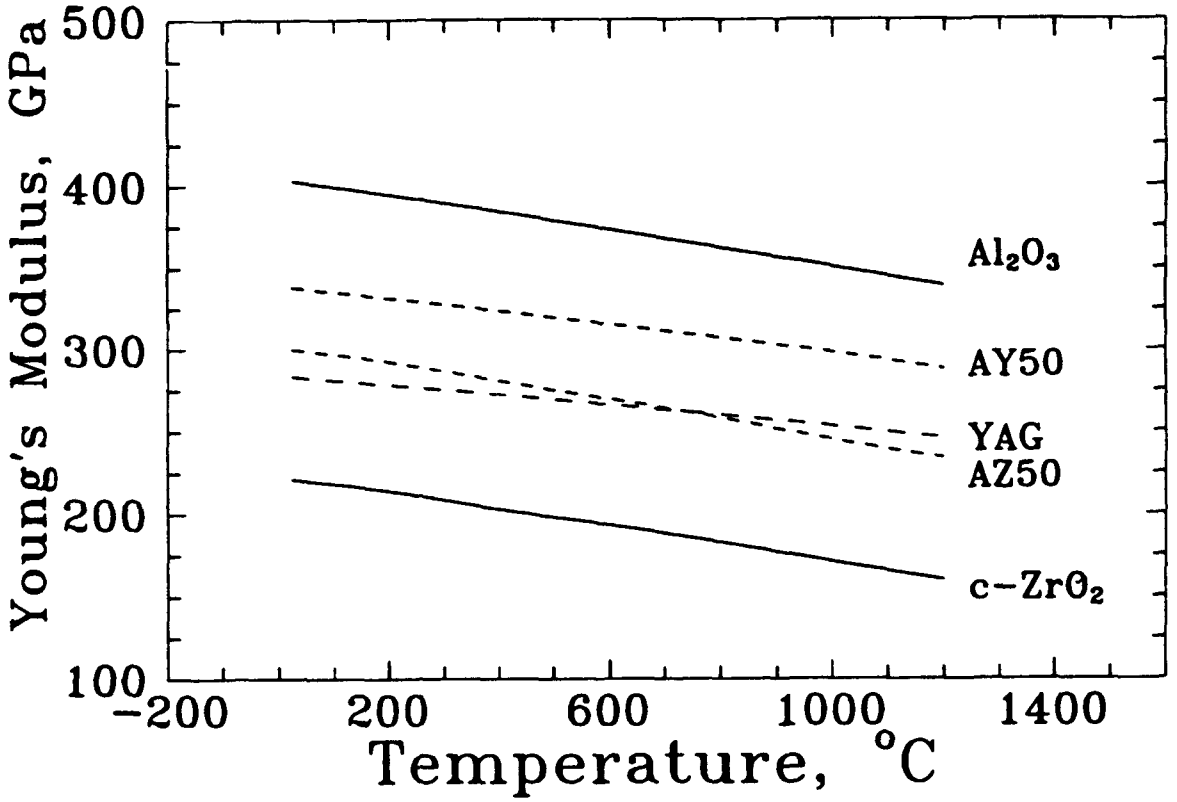
Young's Modulus, GPa
500
400
300
200
100
−200
200
600
1000
1400
Temperature, °C
Al2O3
AY50
YAG
AZ50
c−ZrO2

FIGURE 6.

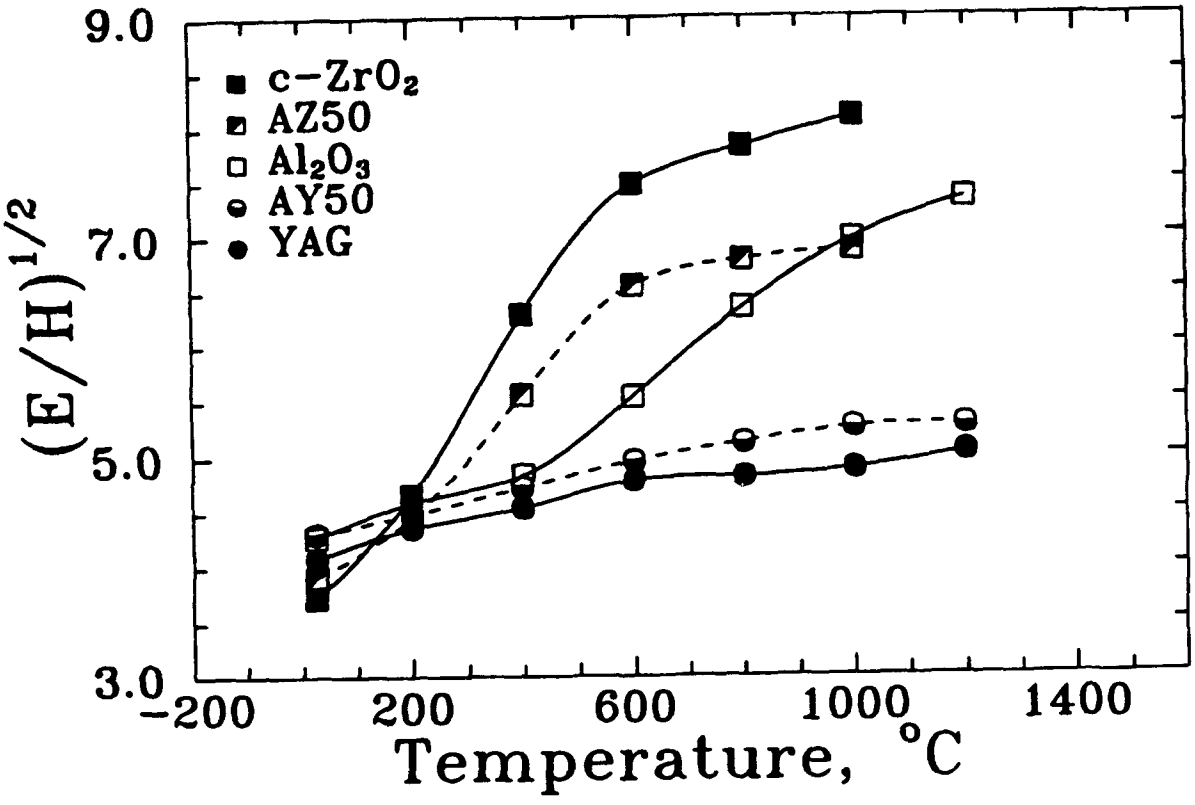
9.0
7.0
5.0
3.0
(E/H)^1/2
c-ZrO2
AZ50
Al2O3
AY50
YAG
-200
200
600
1000
1400
Temperature, °C

FIGURE 7.

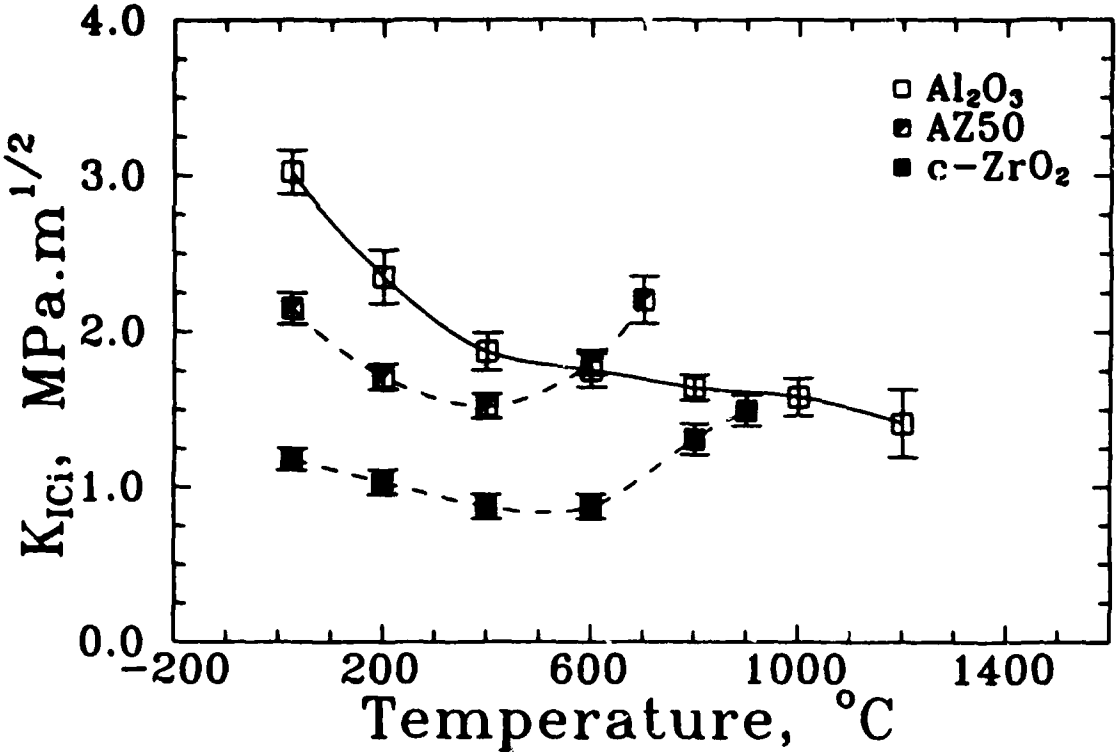
4.0
3.0
2.0
1.0
0.0
K_{ICi}, MPa.m$^{1/2}$
−200
200
600
1000
1400
Temperature, °C
Al_2O_3
AZ50
c−ZrO_2

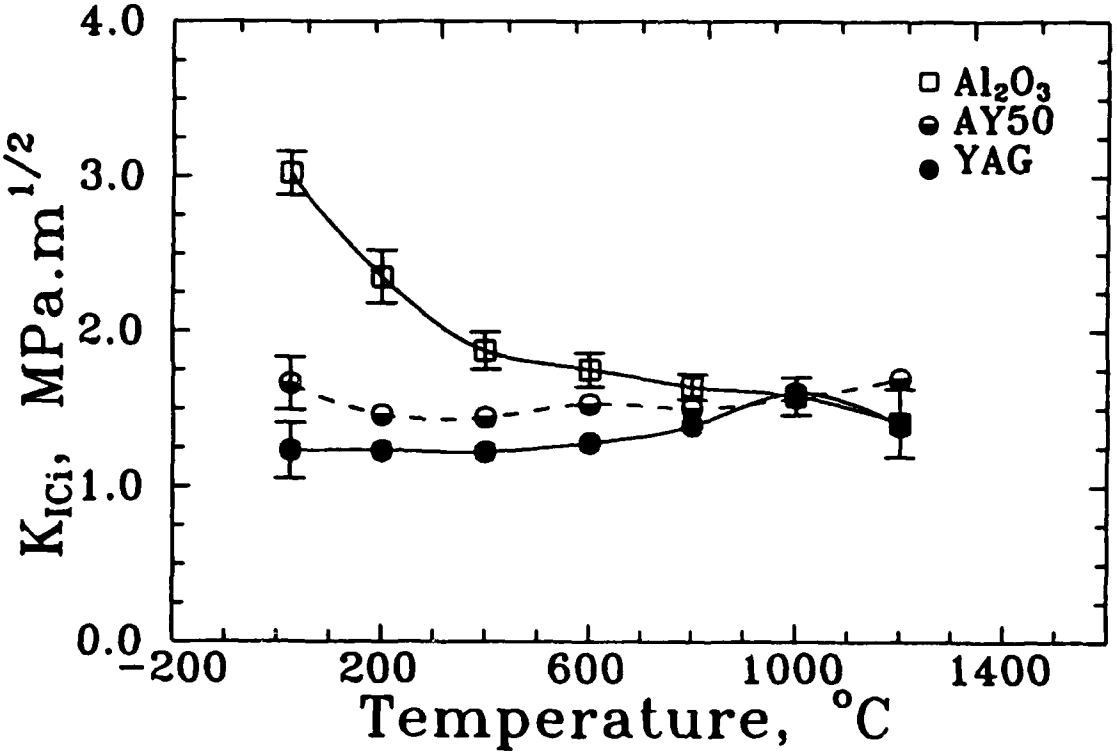
4.0
3.0
2.0
1.0
0.0
K_{ICi}, MPa.m$^{1/2}$
−200
200
600
1000
1400
Temperature, °C
Al_2O_3
AY50
YAG

FIGURE 8.

TENSILE STRENGTH, FLAW TOLERANCE, AND T-CURVE BEHAVIOR OF TRILAYER CERAMIC COMPOSITE

TENSILE STRENGTH, FLAW TOLERANCE, AND T-CURVE BEHAVIOR OF TRILAYER CERAMIC COMPOSITES

by

Charles James Russo

Presented to the Graduate and Research Committee

of Lehigh University

in Candidacy for the Degree of

Doctor of Philosophy

in

Materials Science and Engineering

Lehigh University

May 1993

CERTIFICATE OF APPROVAL

Approved and recommended for acceptance as a dissertation in partial fulfillment of the requirements for the degree of Doctor of Philosophy in the Department of Materials Science and Engineering.

10 May 1993
Date

Martin P. Harmer
Dissertation Director

10 May 1993
Acceptance Date

This dissertation has been accepted by the special committee members:

Martin P. Harmer
Dr. Martin P. Harmer (Chairman)

Helen Chan
Dr. Helen M. Chan

Robert F. Cook
Dr. Robert F. Cook

Gary A. Miller
Dr. Gary A. Miller

Raymond A. Pearson
Dr. Raymond A. Pearson

ACKNOWLEDGEMENTS

First of all, I thank Dr. Martin Harmer for providing the opportunity to pursue my graduate studies at Lehigh, the Air Force Office of Scientific Research for funding my project, and the U.S. Army for allowing me to defer my service obligation until completion of my graduate degree. Perhaps most of all, I thank my wife, Alysha, for her patience, support, and understanding, for putting up with the many late nights and weekends I spent in the lab, and for accepting a job well below her ability level in order to stay with me, in Bethlehem.

Over the course of the last six years, many people have contributed to this research in ways both large and small, and are deserving of my sincere gratitude: Dr. Steve Bennison and Dr. Robert Cook, for taking active interest in my work, and providing numerous significant and helpful suggestions. Steve provided the initial fracture mechanics framework for the T-curve modeling, as well as useful general advice. Robert provided many helpful comments and criticisms, suggested an alternative K-factor solution, instilled in me an appreciation for the effects of lateral cracking, and helped me to refine the computer models with respect to both the underlying science, and the efficiency of the programs themselves. Brian Lawn provided many stimulating discussions, as did Nitin Padture. Martin Stuart was a valuable sounding board for mechanical properties and processing ideas; our many discussions on these topics were sorely missed, following his return to Australia. In addition, the discussions with Yang-Haw Hu and his tape-casting group at DuPont were very helpful. Saikumar ('Psycho') Vivekanand provided me with numerous tips, suggestions, and instructions on the use of the IBM RISC System 6000 Workstations and the other computers and software used for this project. Mark Thompson and Junhong Zhao patiently showed me around the lab and taught me how to do things when I was a ceramic-illiterate new graduate student, and are probably responsible for my not blowing up the building. Finally, I thank my Ph.D. committee members - Dr.'s Martin Harmer, Helen Chan, Gary Miller, Ray Pearson, and Robert Cook - for their support and guidance. Dr.'s Chan and Miller worked with me on this research project from the beginning, and provided many helpful comments, criticisms, general discussions and advice.

The valuable support of the technical staff is gratefully acknowledged: Jim Kerner, Dave Ackland, Kathy Repa, and Dave Calvert for keeping the SEM fleet in prime operating condition, and for teaching me how to use them well; Gene Kozma, for installing the equipment bought for this project, and for fixing them when they broke; Arlan Benscoter, for teaching me the value of optical microscopy; and Andrea Pressler, for providing consistently excellent slides.

I thank Dr.s Williams, Lyman, and Goldstein for providing the opportunity to serve as a teaching assistant for Mat. 334 and Mat. 427, which allowed me to sharpen my skills as an SEM operator, broaden my knowledge of electron microscopy, and gain valuable teaching experience. I also thank Dr. Hertzberg for the opportunity to TA Mat. 192, which allowed me to re-learn some of the techniques for testing the mechanical properties of metals (i.e., *real* materials).

It would not have been possible to make it through graduate school with my sanity intact without the friendship and comaraderie of the Von Laue Society, especially Mark Thompson, Brian Smith, Ali Westwood, Martin Stuart, Kevin Luer, Psycho, Tom P., Tom C., Scott B., Chris B., Laura S., J. Zhao, J. Yun, etc. Finally, I thank the Washington Redskins for giving me *two* Super Bowl victories during my stay here, the Philadelphia Phillies for teaching me the value of good pitching, and the Philadelphia 76ers for providing an ongoing case study of poor management and player personnel decisions.

TABLE OF CONTENTS **PAGE NO.**

List of Figures **Page No.**

ABSTRACT

This research has been directed toward the development of laminated ceramic composites for improved strength and toughness properties. The low toughness of ceramics is possibly the single most important problem limiting their use as structural materials. Over the last fifteen years or so, significant improvements in the toughness of ceramics have been achieved, primarily through the exploitation of T-curve phenomena, such as transformation toughening and grain bridging. A serious problem with T-curve toughening mechanisms, however, has been the reduction in strength which often accompanies the improvement in toughness. A goal is therefore to achieve both high strength and high toughness in the same body. The research presented here has been directed primarily toward this goal.

A trilayer composite design was conceived as a means to overcome the tradeoff between strength and toughness. The design calls for a high strength surface layer of controlled thickness to be combined with a high toughness bulk material. This trilayer concept was thoroughly tested on a model system of alumina + 20 vol% aluminum titanate (AAT20). The surface material was a homogeneous, fine-grained mixture of the two phases; while the bulk was an inhomogeneous mixture having a bimodal grain structure. When the surface layer was too thick, the trilayer composite behaved in the same manner as the surface material alone; and when the surface was too thin, the composite displayed the monolithic body material response. With an optimal surface layer thickness of 104 μm, this composite system exhibited the best strength properties of the surface material, together with the best toughness and flaw tolerance properties of the underlying bulk material. A simple approach for estimating the optimal surface layer thickness was shown to be applicable for this AAT20 system.

In order to determine whether the trilayer concept could be applied to materials of greater practical interest (that is, better strength and toughness than the AAT20 materials), a second

composite system based on zirconia materials was investigated. For this trilayer system, a very high strength zirconia + 20wt% alumina material was used for the surface layer; and a high toughness Ce-zirconia material was used for the interior. These composites exhibited excellent indentation strength behavior, demonstrating that the trilayer design is indeed a viable processing strategy for achieving the ideal of high strength together with high toughness.

A toughness-curve (T-curve) model based on strips of constant closure pressure acting in the crack wake was developed to account for the observed strength behavior, in the AA120 system. The main focus of this modeling effort was to predict the trilayer composite T-curve and strength properties, based on the T-curves of the two base materials. The base material T-curves were characterized by four adjustable parameters: (i) T_0 - the intrinsic material resistance to crack growth; (ii) σ_c - a constant closure pressure acting in the crack wake; (iii) b - the distance from the surface at which σ_c begins to act; and (iv) c* - a steady state crack size, at which the wake closure zone has reached a maximum size, and beyond which the zone translates with the advancing crack front. The modeling consisted of incrementally adjusting these four parameters through a computer program, until the T-curve was able to 'predict' the experimentally measured strength data. The best fit T-curves produced good matches between the measured and calculated strengths for the monolithic base materials. The best fit parameters characterizing the base material T-curves were then used to define the trilayer composite T-curve. The resulting composite T-curve was able to describe the experimentally measured trilayer strength behavior, including the influence of surface layer thickness on the strength response.

I. INTRODUCTION

This section presents background information which will allow the subsequent discussion of this research to proceed from a firm foundation. Since the work presented here deals primarily with the strength and toughness of ceramics, various strengthening strategies and toughening mechanisms relevant to ceramic materials are introduced. This is followed by a description of the testing technique employed to characterize the materials of this study, the indentation - strength - in - bending test (ISB). The fracture mechanics analysis of the ISB technique is described, along with typical strength and cracking behaviors. This leads into a discussion of flaw tolerance and toughness curve (T-curve) behavior, the tradeoffs between strength and toughness properties, and the methods which have been used to model T-curve behavior based on the ISB test. Then, a selection of research from the literature, having particular relevance to the present work, will be reviewed. Finally, in order to better understand the processing of the materials of this work, a brief discussion of tape casting is provided.

A. Strategies for the Strengthening of Ceramics

Discussion of the strength of ceramics appropriately begins with the work of A. A. Griffith (1920). Griffith described a body containing a crack as a thermodynamic system, whose total energy, U, was simply given by the sum of the mechanical energy (the elastic energy in the body minus the energy of the loading system) and the surface energy required to create the crack:

$$U(c) = (-\pi c^2\sigma^2/E) + 4c\gamma \qquad (1)$$

where c is crack size, σ is applied stress, E is Young's modulus, and γ is surface energy, (and U is in energy per unit width of crack). At equilibrium, $dU(c)/dc = 0$, or

$$dU(c)/dc = (-2\pi c\sigma^2/E) + 4\gamma = 0 \qquad (2)$$

This relation may be solved for σ to obtain the stress level associated with the equilibrium. Any applied stress below this value will not affect the crack; but an infinitessimal increase beyond this

stress will result in crack extension. Since the equilibrium is unstable ($d^2U/dc^2 = -2\pi\sigma/E < 0$), the crack will extend unstably, and run completely across the body. Therefore, this critical stress level defines the fracture strength, as given by

$$\sigma_f = (2\gamma E/\pi c)^{1/2} \tag{3}$$

It may be readily seen that the fracture strength is dependent on the crack size. When the pre-existing crack is small, the strength is high; but when the initial crack size is large, the strength is reduced. This illustrates two significant, and related, problems with ceramics. First of all, unless a ceramic is processed such that it contains small flaws, its strength will be low. Second, a single ceramic body may be produced with the necessary small flaw size, but for the industrial production of large quantities of ceramic bodies, it is of course not good enough to produce an occasional body possessing the desired strength level. Unless the ceramics are processed with a narrow flaw size *distribution*, from piece to piece, they will display widely varying strength values. Historically, such wide variation in strength values has been a contributing factor in the poor reliability of ceramics, limiting their use as structural materials. Unreliable strength values require a designer to introduce excessive factors of safety, by either designing with larger cross-sections (more material), or reducing the allowable stress ranges. Neither is a very satisfactory solution.

To overcome the variability in strength, many researchers have sought ways to eliminate the source of variability, namely the flaws. Strength variability is caused by differences in the flaw population from batch to batch, or piece to piece. Since the flaws in a ceramic are often related to microstructural features like the grain size, or to processing defects such as large voids from binder burnout, processing refinements could help reduce the strength variability. Furthermore, as shown in Eq. 3 above, if the flaws could be eliminated, or reduced in size, then the fracture strength could be increased as well. Efforts to achieve fully dense, very fine-grained,

uniform microstructures were vigorously pursued, and resulted in considerable success (Lange, et. al., 1983; Alford, et. al., 1987; Lange, 1989; Kendall, et. al., 1989). Flaw elimination strategies included cold isostatic pressing of powder compacts (Richerson, 1982); hot pressing; hot isostatic pressing (Lange, et. al., 1983; Tsukuma & Shimada, 1985); control of grain size and grain size distribution using sintering additives; improvements in raw materials (finer, more uniform particle sizes (Coble & Cannon, 1978; Aksay, et. al., 1983; Velazquez & Danforth, 1984), and higher purities); cleaner processing; use of colloidal methods (Aksay, et. al., 1983; Aksay, 1984; Alford, et. al., 1987; Lange, 1989), and surface treatments (Gruszka, et. al. 1970; Kirchner, et. al., 1971). These strategies of strength improvement (that is, increasing the strength level, as well as reducing the strength variability) through flaw elimination dominated the ceramics field for many years.

Gradually, researchers began to realize that eliminating the *initial* flaws was only a partial solution to the strength problem. Just because a ceramic piece *begins* its life in a flaw-free condition does not mean that it will *remain* in such good condition. An important strategy was developed for strengthening ceramics, which was capable of inhibiting both the initiation of flaws, as well as their subsequent propagation. This strategy was to introduce residual compression in the surface region. Residual compression counteracts an applied tension, effectively reducing the applied stress felt by the surface flaws (Marshall and Lawn, 1977; Lawn & Fuller, 1984; Tandon, et. al, 1990), and thereby increasing the stress required to extend a flaw of given size. There are many ways to produce macroscopic residual stresses. Thermal tempering of glass is a well-known example (Lee, et. al., 1965; Kingery, 1976), and similar thermal treatments have been applied to crystalline ceramics (Richerson, 1982). Residual compression has also been introduced into glass surfaces by ion exchange reactions, whereby smaller ions in the glass material are exchanged for larger ions by reaction with a surrounding bath solution (Kistler, 1962; Olcott, 1963; Kingery, 1976). Another well-known example is the use of glaze materials having different thermal expansion than the substrate

underneath (Kirchner.et.al. 1968, 1979; Kingery, 1976; Richerson, 1982). This technique of exploiting differences in thermal expansion properties has been applied to many different ceramic systems, and will be discussed in greater detail in part E of this section. Finally, phase transformations may be accompanied by volume changes, and if such a transformation may be preferentially induced in the surface region, residual compression may result (Green, 1983; Virkar, et. al., 1987; Cutler, et. al., 1987; Hansen, et. al., 1988). Zirconia materials having surface compression have been produced in this manner.

With the residual compression strategy described above, material microstructures are unchanged, so the toughness, considered as a material property, is also not changed. However, residual compression may be considered to increase the *apparent* toughness of a material, as the crack sizes for a given applied load are smaller, and the fracture strength is higher (Green 1983; Swain 1980; Lawn and Marshall, 1977; Grunnger, et. al., 1987; Lawn and Fuller, 1984). In the following section, methods of improving the actual toughness of a material will be discussed.

B. Toughening Mechanisms

Following Griffith, Irwin used the solutions of Westergaard and Muskhelishvili, to describe the stress field surrounding a crack tip in a homogeneous, elastic body subjected to an applied, external stress (Atkins & Mai, 1985; Lawn, 1993). For a Mode I crack (opening, tension), the local stress in the vicinity of the crack tip, acting in a direction normal to the crack plane is given by

$$\sigma_y = \frac{K}{\sqrt{2\pi r}} \cos\frac{\Theta}{2} \left[1 + \sin\frac{\Theta}{2} \sin\frac{3\Theta}{2} \right] \qquad (4)$$

where r and Θ specify the radial and angular distance between the crack tip and the point of interest. For $\Theta = 0$, this reduces to

$$\sigma_y = K/(2\pi r)^{1/2} \qquad (5)$$

The K term is defined as the stress intensity. For uniform tension, dimensional analysis reveals the form of K to be

$$K = \psi \sigma_a c^{1/2} \tag{6}$$

where ψ is a geometrical constant, and σ_a is the remote applied stress (Paris, 1961; Paris and Sih, 1965). K in Eq. 6 is thus the stress intensity felt by a crack of size, c, caused by the applied stress, σ_a. It may be seen (Eq. 5) that the local stress is magnified to large multiples of the remote applied stress, as r decreases toward the crack tip itself.

This stress intensity factor provides an alternative description to Griffith's thermodynamic energy balance, as it also represents a driving force for crack growth. The main appeal of using stress intensity factors is that K terms arising from superposed loadings are additive (for a given mode of loading). Consequently, when more than one source of loading is active, the various stress intensity factors associated with each may be added together to define a net driving force for crack growth. This feature of stress intensity factors is particularly useful in modeling the T-curve, as will be discussed in considerable detail in part D of this section, and in section V.

The stress intensity description leads to a new material property, the toughness. Fracture of a material may be explained to occur at a critical value of stress intensity, K_{IC}. This is a characteristic property of the material, describing its resistance to crack growth. Griffith defined a material's resistance to crack growth in terms of its fracture surface energy. Comparing Griffith's equation (3), with Eq. (6), it may be seen that K_{IC} is simply equal to $(2\gamma E)^{1/2}$. Griffith's equation (Eq. 3) was derived for homogeneous, isotropic, elastic materials (he used glass in his experiments). In such materials, the only means of dissipating the energy of fracture (or, of relieving the applied stress intensity) is through creation of new surfaces, so associating K_{IC} with the surface energy is valid. In tougher systems, however, there will exist other dissipative mechanisms (e.g. plastic deformation, phase transformations, crack face bridging, etc.), so it is

important to realize that the material toughness is *generally* associated with more than just the surface energy (Lawn, 1993; Hertzberg, 1989).

The concept of a material toughness suggests a different approach to improving fracture strengths than the flaw elimination strategy described in the previous section. Referring to Griffith's equation, modified to include toughness rather than surface energy,

$$\sigma_f = K_{IC}/\psi c^{1/2} \tag{7}$$

it may readily be seen that fracture strength can be increased by increasing the toughness. The remainder of this section will discuss ways to improve the toughness of ceramics.

Crack Deflection.

The simplest way to increase toughness is to add second phase particles to the ceramic. This can give rise to toughening in a number of ways, depending on particle shape, thermal expansion mismatch, elastic mismatch, and interfacial toughness. The particles may force a crack to deflect away from its original plane, which was normal to the applied tension. This can have two effects: an increase in crack path tortuosity, and therefore fracture surface area; and a change in the nature of the crack tip stress field, decreasing the mode I component. Faber and Evans (1983) determined a rod-like particle shape to be most effective in deflecting a crack. Thermal expansion mismatch can either draw a crack into a particle ($\alpha_p < \alpha_m$, hoop tension), or deflect it away ($\alpha_p > \alpha_m$, radial tension), depending on the nature of the residual stress fields in and around the particles (Selsing, 1961). If the crack is attracted to the particle, toughening may result if the particle is inherently tougher (e.g. has greater surface energy) than the matrix, or if the particle is able to pin the crack, causing crack-bowing between neighboring particles. An example of toughening via second phase additions was reported by M. D. Stuart (1991), for the mullite + alumina system. As the volume fraction of the tougher alumina phase was increased, the toughness and fracture strength of the composite increased. Similar results were reported by

French, et. al. (1992), for the cubic zirconia + alumina system.

The examples described above result in only minor improvements in toughness, all brought about by one-time interactions occurring at the crack tip. After the crack front has passed the particles, they no longer influence crack propagation (a particle can only deflect a crack once). More substantial improvements in toughness can be achieved through mechanisms which continue to operate and exert their influence even after the crack tip has passed by. It is these long-range, cumulative toughening mechanisms which give rise to so-called 'T-curve behavior', in which a materials resistance to crack growth (its Toughness) *increases* with crack extension (Mai & Lawn,1986). The notion of a T-curve clearly implies that the material toughness is not constant, contrary to the above discussion of K_{IC} in the context of the Griffith equation. For a material of non-unique toughness, the concept of a critical stress intensity factor, K_{IC}, as a material property is confusing at best. Therefore, this term will be dropped, in favor of T, the toughness, which may or may not be constant (Mai and Lawn, 1986; Lawn, 1993, Cook, *et. al.* 1987). Several toughening mechanisms which give rise to T-curve behavior will now be discussed.

Transformation Toughening.

Transformation toughening is one of the most well-studied and effective toughening mechanisms in ceramics [Science and Technology of Zirconia, Vol.'s I - IV; Garvie, 1975; McMeeking & Evans, 1982; Green, et. al., 1989]. Nearly all transformation toughening research (in ceramics) has been conducted on zirconia materials. In pure form, zirconia is tetragonal above ~1000° C, and transforms to a monoclinic structure below that temperature (Subarao, 1981). The transformation is martensitic, and is accompanied by a volume expansion of about 4%, and shear strain of about 7%. By adding sufficient amounts of a suitable dopant oxide (such as MgO, Y_2O_3, or CeO_2), the tetragonal phase may be retained in metastable form at low temperatures. It is then possible to force the transformation to occur under the influence of an applied stress, especially in the highly

stressed region near a crack tip. The transformation results in increased toughness, because the accompanying volume expansion establishes a zone of residual compression within the matrix, forming initially at the crack tip, and then extending along the crack surfaces as the crack grows through the frontal zone. This residual compression supplies a closure stress, acting along the crack wake, which effectively reduces the applied stress intensity felt by the crack tip (McMeeking and Evans, 1982). The toughening increment provided by the transformation zone depends on the volume fraction of transforming phase, the transformation strain, the width of the transformation zone, and the critical stress required for transformation.

Two classes of transformation toughening materials may be identified. The first, 'partially stabilized zirconia' (PSZ), consists of cubic grains of zirconia, which contain tetragonal zirconia precipitates. It is the precipitates which transform under applied stress. The most common example of PSZ uses MgO as the stabilizer. The second class, 'tetragonal zirconia polycrystals' (TZP), consists entirely (or nearly so) of tetragonal grains, and whole grains transform to monoclinic. In TZP materials, typical stabilizers are Y_2O_3 or CeO_2. A common variation of TZP is the incorporation of tetragonal zirconia particles into a matrix of different material, such as alumina (this material is often called 'zirconia toughened alumina', or ZTA).

Microcrack Toughening.

A different toughening mechanism which operates in essentially analogous manner to transformation toughening is stress-induced microcracking. Microcrack toughening may arise in single phase materials having thermal expansion anisotropy, or in multiphase materials possessing thermal expansion mismatch between the constituent phases. The pre-existing, localized thermal expansion stresses act in concert with an applied stress to produce microcracks in the frontal zone of a crack tip. As the main crack grows through the frontal zone, the 'microcrack cloud' extends along the walls of the crack, similar to a transformation zone. If the microcracked material

experiences a dilational strain (and the microcracks remain open), a residual compression acts along the crack wake, providing a closure stress to the crack tip. The increment of toughening depends on the microcrack density, the width of the microcracked zone, the residual strain in the wake zone, and the critical stress required for microcrack initiation. Little evidence exists for microcrack toughening in single phase ceramics (Swanson, et. al., 1987; Lawn, 1991); but this mechanism has been reported to operate in several two-phase materials, such as alumina containing unstabilized or metastable zirconia (Ruhle, et. al., 1986), other zirconia - alumina composites (Lutz, et. al., 1991), a borosilicate glass - alumina material (Faber, et. al., 1988), and in SiC-TiB_2 composites (Magley & Faber, 1989).

Grain Bridging.

T-curve behavior can be induced through the restraining influence of intact grains bridging the crack walls. Two different explanations may be offered to account for grain bridging. One was offered by Swain (1986), Vekinis, et. al. (1990), and by Roedel, et. al. (1992). These researchers observed bridging ligaments, spanning the crack faces behind the crack tip, and explained the restraining force associated with these bridges on the basis of elastic deformation. The bridges deformed elastically, and were able to continue supporting a portion of the applied load, effectively reducing the crack tip loading. The second explanation describes the frictional sliding of bridging grains being either pulled out of their sockets in the surrounding matrix, or being simply interlocked mechanically across the crack faces, and sliding against the mating surface as the crack opens up (Swanson, et. al., 1987; Cook, et. al., 1987; Bennison & Lawn, 1989). This frictional sliding produces a closure stress, opposing the crack-opening applied stress field at the crack tip. The mechanics of frictional grain bridging will be considered in part D of this section.

Grain bridging was firmly established as the primary toughening phenomenon occurring in alumina materials by Knehans and Steinbrech (1982), and Swanson, *et. al.* (1987). Knehans and

Steinbrech devised an experiment which clearly demonstrated that the T-curve of alumina was derived from processes occurring in the crack wake. They grew a stable crack, monitored a portion of the T-curve, and then halted the test. Then, they sawed through the crack wake, taking care not to cut through the crack tip itself. Upon reloading, the T-curve immediately reverted back to its initial level, and rose again with the same shape as before, rather than simply continuing from where it left off. Although this proved the importance of the crack wake, it did not establish the operative toughening mechanism, as microcracking is also a wake-dominated toughening phenomenon. Microcracking remained as a possibility until the *in situ* crack path observations of Swanson, *et. al.*, (1987) who monitored the crack-microstructure interactions occurring in the wake during slow, stable crack growth in alumina. Subsequent *in situ* work conducted by the NIST group, headed by B. R. Lawn, and by the Dortmund group, headed by R. Steinbrech, on various aluminas and composites of alumina plus aluminum titanate, has established unambiguously that the mechanism responsible for the toughness in these materials is grain bridging, and not microcracking.

The essential feature of grain bridging is frictional sliding. Similar bridging behavior occurs with second phase particles, such as whiskers, platelets, or short fibers. Continuous fiber reinforced materials also exhibit the same basic behavior, with fibers pulling out of the matrix in the crack wake and thereby providing closure stresses to counteract the applied tension (Marshall & Evans, 1985; Lawn, 1993).

C . T-Curve Modeling.

The essential feature of the T-curve mechanisms described above is the presence of closure stresses acting in the crack wake. If these closure stresses can be quantified, then a stress intensity factor description of the driving force for crack growth may be defined. In this manner, it is possible to model or define the crack growth resistance properties of the material, its T-curve.

A stress intensity description for crack growth may be developed in analogous fashion to Griffith's energy balance. At equilibrium, the driving forces for crack growth are equal to the forces resisting crack growth, that is

$$\Sigma K(c) = \Sigma T(c) \tag{8}$$

The crack driving forces will generally be known, as they derive from external loading (and from internal loading, in the case of an indentation crack). The T-curve function, T(c), consists of the material's intrinsic resistance to crack growth, T_0, which is independent of crack size, and any other microstructure-associated toughening mechanisms. T_0 represents the resistance to the material separation process occurring at the tip of the crack, and is therefore related to the surface energy. Other toughening mechanisms, such as grain bridging or transformation toughening, are seen as contributing a crack-growth-resisting stress intensity factor to T(c), rather than as modifying T_0 (Mai & Lawn, 1986; Mai & Lawn, 1987; Cook, et. al., 1987;Lawn, 1993). Any such resistance terms are labeled $T_\mu(c)$, and the equilibrium condition may be redefined as

$$K(c) = T_0 + T_\mu(c) = T(c) \tag{9}$$

Modeling of the T-curve thus consists of specifying $T_\mu(c)$. It should be noted that $T_\mu = -K_\mu$, so that in order to obtain an increasing T-curve function, $K_\mu(c)$ must be either positive and decreasing, or negative and increasing. The mechanisms considered above are all examples of negative increasing K_μ functions, as they consist of residual closure (*compressive*) stresses acting in the crack wake.

The T-curve modeling of grain bridging in aluminas will now be considered in some detail. The weight of experimental evidence indicates that bridging grains are distributed more or less randomly throughout the wake zone, and that they provide closure stresses to oppose crack growth. The crack wake thus contains a distribution of discrete closure stresses. It should be possible to simply sum up the closure stress intensity contributions from the individual bridges,

and thereby obtain $T_\mu(c)$. The solution becomes unmanageable, however, as the number of bridges increases. Therefore, the discrete bridging forces are replaced by a continuous closure stress distribution, acting over the crack wake. The stress intensity factor solution for a (penny-shaped) crack containing such a wake zone is given by (Tada, et. al., 1985; Cook, et. al., 1987)

$$T_\mu = -K_\mu = \left(\frac{\Psi}{c^{1/2}}\right) \int \sigma(r)\, r\, \frac{dr}{(c^2-r^2)^{1/2}} \qquad (10)$$

Thus, specification of $T_\mu(c)$ requires knowledge of the closure stress distribution function, $\sigma(r)$. Such knowledge does not exist. However, the experimental observations of Swanson provide insight into the general form of a closure stress - crack opening displacement function, $\sigma(u)$. The developers of the bridging theories [Mai and Lawn (1987), Cook, et. al. (1987), Bennison and Lawn (1989)] therefore elected to describe T_μ using a $\sigma(u)$ function instead, and (assuming an unperturbed crack opening displacement profile) made appropriate substitutions into Eq. 10 to give

$$T_\mu = -K_\mu = \left(\frac{E}{T_0}\right) \int \sigma(u)du \qquad (11)$$

The $\sigma(u)$ function for bridging processes generally rises from zero at u=0 (i.e., at the crack tip), increases to a maximum, σ^*, at some point behind the crack tip, and then gradually decreases to zero as the bridges slide toward disengagement at a critical half crack-opening displacement, u^*. The *in situ* work (Swanson, et. al., 1987; Swain, 1986) indicated that grain bridges remained active over large distances behind the crack tip, and it was therefore assumed that the stress-separation function was tail-dominated. The $\sigma(u)$ function could therefore be described by a relation of the following form:

$$\sigma(u) = \sigma^*(1 - u/u^*)^m \qquad (12)$$

for $0 \le u \le u^*$. Several values for the exponent m were considered, and eventually m = 1 was chosen. The value for m influences the shape of the decreasing tail of $\sigma(u)$, with m = 1

representing a linear decrease in σ with u; m = 2, a parabolic decline; and m = 0, a constant valued closure stress. The fits provided by the bridging theory were not very sensitive to the value of m, however (Mai and Lawn 1987; Cook, et. al. 1987).

This model was originally used (Mai and Lawn, 1987) to describe the directly measured (DCB) T-curve of approximately 20 μm grain size alumina, reported by Swain (1986). Unknown parameters in the above equations were treated as adjustable variables in computer fitting of Swain's experimental toughness curve. Reasonable fits to Swain's data were obtained. Shortly afterwards, Cook, et. al (1987), extended the model to allow for the description of indentation strength behavior. In so doing, it became possible to extract the T-curve from the experimentally measured indentation strength data. This was accomplished by incorporating the residual stress intensity field, K_r, associated with the indentation zone (Lawn, Evans & Marshall, 1980) into the applied stress intensity factor of Eq. 9. The equilibrium condition then becomes

$$K_A(c) = \psi\sigma_a c^{1/2} + \chi P c^{-3/2} = T_0 + T_\mu(c) = T(c) \qquad (13)$$

This equation is rearranged and solved to obtain $\sigma_a(c)$, using calculated values for $T_\mu(c)$ from Eq.s 11 and 12, and with T_0 as an adjustable parameter. The instability condition, $dK/dc \geq dT/dc$, corresponds to the maximum in the $\sigma_a(c)$ function. Thus, the T-curve used in calculating the $\sigma_a(c)$ function predicts the strength for any given indent load as the maximum in $\sigma_a(c)$. After the indentation strengths are calculated by the T-curve model, they are compared to the experimentally measured values. Then, the adjustable parameters characterizing the T-curve are incremented, and new strengths are calculated until a good match between predicted and measured strengths are obtained. The T-curve which produced the best fit to the strength data is then identified as the T-curve for the material. Using this procedure, Cook, et. al., obtained good fits to the indentation strength data for a range of alumina, glass ceramic, and barium titanate materials.

The successful application of these initial bridging models was encouraging, but could

be viewed as a starting point for further refinements. The model was able to produce reasonable values for the maximum closure stress, σ^*, the crack opening displacement corresponding to bridge disengagement, u^*, the intrinsic toughness, T_0, and the peak, steady state toughness, T_{ss}. However, a strong element of empiricism remained, as the factors *controlling* σ^* and u^* were left unknown. Without such knowledge, materials processors would be left with no guidelines for producing optimally toughened ceramics. This issue was addressed in the next modification of the T-curve model, by Bennison and Lawn (1989).

Bennison and Lawn explained the origin and development of the bridging stresses, based on frictional pullout of the bridging grains from their sockets in the surrounding matrix. Bridging grains were considered to be clamped into the matrix by localized, residual, thermal expansion mismatch stresses. When a crack intersects a potential bridge, the bridge matrix interface debonds, and as the crack continues to grow (crack opening displacement increases), the debonded bridge begins to pull out of the matrix. The clamping stresses lead to considerable sliding friction accompanying this pull-out, which gives rise to a closure stress. The Bennison-Lawn model employed the same basic form for the $\sigma(u)$ function as the previous models; the key difference was that their model went one step further by assuming the *form* of σ^*, the maximum closure stress,

$$\sigma^* = (\mu\sigma_R\lambda u^*/d^2)(2d^2/l^2 - 1) \qquad (14)$$

where μ is a friction coefficient, σ_R is the localized residual clamping stress, λ is the circumferential distance around the bridge at the debonding interface, d is the bridge spacing, and l is the grain size. In the earlier models, σ^* was treated as a simple adjustable parameter in computer fitting of the experimental data. The Bennison-Lawn model accounted for the microstructural variables which control the closure stress term. Thus, in theory, once they determined the values of the controlling microstructural variables, μ, σ_R, and u^*, then the T-curve

(and strength) could be determined as a function of grain size, grain shape, second phase additions, etc. These microstructural differences manifest themselves as changes in the bridging peak closure stress term, σ^*, and/or in the critical crack opening for bridge disengagement, u^*. In the previous model, these terms would have to be evaluated anew whenever the microstructure was altered.

Some observations on the influence of microstructure on the closure stress are in order. Close examination of Eq.s 12 and 14 indicates that the peak closure stress does not change with grain size ($\lambda = 4l$ for idealized grain of square cross-section; and $u^* \propto l$, see Bennison and Lawn, 1989). The critical crack opening required for bridge disengagement, u^*, does change. Thus, for increasing grain sizes, the bridging closure field is seen to operate over larger distances behind the crack tip, resulting in enhanced toughness for larger grain sizes. The peak closure stress does change with grain *shape*, however, increasing in magnitude as the grain aspect ratio increases. The σ^* also increases with friction coefficient, μ, and with the residual clamping stress, σ_R. This last term is controlled by thermal expansion mismatch, and can therefore be altered through processing. For example, by adding appropriate second phase additions, the internal residual thermal expansion mismatch stresses can be controlled. This explains the rationale behind adding aluminum titanate (Runyan & Bennison, 1991; Padture, 1991; Russo, et. al., 1992), mullite (Stuart, 1991; Khan, unpublished), or various grain boundary glass phases (Padture, 1992) to alumina. Clearly, the model of Bennison and Lawn provides the processing engineer with valuable guidelines for improving strength and toughness.

D. The Indentation-Strength-in-Bending Test (ISB).

There are many ways to characterize strength and toughness. The indentation strength test provides a means to characterize both, has many advantages over other techniques, and was consequently used to evaluate the materials of this work. With the ISB test, the location, size and

shape of the fracture-producing flaw are controlled by indenting the center of the prospective tensile surface with a Vickers diamond indenter. By varying the indentation load, a wide range of starting crack sizes can be produced. Subsequent bend testing - 3 or 4 point bend bars, or biaxial flexure disks - provides strength data as a function of the indent load (or, initial crack size). By essentially providing strength as a function of crack size, the two main variables required to describe stress intensity, the ISB test may be used to determine T-curve properties.

First consider the cracking behavior produced by the Vickers indenter. The possible cracking patterns which may evolve during or after indentation are illustrated in Figure I.1 (from Cook and Pharr, 1990). Although it is usually assumed that the Vickers flaw has half-penny shape (i.e., semi-circular), Fig I.1 indicates that the true crack shape is not always so simple. The actual shape, and the sequence of crack growth during the indentation loading-unloading cycle varies from material to material, and are largely dependent on the ratio of Young's modulus to hardness, E/H. Nevertheless, the half-penny shape has been assumed for this research, and the mechanics of this flaw system will now be discussed.

The driving force for half-penny crack growth arises from the elastic-plastic mismatch strain between the plastic deformation zone under the indent impression and the surrounding bulk of elastic material. The volume of material displaced by the hardness impression is accommodated by plastic deformation in a zone underneath the impression, which is resisted by the elastic bulk. The indentation system may therefore be modelled as an expanding cavity, having as the key feature a residual tensile stress field surrounding the indent, distributed as a hoop stress which decreases in magnitude with (distance from the indent)$^{-3}$. Half-penny cracks nucleated in this residual stress field are driven by the residual stress intensity factor, given by

$$K_r = \chi P c^{-3/2} \tag{15}$$

where χ is a constant ($=\xi(E/H)^{1/2}$), P is indentation load, and c is the initial crack size produced

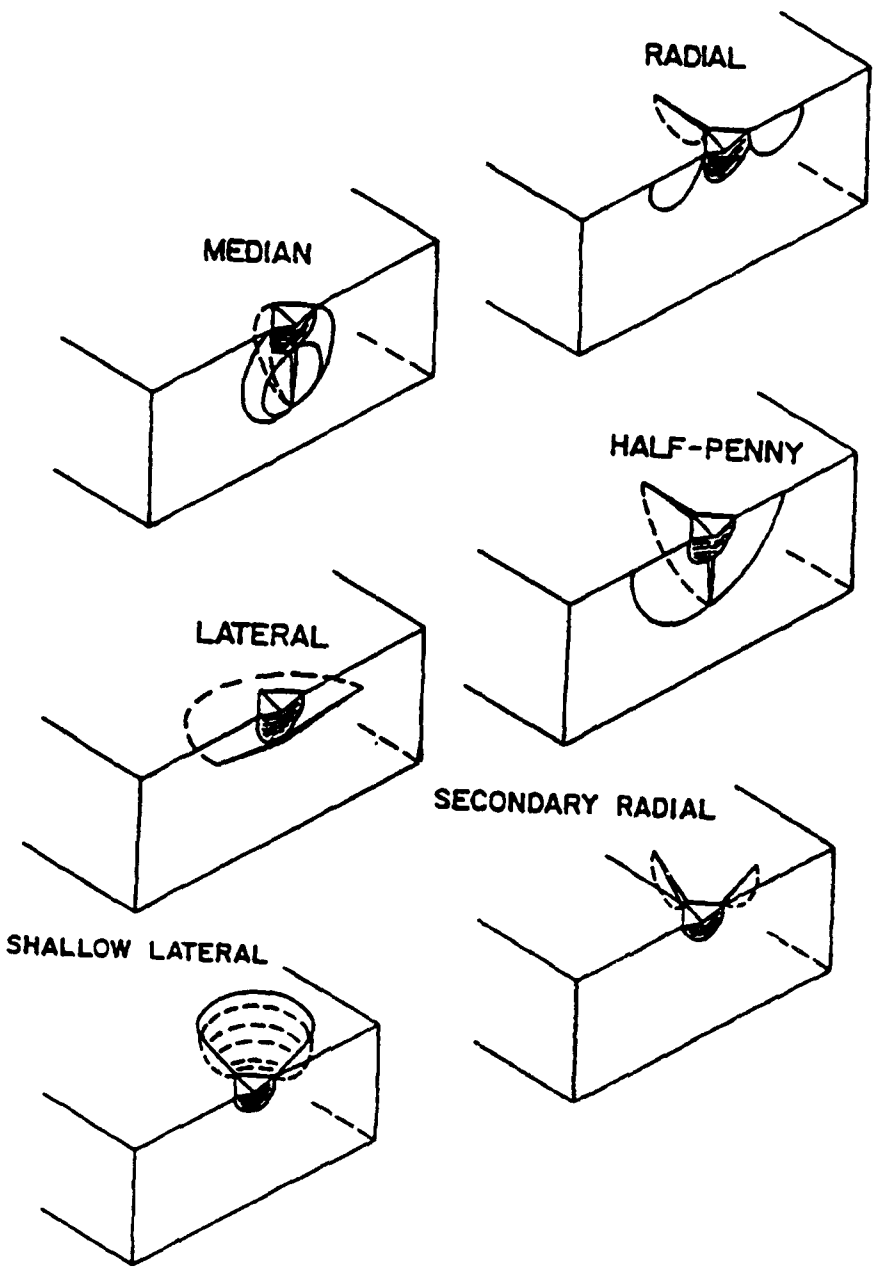

Figure I.1. The various types of cracks which may be observed at a Vickers indentation site (from Cook & Pharr, 1990).

by the indent of load P. Under external loading, as in a strength test, the residual field is augmented by the applied field, producing a net applied stress intensity factor for crack growth, K_A,

$$K_A = K_a + K_r = \psi\sigma_a c^{1/2} + \chi P c^{-3/2} \quad (16)$$

As mentioned in the previous section, the crack is in equilibrium when $K_A = T(c)$. For a material of constant toughness, T_0 (i.e., $T_\mu = 0$), instability (fracture) occurs when $dK_A/dc \geq dT(c)/dc = 0$. This instability relation may be solved for c to obtain the crack size at fracture, by substituting the applied stress at equilibrium for σ_a (i.e., set Eq. 16 equal to T_0, solve for σ_a). This operation demonstrates that the crack size at fracture is ~2.52 times as large as the initial crack size, indicating that the residual field of the indentation exerts a *stabilizing* influence on crack growth (positive decreasing). That final crack size may then be substituted for c in the equilibrium equation (set $K_A = T_0$), to solve for the fracture stress:

$$\sigma_f = (3/4\psi)(T_0)^{4/3}(4\chi P)^{-1/3} \quad (17)$$

This gives the often stated $P^{-1/3}$ dependence of strength for materials having a constant toughness. Typically, indentation strength data are plotted in terms of log σ_f vs. log P, such that a constant toughness material will exhibit a linearly decreasing strength response, with slope -1/3, for increasing indent loads.

There are two commonly observed departures from the linear -1/3 strength response. The first appears as a flattening out of the curve at small P, tending toward an upper plateau of nearly constant strength. This is termed 'flaw tolerance', as the strength in this region is independent of the starting indentation flaw size. Flaw tolerance is indicative of a non-unique toughness, i.e. T-curve behavior. The stronger the T-curve, the flatter the strength response becomes. This behavior will be explored in greater detail in the T-curve modeling section (Section V). For now, it should simply be noted that the indentation strength test provides a means of qualitatively

assessing T-curve behavior.

The second deviation from the $P^{-1/3}$ strength response occurs in the large P region, and is caused by lateral cracking (Fig. 1.1). Lateral cracking reduces the driving force for half-penny crack growth during indentation, resulting in smaller indentation crack sizes, and ultimately leading to inflated strength values (compared to what would be expected in the absence of lateral cracking). Cook has described the effect of lateral cracking as a reduction in the χ term of Eq. 15, as follows:

$$\chi = \chi_0/(1+P/P_L) \tag{18}$$

where χ_0 is the unmodified χ term (obtained in absence of lateral cracking), and P_L is the indent load 'characterizing the onset of the reduction in the residual field by the lateral crack influence' (Cook, et. al. 1990). Lateral crack development, L_D, may be evaluated empirically using the relation,

$$L_D = (2V+R)/12 \tag{19}$$

where V is the number of Vickers indent quadrants containing lateral cracks, and R is the number of lateral crack chips removed. Thus, an indent containing lateral cracks in each quadrant, but no chips removed, has an $L_D = 0.67$. Cook, et. al., estimated that the lateral crack influence becomes significant when $L_D \rangle \sim 67\%$, and when $P/P_L \approx 0.01$, and therefore suggested that P_L may be estimated by $P_L \approx 100 \times P$(at which $L_D = 0.67$). Their data may actually suggest a relation closer to $P_L \approx 10$ or 20 times the load for $L_D = 0.67$, however. The P_L term may alternately be estimated by fitting the indentation crack length data to the relations (Cook, et. al., 1990)

$$c_0 = c_L[(P/P_L)/(1+P/P_L)]^{2/3} \tag{20}$$

$$c_L = (\chi_0 P_L/T_0)^{2/3} \tag{21}$$

The primary significance of lateral cracking is that it produces artificially inflated strengths, and may therefore lead to inflated toughness values. If T-curve modeling is to be attempted based on indentation strength data, the lateral cracking influence must be assessed and

incorporated into the fracture mechanics formulation, via Eq. 18 above.

E. Literature Review: Laminated Composites and Other Layered Microstructures.

In the late 1960's, Paul Gutshall and Gordon Gross (1968, 1969) of Midwest Research Institute observed that the fracture energy of alumina *increased* with increasing grain size, and noted that such an observation ran counter to conventional wisdom. It had generally been accepted that the strength of alumina, indeed all brittle ceramics, *decreased* as the grain size increased. Since strength and toughness are related, the frequently observed strength-grain size relation could be explained in either of two ways: (1) the strength was greater for fine-grained materials because they had inherently smaller flaws; or (2) the strength of the fine-grained material was greater because it had a higher toughness. The first explanation was universally accepted, as no one believed there was any difference in toughness associated with differences in the grain size of brittle materials. Gutshall and Gross were the first to recognize that there was in fact a difference in toughness associated with differences in grain size, but that the difference was the exact opposite of the view presented above. They explained the difference in toughness on the basis of a marked difference in the fracture paths. Fine grained alumina was observed to exhibit a much greater amount of intergranular fracture than transgranular, and the amount of transgranular fracture increased with the grain size. To Gutshall and Gross, the coarse-grained alumina was tougher simply because it forced the crack to propagate through the grains rather than along the grain boundaries, which were inherently weaker due to the inevitable presence of grain boundary impurities used as sintering aids. Although their accounting of the reasons behind the observed toughness-grain size relation falls clearly short of today's generally accepted view (grain bridging, with crack wake effects and T-curve behavior), these researchers nevertheless understood that their discovery could be exploited through intelligent microstructural design. They suggested that a fine/coarse structure might result in 'optimum strength'. A fine-grained surface region

would reduce the critical flaw size in the highly stressed surface, which would provide increased resistance to initiation of crack growth; and the coarser interior would then provide increased resistance to propagation of the crack.

It should be noted that Gutshall and Gross made no mention of crack wake effects or T-curve behavior, nor did they discuss the possible effects of stable vs. unstable crack growth. Importantly, they also did not discuss any need to control the thickness of the fine-grained surface region.

Following Gutshall and Gross, Mistler (1973) produced tape-cast, trilayer alumina materials having a fine-grained surface layer and a coarser interior. The grain sizes were controlled by addition of impurities. The surface material employed any one of several grain growth inhibitors (e.g., talc, or MgO), while the interior material contained a grain growth enhancer (e.g., MnO, or TiO_2). Composites processed in this manner possessed a surface region having about one half the grain size of the interior material, but the actual grain sizes were very small. Average surface grain sizes were 0.78 μm, and average interior grain sizes were 1.48 μm. The strength of these composites (~119 ksi) were compared to the monolithic base materials, and the composites were found to have strengths ~20% greater than the surface material (100 ksi), and ~65% greater than the interior material (72 ksi). Mistler concluded that he had successfully exploited the 'Gutshall-Gross mechanism', and received a patent for his efforts (1972).

There are three important points that should be made concerning Mistler's work. First, like Gutshall and Gross, Mistler did not address the question of the necessary thickness of the surface material. The surface layer thickness in his composites was about 127μm, but no rationale for that value was provided. Second, he explained the improvement in the composite strength on the basis of the grain size difference between surface and bulk. As mentioned above, that grain size difference was rather small. Although he did mention the possibility that the improved strength

could have been caused by a difference in thermal expansion between surface and bulk (resulting in residual compression in the surface), this explanation was clearly given less credence than the grain size difference. However, thermal expansion mismatch stresses (caused by the concentration differences between surface and interior materials) seem much more likely to explain Mistler's composite strength behavior, to this author, than a difference in strength (or toughness) between 0.78 μm alumina and 1.48 μm alumina. Indeed, Gutshall and Gross reported toughness differences for aluminas of different grain sizes, but they tested a much wider range of grain sizes (10 μm, 30 μm, and 45 μm). Mistler noted that there "did not appear to be a good explanation for the increase in strength" of the composite, compared to the monolithic surface material. This was true; there was no reason to expect the strength of his composite to be *greater* than that of its base materials, *unless residual stresses were present.* If it may be assumed that the strength of Mistler's fine-grained materials was controlled by natural flaws, which would be of about the same size as the grains, then it is certainly reasonable to conclude that such small flaws would never enter the underlying bulk material prior to catastrophic, unstable fracture. Therefore, the coarseness of the bulk material would not be expected to influence the strength properties of the composite in any way.

Mistler's work should more properly be classified as a residual surface strengthening technique. There are many ways to impart a layer of compressive residual stress to a material's surface, which would then counteract an applied tensile stress, thereby improving the strength and damage resistance of the material. Throughout the 1960's and 1970's, Kirchner, *et. al.*, examined ways to produce alumina materials having a layer of residual surface compression. They successfully improved the flexural strength of alumina by allowing solid solution dopants (notably Cr_2O_3) to diffuse into the surface during a high temperature anneal. When a solid solution has a lower thermal expansion than the unmodified interior, the surface region will be left in a state

of residual compression upon cooling. (Observe that this technique is quite similar, in effect, to Mistler's, although the procesing routes were different.)

In similar fashion, Kirchner, *et. al.* (1971), modified the surface region of alumina through high temperature reactions with packing powders, to form second phase particles of lower thermal expansion (such as mullite, or various calcium aluminates). In addition to the lower thermal expansion, these second phases experienced substantial volume expansion upon formation, which could have further enhanced the residual compression, provided those stresses were not relaxed by plastic deformation before cooling. Both techniques were able to increase the strength of the alumina, anywhere from 14% to about 65%.

Kirchner and Mistler both measured the flexure strengths of unindented bars, and therefore their knowledge of the strength response was liminted to a narrow range of (small) flaw sizes. This made it more difficult for them to assess the effect of the surface layer on strength and toughness. Indentation strength testing provides a means for separating the effects of residual surface stresses from the 'Gutshall-Gross mechanism'. Of course, the indentation strength method had not yet been developed, but the main point is that their incomplete knowledge of strength properties prevented them from firmly establishing a mechanism for the observed behaviors, and from determining an optimum thickness for the surface layer. Kirchner recognized this, stating,

> a rational basis for determining the optimum thickness of compressive surface layers is not available at present. It is clear however that the compressive surface layers should be thicker than the flaws expected from abrasion.... On the other hand, the compressive surface layers should not be so thick that they result in substantial tensile stresses in the core.

This statement represented the extent of concern over surface layer thickness, and it indicates that they were not considering the possibility of stable crack growth, assuming instead that all fractures were of the classical Griffith character - unstable, with cracks failing spontaneously from their initial configurations. It is now recognized that an abrasion flaw only represents an *initial size*,

and that strength is not necessarily dependent upon initial flaw sizes. Stable crack growth might be expected to significantly influence the optimum surface layer thickness, resulting in an optimum value which is quite different from the width of the compression zone.

There are other ways to introduce residual compression into a surface, as mentioned above, in part A. Those methods are generally well studied, and information about them is readily available in the literature. Most of those techniques, as well as the ones described in the preceeding paragraphs, are limited in the depth of the compressive zone which can be produced. In recent years, Virkar & Cutler, *et. al.*, (Virkar, et. al., 1987; Cutler, et. al., 1987; Hansen, et. al., 1988) have developed trilayer composites which take advantage of zirconia transformations in the surface. The transformations are achieved in a different manner than was described above, and this allows much greater control over the depth of the compressive zone. The composites consisted of Al_2O_3 + 15 vol% ZrO_2 (AZ15). In the interior layer, the zirconia was in tetragonal form (2 mol% Y_2O_3); but the zirconia in the surface layer contained no stabilizer, and therefore transformed to monoclinic upon cooling below about 1000° C. The transformation resulted in a volume expansion of about 4%, leading to substantial residual compression in the surface layer. Since the transformation was not caused by a concentration gradient or surface localized stress, the compression zone was not restricted to the near surface region. Compressive stress could be produced to almost any desired depth, simply by changing the initial thickness of the unstabilized AZ15 surface layer.

Using this technique, Virkar, *et. al.*, fabricated trilayers having surface layer thicknesses of 375 μm, 750 μm, and 1500 μm. Since the total thickness was kept constant, the surface residual stresses decreased as layer thickness increased. Residual compression values were determined to be 596, 477, and 238 MPa, respectively. Composite strengths were consistently and substantially higher than that of the base materials (up to a 70% increase). However, the strength

behavior as a function of thickness showed an unexpected trend. Strengths increased with increasing surface layer thickness. Since residual compression *decreased* with increasing thickness, the results were unexpected and surprising. This was explained on the basis of the bending stress profile. Fractography revealed the presence of gross voids in the bulk material, from processing. Fracture was seen to originate from these flaws, which were located far enough away from the surface so that the measured strength was effectively increased over that of the monolithic bulk material. As surface layer thickness increased, these flaws were pushed further in toward the neutral axis, resulting in further increases in the measured strengths. In subsequent work, they were able to improve the processing to produce surface material - controlled fractures, which lead to the expected strength-thickness trends (i.e., composite strength increasing as layer thickness decreased, and residual compression increased).

Virkar's group also examined the indentation strength response of these materials. The composites maintained their strength improvement compared to the base materials all the way out to P = 1000 N, which was the largest load tested. In addition, the composite displayed a relatively flat indentation strength response, indicative of significant flaw tolerance. This flaw tolerance was a direct result of the compressive stress, which caused the indentation crack sizes to be much smaller than they would have been in the absence of the residual stress. The residual compression also counteracted the applied stress, resulting in an increase in apparent toughness. A compressive surface layer imparts flaw tolerance by providing a stabilizing influence on crack growth.

Virkar, *et. al.*, also measured the strength as a function of temperature, and found that the composites maintained their strength advantage at temperatures as high as 750°C. (Beyond that, the strength rapidly decreased, due to reverse transformation of the monoclinic zirconia back to tetragonal.) This was seen as an encouraging result, and they proposed their composite strategy as a high temperature strengthening mechanism. Residual compression introduced by their

technique is more thermally stable than compression resulting from thermal expansion mismatch (as in Kirchner's work), because the mismatch stresses decrease as temperature increases. Similarly, grinding-induced residual compression can be relieved at high temperature.

F. Tape Casting

Tape casting is a processing method in which a wet slurry is cast onto a flat sheet and made to pass underneath a doctor blade in order to control the thickness. Through tape casting, it is possible to create large areas of thin ceramic sheets, having well controlled thickness and surface roughness. The slurry consists of the ceramic powder, suspended in a solution of solvents, polymer binders, plasticizers, and dispersants. After casting, the solvents evaporate, leaving behind a powder compact which is held together by the polymer binder. What follows is a brief explanation of the roles of the various slurry constituents, and a discussion of casting variables or problems having particular relevance to this research.

The solvents may be either organic or aqueous, although use of organic solvents is more common. The solvent simply provides a vehicle for mixing and dispersing the other constituents. Thus, the binder, plasticizer, and dispersant must be soluble in the solvent, but the solvent should not react with the powder (Roosen, 1988).

The binder is used to hold the dried tape together, and must provide enough strength and flexibility to allow easy handling of the green tape. In addition, the binder should have a low glass transition temperature, to allow ease of lamination. The amount of binder is important; as little as possible should be used. In the tape casting literature (or, the paints literature) the concept of a critical powder volume concentration, CPVC is described (Patton, 1979; Roosen, 1988; Castells, et. al., 1983; Bierwagen, 1972; Hegedus & Eng, 1988). The CPVC is the powder volume fraction (volume of powder/ total volume of non-volatiles) at which the binder just fills the voids between the packed powder particles. If the tape contains less powder (or, more binder) than the CPVC, there will

be excess binder between the powder particles. That excess binder burns out upon firing, leaving behind void space and resulting in a decreased green density. If, however, the tape contains more powder (or, less binder) than the CPVC, there will not be enough binder to fill the voids between the particles, and the green strength will decrease.

The plasticizer increases the flexibility of the binder, and thereby, of the green tape as well. It may also aid in dispersion of the powders. The dispersants prevent the powder particles from agglomerating in the slurry, and are therefore of critical importance in producing a homogeneous, well mixed slurry.

Three of the many potential problems which can occur in tape casting have special relevance to this research: Benard cells, preferential settling, and agglomeration. Benard cells are a pattern of circular or hexagonal cells which may form on the surface of a drying tape (Patton, 1979; Nylen & Sunderland, 1965; Van Loo, 1956). The cell structure arises from vortex flow of the solvent during evaporation, caused by localized variations in surface tension. Since the ceramic particles are swept along in the vortex currents, this vortex flow changes the distribution of the ceramic particles during drying, leading to inhomogeneities in the dried tape. These cells remain after sintering, and therefore may affect the final microstructure of the body. Figure I.2 shows Benard cells in some of the initial tapes produced for this project. In the fired microstructure, the inhomogeneity associated with Benard cells may show up as pockets of partially sintered powder aligned along the original layer interfaces, as seen in Figure I.2. If the condition of these interfaces is poor enough, substantial amounts of delamination may occur during fracture, potentially giving rise to increased toughness (Clegg, 1990) or, more likely, leading to reduced strength (M. D. Stuart, unpublished work).

Preferential settling is a phenomenon which may occur in drying tapes containing more than one kind of powder. If there are size or density differences between the powders, one species

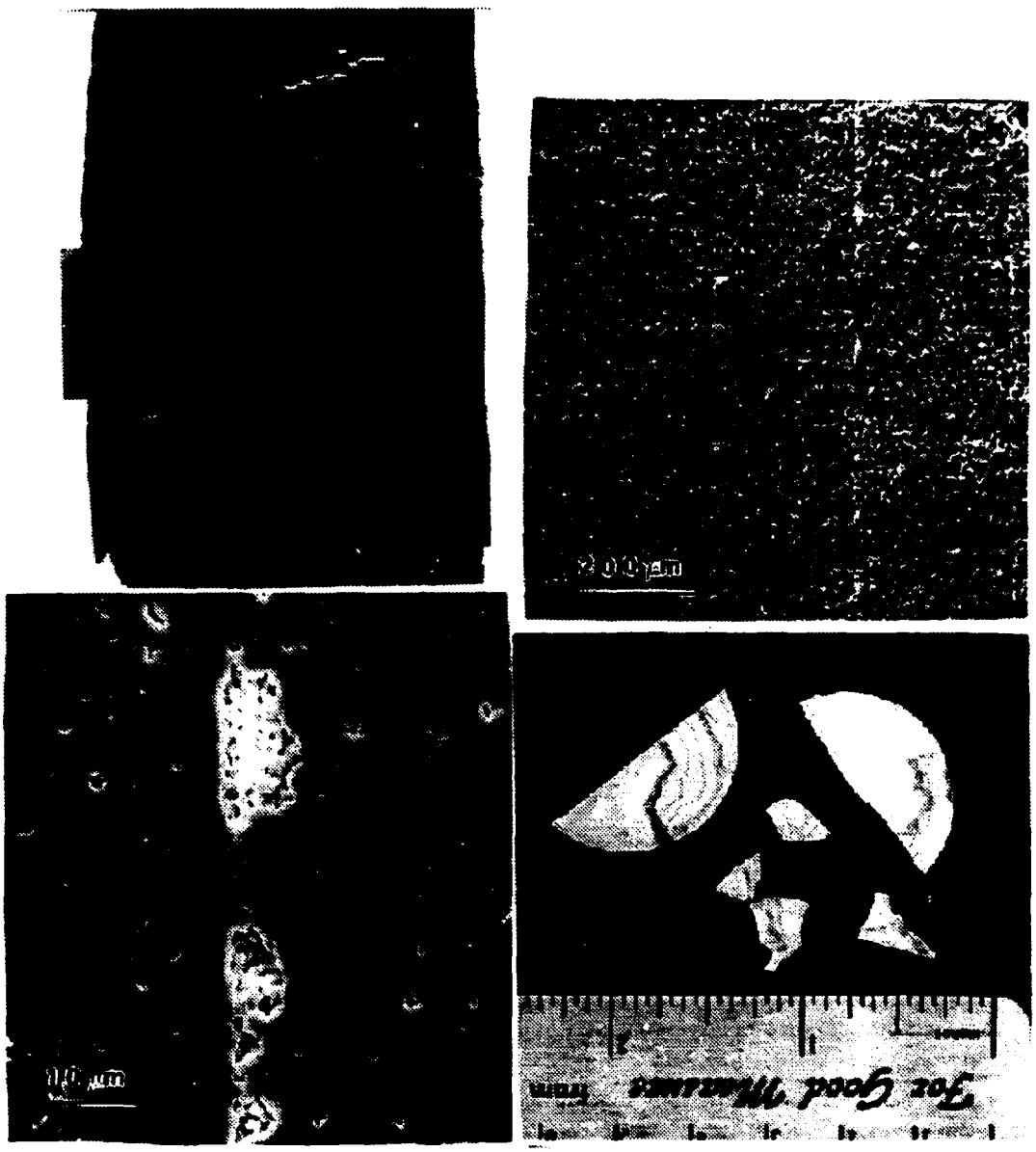

(a)	(b)
(c)	(d)

Figure I.2. Benard cells (general pattern of mottled contrast in (a)) in the green tape may lead to pockets of incompletely sintered powder aligned along the original layer interfaces (b) and (c). These, in turn, may result in weak interfaces, causing delaminations to occur during fracture, as shown in (d).

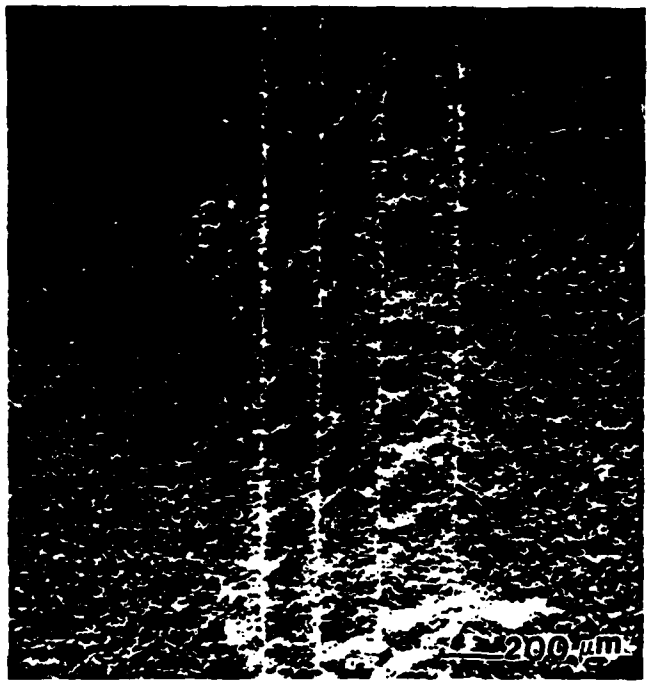

Figure I.3. Fracture surface showing the full cross-section of an Al_2O_3 : Al_2O_3 + 12 vol.% ZrO_2 laminated composite. This composite consisted of four layers of the AZ12 sandwiched between three layers of undoped alumina on either side. At center, the four AZ12 layers are shown to be generally brighter than the undoped alumina layers to the left and right. Within the central AZ12 region, there are four narrow bands of much greater brightness. These bright stripes are zirconia; and they formed as a result of preferential settling of the zirconia particles during drying of the as-cast tape.

may settle more toward the bottom of the tape. Figure 1.3 shows preferential settling of zirconia in an Al_2O_3 + 12 vol% ZrO_2 multilayered body. Such gross macroscopic inhomogeneity is generally avoided (although it could conceivably be exploited to produce unusual microstructures).

Agglomeration is simply the clumping together of particles in the slurry. If uniform, homogeneous microstructures are desired, agglomerates must be eliminated. According to Tomney, dispersion of a powder in liquid occurs in three stages. First, the liquid wets the particle surfaces. Second, in order to achieve complete wetting, mechanical breakdown of agglomerates is required (usually accomplished by ball milling). Finally, continued, stable dispersion of the powder requires repulsive forces between the particles, otherwise they will constantly re-agglomerate. Providing those repulsive forces is the function of the dispersant, and the forces may arise from either of two mechanisms. In polar solvents, the dispersant normally works by electrostatic repulsion, involving charged layers of adsorbed ions (Lewis, 1961; Mysels, 1959; Tadros, 1984; Sato & Ruch, 1980; Reed, 1988). A different mechanism is required for nonpolar solvents, however, and dispersion in these systems is achieved through 'steric hindrance' (Lewis, 1961; Tomney, 1984; Napper, 1977; Sato & Ruch, 1980; Tadros, 1984). This requires the adsorption of long chain polymers onto the powder surfaces, which prevent the particles from approaching too closely. When two particles do approach each other, interpenetration and compression of the adsorbed polymer chains can occur, resulting in 'a loss of configurational entropy per adsorbed molecule, and a corresponding increase in the free energy of the system, which leads to a steric (entropic) repulsion' (Tomney, 1984). If, however, a non-uniform, heterogeneous microstructure is desired, then the tape casting operation is made much easier, simply by allowing the particles to agglomerate. Producing heterogeneous microstructures in this manner has some advantages over the method of Padture (1991), Stuart (1991), and Claussen. No pre-mixing of powders is required, and there is no need to use spray-dried agglomerates.

II. STATEMENT OF PURPOSE

The previous section described various strategies for improving strength and toughness properties. In ceramics, high strength is not uncommonly observed (Lange, 1982; Richerson, 1982, 1992; Tsukuma, et. al., 1985; Chantikul, et. al. 1990, Science and Technology of Zirconia, Vol.'s I-IV; Cook & Pharr, 1992; Lawn, 1993), provided the inherent flaws are not too large. The main problem to be overcome in order for ceramics to be used in structural applications is low toughness. Some improvements in toughness have been reported for ceramics, most notably in the areas of transformation toughening (Science and Technology of Zirconia, Vol.'s I-IV; Ready, et. al, 1988; Heuer, et. al., 1988; Yu & Shetty, 1989) and fiber-reinforced composites (Prewo & Brennan, 1982; Zok, et. al, 1991). In non-fibrous ceramics, the most significant gains in toughness have been produced by T-curve mechanisms, which usually have the unfortunate, accompanying side-effect of a reduction in strength (Swain and Rose, 1986; Cook, et. al, 1987; Heussner & Claussen, 1989; Chantikul, et. al, 1990). This frequently encountered trade-off between strength and toughness properties (Swain, 1985; Marshall, 1986; Swain and Rose, 1986) is a serious problem in ceramics, and is the primary motivation behind this research. If the strength reduction associated with the T-curve approaches or falls below the required design stress for a potential application, then any improvement in toughness has been negated. Thus, a goal in ceramics processing has been to produce a body possessing **both** high toughness and high strength. The usual strategy involves an optimized processing procedure, designed to compromise a little on both the strength and the toughness, resulting in acceptable levels for each. This section will describe a laminated composite design, which has the potential of achieving both highest strength and highest toughness, *without compromising either*.

The design concept is illustrated in Figure II.1. Curve A depicts the indentation strength response for a typical low toughness ceramic. For small flaw sizes, the material exhibits a high strength. Without a T-curve, however, this material is flaw-sensitive, and its strength falls of

THIS
PAGE
IS
MISSING
IN
ORIGINAL
DOCUMENT

34

dramatically as the flaw size increases. If a T-curve mechanism can be activated, the material becomes flaw tolerant, displaying a nearly invariant strength, as shown by material B. This flaw tolerance usually means an improved strength for large flaw sizes, but a much lower strength for small flaws, compared to material A. By placing a layer of A-type material on the top and bottom surfaces of a B-type material, a laminated composite is produced which may possess the toughness and flaw tolerance properties associated with the T-curve of material B, without sacrificing the small flaw strength displayed by material A. With an optimal surface layer thickness, the trilayer composite exhibits the best strength behavior of the two materials, as shown by curve C.

A simple technique may be used to estimate the optimum surface layer thickness. The strength curves of the two base materials intersect at a certain indent load, P_i. The crack size produced in the surface material by an indent of load P_i is given by Eq. 15 -

$$c = (\chi P_i / T_0)^{2/3}$$

where χ is a constant, equal to $0.016(E/H)^{1/2}$; and T_0 is the constant toughness of the surface material. For example, using $E/H = 22$, $T_0 = 2.1$ MPa$\sqrt{m}$, and $P_i = 30N$, a calculated crack size of 105 μm is obtained. The trilayer composite would then be made such that the final fired thickness of the surface layer was about 105 μm. This calculation is somewhat sensitive to the values of E, H, and T_0; but if these values are not known, then the crack size resulting from P_i could simply be measured, and the surface layer thickness set to this measured crack length. It must be emphasized, however, that this estimation of the optimum thickness provides only an approximate guide. The flaw produced by P_i is simply the largest possible flaw which (prior to loading) is completely contained within the surface layer. Clearly, this technique ignores crack shape effects, and the possibility of stable crack growth.

The goals of this research were the following:

(1) To produce Al_2O_3 + 20 vol.% Al_2TiO_5 materials ('AAT20') having the highest possible

strength throughout the entire range of flaw sizes, using a model trilayer laminated composite design;

(2) To evaluate the effect of surface layer thickness on the strength response of the trilayer composites;

(3) To model the strength, flaw tolerance, and T-curve properties of the AAT20 trilayer composites, based on the individual T-curves of the two base materials;

(4) To demonstrate the trilayer design concept using zirconia-based materials of higher strength and toughness than the AAT20 system.

III. EXPERIMENTAL PROCEDURES

A. Material Details.

The main part of this work was carried out using high purity alumina and aluminum titanate powders. The alumina was made by Sumitomo, grade AKP-HP, with a purity of 99.995% and mean particle size of 0.45 μm. The aluminum titanate was custom made for this project by Trans-Tech, with a purity of 99+%, and mean particle size of ~1μm. All materials for this research were made by tape casting. A commercial binder - solvent solution was used to make the tape casting slurries. This solution contained the solvents, binders, plasticizers, and dispersants, already mixed together, and was made by Metoramic Sciences, Inc. (grade B73181). The solvent system consisted of acetone and naphtha; the binder was an acrylic polymer; and the plasticizer was dioctyl phthalate. Additional surfactant was obtained from MSI for use as plasticizer and dispersant (grade M1114), but no information about this surfactant was available (proprietary).

Zirconia composites were also produced. All zirconia powders were made by Tosoh. Powder grades used were TZ-3Y20A and TZ-12CE. The 3Y20A is a spray dried powder, consisting of 3 mol% Y_2O_3 - doped ZrO_2 + 20 wt% Al_2O_3 as second phase reinforcement. This powder had a high specific surface area, 17.2 m^2/g. The 12CE is 12 mol% CeO_2 - doped ZrO_2, which is a transformation toughening grade.

Additional information about equipment and suppliers may be found in Appendix III.

B. Slurry Processing.

Tape casting slurries were prepared inside a clean room. The slurries were mixed by ball milling, inside high density polyethylene bottles. The milling media were 99.5% alumina rods, 0.5 in. x 0.5 in. (U.S. Stoneware Corp., Mahwah, NJ). Both bottles and milling rods were acid washed before using, to remove any impurities. Acid washing consisted of rinsing with trichloroethylene, then acetone, then ethanol, then deionized water. Next, the labware was soaked in aqua regia (3:1

$HCl:HNO_3$) for one hour, rinsed with deionized water, soaked in HF for one hour, rinsed again with deionized water and dried in an oven. Slurries were cast using a laboratory scale batch-type tape caster and drying table (TAM), on top of Mylar sheet (DuPont), which was lying on top of glass plates. The Mylar was pretreated on the top surface with a silicone release agent.

Slurry ingredients were always added in the same order: first, the binder-solvent solution, then the extra dispersant, then the powder, then any additional methylene chloride solvent (as needed). After ball milling, a de-airing step was required in order to prevent formation of air bubbles in the green tape. De-airing was accomplished by transferring the slurry to a smaller bottle to remove the milling rods, and slow-rolling on the ball mill at as slow a speed as possible for at least 16 hours. The slurry was cast immediately following the de-airing step. It is worth noting that no filtration step was used. The slurries produced for this research were considered too viscous and dried too rapidly to allow any filtration. Important details relevant to the processing of each kind of slurry follow.

1. AAT20 Materials:

Homogeneous AAT20 was prepared by first ball milling the aluminum titanate powder in the full amount of binder solution for one day. Then the alumina powder was added, plus some methylene chloride to decrease slip viscosity (to improve mixing), and the slurry was ball milled for another two days. This resulted in an excellent dispersion of the two powders, as well as breakdown of agglomerates. The inhomogeneous AAT20 was made by slightly increasing the powder-to-binder loading ratio, decreasing the amount of extra dispersant added, and reducing the milling time to a single step of six hours. This procedure resulted in poor mixing of powders and a severely agglomerated green tape. These agglomerates were soft, and had a wide range of sizes (occasionally as large as a few mm; such very large agglomerates were avoided in the stamping operation). When sintered, such a tape produced a fine-grained matrix of fairly well dispersed

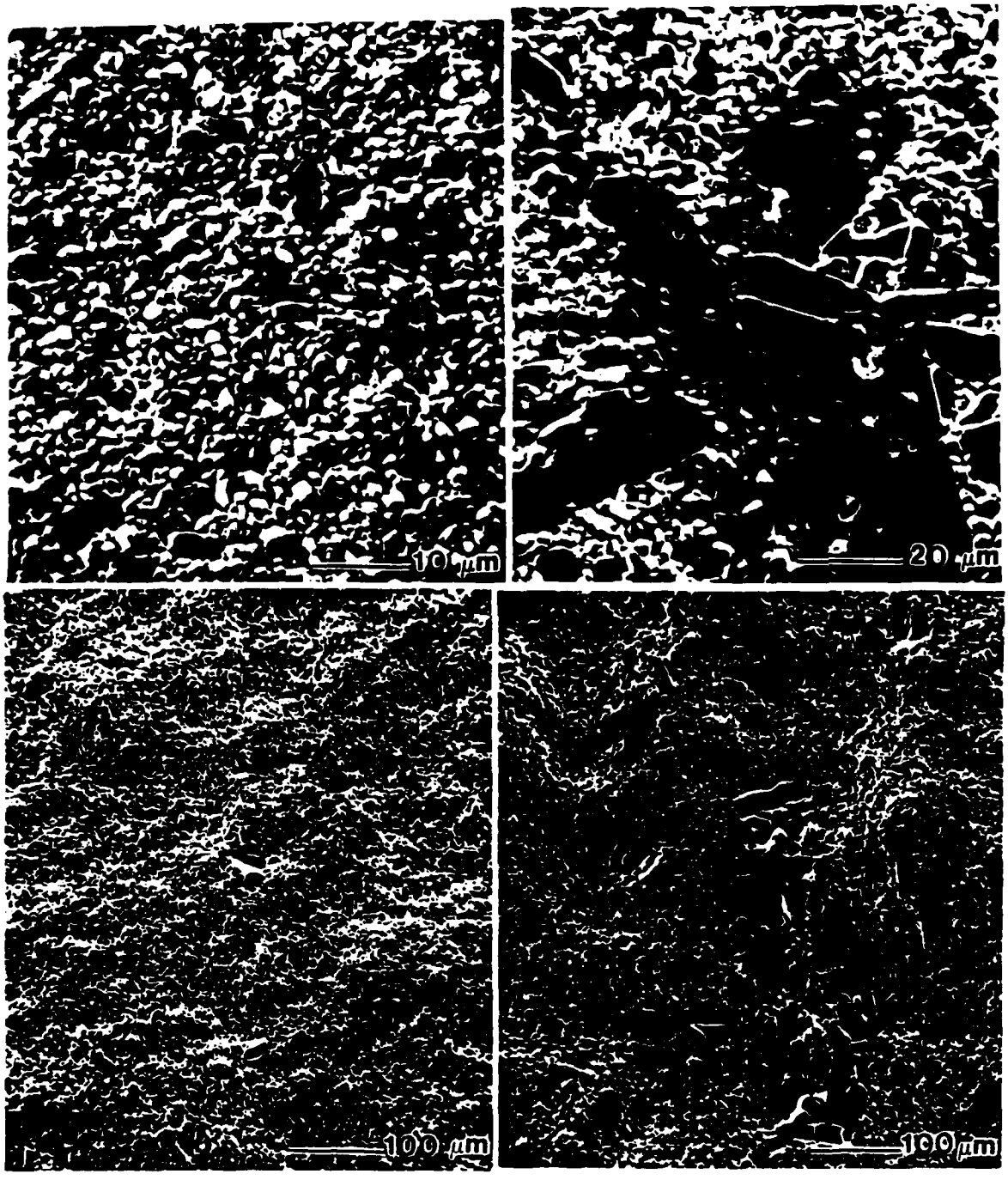

Figure III.1. Sintered microstructures of the two kinds of AAT20: (a) Homogeneous, as-fired surface; (b) Inhomogeneous, as-fired surface; (c) Homogeneous, fracture surface; (d) Inhomogeneous, fracture surface. All samples sintered 1600°C for 20 min.

alumina + aluminum titanate, which contained coarse, polycrystalline islands of both alumina and aluminum titanate. Figure III.1 shows the microstructure of both types of AAT20.

The actual slurry recipes were as follows:

a.) Homogeneous AAT20.

50 wt% binder solution

50 wt% powders

Then, based on total combined weight of those, add

1.7 wt% additional surfactant

~5.0 wt% methylene chloride

So, the standard size batch used the following recipe -

500ml bottle, with 55 milling rods

197.4 g B73181 binder solution + 6.7 g M1114 surfactant + 37.4 g Al_2TiO_5

ball mill one day, then add 160.0 g Al_2O_3 powder + ~20.0 g methylene chloride;

ball mill 48 hours, transfer to a 250 ml bottle, and slow roll for at least 16 hours.

b.) Inhomogeneous AAT20.

47.5 wt% binder solution

52.5 wt% powders

Then, based on total combined weight of those,

0.4 wt% additional surfactant

So, the standard size batch used the following recipe:

178.6 g binder solution + 1.5 g surfactant + 37.4 g Al_2TiO_5 + 160.0 g Al_2O_3

[*note - no extra methylene chloride was added]

This slurry was considerably more viscous than the homogeneous one. In fact, it would not mill properly in the usual manner of lying the bottle on its side. These slurries were

milled by *tumbling end-over-end*, at slightly lower speed than used for the homogeneous material.

It is interesting to note the reproducibility of these slurries. They were very consistently reproducible. For this research, *hundreds* of samples were made from at least eight homogeneous tapes and at least 14 inhomogeneous tapes, using three different batches of binder solution, and two different batches of surfactant, over a period of 2 - 3 years. Green tape and slurry appearances were very consistent, as were sintered microstructures and measured strengths.

2. Zirconia Materials:

The zirconia materials were made using the same binder solution and dispersant as the AAT20. The relative amounts of powder, binder solution, and dispersant had to be altered, however. The first slurries were made using the exact same recipe as for the homogeneous AAT20. There was a considerable amount of damage evident in these samples after firing. The damage was in the form of cracking and chipping: severe delaminations (occasionally running completely across the sample), radial cracks originating at the edges, and randomly distributed, finer - scale surface cracking. Varying the binder burnout and the sintering schedules, especially heating and cooling rates, established that these cracking problems were probably *not* caused by the firing cycle. Furthermore, observation of the samples after binder burnout, before sintering, confirmed that all forms of cracking were present, regardless of heating schedules. Thus, it appeared that these problems were a result of defective green microstructures.

Because both the 3Y20A and 12Ce zirconias have higher density than AAT20, using the AAT20 recipe resulted in tapes with relatively lower powder loadings. Equal powder masses of 3Y20A and AAT20 occupy different volumes; the higher density powders (the zirconias) occupy less volume and therefore their green tapes had relatively more binder than the AAT20 tapes did. This excess binder burned out to leave excess void space in the green body, resulting in lower green density. Using alumina as a reference standard, the 3Y20A occupies 27.5% less volume,

and the 12Ce occupies 35.7% less volume. New slurry recipes were developed, with powder loading ratios adjusted to reflect these volume differences. Thus, the new 3Y20A slurry used 27.5% less binder solution than the original recipe; and the 12Ce used 35.7% less. These changes were intended to return the green density of tapes back to the level of the successful AAT20 tapes.

The amount of surfactant was also changed. These powders were not only denser than alumina, but they also had much higher specific surface areas (SSA). Dispersion is determined by surface properties, so it seemed reasonable to increase the surfactant by an amount based on the difference in SSA between alumina and these powders. The alumina had SSA = 5.7 m^2/g; the 3Y20A, 17.2 m^2/g; and the 12Ce, 12.3 m^2/g (numbers supplied by the manufacturers). Thus, surfactant was increased by a factor of 3 for the 3Y20A, and by 60% for the 12Ce. These changes greatly improved the 12Ce material, almost completely eliminating instances of delamination. The trilayers were also much improved, but still contained occasional radial cracks, and some delaminations between surface and bulk material. The 3Y20A material remained in bad condition, however, with delaminations, radial cracks, and random surface cracking.

Examination of green tape, calcined, and sintered body microstructures in the SEM revealed that the slurry processing was apparently not breaking down the spray dried agglomerate structures in the 3Y20A. Microstructures at all three stages of processing contained roundish agglomerates of about 10 - 20 μm in diameter, separated by regions of binder (green tapes), or void space (calcined and sintered bodies), as shown in Figures III.2 - 4.

In order to produce good 3Y20A materials, without further refinements to the slurry processing, all subsequent samples were isopressed at 57 ksi (393 MPa), for 1 minute, following binder burnout. This isopressing step resulted in tremendous improvement in the sintered bodies. As a general rule, the calcined bodies contained some damage - delaminations, radial cracking, etc. After isopressing, all such damage was eliminated. To illustrate how effective the isopressing

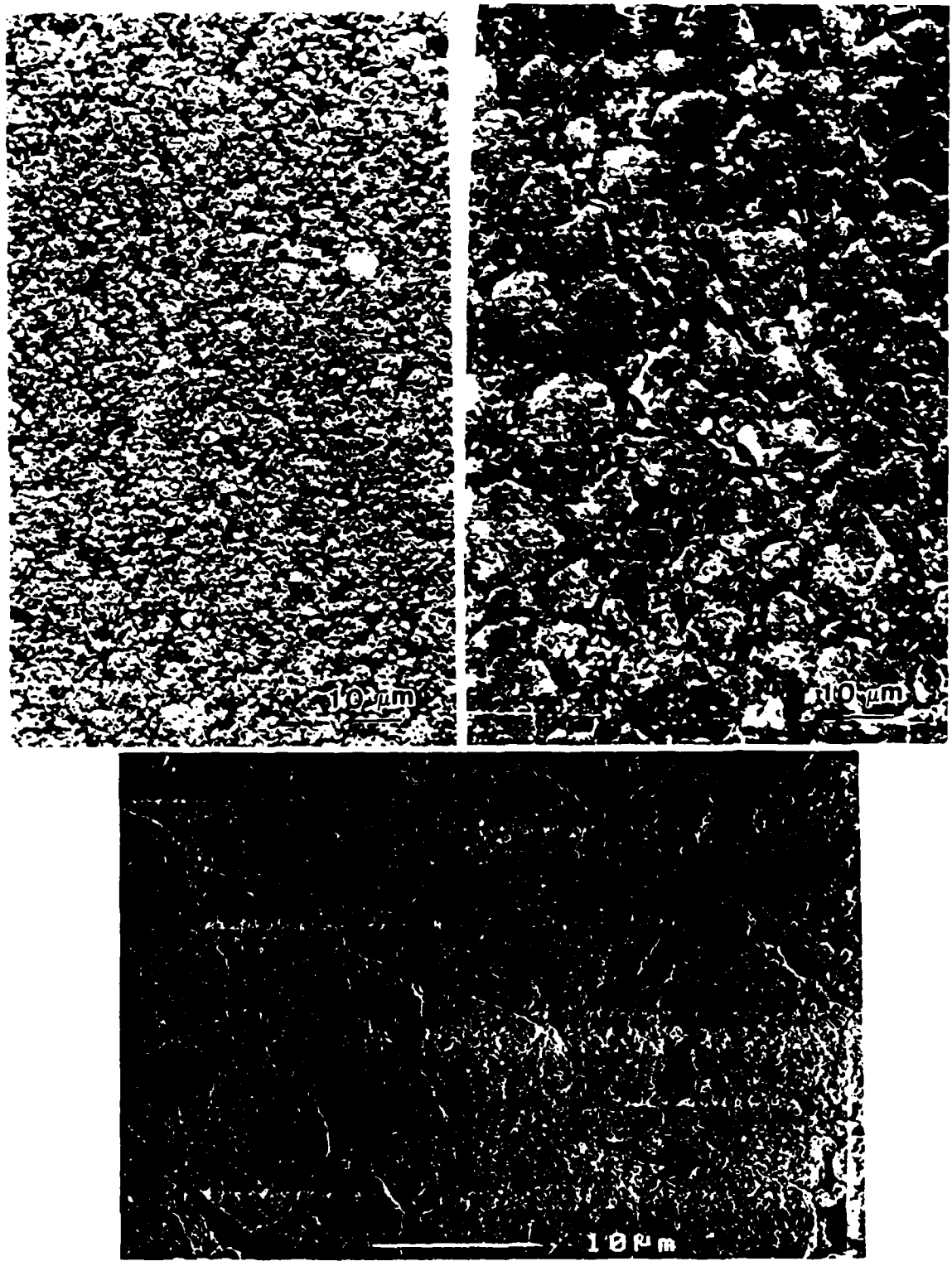

Figure III.2. (top left) 12Ce green tape microstructure, with well-dispersed particles; (top right) 8Y20A green tape microstructure, showing agglomerates separated by binder; (bottom) calcined 8Y20A showing voids from binder burnout.

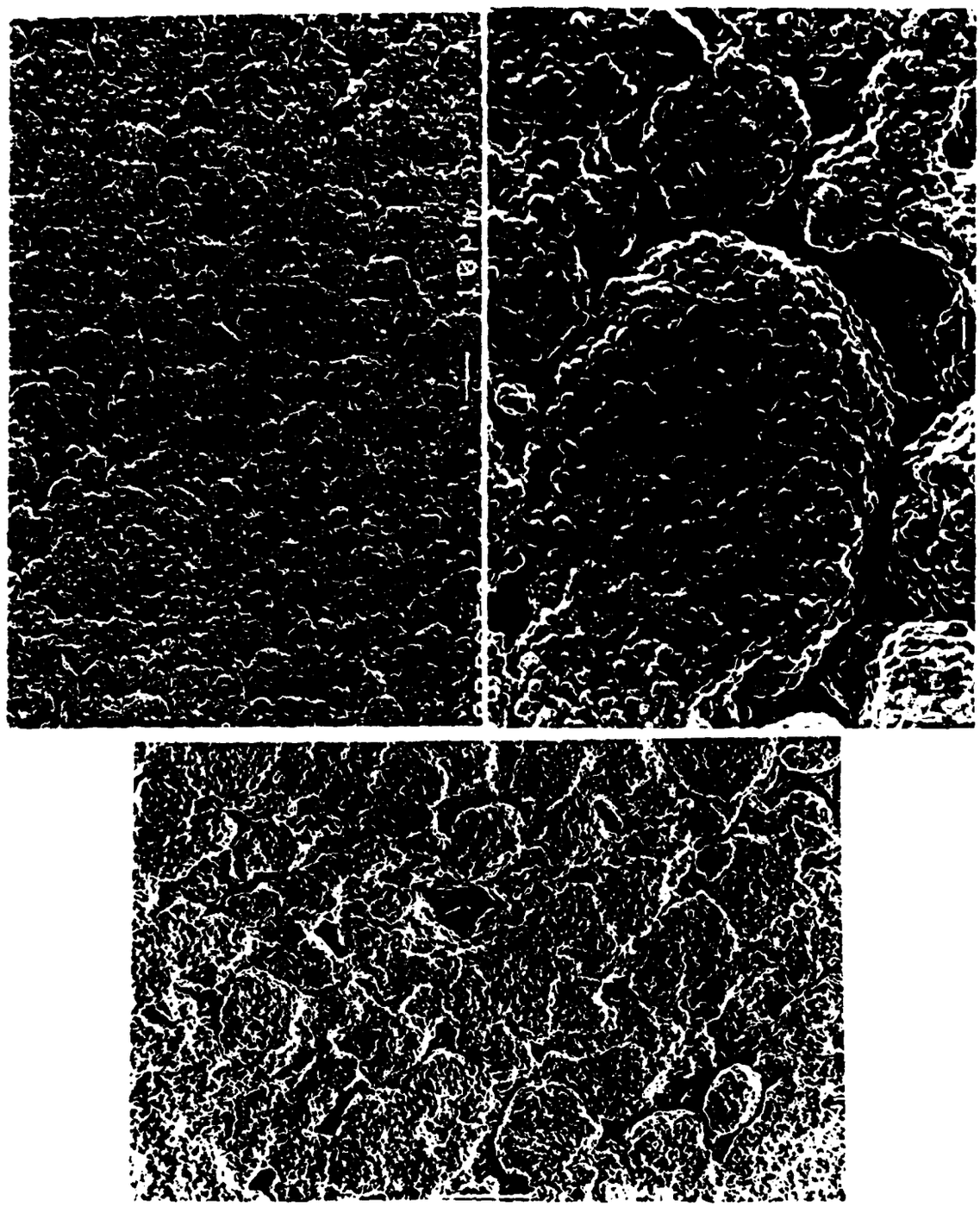

Figure III.3. As fired surfaces showing sintered microstructure of 3Y20A. (top) sintered at 1500 C for 2 hrs; (bottom) sintered at 1500 C for 3 hrs.

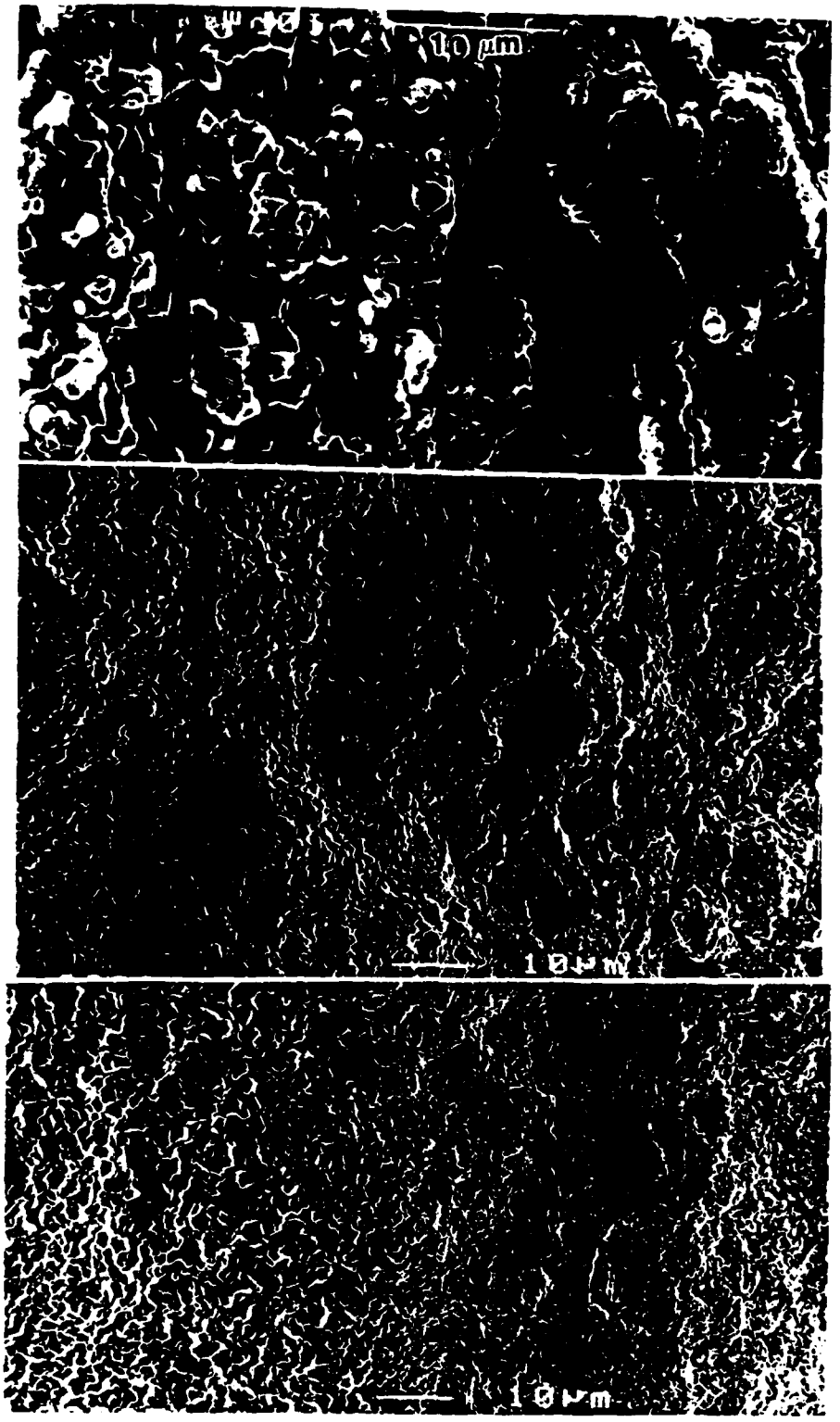

Figure III.4. Fracture surface view of the interface in zirconia trilayers. (top) first batch, before altering slurry recipe, sintered 1500 C for 2 hrs; (center) using modified slurry recipe, 1500 C for 2 hrs; (bottom) sintered 1500 C for 3 hrs. Density improved with each new treatment.

step was in removing crack damage, consider the following example. Occasionally, a calcined sample would contain a complete delamination, which separated the sample into two halves. One of these samples was pieced back together in such a way that the two halves were slightly displaced from each other, and isopressed. After isopressing, all evidence of the delamination was gone, except for the two halves still being displaced from each other (by about 1mm). This sample was subsequently fired, and it exhibited the same strength level as the other undamaged samples.

C. Green Tape Processing.

After allowing the tape to dry, usually for at least one day, the tape was transferred to the clean room for stamping of disks. Disks (1.25 in. diameter) were stamped from the tape inside a laminar flow hood, to minimize airborne contamination. Samples consisted of between nine and twenty individual disk layers (typically ten). Handling of the dried tapes usually introduced significant static charge, which could be quite bothersome, especially for the thinnest tapes. In order to eliminate this static charge, an electronic static charge removal device ('X-Static') was used during stamping and stacking of disk layers. Tapes having thickness greater than about 70 μm were easily stripped from the Mylar film; but below this thickness, a special technique was required. A U-shaped Mylar stripping tool was made, rounded on one end and ground thinner at the leading edge (using a coarse diamond grinding wheel). This tool was carefully inserted between the stamped disk and the Mylar casting film, and slowly pushed underneath the disk. Normally this would cause the stamped disk to adhere strongly to the Mylar tool by static charge. So, the stamped disk was then passed in front of the X-Static device to eliminate the static charge.

Green samples were produced by stacking layers in a stainless steel die, with one mylar disk on top and bottom (to prevent sticking), silicone side facing the tapes, and warm pressing at 10 ksi (69 MPa) and 75° C for 15 minutes. Warm pressed samples were arranged in 99.8%

alumina dishes with lids, surrounded on top and bottom with sacrificial powder (alumina for the AAT20s, 3Y20A for the zirconia trilayers and 3Y20A monoliths, 12Ce for the 12Ce monoliths). These were calcined in an L&L furnace (Appendix III), using the following heating schedules:

1. AAT20s: 12 hours from room temp up to 550° C, dwell for 5 hours (binder burnout)

2.5 hours from 550 to 700° C, dwell for 8 hours (calcine residual carbon)

5 hours down to room temperature

2. Zirconias: 12 hours from room up to 550° C, dwell for 5.5 hours

4 hrs, 16 min from 550 to 800° C, dwell for 16 hours

12 hours down to room temperature

D. Sintering Schedules.

Sintering was performed in air, using a CM Rapid Temp furnace, as follows:

1. AAT20s: 9° C/min to 750°C, dwell for 5 minutes

18° C/min to 1300°C, dwell for 1 minute

9° C/min to 1600°C, dwell for 20 minutes

33° C/min down

The high heating rates between 750° and 1300° C were designed to avoid decomposition of the aluminum titanate into alumina and titania (Kato, et. al., 1980; Thomas & Stevens, 1989). Also, the very high cooling rate was used in order to maximize the localized residual thermal expansion mismatch stresses (Blendell & Coble, 1982).

2. Zirconias: 5°/min to 800°C, dwell for 30 minutes

5°/min to 1500°C, dwell for 2, or 3 hours

3°/min to 850°C, 5°/min down to room temperature

E. Thickness Control.

The final fired thickness of the surface layer was determined by three primary factors:

the original thickness of the dried, green tape, the warm pressing step, and the sintering shrinkage. The second two were eventually maintained as invariant processing steps, having known and reproducible amounts of shrinkage associated with them. Hence, the most important variable affecting the final layer thickness was the thickness of the green tape. This was roughly controlled by the doctor blade opening, using an experience-based correlation between the micrometer setting and the dried thickness. Tape thicknesses ranged from about 35 μm to 400 μm. Warm pressing resulted in about 11% shrinkage in thickness; and sintering resulted in an additional 20% shrinkage in thickness. Thus, the final fired thickness was approximately 31% less than the original green tape thickness.

F. Strength Testing.

Unpolished disk-shaped samples were indented on one surface with a Vickers diamond indenter, and the indentation sites were immediately covered with a drop of silicone oil (Dow-Corning 704 diffusion pump oil) to prevent moisture attack. Samples were tested in biaxial flexure within 2 hours of indenting. Testing in biaxial flexure provided two benefits. First, this geometry was able to accommodate the slight warpage of the samples which often arose during handling of the warm-pressed disks. Second, biaxial flexure testing prevented fractures from spurious edge flaws. When testing could not be performed within 2 hours, samples were stored in a vacuum dessicator. Specimens were tested in stroke control, using a cross-head speed of about 200 mm/s. All fractures occurred in 20 ms or less, and load-time traces were recorded on a digital storage oscilloscope. It should be noted that for the AAT20 materials, the surface and bulk materials had the same composition, so the elastic moduli were assumed to be equal. Thus, the strengths were determined from the maximum bending stress, at the tensile surface. (For the zirconia trilayers, this assumption was not valid. Nevertheless, the modulus difference between surface and bulk in those materials was *not* accounted for.) The stress equation used was given

by Roark (1954), with a modification by Westergaard (see Roark, 1954; deWith and Wagemans, 1989):

$$\sigma = -\{3P/(4\pi t^2)\}(X-Y)$$

where $X = (1+\nu)\ln(R_L/R)^2 + \{(1-\nu)/2\}(R_L/R)^2$;

$Y = (1+\nu)\{1+\ln(R_S/R)^2\} + (1-\nu)(R_S/R)^2$;

R_L = Radius of the region of uniform Loading = $(1.6z^2+t^2)^{1/2}-0.675t$ [z=contact radius of the loading flat]

R_S ; R = Radius of Support circle: and specimen, respectively;

P = load at failure; ν = Poisson's ratio; and t = specimen thickness.

For AAT20 materials, the value used for Poissons ratio was 0.233 (i.e., the value for pure alumina); and for zirconias, 0.3. Reported strengths represent the average value from at least (and typically more than) four samples. All broken samples were examined with an optical microscope to determine whether fracture proceeded from the indent. If not, the samples were included in the unindented group.

G. Indentation Measurements.

Indentation impression diagonals, radial crack lengths, and lateral crack development were measured for the AAT20 materials, using an optical microscope with digital image analysis pad (MicroPlan II, DonSanto Corp.). At least four indents were measured for each reported indent load, and all measurements were made within 3 hours of indenting (except for the lateral cracks). All measurements were conducted on broken fragments left over from strength testing, on the surfaces which had been in tension, but far away from the area of maximum stress, and far away from any other indent (i.e. several mm). The measuring procedures follow.

1. Impression diagonals, and radial crack length. Using the digitizing pad, the distance between any two points in the field of view was easily measured. For a given magnification, a scaling factor was entered into the computer. Then, the starting and ending points of the crack or impression diagonal were marked with the cursor, and the computer calculated the distance

between them. Best results were obtained under the following conditions, using a Nikon optical microscope:

a. Dark-field imaging - i.e., the field limiting aperture closed most of the way;

b. Light intensity turned up all the way;

c. Light limiting aperture opened all the way;

d. Polarizer out;

e. Magnification as high as possible, with a field of view that includes the entire feature of interest. This feature was kept as close as possible to the boundary between the bright and dark fields. It was sometimes helpful to be able to move the (bright) field of view, without moving the sample. This was done by pushing or pulling the rod which selects true dark field imaging or bright field imaging. All reported crack lengths were measured from the center of the indent to the tip of the radial crack. No estimate of experimental measuring error was made, other than the following qualitative observations. As indent load decreased, it became more difficult to see the cracks at all, and especially the crack tips. This is primarily because the decrease in crack length required higher magnification to view the cracks, and as the magnification was increased, it became more difficult to differentiate between cracks and the grain boundaries (all measurements were conducted on as-fired surfaces; polishing might have improved crack visibility). Thus, the values reported for the lower indent loads (esp. $\leq$ 10N) are considered less reliable than the values for the higher indent loads.

2. Lateral crack development. Lateral cracking was *evaluated*, not really measured. The number of indent quadrants containing a lateral crack, and the number of lateral crack chips were recorded. Once again, dark field imaging was much better for viewing lateral cracks, however true dark field imaging was used here, together with the following conditions:

a. Adjustable polarizer in

b. Analyzer in

c. Field aperture open all the way

d. Light limiting aperture ~3/4 closed

e. Focus just below surface, i.e. focus down into impression

IV. EXPERIMENTAL RESULTS

There have been numerous studies conducted on layered microstructures (Mistler, Kirchner, Green, Virkar, etc.), but the 'Gutshall-Gross' mechanism discussed in section I-E has never been successfully exploited. The original goal of this project was to produce simple fine-grain/coarse-grain layered microstructures out of essentially pure alumina materials, in order to determine the effect of a toughness difference between the surface and interior materials, on the strength and flaw tolerance behavior of the composite. Several different processing strategies were pursued in this effort to produce the neccessary grain size difference between surface and bulk. These initial, unsuccessful attempts are discussed in Appendix I. It should be observed that the processing of such a composite is rather difficult.

The many problems encountered in producing the initial composites were largely responsible for the change in focus toward a fully AAT20 system. This section describes the main results from the indentation characterizations and strength testing of the AAT20 materials. In addition, the strength results from a zirconia-based, trilayer demonstration system are presented, although this system has not been fully characterized.

A. AAT20 Materials.

1. Indentation Measurements

Several parameters characterizing the indentations were measured in the AAT20 materials: impression diagonals, surface traces of radial cracks, and lateral crack development. Figure IV.1 illustrates the Vickers indent system, and shows how the impression dimension and crack lengths were measured. A hardness value was calculated based on the impression diagonals. The radial crack length dependence upon indentation load was evaluated. These crack lengths were used in conjunction with the lateral crack observations, to modify the χ term in the residual stress intensity field of the indentation (as discussed in section I-D).

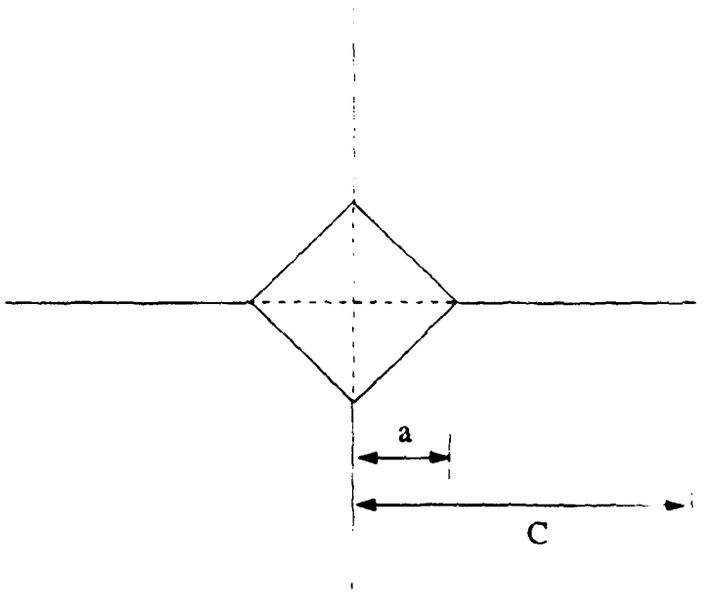

Figure IV.1. Top view of Vickers indentation, showing the parameters which were measured in Figures IV.2 and IV.3 below.

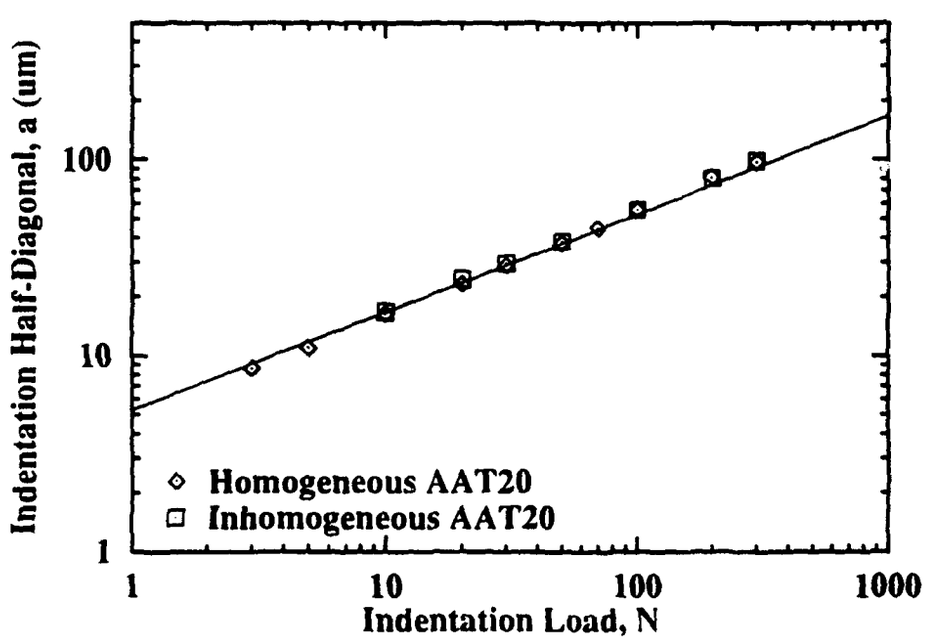

Figure IV.2. Indentation impression half-diagonals. Line shows response for constant hardness of 18 GPa (best fit to Eq. 24 for homogeneous AAT20). Error bars same size as symbols.

Figure IV.2 shows the impression half-diagonal, a, as a function of indent load. For a material with constant hardness, the general relation between P and a is given by

$$a = (P/2H)^{1/2} \tag{24}$$

As seen in Fig. IV.2, both the homogeneous and inhomogeneous AAT20 materials obey this $P^{1/2}$ dependence (empirical power law fits through the data yielded slopes of 0.53 and 0.52, respectively), and it is therefore concluded that they possess constant hardness. Hardness values for each material were obtained from a best fit of the experimental data to the above equation. (The FORTRAN code used in fitting the data is presented in Appendix II.) The hardness of the homogeneous and inhomogeneous materials was 18.0 ± 0.7 GPa, and 15.8 ± 0.6 GPa, respectively. The two materials may seem to have significantly different hardness; however, Fig IV.2 shows that the best fit to Eq. 24 for the homogeneous data (constant hardness of 18.0 GPa) also gives an excellent fit to the inhomogeneous data, even if it was not the *best* fit. Thus, for the purposes of this research, the two materials are considered to have the same hardness.

Figure IV.3 shows the measured surface traces of radial cracks as a function of indent load. All values represent the length from the tip of the crack to the center of the indentation. Since a half-penny flaw shape was assumed, these surface traces were taken to be equivalent in length to the crack depth. Empirical power law fits to these crack length data yielded slopes of 0.656 and 0.589 for the homogeneous and inhomogeneous AAT20, respectively. Both slopes are less than the theoretical 0.667 slope for half-penny indent flaws in a material of constant toughness, which may be taken as an indication that both materials exhibit some T-curve behavior (if it is still assumed that the crack is of half-penny shape). However, it should also be noted that a line of 2/3 slope can be forced through the error bars of the crack length data for both materials.

Lateral crack development was evaluated, and the results are presented in Fig. IV.4. It may be seen that the lateral cracking behavior was similar for the two base materials. A value

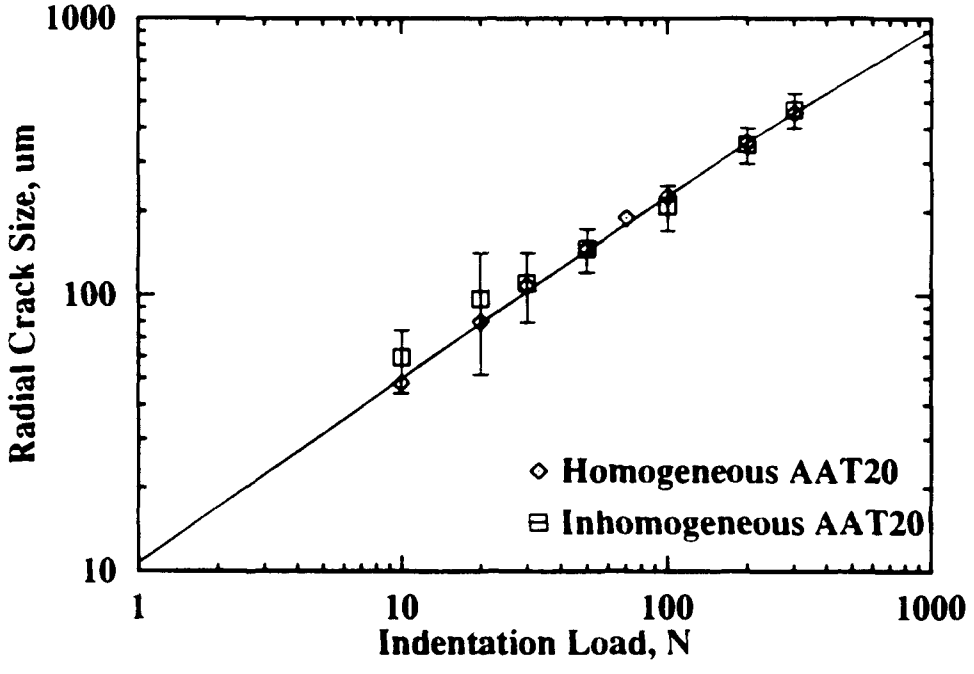

Figure IV.3. Radial crack lengths. Line shows best fit to Eq. 20 for the homogeneous material (giving a P_L=2445N). This line passes through error bars for the inhomogeneous AAT20.

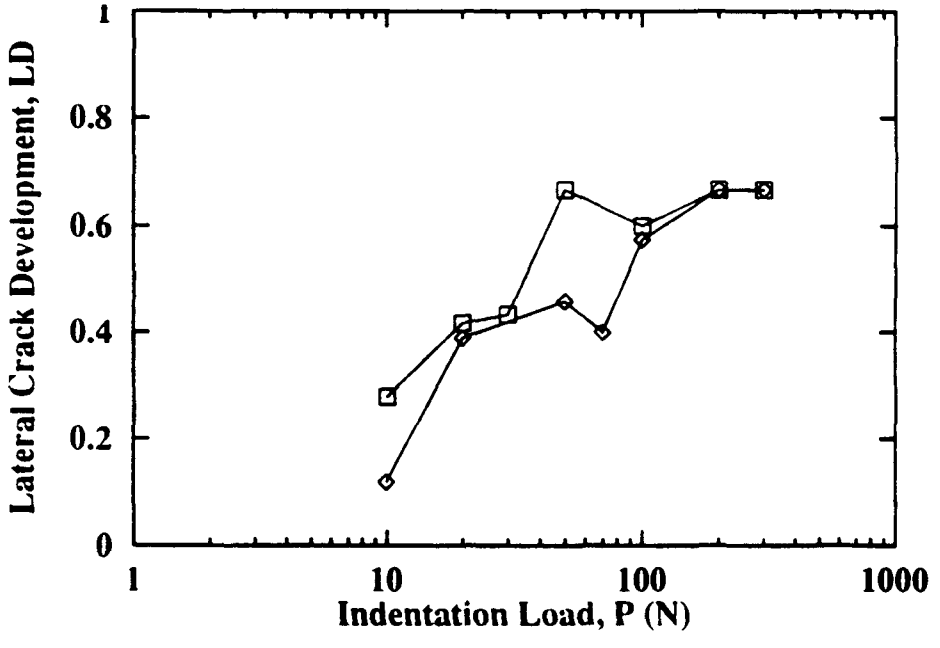

Figure IV.4. Lateral crack development in the two base AAT20 materials. Again, note the similarity in lateral cracking behavior.

for P_L, the indent load at which lateral crack influence becomes significant, was determined by fitting the radial crack length data to Eq.s 20 and 21, from Section I-D. (The FORTRAN program used in fitting the crack length data is given in Appendix II.) The value thus determined was 2445 N, for the homogeneous AAT20. Note that this P_L is about 20 times the indent load at which the lateral crack development factor (L_D) reaches the 67% level (this is of similar order of magnitude as the approximate correlation between L_D and P_L suggested by Cook, *et. al.* (1990), i.e. $P_L = 100 \times P_{(L_D = 67\%)}$). Finally, since the inhomogeneous AAT20 exhibited very similar hardness, radial cracking, and lateral crack development behavior, the same 2445 N value for P_L was assumed for this material, and also for the trilayer composites (for use in subsequent T-curve modeling).

2. Strength Results

The main experimental strength results are presented in Figures IV.5-7. The indentation strength response of the two base materials, tested in bulk form, is shown in Fig. IV.5. The inhomogeneous AAT20 displays extensive flaw tolerance, having a nearly invariant strength level throughout the entire range of indent loads tested. As discussed in section I, this flaw tolerance is indicative of T-curve behavior. The homogeneous AAT20 exhibits a steady decrease in strength with increasing indentation load (Fig. IV.5), although this is not quite the 'ideal' $P^{-1/3}$ relation described earlier (an empirical power law fit yields a slope of -0.21, including only the data between 3 N and 100 N). This material is therefore described, qualitatively, as exhibiting limited T-curve behavior, and this will have significant consequences for the T-curve modeling of the trilayer composites (to be discussed in Section V).

The indentation strength response of AAT20 trilayers was evaluated for surface layer thicknesses of 33, 53, 66, 104, 142, 169, and 188 μm. As a general rule, the strength was measured at one low indent load (3 N), and at one high indent load (100 N), in order to determine

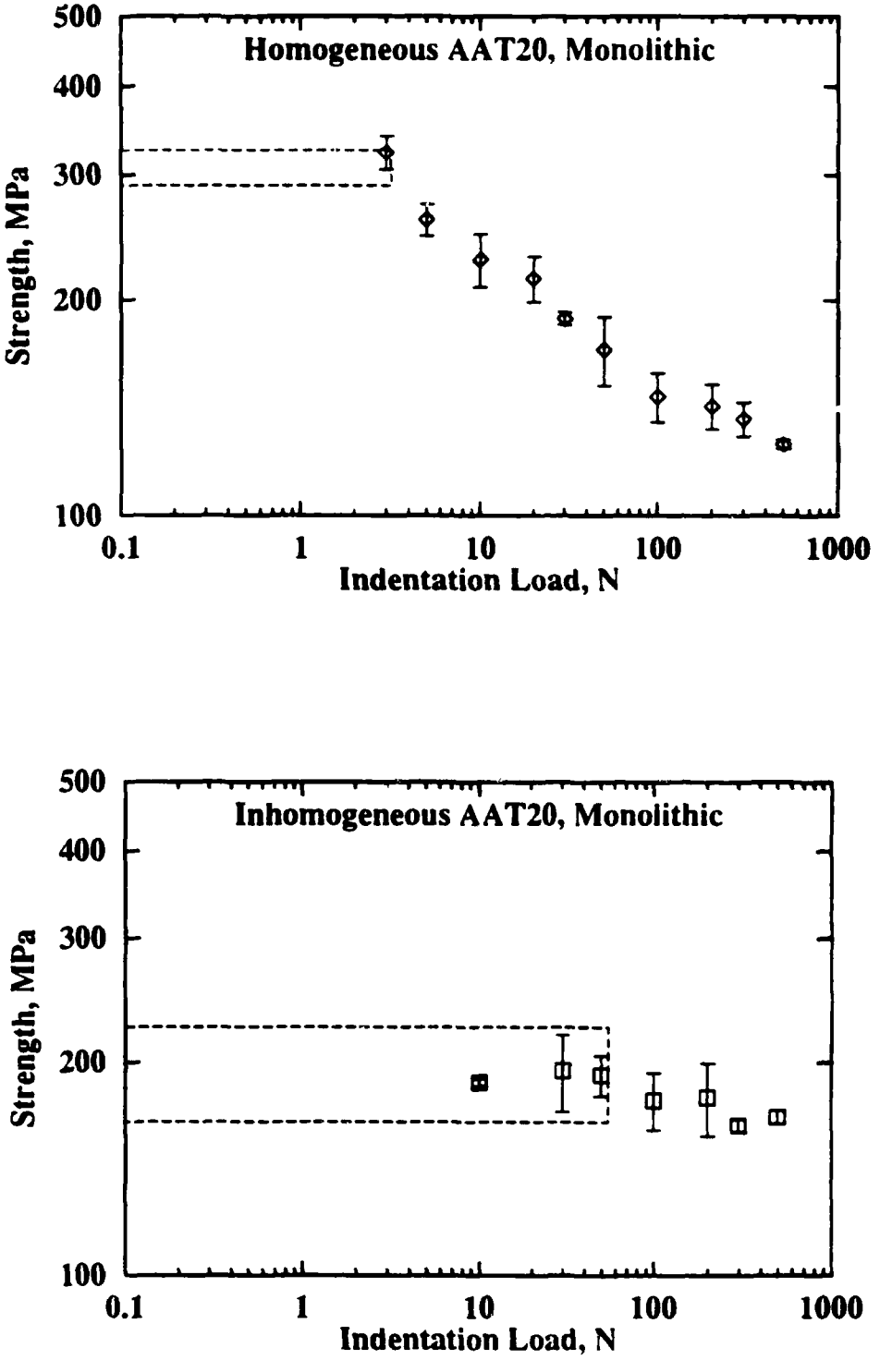

Figure IV.5. Indentation strength response of the two AAT20 base materials, sintered at 1600°C for 20 min. Dashed bands represent strength levels for natural flaws (i.e., unindented), and indicate the P limit, above which all indentations (for given P) produced fracture.

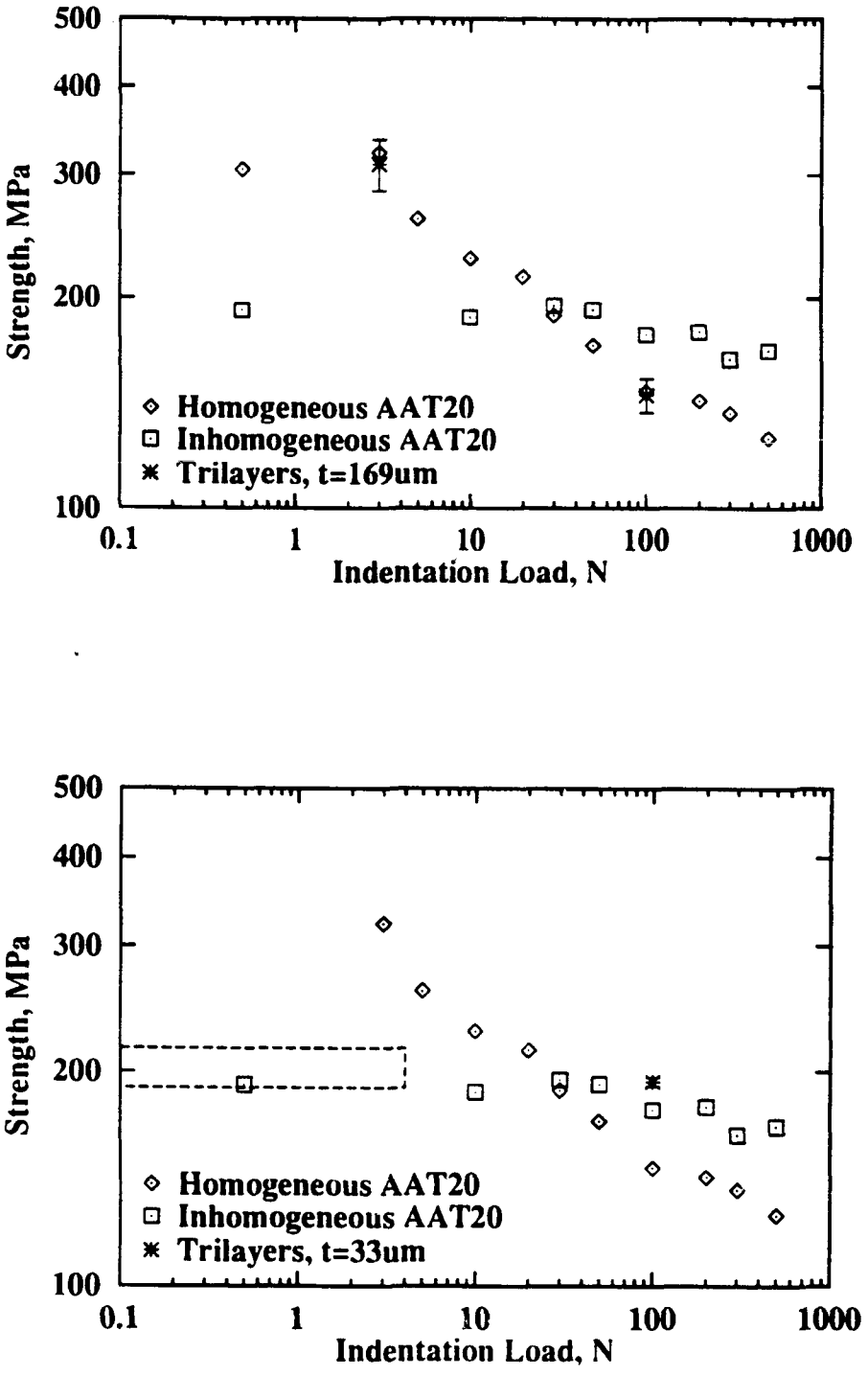

Figure IV.6. Typical indentation strength behavior of AAT20 trilayer composites of various thicknesses. Top graph shows response when surface layer is too thick; bottom graph, too thin. The points at extreme left (0.5N) represent *unindented* strengths, for monoliths; hatched band shows unindented strength for the 33μm trilayers.

whether composite strength behavior was produced for a given surface layer thickness. Some typical strength responses are shown in figure IV.6. It may be seen that when the surface layer was too thick, the composite behaved in the same manner as the surface material alone. On the other hand, when the surface layer was too thin, the composite essentially ignored the surface material and displayed the monolithic body material response. There was an optimum thickness - 104 μm - for which the composite displayed the high strength of the surface material for small flaws, as well as the high strength of the body material for larger flaws (Fig. IV.7). For clarity, these strength data were not plotted with error bars; however, the actual strength values are given in Table I, together with an estimate of the experimental scatter.

It is interesting to note that the optimum thickness (104 μm) corresponded almost exactly to the crack length produced by a 30 N indentation in the homogeneous AAT20 (108μm). This was in fact the load at which the base material strength curves intersected, as shown in Fig. IV.5. Thus, it appears that the simple approach for estimating the optimum surface layer thickness (section II) was fairly accurate for this material system.

The strength trends may be partially explained in terms of the nature of the material sampled by a crack (Figure IV.8). When a growing crack experiences only surface layer material throughout its entire evolution (prior to catastrophic, fast fracture), the strength (and toughness) will be determined solely by surface material properties. Thus, for trilayers having the optimum layer thickness or greater, the strengths for small indent loads (≤30 N) were the same as the corresponding strengths of the monolithic surface material. Furthermore, trilayers with the largest layer thickness displayed surface material strength even for higher indent loads (100N). For trilayers having a layer thickness less than the optimal value, this same argument should have held true for the smallest indent loads (⟨10 N); the crack lengths produced by these indents should generally have been contained within the surface layer (see crack lengths, in Fig. IV3). However,

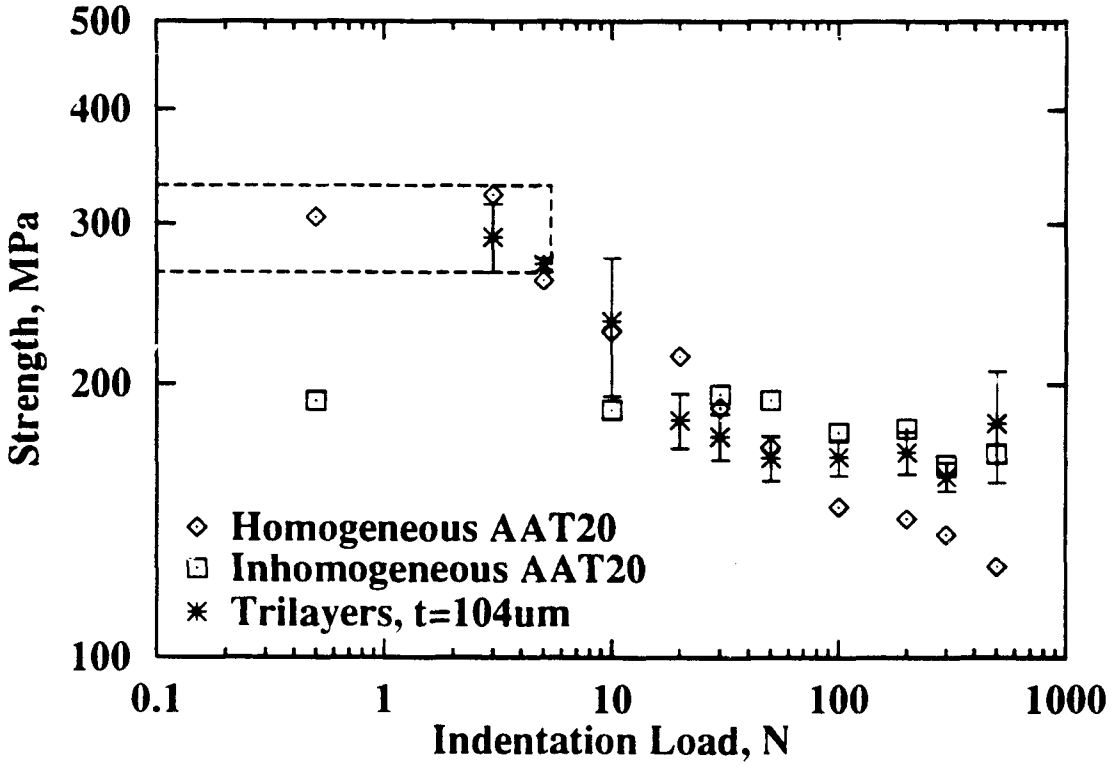

Figure IV.7. Indentation strength response of trilayer composites having the optimum surface layer thickness, 104μm. The hatched band represents unindented strengths for the trilayers; while the points at 0.5N represent unindented strengths for the base materials. Note the similarity between this behavior and Figure II.1.

Table I. Strengths of the AAT20 Materials

	Homogeneous	Inhomogeneous	104 μm Trilayers
P	σ ± (std. dev.)	σ ± (std. dev.)	σ ± (std. dev.)
0 N	304.8 (17.0) MPa	191.7 (14.5) MPa	298.0 (33.7) MPa
3	322.7 (17.4)	-------	289.7 (25.2)
5	259.5 (13.3)	------	270.6 (4.2)
10	228.1 (19.7)	187.3 (2.2)	234.3 (40.4)
20	214.6 (15.8)	-------	182.6 (12.7)
30	188.5 (3.8)	194.9 24.3)	175.2 (10.2)
50	170.6 (18.8)	192.05 (12.7)	165.9 (9.4)
100	146.5 (11.6)	177.0 (16.3)	166.2 (7.6)
200	142.2 (10.1)	178.7 (20.9)	168.2 (9.0)
300	136.5 (7.4)	163.1 (3.1)	158.2 (5.7)
500	125.8 (1.9)	167.7 (3.6)	181.2 (25.5)

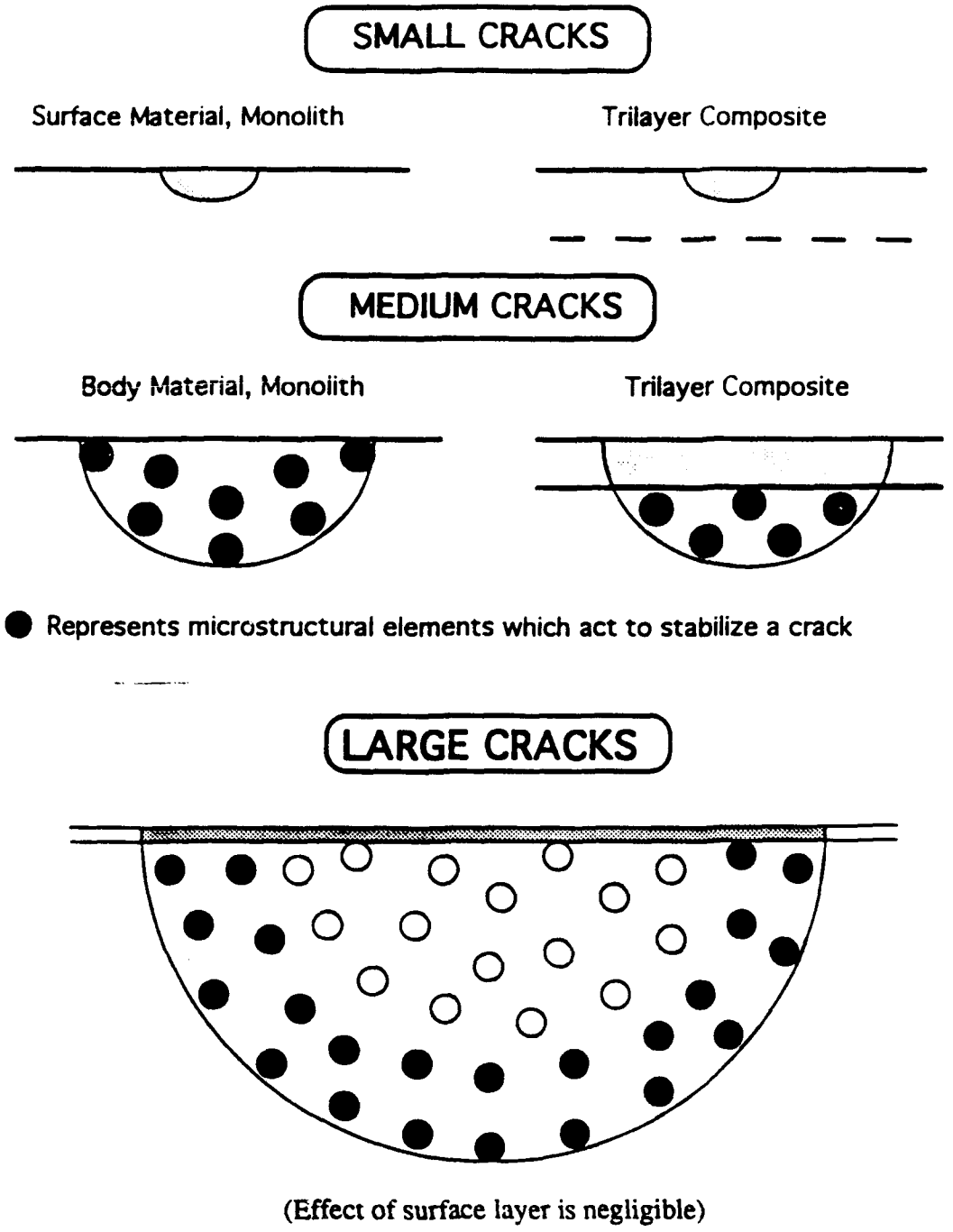

Figure IV.8. Interaction of cracks of various sizes with the microstructure in monolithic AAT20 and trilayer composites. The smallest cracks are fully contained within the surface material; intermediate sized cracks sample a significant portion of both surface layer and bulk materials; and the largest cracks are interacting almost exclusively with bulk material.

it was impossible to produce fractures from these small indent flaws, because the flaws in the underlying bulk material were dominant. Note, for example that the 33 μm trilayers did not produce any legitimate indentation-controlled fractures at small P. Indeed, it may be further noted in Figs. IV.5-7 that the inhomogeneous AAT20 monoliths produced no legitimate indent-controlled fractures at any loads below 10N, although many attempts were made at both 3N and 5N. Thus, the trilayers having the thinnest surface layers behaved as if that layer of surface material was not there, even though the cracks produced by the lowest indent loads were contained within the surface layer.

At the other extreme, for the largest flaw sizes (≥300N), the amount of crack surface area contained within the surface layer was reduced, and the surface material eventually exerted an insignificant influence over crack growth. For the largest flaws, therefore, the composites having $t \leq 104\mu m$ behaved just like monolithic body material.

For a certain intermediate range of indent loads, the crack should intersect a significant fraction of both surface and bulk material. It is the bulk material which contains microstructural elements (e.g., grain bridges) which act to stabilize a crack, by exerting closure stresses on the crack tip. The presence of the surface layer effectively removes those stabilizing elements from a certain area fraction of the crack wake. Over this intermediate range of flaw sizes, therefore, the composite might be expected to exhibit a strength and toughness somewhere between the values for the two base materials. Although this intermediate strength behavior was not observed in these AAT20 materials, it should be noted that the relatively small differences in strengths over this indent load range would make experimental detection of this effect very difficult. When experimental error is considered (Table I), the composite strengths are indistinguishable from the monolithic body strengths, for all indents greater than 30N.

B. Zirconia Materials.

In order to demonstrate the trilayer concept in a system of greater practical interest, a composite based upon zirconia materials was designed. For the surface material, a commercially available mixture of 3 mol% Y_2O_3-doped ZrO_2 with 20 wt% alumina as second phase particulate reinforcement was selected ('3Y20A'). The strength of this material has been reported (Lutz, et. al., 1991) among the highest known values for ceramics, (occasionally exceeding 2 GPa, under optimum processing conditions- i.e., HIP). The material selected for the bulk was a commercially available 12 mol% CeO_2-doped ZrO_2 ('Ce-ZrO_2'), which is a transformation toughening grade. This material has been reported to have some of the highest toughness values known for non-fibrous ceramics (as high as 17 $MPa*m^{1/2}$, see Tsukuma & Shimada, 1985; Swain & Rose, 1986). Trilayer composites based on this combination were fabricated using two different sintering schedules.

The first set of trilayers was produced with a surface layer thickness of about 140 μm, and was sintered for 2 hrs at 1500°C. The original intention was to test a small number of these composites to determine what processing problems might arise. If there were no major problems, then more samples were to be made with a pre-estimated optimum surface layer thickness, based on the intersection of the base material strength curves. This estimation depended on the assumptions made for the various material parameters (T_0, E/H, P_1), and ranged from about 30 to 50 μm - considerably lower than the 140 μm layer thickness of the first trial group. However, this first attempt seemed to produce optimal composite strength behavior. Figure IV.9 displays the indentation strength response of zirconia trilayers (surface thickness of 140 μm) and base materials, fired at 1500°C for 2 hrs. It may be seen that the composites exhibited the high strength of the surface material for unindented samples, and that the trilayer strength *exceeded* that of the bulk Ce-ZrO_2 for larger flaws.

While these trilayer strength results were encouraging, they brought attention to two problems. First of all, it became clear that the simple approach to estimating the optimal surface

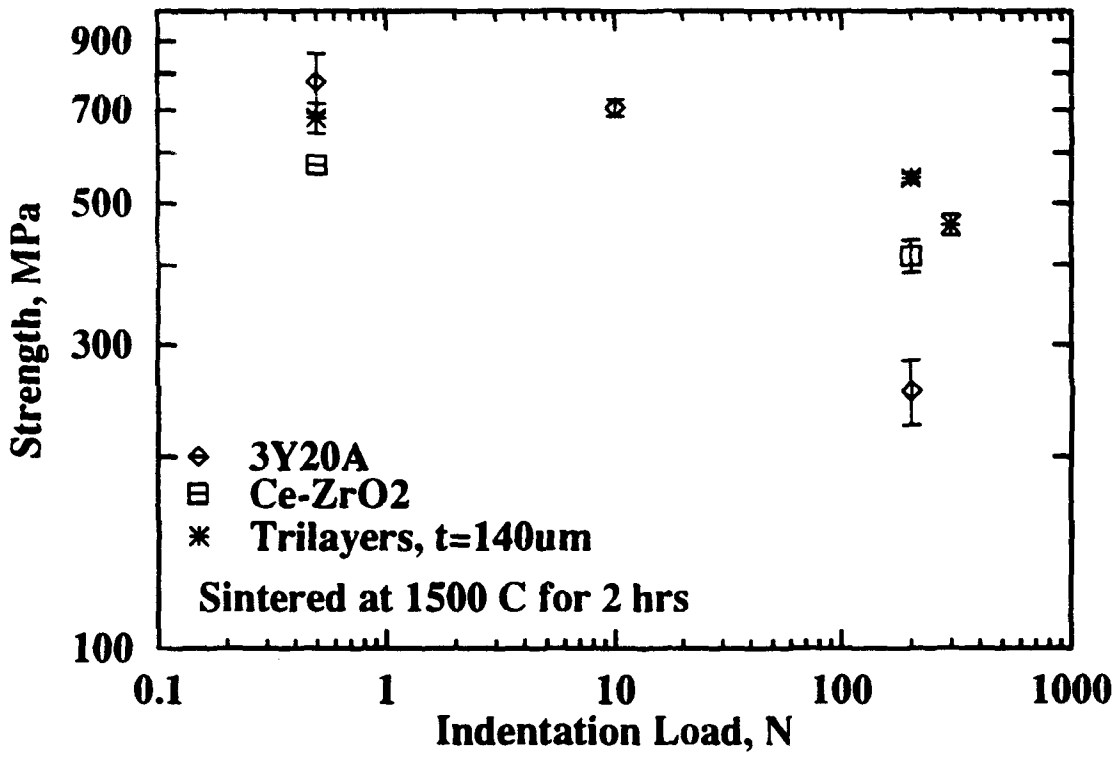

Figure IV.9. Indentation strength response in the zirconia trilayer system, sintered at 1500° C for 2 hrs. Trilayers seem to indicate composite strength behavior. Points at extreme left represent unindented samples.

layer thickness was inappropriate for these zirconia materials. Perhaps this was to be expected: there are significant differences between the two composite systems. In the AAT20 system, there were no thermal or elastic modulus differences between the surface and bulk. It was an ideally simple system. In the zirconia system, there are both elastic modulus differences, and differences in average thermal expansion coefficients. Elastic modulus differences alter the applied stress distribution. Thermal expansion mismatch (for this zirconia system) would result in residual compression in the surface layer. Both effects would be expected to influence any considerations of optimum surface layer thickness. In addition, the large differences between dopant levels and dopant species between the surface and bulk materials (3Y *vs.* 12Ce), and the presence of alumina in the surface layer, could well lead to differences in the intrinsic toughness (T_0, see Section I-C). Finally, the microstructure-associated toughening mechanism operating in zirconia (transformation toughening, with phase transformation occurring in a volume of material ahead of the crack tip) is different from the mechanism operating in AAT20 (grain bridging, with bridging ligaments distributed in the crack wake). Any one of these complicating factors could influence the magnitude of the optimum surface layer thickness.

The second issue raised by the initial zirconia strength results was that the surface material did not exhibit as high a strength level as was expected. Published strength values for this material, using the same firing schedule, indicated that 1300 MPa may have been possible (Lutz & Swain, 1991). A probable explanation for the difference was found upon examining the 3Y20A microstructure in the SEM. Considerable porosity remained after sintering. The shape and distribution of this porosity seemed to indicate that the spray-dried agglomerate structures, present in the original powder, were not being broken down during slurry preparation (Fig. III.2 - 4). This was confirmed by SEM observations of the green tapes and calcined disks. The spray dried agglomerates were separated by a significant amount of binder in the green tapes, which burned

off during firing to leave void space. It was believed that if the density could be increased, the strength of this 3Y20A material (and therefore, the trilayers) could be significantly improved.

With this in mind, a new set of zirconia materials was sintered for 3 hrs (one hour longer than before) at 1500°C. The strength of the 3Y20A was indeed increased, by about 150 MPa, and some individual samples exhibited strength in excess of 1 GPa. New trilayers were fabricated as well, using the same 140 μm layer thickness as before. The indentation strength response of these materials is shown in Figure IV.10. The 3Y20A material displayed improved strength for small flaws, while the strength level of the Ce-ZrO_2 bulk material remained at about the same level as before. It is clear that the trilayer composites did not benefit from the extra sintering time; rather, they displayed the same strength behavior as the monolithic bulk material. These trilayers had the same surface layer thickness as the earlier batch which displayed composite strength behavior. However, the microstructures were different. Not only did the 3Y20A material achieve increased density, as desired, but the Ce-ZrO_2 bulk material displayed a larger grain size (see Fig. III.4), which leads to a greater transformability (Becher & Swain, 1992). In highly transformable zirconia materials, such as MgO-PSZ and the Ce-ZrO_2 material considered here, transformation of the tetragonal grains begins at stresses well below the fracture stress (Swain, 1985; Marshall, 1986; Swain & Rose, 1986; Becher & Swain, 1992). It is possible, therefore, that the strength of the trilayers sintered for three hours became transformation-limited, and controlled by the bulk material, despite the higher strength of the surface layer.

It is clear that the strength behavior in the zirconia system is much more complicated than in the AAT20 system, and that the design of trilayer composites using zirconia materials becomes much more complicated as well. It seems possible, however, that if the green microstructure of the 3Y20A material could be improved further, such that the sintering time could be reduced back to the original 1500° C/ 2 hrs schedule, then the trilayer composites may display the desired

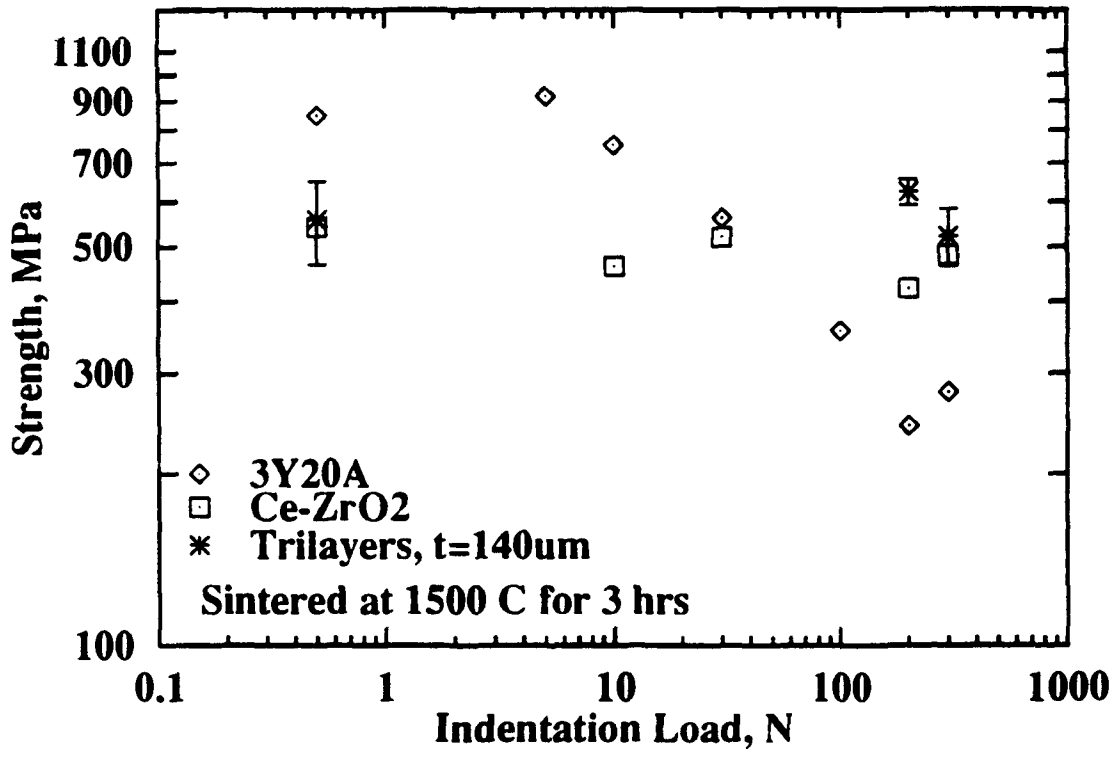

Figure IV.10. Indentation strength behavior for the zirconia trilayer composites, sintered for 3 hrs at 1500°C. Trilayers exhibit the strength of the bulk Ce-ZrO_2 material. Points at extreme left (0.5N) represent *unindented* strengths.

composite strength response. That original sintering schedule produced trilayers which seemed to show composite strength behavior. In any event, if optimum trilayer composites are to be produced in the zirconia system, further processing work is required.

There is an alternative explanation for the observed strength behavior of the zirconia trilayers. The samples fired for only two hours seemed to display composite strength response, but the strengths might alternatively be explained on the basis of elastic modulus enhancement. If the trilayers are considered as essentially a Ce-ZrO_2 body, the surface layer may be considered to effectively increase the modulus of the material, at the surface. This would have the effect of increasing the stress which the material could support, leading to improvement in the measured trilayer fracture strengths. It should be noted, however, that the same argument applied to the trilayers sintered for three hours, is incapable of accounting for the observed strengths. The three hour samples did not exhibit any increase in strength compared to the monolithic Ce-ZrO_2 material, even though the modulus difference was likely even greater, due to the increased density of the surface material. Thus, while the modulus argument should be retained as a possible explanation, and should be addressed in a more rigorous fashion in any future work on this system, it does not invalidate the earlier claim that the two-hour trilayers seemed to display composite strength behavior.

V. T-CURVE MODELING

In the previous section, some qualitative descriptions were offered in explanation for the trilayer composite indentation strength results. This section will present a more detailed, quantitative explanation for the observed strength behavior. First, the relation between toughness and strength behavior will be discussed. Then, the development and results of a new T-curve model will be presented. Finally, an alternative model will be described.

A. T-curves and Strength.

The strength response of any material can be explained on the basis of its toughness. As described in Section I, a crack is in a state of equilibrium when the crack driving forces are balanced by the crack resisting forces:

$$K_A = T(c) \qquad (1)$$

where K_A is the net applied stress intensity, and T(c) is the sum of all material-associated crack resistance terms (i.e. the toughness curve). If $K_A > T(c)$, the crack will grow. The crack may grow stably for some time before fracture, or unstably, resulting in immediate, catastrophic fracture. Whether the crack extends stably or unstably depends on the relative shapes of the $K_A(c)$ and T(c) functions. The condition required for unstable fracture is given by

$$dK_A/dc > dT(c)/dc. \qquad (2)$$

These two criteria, equations (1) and (2), can be used to predict fracture, and hence strength, on the basis of the loading configuration and the material toughness characteristics. Figure V.1 depicts the T-curve, T(c), of a hypothetical material, for which T(c) = constant. Superimposed on this plot are several loading lines, representing states of increasing applied stress intensity ($K_a = \psi\sigma_a c^{1/2}$). A crack of size C1 will extend unstably as soon as K_A exceeds the material toughness, because the second condition (Eq. 2) is also met at the same time; and the material will exhibit a fracture strength given by σ_2 (Fig. V.1). The crack of size C2 will also extend unstably as soon

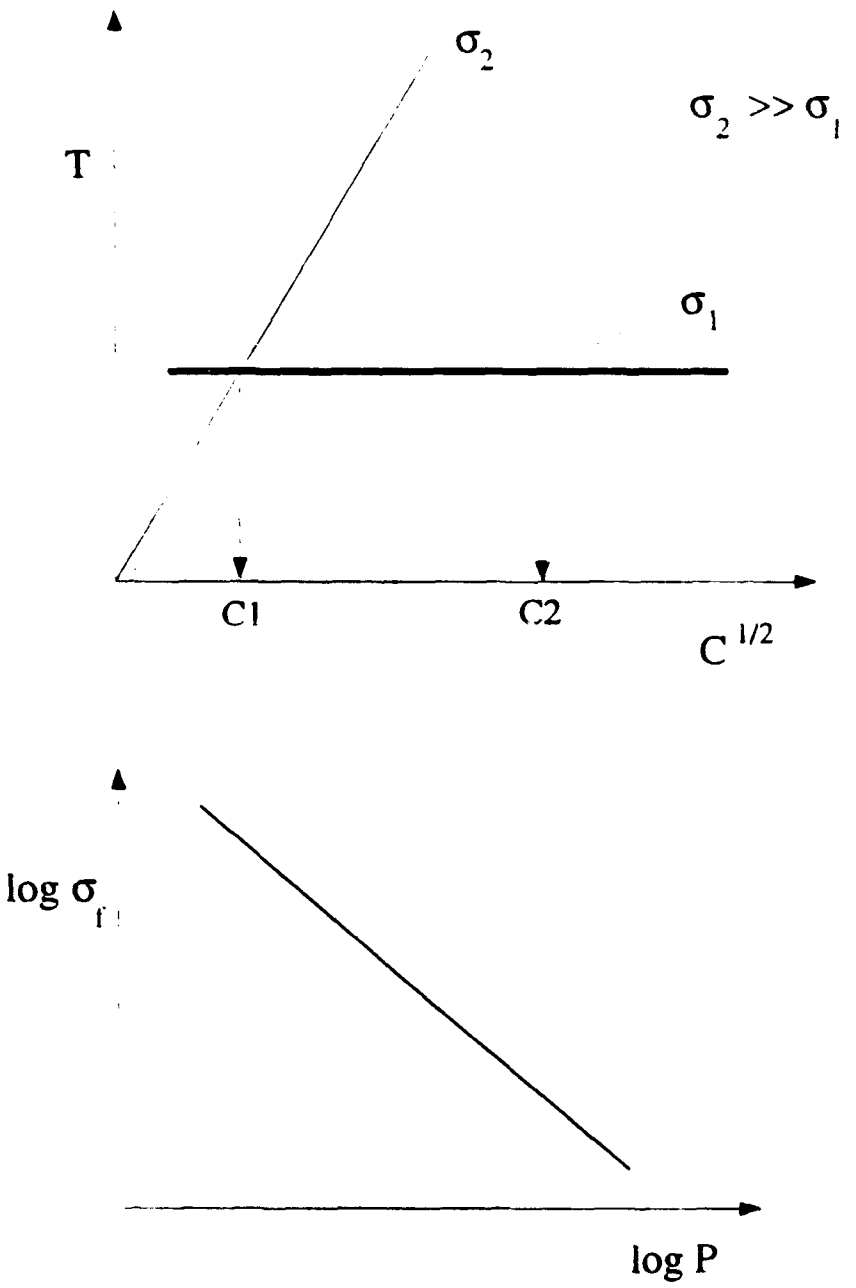

Figure V.1. T-curve (above) and corresponding strength (below) for a material which possesses a constant toughness. Such a material is flaw-sensitive, and would display the classical $P^{-1/3}$ strength response.

as $K_A > T$, but this fracture occurs at a much lower level of applied stress than for C1. This material is therefore described as flaw sensitive, with the strength falling as initial crack size increases.

Figure V2 shows the T-curve for a different hypothetical material, one with a crack size dependent toughness. This material exhibits increasing crack resistance with crack growth. Superimposed on this plot are again several loading lines. This time, a crack of size C1 extends *stably* when K_A exceeds the material toughness, because $dK_A/dc < dT/dc$. The slope of the T-curve is greater than the slope of the loading curve. Stable crack growth continues with increasing applied stress, until C2 is reached. At C2, the $K_A = T(c)$, and the crack driving force is increasing faster than the material's resistance to fracture. Thus, C2 represents the crack size at instability, and the applied stress, σ_3, is the fracture strength. All flaw sizes from C1 to C2 will grow stably until fracture occurs at C2, and all will have the same fracture strength. This material is therefore described as 'flaw tolerant', with the strength being *independent* of flaw size, within the range of C0 to C2. Flaws bewteen C0 and C1 will begin growing unstably (sometimes called 'pop-in'), but will arrest on the rising portion of the T-curve, and grow stably to C2.

From the preceeding discussion, it should be clear that knowledge of the T-curve allows prediction of strength. However, for many ceramics the rising portion of the T-curve occurs substantially in the domain of small flaw sizes. This makes direct, experimental measurement of the T-curve very difficult. Conventional toughness measurements (DCB, SENB, compact tension, etc., require starter cracks; and it is very difficult to produce starter cracks smaller than about 500 μm. Thus, any portion of the T-curve which falls in the range of small flaw sizes cannot be assessed by these conventional toughness techniques. This presents a dilemma, as all segments of the T-curve represent valuable information. Indeed, the danger of ignoring the small flaw domain is significant, since predictions based upon extrapolations from the large flaw domain may

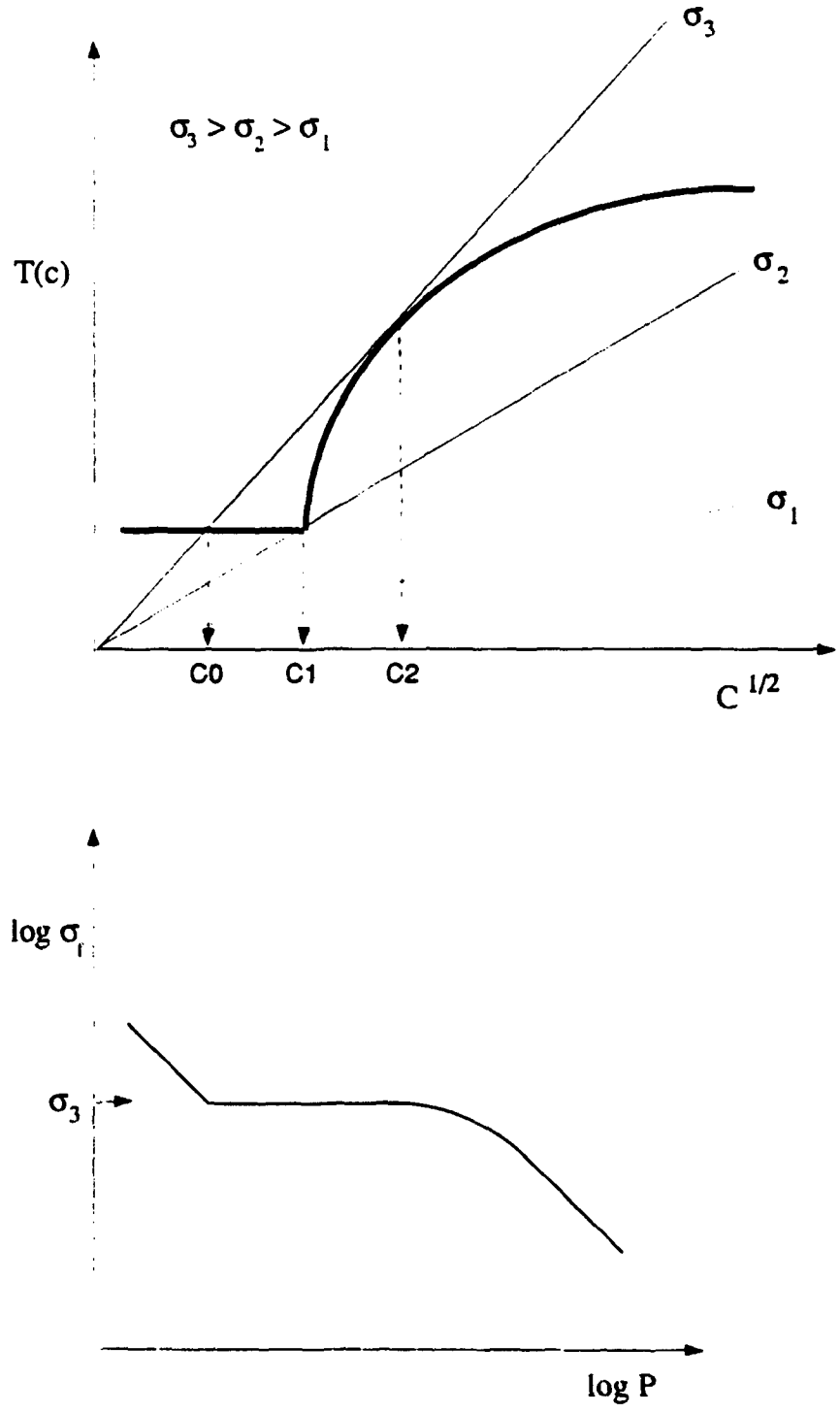

Figure V.2. T-curve (above) and corresponding strength (below), for a material which displays a toughness which increases with crack size. This material is flaw-tolerant, with a nearly constant strength over a range of flaw sizes.

overestimate the strength for smaller flaws.

The indentation strength test essentially provides strength data as a function of crack size, and can therefore be used to indirectly evaluate the T-curve in the critical small flaw size domain. This method involves computer fitting of the experimental strength data, by guessing the T-curve and determining how well that guess was able to 'predict' the measured strengths. The trial T-curve is then incrementally adjusted, until the variance between the predicted and experimental strengths no longer changes with further adjustments in the T-curve parameters.

There are significant limitations to this type of T-curve evaluation. The end result is simply a T-curve which produced a good fit to a set of strength data. That T-curve is characterized by a number of adjustable parameters, which may or may not have some relation to microstructural variables. Ideally, the T-curve would be characterized by material properties, so that knowledge of those properties would allow *a priori* specification of the T-curve parameters. This would minimize the number of unknown, adjustable parameters used in computer fitting of subsequent T-curves for similar materials. The model would then be able to account for alterations in the microstructure or processing, without requiring a completely new, computer T-curve evaluation. Finally, it should be noted that whether the T-curve parameters bear any relation to material properties or not, it is quite possible that an alternative T-curve model characterized by a different set of adjustable parameters could produce as good a fit. Thus, it is important to bear in mind that goodness of fit does not constitute proof of the particular model used in calculating the T-curve.

B. General Approach to T-curve Modeling.

This section will explain in greater detail the approach taken in the T-curve modeling. Consider a Vicker's indentation crack growing under the influence of an applied stress. The crack experiences a net applied stress intensity, K_A, given by

$$K_A = K_a + K_r = \psi\sigma c^{1/2} + \chi P c^{-3/2} \quad (3)$$

where K_a is the stress intensity due to the applied, external load, and K_r is the residual stress intensity field of the indentation. ψ and χ are constants characterizing the applied field and residual field, respectively (ψ =0.77, χ = 0.076). The values selected for ψ and χ are taken from the results of Braun, et. al., (1992) who calibrated these parameters for very similar alumina and Al_2O_3 + Al_2TiO_5 materials; and the χ value is also consistent with the original calibration of Anstis, *et. al.* (1981), for a wide range of materials. At equilibrium, the net applied field is equal to the intrinsic material resistance to crack growth, T_0, i.e.

$$K_A = K_a + K_r = T_0 \quad (4)$$

Any microstructure-associated stress intensity fields (e.g., a closure field giving rise to T-curve behavior), K_μ, further modify the equilibrium, and must be included in the analysis. Thus, in the presence of such a field,

$$K_A = K_a + K_r + K_\mu = T_0 \quad (5)$$

When the microstructural field acts as a crack-resisting field, rather than a crack-driving field, it is appropriate to group it together with T_0:

$$K_A = K_a + K_r = T_0 - K_\mu \quad (6)$$

The set of crack-resisting terms on the right side of Eq. (6) is called the T-curve, T(c). It is by manipulating the various terms of this equation that the T-curve may be extracted from the experimentally measured strength data. The extraction is complete when a computer-generated T-curve is able to predict the observed strengths.

The T-curve program predicts the observed strengths by solving Eq. (6) for the applied stress as a function of crack size, for each indent load tested. Using appropriate substitutions from Eq. (3) and (6),

$$\sigma_a(c) = [\, T(c) - \chi P c^{-3/2} \,] \,/\, \psi c^{1/2} \quad (7)$$

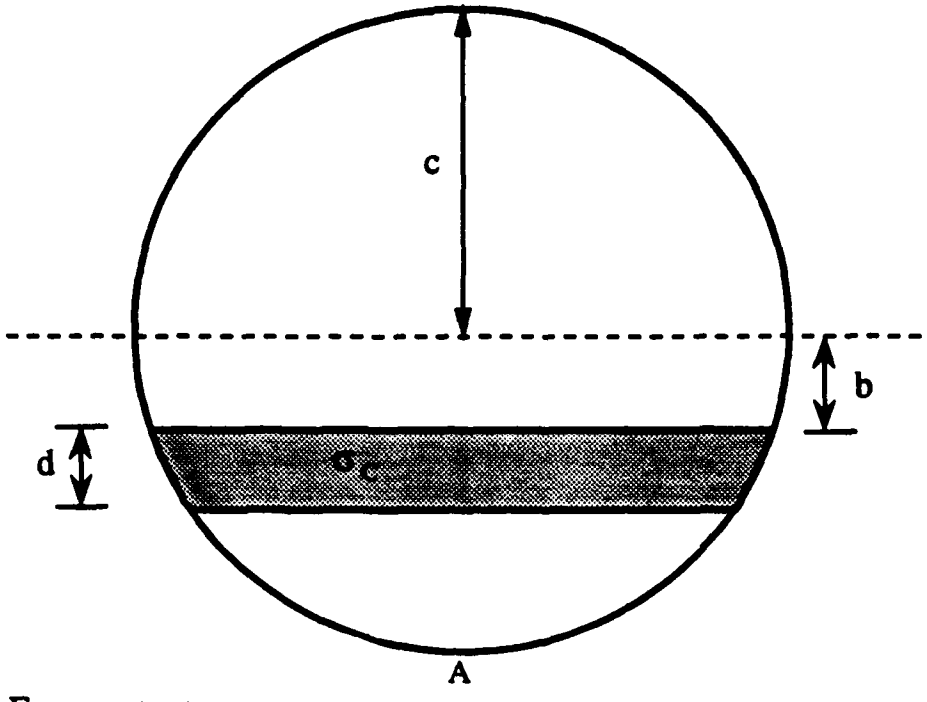

For constant σ_C:

$$K_\mu = \pi^{-1/2}\sigma_C c^{1/2} \left[2(b/c + d/c)^{1/2} - 2(b/c)^{1/2} - d/c\right]$$

With $d = c - b$,

$$K_\mu = \pi^{-1/2}\sigma_C c^{1/2} \left[1 - 2(b/c)^{1/2} + b/c\right]$$

Figure V.3. The stress intensity factor solution for an embedded penny-shaped flaw, subjected to crack-face loading by a strip of constant, normal stress, σ_c .

where $T(c) = T_0 - K_\mu$. Neither T_0 nor K_μ are known. In the computer fitting, T_0 is an adjustable parameter. K_μ contains adjustable parameters, and is based on the solution (Lawn & Fuller, 1984; Tada, Paris, & Irwin, 1985) for an embedded, strip-loaded, penny-shaped crack (see Figure V3):

$$K_\mu = -\psi\sigma_c c^{1/2} \{1 - 2(b/c)^{1/2} + (b/c)\} \quad (8)$$

where ψ is the same geometrical constant as in the applied field, σ_c is a constant closure pressure acting on the crack wake, and b is the distance from the surface at which that closure stress begins to act. Thus, the crack wake is assumed to contain a pressurized strip, acting over a distance extending from b, up to the crack tip. Both of these (σ_c and b) are adjustable parameters. Finally, a steady state crack size, c*, was included in the model to allow the microstructural field, K_μ, to reach a saturation level, beyond which it remains constant (the closure wake zone translates with the crack tip). This c* is the fourth and final adjustable parameter. (An alternative K_μ solution was also used to model the T-curves, and will be discussed in part D, below.)

Figure V4 illustrates the basic geometry of this model for a range of crack sizes, in a *monolithic* material (for simplicity). From this figure, four different domains of crack growth may be defined. When the crack is smaller than the closure pressure depth, b, the microstructural stress field has not yet been activated, and the material toughness is constant (T_0). After growing beyond b, the microstructural elements in the crack wake begin to exert their closure stresses, and the microstructural contribution to the toughness is given by Eq. (8). At the steady state crack size, c*, the microstructural influence saturates out to its maximum value. Beyond c*, the K_μ term maintains that same maximum value, as the most remote bridging ligaments either disengage or rupture. With c* defined in this way, the T-curve truncates abruptly at c*, rather than approaching the steady state value in an assymptotic manner. This physically unrealistic aspect of the model is an unavoidable consequence of the *linear* description of this inherently *nonlinear* crack system. The closure zone defined for this stress intensity factor solution is shown in its proper form in Fig.

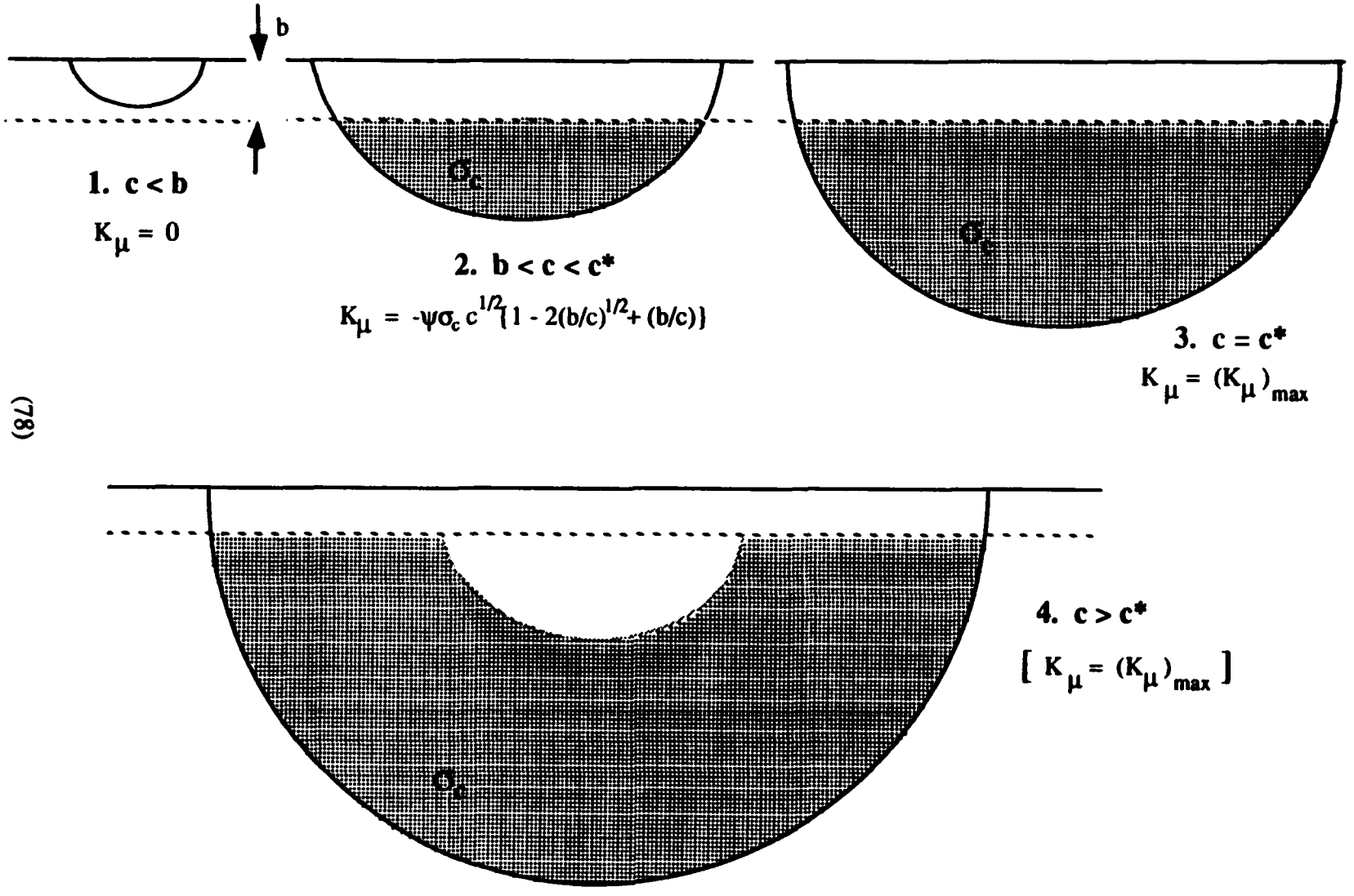

Figure V.4. Crack size domains, for the monolithic materials, illustrating the essential geometry of Eq. (8).

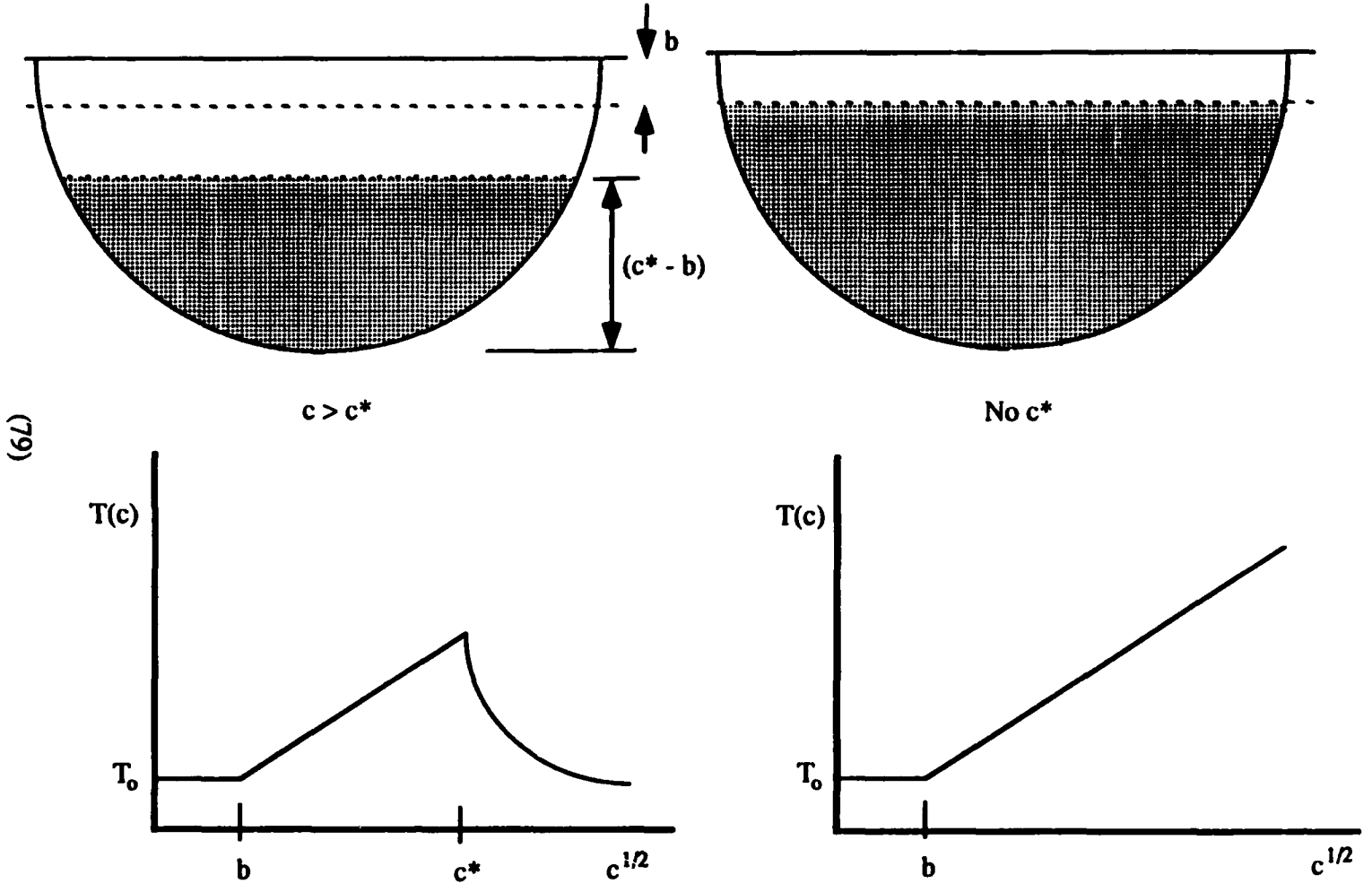

Figure V.5. Two alternatives to the simple truncation of the T-curve at c*. The left side shows a crack larger than c*, with the closure zone defined by the width of the strip when c = c*. This results in a decreasing toughness with further crack growth. The right side depicts the situation for no steady state crack size at all. Here, the toughness increases without limit. Both scenarios were rejected as too unrealistic.

V4, domains 1 - 3. Beyond the steady state crack size, however, this zone shape cannot be maintained in a real material. The concept of a steady state wake zone translating with the advancing crack tip simply cannot be accomodated by this K-factor solution, in a physically realistic manner. The more realistic zone shape is illustrated in Fig. V4, domain 4, and the steady state zone K-factor associated with this configuration is assumed to be reasonably approximated by the maximum K_μ, at c*. The alternatives, other than abandoning this stress intensity factor solution, were to allow K_μ to increase without limit (no c* at all), or to allow a steady state zone of constant width (c* - b) to translate with the advancing crack front. The first is clearly inadequate, and the second would result in a steadily *diminishing* zone size (and hence, toughness contribution), beyond c*, which is also unsatisfactory. These alternatives are illustrated in Figure V5.

Once the four adjustable parameters have been assigned a value within the T-curve program, the toughness may be calculated for any crack size. The heart of the computer program is a crack size loop, in which Eq. (7) is solved for each crack size. As the crack size increments upward, the stress values are tracked by a simple IF test[1], and the maximum stress is labeled the strength, for each indent load. The calculated strengths are compared to the measured strengths, and the quality of fit is determined with a variance calculation, summed over the entire set of tested indent loads, with the calculation weighted toward the loads having the most experimental data. The variance is continuously monitored, and the best fit values of the adjustable parameters are redefined as necessary. Then the adjustables are incremented, and the cycle is repeated.

One of the primary means of assessing the T-curve models was the variance, which was

[1]An IF test is a FORTRAN programming tool which compares the values of two variables. What happens next in the program depends on the results of that comparison. In the present case, the current value of the applied stress is compared to the maximum value calculated up to that point, and IF the current value is greater than the previous maximum, the current stress is defined as the new maximum stress.

calculated according to the following relation:

$$Var = \Sigma\{(\sigma_{calc.} - \sigma_{meas})^2(n/N)\}/(np - 1) \quad (9)$$

where n was the number of samples broken at a given indent load; N was the total number of samples broken; np was the total number of indent loads tested, and $\sigma_{meas.}$ was the average strength value for a given indent load. The number produced by this calculation may be viewed as the average percentage difference between measured and calculated strengths, squared. (Thus, a variance of 16 would indicate an average of 4% difference between measured and calculated strengths.) The FORTRAN codes for these T-curve programs are given in Appendix II.

An alternative modeling scheme will be discussed in part D. in which the microstructural closure field is described by discrete arc-shaped line forces applied at a fixed distance behind the crack tip.

C. Results From The Linear Strip T-curve Model.

There were two main methods by which this model (Figures V3 and V4) was applied: (1) In the simplest case, the trilayer composites were modeled as if the surface layer material exhibited no T-curve behavior. The surface layer thickness was associated with the b term. The second level of complexity, (2), allowed for a T-curve contribution from the surface material. With this method, the surface and bulk materials shared the same T_0 value, but each possessed their own b, σ_c, and c* values. The homogeneous AAT20 surface material was evaluated first (four adjustables), and then the inhomogeneous bulk material was evaluated using the T_0 determined for the homogeneous material (three adjustables). The best fit parameters for the two AAT20 base materials were then used (as constants) to characterize the trilayer T-curve.

(1) Simplest case - surface material of constant toughness.

For this case, the adjustable parameters were varied within the following limits:

$$1.5 \le T_0 \le 4.5 \quad (0.05, 0.01) \quad MPa*m^{1/2}$$

$$50 \leq \sigma_c \leq 450 \quad (20, 1) \text{ MPa}$$

$$10 \leq b \leq 250 \quad (20, 10, 1) \text{ μm}$$

$$50 \leq c^* \leq 2600 \quad (200, 100) \text{ μm}$$

where the numbers in parentheses indicate the step sizes used to incrementally adjust the parameters in the program. The strategy for determining the best fit parameters involved an initial run using coarse step sizes, redefining the limits based on the results from the previous run, and repeating the program with finer and finer step sizes. (This was done to save computer time.) These runs eventually produced the best fit values displayed in Table II. The variance was 16.38, indicating an approximate average difference of 4% between measured and calculated trilayer strengths.

It is of interest to note that the best fit value for b (67 μm) was not the same as the surface layer thickness (104 μm). The fact that the best b was *less* than the thickness indicates that the surface material contributed to the T-curve, because the closure wake zone began before the crack entered the flaw tolerant bulk material.

The value for T_0 (2.26 MPa$\sqrt{m}$) is in the low range of values reported for similar alumina materials, using long crack toughness measurements (Swain, Steinbrech). It is very close, however, to the T_0 values determined (by T-curve modeling) for similar alumina materials by Bennison and Lawn (1989) - 2.75 MPa$\sqrt{m}$, and by Cook, et. al. (1987) - 1.49 to 3.1 MPa$\sqrt{m}$.

While this model provided a reasonably close fit to the experimental strength data, there is at least one problem with it. It was incapable of predicting the influence of surface layer thickness on the trilayer strengths (using the closure pressure depth term, b, to simulate changes in surface thickness). This was most likely a result of ignoring the surface material contribution to the T-curve. As discussed briefly in section IV, the surface material does provide indications of T-curve behavior, both in the indentation strength response, and in the radial crack lengths.

(2) Allowing surface contribution.

To make the model seem more physically realistic, the surface layer was allowed to contain its own closure pressure strip. The homogeneous AAT20 strengths were run through the program, with the adjustable parameters having the following limits:

$$1.0 \le T_0 \le 5.0 \quad (0.5, 0.05, 0.01) \quad MPa*m^{1/2}$$

$$10 \le \sigma_c \le 170 \quad (20, 5, 1) \quad MPa$$

$$5 \le b \le 125 \quad (10, 2, 1) \quad \mu m$$

$$50 \le c^* \le 2450 \quad (200, 50, 20) \quad \mu m$$

where, again, the numbers in parentheses represent step sizes. The best fit values for the parameters are shown in Table II. The T_0 value (2.27 MPa$\sqrt{m}$) was not much different from that obtained above, for the simplest model, from the trilayer strengths. The variance for the homogeneous AAT20 was 4.52. The indentation strength response as calculated by this model is compared to the experimentally measured data in Figure V.6. It may be seen that the fit is quite good. After these best fit values were determined, the inhomogeneous AAT20 strengths were run through the program, forcing T_0 to be the same as for the homogeneous material. The adjustable parameters had the following limits:

$$50 \le \sigma_c \le 330 \quad (10, 2, 1) \quad MPa$$

$$20 \le b \le 500 \quad (10, 5, 1) \quad \mu m$$

$$800 \le c^* \le 2000 \quad (100, 20) \quad \mu m$$

The best fit values are again displayed in Table II. It may be seen that the values for b and σ_c are considerably larger in the more flaw tolerant, inhomogeneous AAT20. The variance for this material was 7.04. Figure V.7 displays the computed strength response together with the experimentally measured values, and again the fit is good. The T-curves calculated by the model for the two base materials are shown in Fig. V.8.

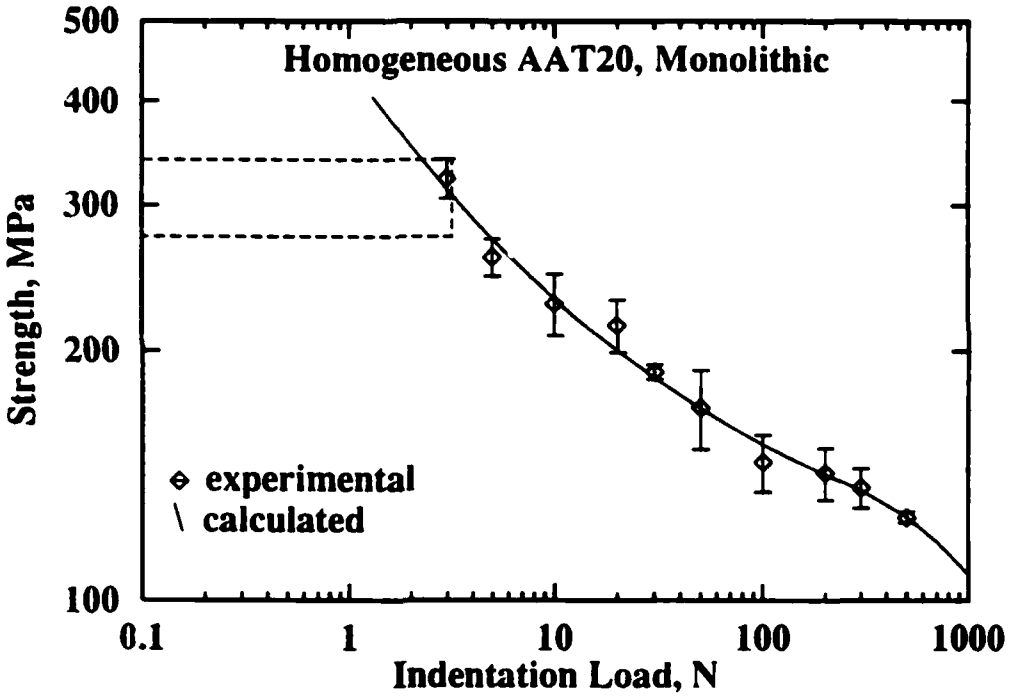

Figure V.6. Indentation strength behavior of the homogeneous AAT20 base material. Symbols and error bars represent experimentally measured strengths; and the solid line represents the values calculated by the linear strip T-curve model, using method 1(d). Best fit parameters were T_0 = 2.27 MPa*m$^{1/2}$; σ_c = 95 MPa; b = 28 μm; and c* = 1180 μm.

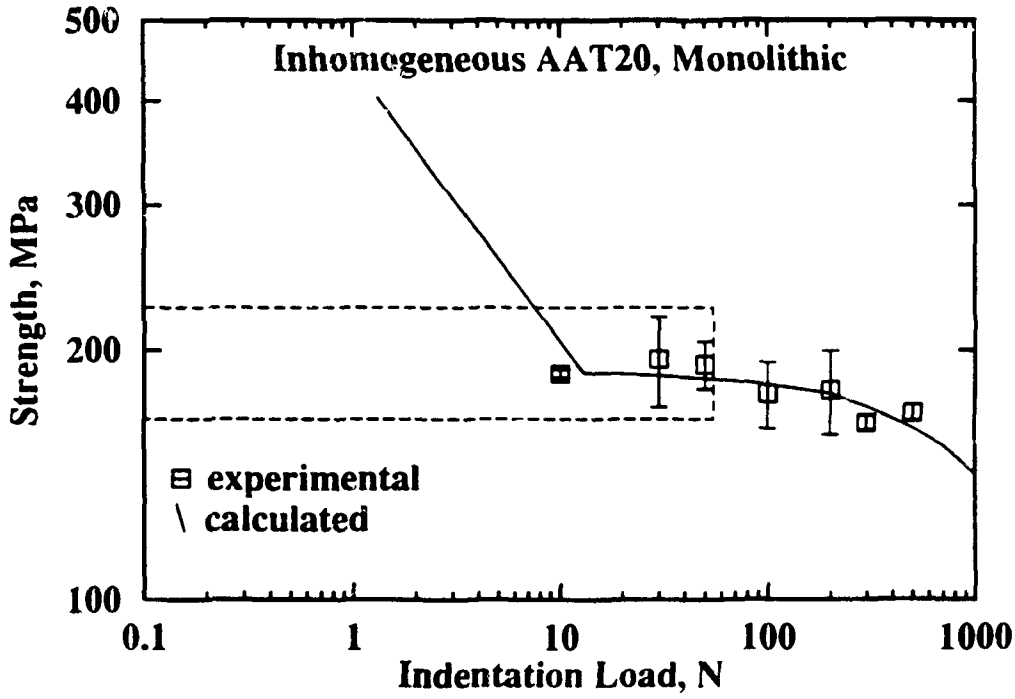

Figure V.7. Indentation strength behavior of the inhomogeneous AAT20 base material. Symbols and error bars represent experimentally measured strengths; while the solid line represents strength values calculated by the linear strip T-curve model, using method (2). Best fit parameters were σ_c = 324 MPa; b = 228 μm; and c* = 1220 μm.

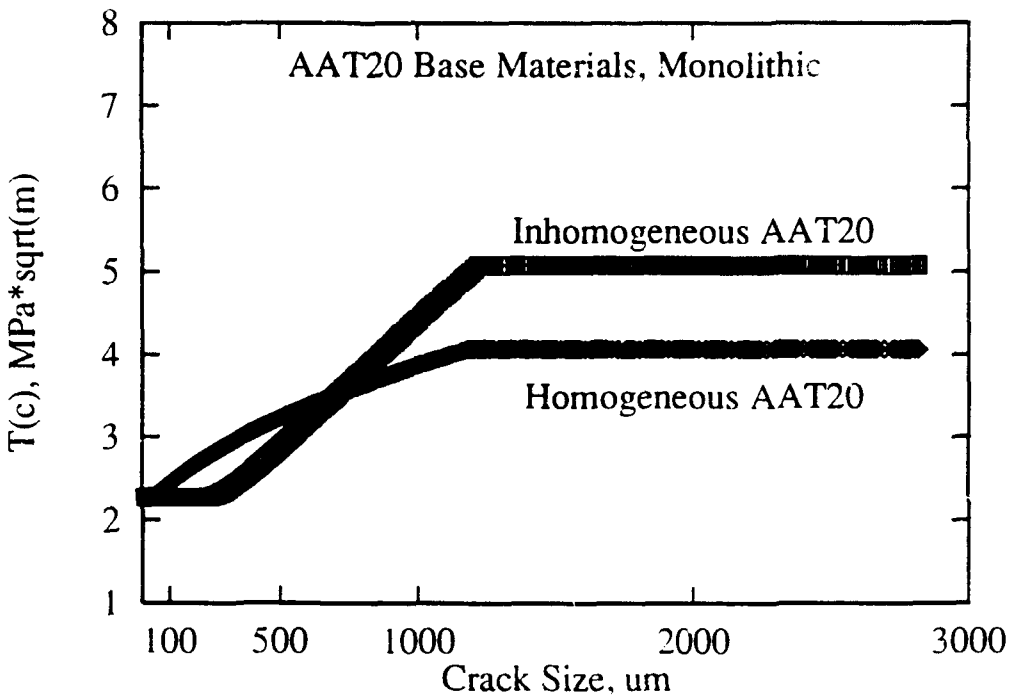

Figure V.8. T-curves calculated using the best fit parameters for the two base materials (see Table II), using the linear strip model.

These best fit parameters from the base materials were then used as constants to define the trilayer composite T-curve. Using this T-curve, the trilayer strengths were calculated, and the variance between calculated and measured strengths was found to be 15.83. The calculated and experimental trilayer strengths are plotted together in Figure V.9, for further comparison. This fit is good, but is only a slight improvement over the fit obtained by the simpler model. The trilayer composite T-curve is shown in Figure V.10.

The T-curve models can be evaluated on the basis of more than just strength predictions. The model can predict crack sizes at fracture (simply, the crack size corresponding to the maximum stress, i. e. the strength), and can assess the effect of the surface layer thickness on trilayer strengths.

The critical crack size predictions were compared to some known crack sizes at failure in similar materials. Braun, et. al., have conducted *in situ* crack growth observations during biaxial flexure testing of indented alumina and (Al_2O_3 + Al_2TiO_5) materials, in order to directly measure the applied stress as a function of crack size (which was *calculated* in the T-curve models, using Eq. (7)). The final crack sizes they reported for materials similar to the two AAT20 base materials compare quite well with the predictions from the T-curve model , as long as no c* cutoff is used (see Table III). The predictions from methods (1) and (2), described above, which used a c* term, do not compare quite as well to the measured crack sizes, although they are still reasonable. The T-curve model thus seems to produce satisfactory descriptions of both strength and crack size behavior.

The simplified T-curve model (no surface contribution) was unable to account for the influence of surface layer thickness on trilayer strength response, whether a c* term was included or not. The model which did allow for a surface influence on the T-curve was able to describe variations in the indentation strength behavior as a function of layer thickness, with moderate

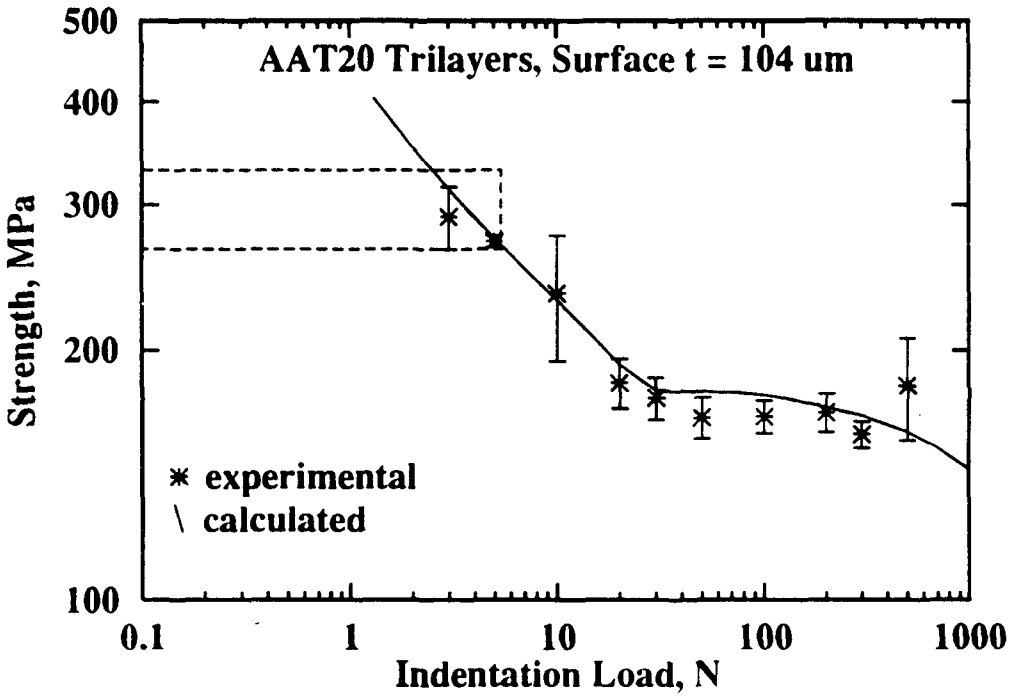

Figure V.9. Indentation strength behavior of the AAT20 trilayer composites having layer thickness of 104 μm. Symbols and error bars represent experimentally measured strengths; solid line represents strength values calculated by the linear strip T-curve model, using the best fit parameters from the two base materials (see Figure V.8. and Table II).

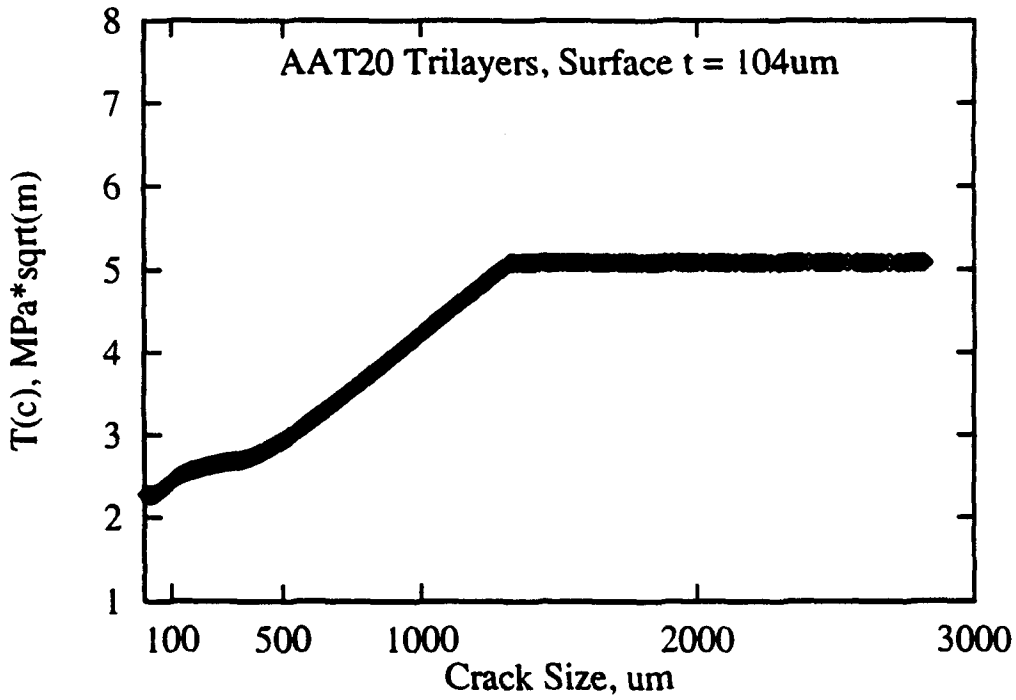

Figure V.10. Trilayer composite T-curve calculated by the linear strip model (method (2)), in which both the surface layer and the bulk material contain their own closure zone.

Table II. Best Fit Parameters From T-Curve Models

Methods	T_0 (MPa•m$^{1/2}$)	b (μm)	σ_c (MPa)	c^* (μm)	Variance
Linear Strip Model					
1 - Trilayers	2.26	67	156	2500	16.38
2 - Surface Material	2.27	28	95	1180	4.52
2 - Bulk Material	(2.27)	228	324	1220	7.04
2 - Trilayers	----------→				15.83

	T_0	δ (μm)	P (kN/m)	Variance
Arc Forces Model				
Surface Material	2.32	155	26	9.55
Bulk Material	(2.32)	441	117	9.32
Trilayers	----------→			32.42

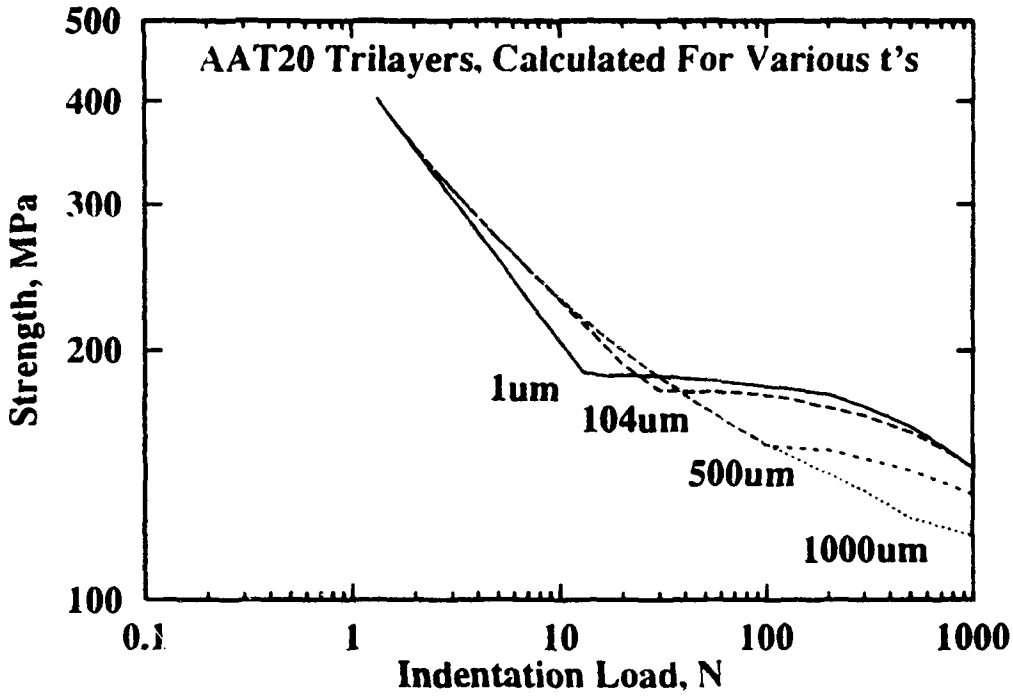

Figure V.11. *Strength predictions for trilayer composites, using the linear strips T-curve model (method 2) for a range of surface layer thicknesses. The strength trends are reasonably accounted for by the model, with the extremes of very thin and very thick surface layers producing the monolithic bulk and surface material strength behavior, respectively.*

success. Strength predictions of the model are shown in Figure V.11 for a variety of surface layer thicknesses. The *trends* in strength response were reasonably accounted for, but the actual predicted strength values often fell outside the experimental scatter. The model was best able to describe the thickness effect for the extremes of very thin and very thick surface layers. For a 1 μm surface layer, the calculated strengths were nearly the same as for the bulk inhomogeneous AAT20; and for a 1000 μm layer, the computed trilayer strength curve fell essentially onto the surface material strengths. For the thicknesses which were actually evaluated experimentally, the model provided only a fair match, predicting (for example) higher large flaw strengths for the 169 μm samples than were actually measured. It would be interesting to gather more strength data for these thicknesses, and for a few larger thicknesses (e.g. 500 μm and 1000 μm) in order to more completely evaluate the ability of the model to account for thickness effects. The most obvious shortcoming illustrated by Fig. V.11 is the strength predictions of the model for small indent loads, as surface layer thickness decreases. The model predicts much higher small flaw strengths than were observed, and this is a result of the dominance of larger flaws in the underlying bulk material. The trilayer model is therefore seen as being incapable of accounting for the transition between indentation flaw controlled strengths, and natural flaw controlled strengths. This point will be disscussed in more detail, below.

The preceeding discussion dealt with how well the model was able to account for experimentally measured strength trends. Useful models are able to not only *describe* observed behavior, but to *predict* it before the fact. Furthermore, a model should be able to suggest experimental strategies. In particular, it would be of considerable benefit if the T-curve model were able to predict the optimal surface layer thickness, based on the properties of the two monolithic materials, before an extensive trial-and-error development effort were undertaken. The simple approach for predicting the optimal thickness was described in section II, and it produced

an excellent match between the predicted and actual optimum thickness. However, the zirconia s_ :m demonstrated that this prediction technique may not be generally applicable. A need therefore exists for a better thickness prediction. Ideally, the T-curve program would be able to provide this.

The predictive ability of the trilayer T-curve computer program was evaluated by calculating indentation strength curves for a wide range of surface layer thicknesses, using the best fit parameters from the two base materials. The resulting curves were then examined (qualitatively) for evidence of optimum composite strength behavior. It quickly became clear that the model was able to narrow the range of potential thicknesses, particularly by eliminating the larger thicknesses from contention, but that obtaining a clearly optimum thickness in this manner would be difficult. Below about 300 μm thickness, the strength curves were all similar. 50 μm changes in the thickness resulted in differences in the large flaw strengths of only a few MPa. Further complicating the problem was the predicted strengths at small indent loads, for the smallest layer thicknesses. Experience has shown that the dominance of large flaws in the underlying bulk material prevents indent-controlled fracture at small P, when the surface layer is thin. This is an effect which the model (as presently configured) cannot predict, and this has significant consequences for the computed strength behavior. For example, the model predicts 3N strengths of over 300 MPa, whether the surface layer thickness is 100 μm or 30 μm (see Fig. V.11), even though a 30 μm sample would never fail from a 3N indentation crack (i.e., a 30 μm sample would have a much lower 3N strength, see Fig. IV.6). Thus, if the optimum thickness were to be estimated in this manner, a large degree of subjectivity would necessarily be introduced. The small flaw region would have to be ignored, or assigned less importance than the large flaw region. Clearly, this is unsatisfactory.

A more objective, quantitative approach yielded somewhat more acceptable results. If the

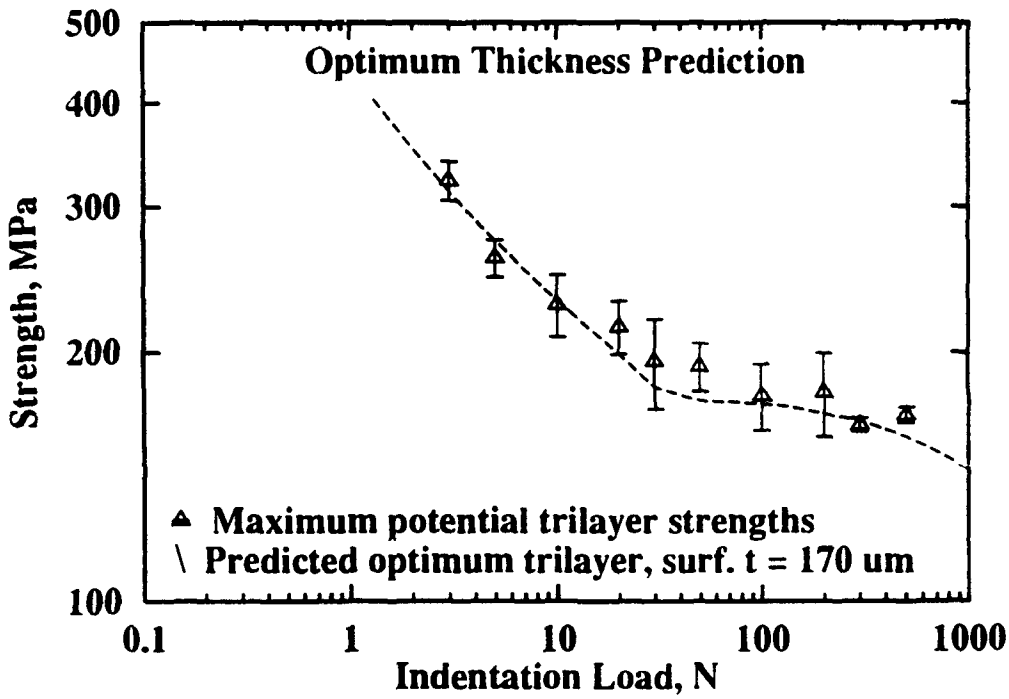

Figure V.12. This plot shows the calculated strength response for the predicted optimum trilayer composite (solid line). The linear strip model predicted an optimum surface layer thickness of 170μm, by comparing the variance between the calculated strengths and the maximum 'potential' trilayer strengths (symbols). 170 μm produced the minimum variance. The 'potential' strengths are simply the greater of the two base material strengths, for each indent load (see Table I, or FigIV.5).

base material strength responses are well characterized throughout the range of indentation loads, then an optimum, *potential* trilayer composite strength response can be defined. The potential strength curve would simply adopt the highest measured strength of the two base materials at each indent load. If this set of potential strength data were then input to the trilayer T-curve program, using the best fit parameters of the two base materials, and allowing the layer thickness to vary, then a variance calculation can be used to compare the predicted strengths to the potential trilayer strengths. The thickness producing the minimum variance would be identified as the predicted optimal surface layer thickness. This method predicted an optimal surface layer thickness of 170 μm for the AAT20 system, after comparing thicknesses between 30 and 1000 μm, at 10 μm intervals (variance was 17.25). Figure V.12 compares the strengths for the 'potential' trilayer (i.e., using the highest strength from the two base materials, for each P) with the strengths predicted by the T-curve program (method (2)), for this 'optimum' trilayer (surface layer thickness of 150 μm). This is a significant improvement over the prediction technique described in the preceeding paragraph, but is not an improvement over the simplest approach described in section II.

D. Alernative Model: Arc-Shaped Line Forces

An obvious extension of the modeling discussed above is to choose an alternative stress intensity factor solution to model the microstructural field, K_μ. In this alternative model, the crack wake is subjected to loading by an arc-shaped closure force. The arc-shaped closure force is thought to better represent the geometry of a growing, half-penny shaped, indent crack, especially with respect to the steady state crack size configurations discussed earlier (illustrated in Figures V4 and V5). This K_μ was obtained from solution 24.4 of The Stress Analysis of Cracks Handbook (Tada, Paris, Irwin, 1983), which is shown in Figure V.13. Solution 24.4 provides the stress intensity factor for an embedded, penny-shaped flaw containing an arc-shaped, constant line force of magnitude P. The line force is applied to the crack face, normal to the crack plane, and is

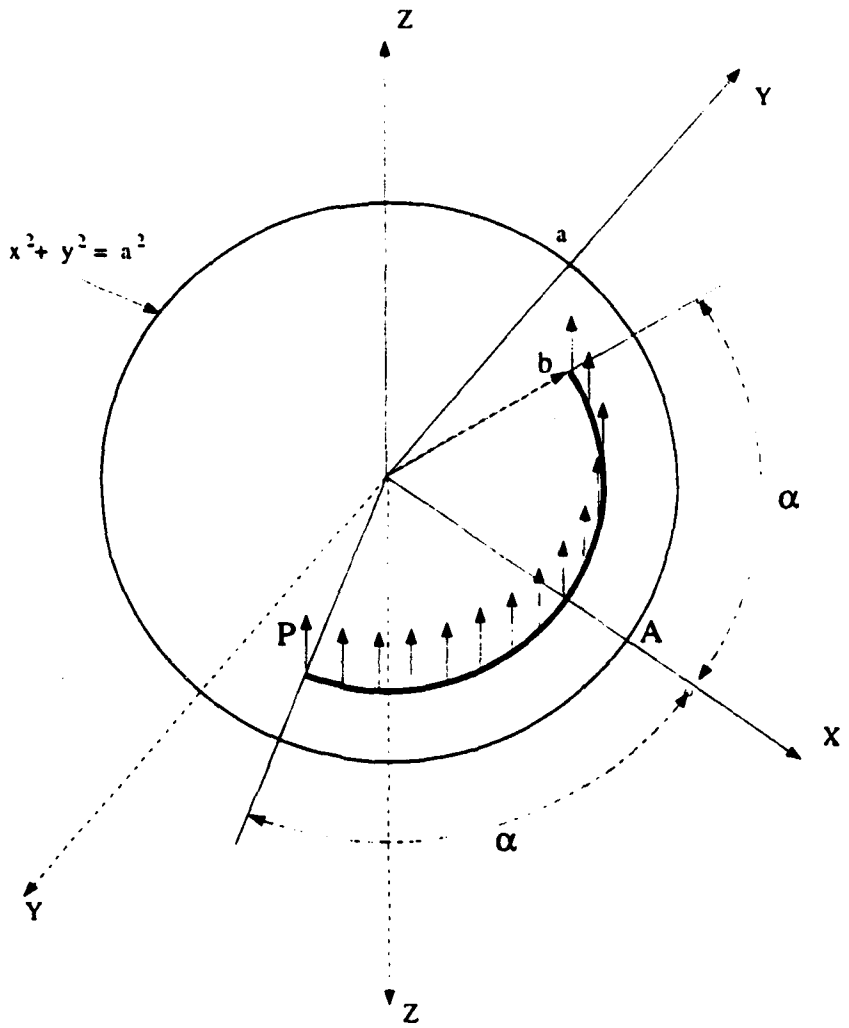

$$K_{IA} = \frac{2Pb}{\pi\sqrt{\pi a}\sqrt{a^2 - b^2}} \left\{ 2\tan^{-1}\left(\frac{(a+b)\tan(\alpha/2)}{a-b} \right) \right\}$$

Figure V.13. Alternative K_μ formulation is based on Solution 24.4 from The Stress Analysis of Cracks Handbook (Tada, Paris, Irwin, 1983). The K-factor given above is for an embedded, penny-shaped crack of radius, a, lying in the XY plane, and subjected to crack face loading by the line force of magnitude P. This line force is applied normal to the crack plane, at a radial distance, b, and is distributed over an arc of half-angle, α.

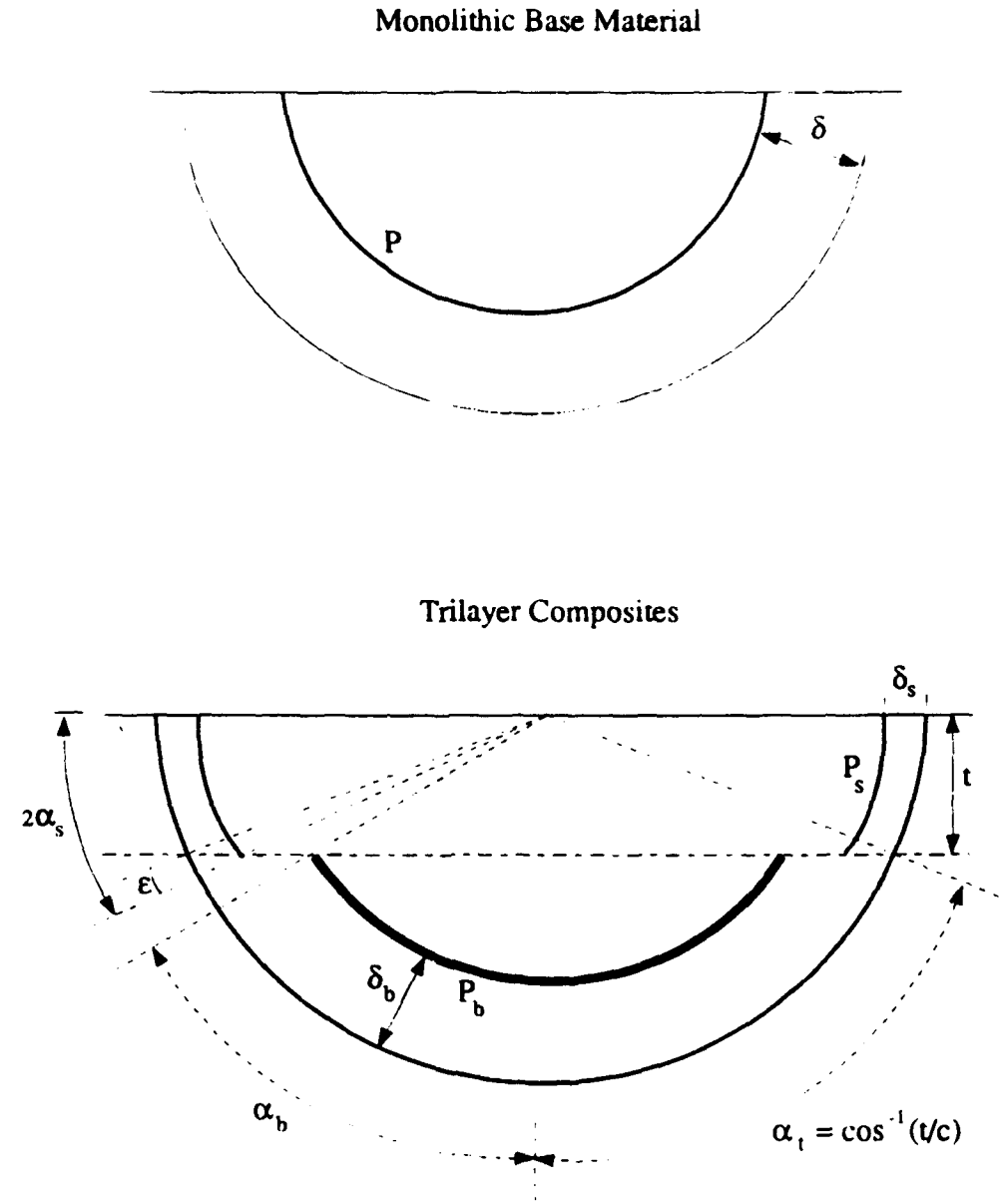

$$\alpha_b = \tan^{-1}\{(c\sin\alpha_t - (\delta_b / \sin\alpha_t))/t\}$$

$$\varepsilon = \alpha_t - \tan^{-1}\{(c\sin\alpha_t - (\delta_s / \sin\alpha_t))/t\}$$

$$2\alpha_s = \pi/2 - \alpha_t + \varepsilon$$

Figure V.14. The microstructural stress intensity contribution is modeled as an arc-shaped line force acting on the crack wake, at a fixed distance, δ, behind the crack tip. At top, this closure force is shown for a crack in the monolithic material. At bottom, the crack (of length, c) in the trilayer composite is shown having three separate line force segments.

further defined by the arc half-angle, α, and the arc radius, b. The stress intensity (at A in Fig. V.13) is given by

$$K_\mu = \frac{2Pb}{\pi\sqrt{\pi a}\sqrt{a^2-b^2}} * [2\tan^{-1}(\frac{(a+b)\tan(\alpha/2)}{a-b})] \qquad (10)$$

where P is in N/m, and a is crack size. In this model, there are three adjustable parameters: T_0, as before; P, the constant line force; and b, the radial distance from the center of the indentation, at the surface, to the point where P begins to act. Rather than model the line force at a fixed b position from the surface, however, it is believed that the physics of the growing crack is better represented by setting the line force at a fixed distance, δ, behind the crack tip, so that the closure force may translate forward with the advancing crack front. Thus, the microstructural stress intensity factor is redefined as

$$K_\mu = \frac{4P(a-\delta)}{\pi^{3/2}a^{1/2}\delta^{1/2}(2a-\delta)^{1/2}} \left[\tan^{-1}[\frac{2a-\delta}{\delta}\tan(\frac{\alpha}{2})] \right] \qquad (11)$$

where δ = a - b. With K_μ redefined in this way, δ replaces b as an adjustable parameter in the computer modeling. This K_μ is illustrated in Figure V.14, for cracks growing in monolithic and composite materials. No arbitrary imposition of a steady state crack size is required in this model; for large crack sizes ($a \gg \delta$), this K_μ approaches a constant value, given by

$$K_\mu = P\sqrt{2}/(\pi\delta)^{1/2} \qquad (12)$$

which corresponds to the steady state toughness (sometimes called 'T_∞').

This model was applied following the same strategy as described for the linear strip model (method 2 only). First, the T-curve characteristics of the two base materials were evaluated. Then, these T-curve parameters were used to define the trilayer T-curve. The homogeneous AAT20 strength data were run through the program, using the following ranges and step sizes for the adjustable parameters:

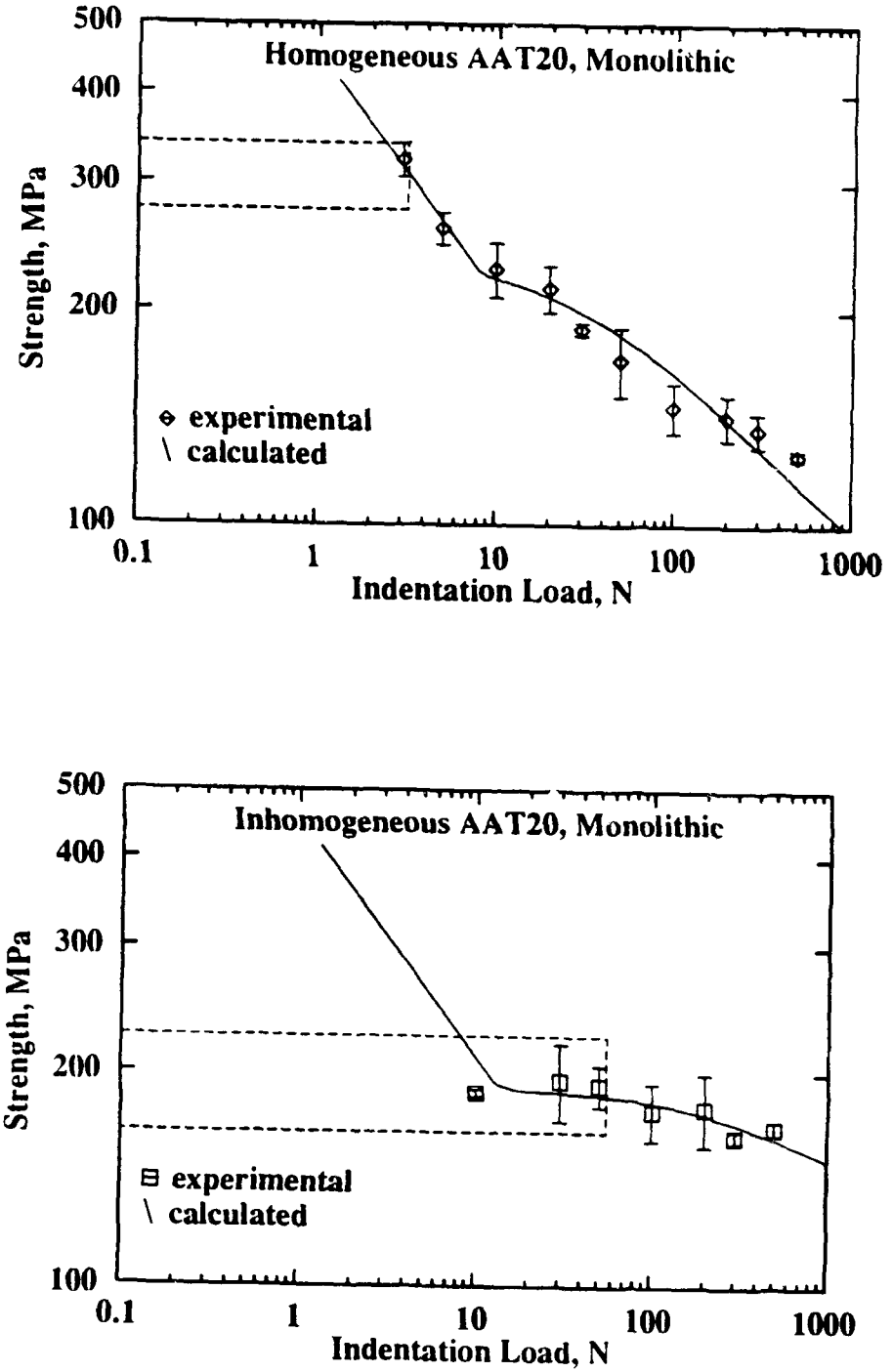

Figure V.15. Strength predictions from the arc-forces T-curve model compared to the experimentally measured strengths in the two AAT20 base materials. The hatched band at left shows the strengths for natural flaws (unindented). Best fit parameters are shown in Table II.

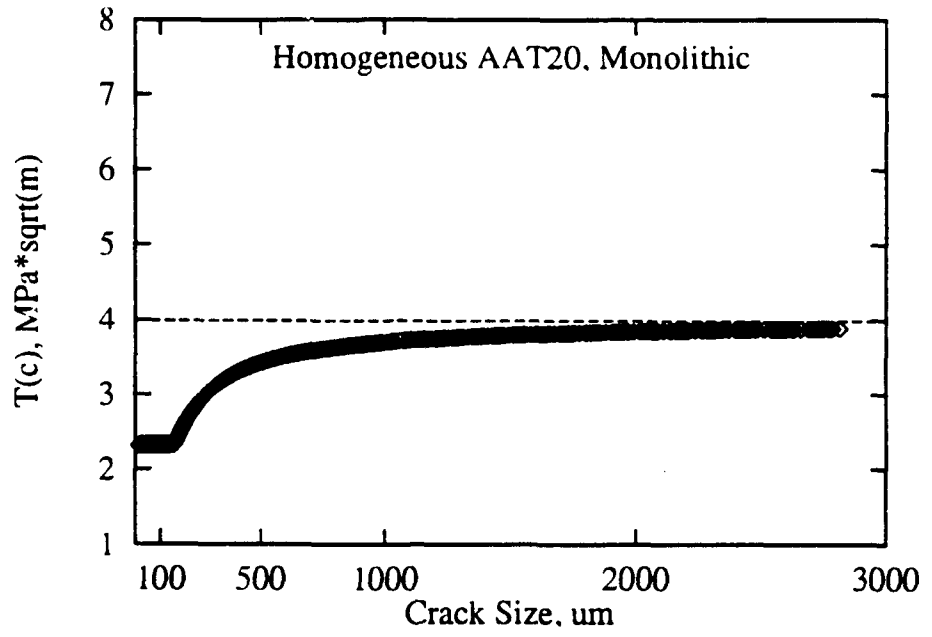

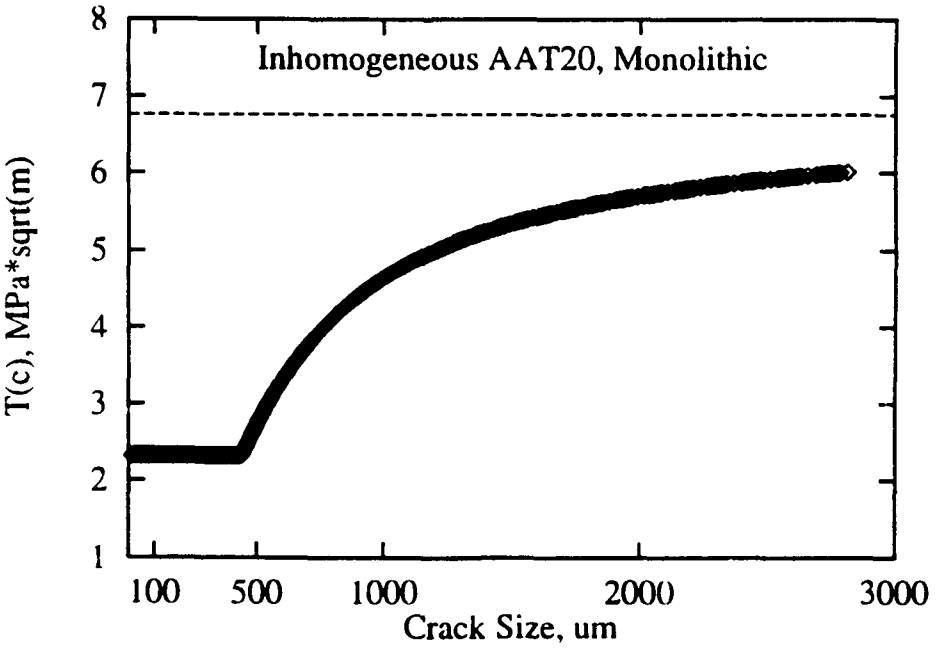

Figure V.16. T-curves corresponding to the best fit parameters (Table II) for the base materials, calculated by the arc-forces model. The dashed lines represent the steady state toughness, T_{ss}. These T-curves produced the strength predictions shown in Figure V.14.

$$2.0 \le T_0 \le 3.0 \quad (0.1, 0.01)\ \text{MPa}\sqrt{\text{m}}$$

$$10 \le P \le 100 \quad (10, 1)\ \text{kN/m}$$

$$10 \le \delta \le 510 \quad (50, 5)\ \mu\text{m}$$

The best fit values are shown in Table II, and the variance was 9.55. The variance indicates a slightly worse fit to the strength data than was obtained using the linear strip model. These best fit parameters give a steady state toughness, T_{ss}, of 3.99 MPa$\sqrt{\text{m}}$ (calculated by adding the result from Eq. (12) to T_0). The inhomogeneous AAT20 strengths were then run through the program, using the same T_0, with the following ranges and step sizes:

$$26 \le P \le 200 \quad (1)\ \text{kN/m}$$

$$150 \le \delta \le 650 \quad (1)\ \mu\text{m}$$

Best fit values are shown in Table II. The variance was 9.32, which is again slightly worse than the fit obtained from the linear strip model for this material. These parameters produced a T_{ss} value of 6.76 MPa$\sqrt{\text{m}}$, an increase of about 300% over T_0. The strengths predicted for the two base materials are compared to the experimentally measured values in Figure V.15, and the fits are seen to be quite good. The T-curves produced by this model are shown in Figure V.16.

The best fit parameters from the base materials were then used as constants to define the trilayer composite T-curve. This T-curve produced strength predictions with a variance of 32.42 compared to the experimentally measured values (i. e., average differences of ~6%). While this variance is a bit higher than that produced by the other model (differences of ~4%), the fit to the strength data is still quite good, as shown by Figure V.17. The trilayer composite T-curve is shown in Figure V.18. The sharp peak in toughness at a crack size of 259 μm corresponds to the transition between having a semicircular line force in the surface layer, and two arc-shaped line forces extending from the surface down to the material interface. The significance of 259 μm is that it is the crack length equal to the layer thickness (104 μm) plus the surface material's closure

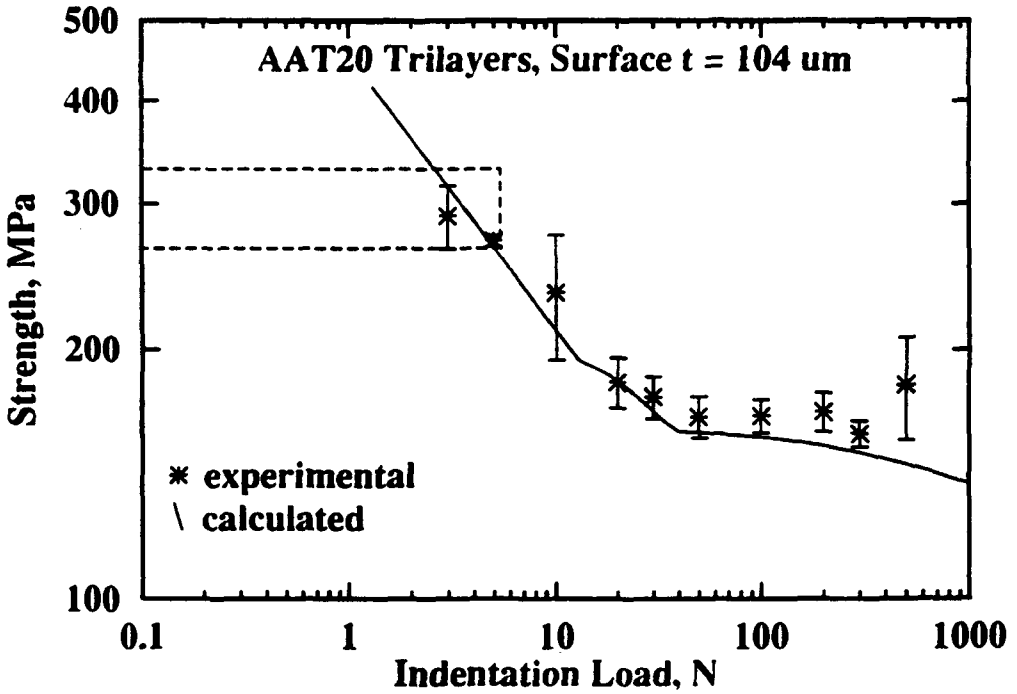

Figure V.17. Strengths predicted by the arc-forces T-curve model (solid line) for the AAT20 trilayer composites (surface thickness of 104 μm), compared to the experimentally measured values (symbols and error bars). The hatched band at left shows the strengths measured for natural flaws (i.e. unindented).

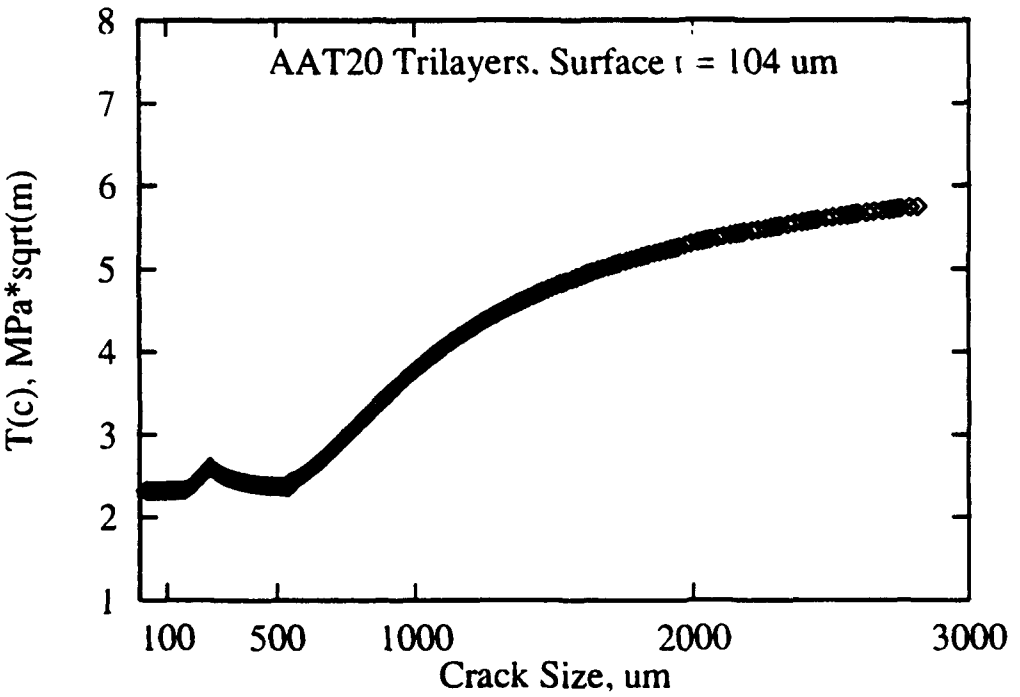

Figure V.18. T-curve for the trilayer composites defined by the best fit parameters of the base materials (Table II), using the arc-forces model. The sharp peak at 259 μm corresponds to the point at which the surface material's closure force has reached the material interface. Beyond this point, the surface layer no longer contains a half-penny shaped arc force; rather, it contains two separate, symmetrical arc forces which extend from the surface down to the interface. These surface arc-forces become smaller with increasing crack length, causing the composite T-curve to decrease until the bulk material closure force is activated at a crack size of ($t + \delta$) = 544 μm.

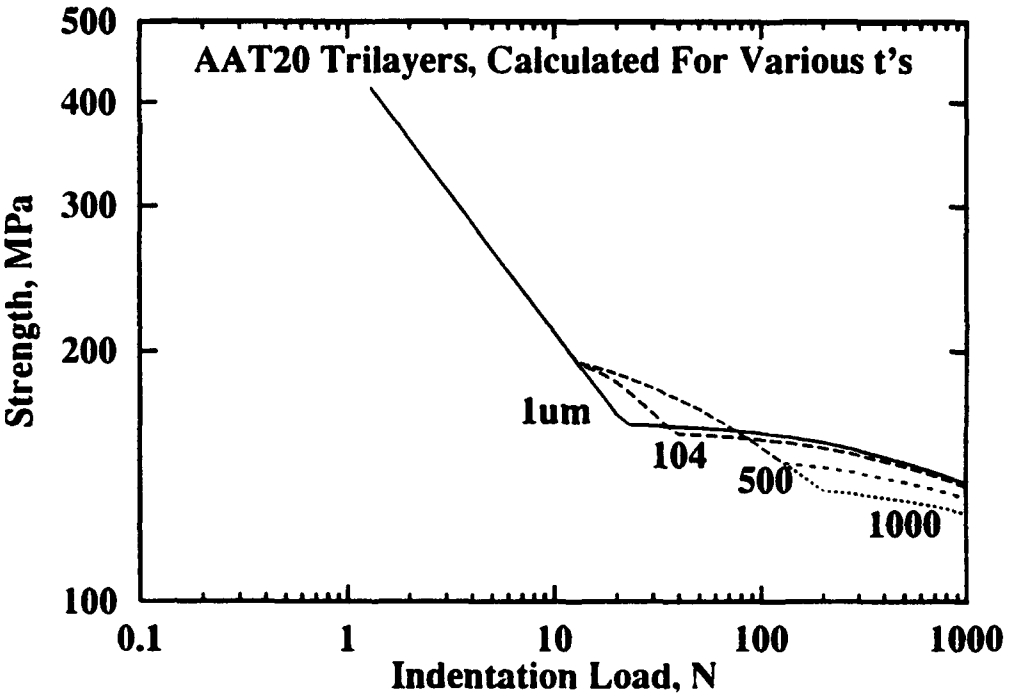

Figure V.19. Strength predictions of the arc-forces T-curve model, for a range of surface layer thicknesses, using the best fit parameters determined for the two base materials. The trends are reasonably well accounted for, and are very similar to the predictions of the linear strips model, shown in Figure V.11.

force lag distance, δ (155 μm). Thus, for the trilayer composite, the surface material closure force is allowed to extend as a full half-penny shaped arc, until that line force has reached the interface. Then, the semicircular line force pinches off into two separate, smaller arcs, symmetrically placed within the surface layer on opposite sides of the indent (see Figure V.14).

There was no real difference between the two models in their ability to pridict the crack sizes a failure, or in their ability to account for the influence of surface layer thickness on the composite strength response. The strength predictions of this model are shown in Figure V.19, for a range of surface layer thicknesses. It may be seen that the thickness trends predicted by this model are very similar to those from the linear strip model (Fig. V.11).

E. Summary

The main conclusion to be drawn from these modeling exercises is that the trilayer composite strength and toughness can be described from the T-curves of its constituent materials. Two different K-factor solutions were used to model the closure tractions exerted on the crack tip by the microstructure. Each of these K-factors was able to provide an excellent fit to the monolithic base material strength behavior; however, certain objections may be raised about the physical significance of the linear strip model, especially regarding its description of steady state crack size configurations. These objections are certainly legitimate, making this model a somewhat unsatisfactory description of the T-curve behavior of the monolithic materials (and, by extension, of the trilayer composites). However, the primary focus of this research was not to describe or investigate the physical mechanisms controlling T-curve behavior in the monolithic materials; but rather, to investigate what happens when two materials possessing different T-curve characteristics are joined together to form a laminated composite. In this regard, it is not particularly important to accurately account for the mechanisms controlling the individual material T-curves. In fact, only cursory references were made to the probable mechanism operating in

these materials (grain bridging), and these were qualitative references. For the purposes of this research, it was sufficient to observe that the effect of grain bridging is to supply a zone of closure stress, acting in the crack wake, to oppose the crack-opening stresses. This closure zone was then modeled by a constant compressive stress, and also by arc-shaped line forces.

That T-curves of the form presented here (e.g., Fig. V8) will produce the observed indentation strength behavior is indisputable - see Figures V6 and V7. The main result of this modeling section is that these individual T-curves can be then be used to define the T-curve of the trilayer composite; and the trilayer T-curve so defined is able to account for the observed strength behavior of the trilayer composites. Further modeling of the toughening mechanism responsible for the base material T-curves may result in a more acceptable description of the factors controlling crack growth, but would not provide a much better fit to the indentation strength behavior. The admittedly unrealistic linear pressure strip T-curve model presented here did nevertheless provide an excellent strength fit. This means that the true T-curve for these materials *must* look similar to the ones shown in Figures V.8 and V.16. If the trilayer T-curve is to be defined on the basis of the constituent material T-curves, then the issue of how those T-curves were obtained is not as important as their ability to describe the observed behavior. Indeed, it is interesting to note that the linear strip model produced the better fits to the strength behavior than did the arc-shaped line force model. Those better strength fits translated directly into better strength modeling of the trilayer composites, even though the linear strip model is considered a less adequate description of the crack growth in these materials than the arc model was. Eventually, the mechanisms controlling the T-curve behavior in these materials will be more accurately modeled. The work by Cook, et. al., Chantikul, et. al, Bennison and Lawn, and Padture are all solid contributions toward that goal. This section has demonstrated that those base material T-curves can then be used to define the T-curve of a laminated composite.

VI. CONCLUSIONS

1. This research has demonstrated that the trilayer design is capable of producing ceramic materials which possess both high toughness and high strength. This combination of properties was achieved *without compromising on either one*, in contrast to most other methods of producing a high strength - high toughness body. For the AAT20 system, an optimal surface layer thickness of 104 μm produced the highest possible strength levels throughout the entire range of indentation loads tested. Thinner surface layers resulted in composites displaying monolithic bulk material properties; while thicker surface layers caused the composite to behave as monolithic surface material.

2. The simplest method for estimating the optimum layer thickness was quite accurate in the AAT20 system, but the results from the zirconia system indicated that it might not be generally applicable. The zirconia system had several complicating factors, however, so it might be reasonably concluded that the simple estimation is valid for simpler ceramic systems which do not possess such complications (e.g., elastic modulus and thermal expansion mismatch between surface and bulk). The T-curve model (linear pressure strips) was no better at predicting the optimum surface layer thickness than the simple approach outlined in Section II.

3. A T-curve model, based on a crack wake containing strips of constant closure pressure, was able to account for the observed indentation strength behavior in the monolithic base materials, producing a good fit between measured and calculated strengths. A typical difference between the experimentally measured strengths and those calculated by the T-curve model was on the order of 2 - 3%.

4. An alternative T-curve model, based on a crack wake containing arc-shaped line force elements, was also able to account for the observed indentation strength behavior in the monoliths, with typical differences between measured and calculated strengths on the order of 3%. This

model was considered to be a more realistic representation of the microstructural stress intensity field, especially in regard to its ability to describe the steady state toughness behavior.

5. The T-curve model employing pressure strips was applied to the trilayer composites in two different ways, and both produced reasonable fits to the strength data, with average differences of about 4% between measured and predicted strengths. The two methods were as follows: (1) a simple model, assuming that the surface layer possessed constant toughness; and (2) a more complex model, which allowed for a surface material contribution to the T-curve. In method (2), the individual T-curves determined for the base materials were used to define the trilayer composite T-curve. The results from this method show that it is possible to model strength and toughness properties of a trilayer composite, based on the T-curves of the individual base materials. This model was able to account for the influence of surface layer thickness on the strength response, but the simpler model was unable to account for the thickness effect. This is interpreted as evidence that the surface material did in fact possess T-curve behavior on its own, and therefore contributed to the composite T-curve.

6. The T-curve model based on arc-shaped line forces was also able to provide reasonable fits to the trilayer composite strength data, with average differences of about 6% between the measured and predicted strengths. This further demonstrated the viability of defining the T-curve of a laminated composite, based on the individual T-curves of its constituent materials.

7. The trilayer concept was demonstrated to show potential for application to a system of greater strength and toughness than AAT20, based on zirconia materials. Trilayers having a surface layer thickness of about 140 μm seemed to exhibit composite strength response, when sintered for 2 hrs at 1500° C. Strength improvement for the monolithic 3Y20A surface material was achieved by sintering for an additional hour, but the trilayer composites then exhibited body material strength response. This was explained on the basis of increased transformability of the Ce-ZrO_2 bulk

material.

8. The tape casting plus lamination processing route is a very efficient and reproducible method for controlling the final layer thickness in laminated composites. Also, tape casting provides a simple and reliable means of producing inhomogeneous microstructures based on agglomerates.

VII. SUGGESTIONS FOR FUTURE WORK

(1) The zirconia trilayer system showed promise. In order to realize this system's potential, substantial improvements in processing are needed. This is particularly true for the 3Y20A material. Eliminating the interagglomerate voids should result in significant strength improvements. This may be accomplished in one of the following ways:

a.) Pre-milling of the 3Y20A powder (by ball-milling) to break down the spray dried agglomerates, followed by drying and crushing, before adding the powder to the tape casting slurry.

b.) Further adjustments in the slurry chemistry to aid in dispersing the 3Y20A powder. The dispersant and the binder-solvent system used in the 3Y20A slurries were the same as the ones used in the alumina and AAT20 slurries. There is no reason to expect the same dispersant to be effective for different materials, or even the same binders and solvents. It might be helpful to seek a (commercial) dispersant-binder-solvent system which is known to be effective in tape casting of zirconia materials.

c.) Preparation of a stock solution of 3Y20A powder dispersed in the solvents used in the slurry. The dispersion of powder in the stock solution could be achieved with an ultrasonic probe, or by ball-milling. The binder-solvent solution could then be added to this stock solution, and subsequently ball-milled to form the tape casting slurry.

d.) Further increases in the amount of excess solvent added to the slurry. This may decreases slip viscosity to a level where the normal ball-milling to mix the slurry could break down the spray dried agglomerates. The excess solvent would then be evaporated in a controlled manner, prior to casting.

(2) The alternative T-curve model described in Section V, based on an arc-shaped line force in the crack wake, should be developed further. This model is clearly more physically realistic than

the model based on linear closure strips used in this research. The model might be improved by altering the manner in which the surface material's closure force switches over from a half-penny geometry to the two separate, symmetrical arc segments. This could smooth out the sharp peak in toughness occurring at the crack size of $t + \delta_s$, and thereby improve the fit for the trilayer composites.

(3) There is an inconsistency between the P_L value determined from radial crack length measurements, and from observations of lateral crack development. Crack length measurements in the homogeneous AAT20 material yield a P_L of 2445 N, while lateral crack observations give a P_L of 40 - 200 N. The values for P_L should be similar, regardless of the method for its determination. The proper means for determining P_L should be investigated; or, perhaps, the exact influence of P_L on modifying the residual indentation stress intensity parameter, χ, should be re-evaluated. For example, Cook has suggested that a relation of the form $\chi = \chi_0/(1 + (P/P_L)^m)$ may be appropriate (for this work, the exponent, m, was simply taken to be 1).

(4) A third alternative plotting scheme should be investigated. It might be argued that the surface material strength response is entirely caused by lateral cracking effects, and that the surface material should be modeled solely on the basis of P_L and T_0. This possibility is difficult to rule out. However, when the surface material strength response is modeled in this manner, the predicted crack sizes at failure are impossibly small (that is, smaller than the known *initial* crack sizes). This could be a result of using an improper P_L, or P_L influence on χ as mentioned above. In any event, this possibility should be investigated further. Once the surface material parameters have been determined (i.e., T_0 and P_L), then the bulk material would be fitted using the T-curve parameters (e.g., b, σ_c, and c*), and then the trilayer composite T-curve would be defined. This modeling scheme is attractive for at least one reason: it employs fewer adjustable parameters.

(5) The effects on the trilayer T-curve of some of the complicating factors present in the zirconia

system should be investigated. Specifically, it should not be too difficult to incorporate any residual stresses arising from thermal expansion mismatch between the surface and interior materials, into the fracture mechanics analysis. Incorporating elastic modulus mismatch should also be investigated. In addition, any differences in T_0 might be expected to play an important role in determining the trilayer composite T-curve behavior.

APPENDIX 1: Trilayer Composite Development - Unsuccessful Attempts

This appendix will describe some of the early attempts at producing trilayer composites. In some of the systems, composites were successfully fabricated, but composite strength behavior was not observed. In other systems, trilayer composites were never successfully processed. For each case, a brief explanation of the problems encountered will be offered.

A. Coarse/Fine Alumina Composites

The original motivation for this project derived from work by B. R. Lawn, *et. al.* at NIST, as well as work by earlier researchers such as Gutshall and Gross, which demonstrated the effect of grain size on the strength, toughness, and flaw tolerance of alumina. Based on their work, it was hypothesized that if a coarse-grained alumina body could be fabricated with a fine-grained surface region, the best strength properties of the two materials might be transferred to the new, composite body. Various strategies for producing such a coarse/fine alumina material were pursued.

Since different grain sizes are produced in pure alumina by using different firing schedules, it was necessary to introduce some impurity in order to control the grain size in the surface layer. Previous experience at Lehigh had indicated that solid solution dopants often simply diffuse throughout the body (resulting in uniform grain structure); so it was decided that grain size would be controlled with the use of second phase particles. Cubic zirconia was selected. Since cubic zirconia is not a reinforcing phase for alumina, it was necessary to use as little as possible in order to maintain high strength in the surface material. Also, by using a small amount, thermal and elastic mismatch between surface and bulk materials could be minimized. An amount of 5 vol% was chosen.

Laminated composites, consisting of alternating ~250 μm layers of undoped and 5 vol% ZrO_2-doped alumina (AZ5) were sintered at 1675°C for 30 hrs, in air. Resulting grain sizes were

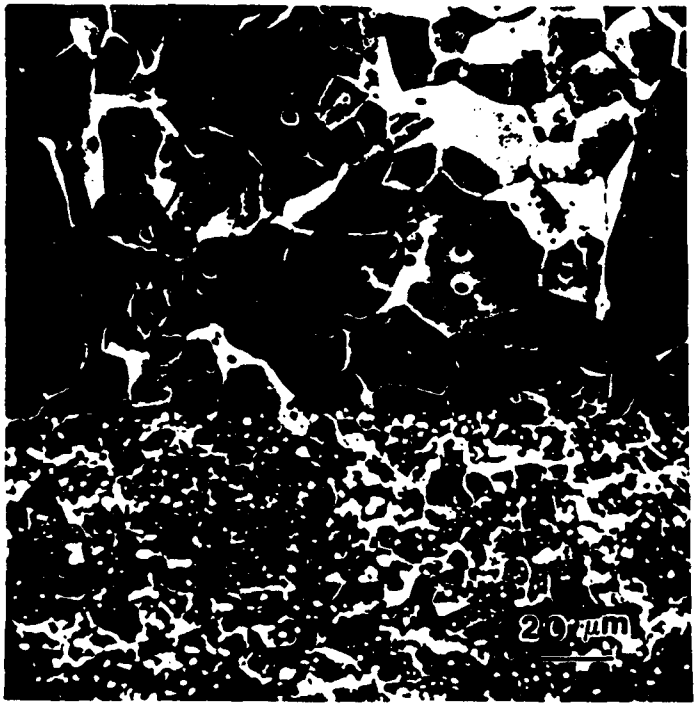

Figure A1. Fracture surface of a laminated alumina composite, showing the interface between the coarse-grained, undoped alumina layer (top), and the fine-grained, Al_2O_3 + 5vol% ZrO_2 layer (bottom). Sample was sintered in air at 1675° C. for 30 hrs.

20 and 8 μm, respectively, and interfaces between the two regions were well controlled (see Fig. A1). Samples having the coarse grains on the surface exhibited the same indentation strength as the monolithic coarse grained alumina; and the composites having the AZ5 on the surface exhibited the same strengths as the monolithic alumina of the same grain size. No composite strength behavior was observed. There are two reasons for this. First of all, the layer thickness was most likely too large. Secondly, the grain size difference was not large enough, and therefore the possible difference in strengths was not great enough to be experimentally detected in the composites (see, for example, Chantikul, *et. al.* 1990). Even if the grain size difference could be increased, which is unlikely (considering the sintering trade-offs involved), the strength differences in the large flaw region would still be small, making experimental detection of composite strength response difficult. In short, this was not a model laminated composite system.

B. Alumina/AAT20 Composites

Padture and Bennison each showed that inhomogeneous alumina - aluminum titanate materials displayed even better flaw tolerance than pure, coarse-grained alumina. The focus of the laminated composite effort consequently changed to the production of a bulk AAT20 material having a fine grained, high strength alumina surface layer. Such a material was never successfully produced, primarily because of interdiffusion problems. In order to obtain the fine grained alumina layer, four different strategies were employed:

1. AZ5. The first attempts were made using AZ5 as the surface material. The typical 1600° C/ 1 hr sintering run needed to produce the best flaw tolerance in the AAT20 material, resulted in an interfacial reaction between the surface and bulk. This reaction caused the zirconia particles to disappear from a region within about 20 μm of the interface. This region was left in a much more porous condition than the surrounding areas. The alumina grain size throughout the surface layer, and especially in the reaction zone, was considerably larger than would be expected

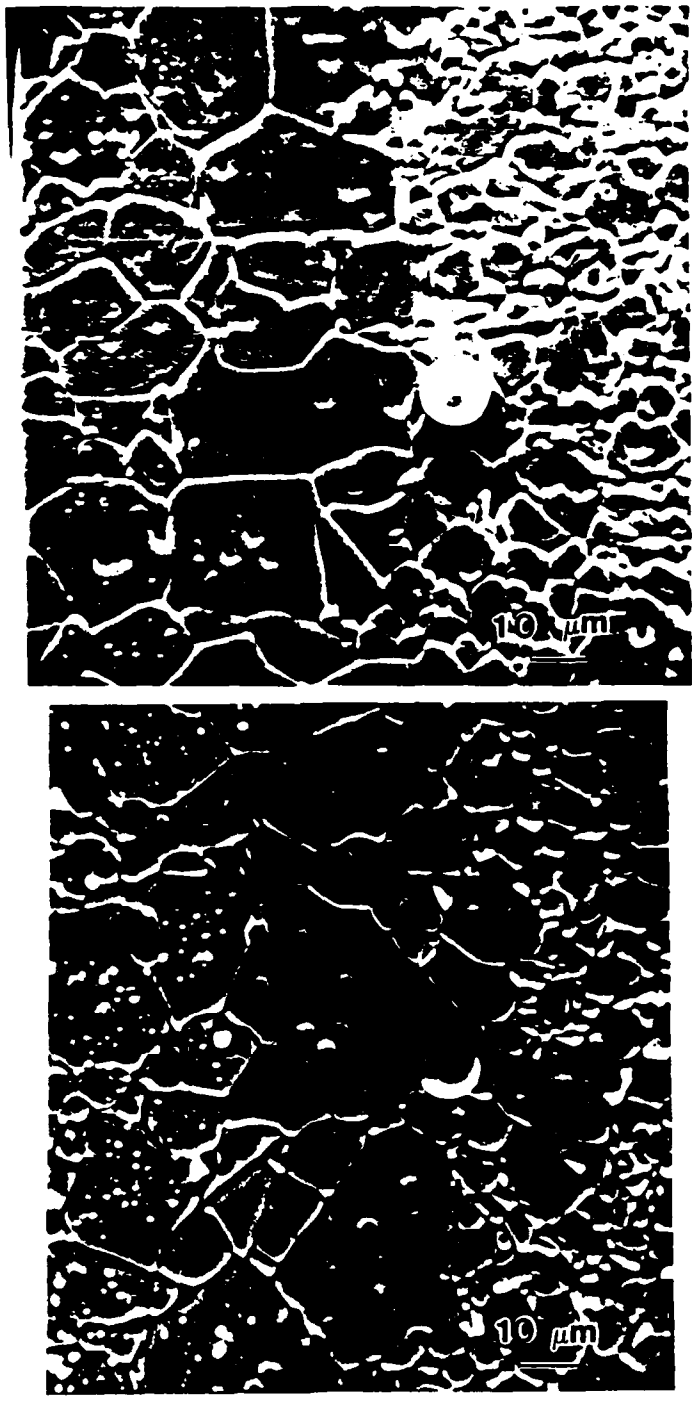

Figure A2. Secondary electron (top) and backscattered electron (bottom) micrographs from different areas of the polished cross-section of a trilayer composite, showing the interfacial region between the AXT20 bulk (right), and the AZ5 surface layer (left). The original, as-fired, free surface is at the left edge of the image. Note the reaction zone of about 20 μm width at the interface, containing increased porosity and a complete absence of zirconia particles. [The blob in the center is a latex calibration sphere (10.3 μm diameter).]

for that sintering schedule. Also, the zirconia particles were more likely to be found *within* the alumina grains, rather than at the grain boundaries, as desired. Figure A2 shows the polished cross-section of the interfacial region. It was possible to prevent the reaction from occurring by firing at reduced temperatures (e.g. 1500° C); however, the body material then lost its coarseness and consequently its flaw tolerance. When longer sintering times at the lower temperature were used in order to regain the flaw tolerance of the body material, then the surface material reverted back into its original, coarse and porous condition. AZ5 was abandoned as a surface material.

2. 500 ppm MgO-doped alumina. Work by various researchers on MgO-doped alumina has indicated that MgO is sometimes able to counteract the effects of other impurities which would otherwise produce coarsening or abnormal grain growth in alumina

. It was thought that the reaction described above might possibly have been caused by diffusion of impurities from the AAT20 bulk, and that those impurities might have produced a liquid phase at the sintering temperature. Titanium, calcium, and silicon were detected (by EDS) throughout the AZ5 surface layers (the Al_2TiO_5 was only '99+%' pure). Thus, new composites were fabricated with a 500 ppm MgO-doped alumina surface layer. This resulted in an even worse surface material, after sintering at 1600° C for 1 hr. The surface layer was characterized by a large number density of huge, elongated grains, distributed throughout, as shown in Figures A3 and A4. This microstructure was likely caused by diffusion of the various impurities into the surface, from the AAT20 interior. Attempts to eliminate this problem followed a strategy similar to the one outlined above for the AZ5 reaction problem, and met with similar results. 500 ppm MgO-doped alumina was also abandoned as a surface material.

3. 3 wt% Mgo-doped alumina. It was hoped that perhaps 500 ppm of MgO was simply not enough, and that by flooding the alumina surface material with MgO, the effect of the other impurities could be suppressed. This strategy was also unsuccessful. Problems were encountered

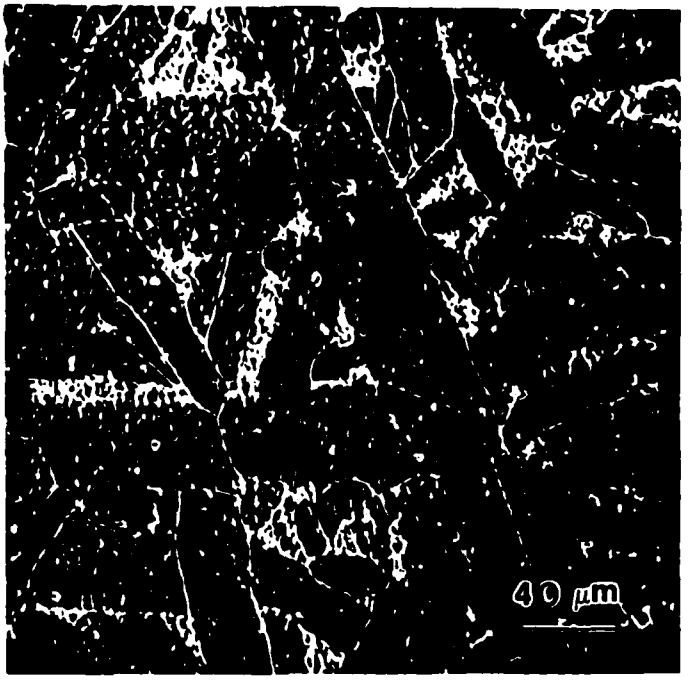

Figure A3. SEM micrograph showing as-fired surface of trilayer composite which had a surface layer of (originally) 500 ppm MgO-doped alumina, on an AAT20 bulk

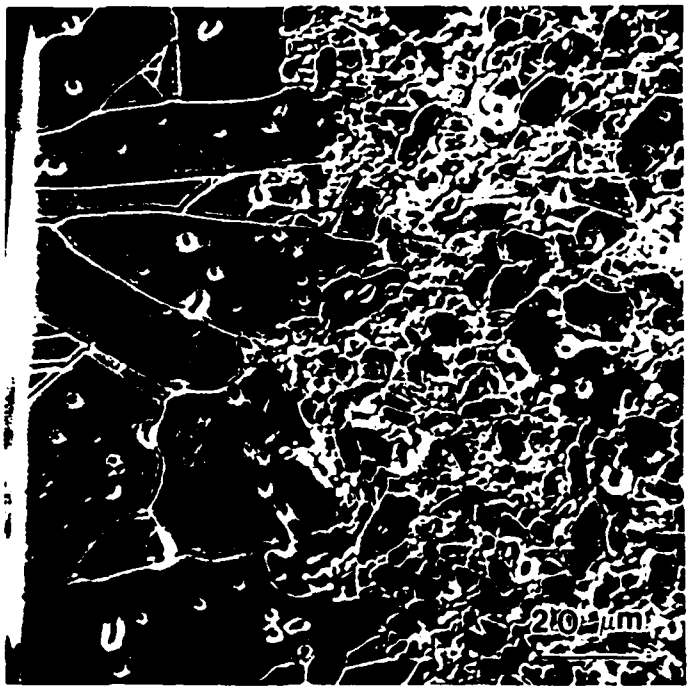

Figure A4. SEM micrograph showing polished and thermally etched cross-section of the same type of sample shown in A3, above. 500 ppm MgO-doped alumina layer at left; AAT20 at right.

in successfully tape casting the 3 wt% MgO-doped alumina powder. Fired samples from the most successful tape (which was not a good tape) contained extensive blistering and cracking defects. The as fired surface showed the same elongated grain structures as the 500 ppm samples did, for surface layer thicknesses of 40 μm and 70 μm. A thicker surface layer (about 200-300μm) exhibited a fine-grained microstructure on the as-fired surface, and also contained second phase particles (probably spinel). The cross-sections of these samples were never examined. No further work was carried out using 3 wt% MgO-doped alumina.

4. In a final attempt to produce the desired microstructure, a composite was fabricated with an undoped alumina surface layer, and sintered at 1600° C for 1 hr, just to see whether an absence of dopants would be more successful. It was not. The same, elongated grain structure was observed.

APPENDIX 2: FORTRAN COMPUTER CODES

This appendix presents the FORTRAN codes developed for the computer modeling. Included here are the codes for six programs:

1. The program used to determine the hardness values, based on measurements of the indentation impression diagonals;

2. The program used to determine P_L, the indent load at which the lateral cracking influence becomes significant, based on radial crack length measurements;

3. The program which modeled the T-curve based on linear strips of constant closure pressure, which was used for the monolithic AAT20 materials, as well as for the simplest method of modeling the trilayer composites (methods 1 and 2 of Section V-C);

4. The program which modeled trilayer behavior, based on the best fit parameters of the two monolithic base materials, using the linear strips model.

5. The program used in modeling T-curve behavior in the monoliths, using the arc-shaped line force model.

6. The program used to model trilayer composite behavior, using the best fit parameters from the two base materials, using program 5, above.

```
      PROGRAM HARDNESS
      real p(12),a(12),xa(12),var(120),xh,xan(12)
      print *,'how many indents did you measure?'
      read *,np
      print *,'do you want to run the whole program(1),'
      print *,'or do you just want final results(2)?'
      read *,ians
      sum1 = 0.
      do 10 j = 1,np
          print *,'enter indent load in N'
          read *,p(j)
          if(ians .eq. 1)then
          print *,'enter measured half-diagonal, a, in microns'
          read *,xa(j)
          print *,'how many measurements for that P?'
          read *,xan(j)
          sum1 = sum1 + xan(j)
          endif
   10 continue
      varmax = 10000000.
      sum = 0.
      print *,'enter minimum hardness, in GPa'
      read *,xhlow
      print *,'enter max hardness, in GPa'
      read *,xhhi
      print *,'enter hardness step size, in GPa'
      read *,xhstep
      do 2 x = xhlow,xhhi,xhstep
          if(x .eq. xhlow)then
              i = 1
          else
              i = i + 1
          endif
          xh = x*1.e9
          do 1 n = 1,np
              a(n) = (p(n)/(2.*xh))**(1./2.)
              a(n) = a(n)*1.e6
              if(ians .eq. 1)then
                  diff = a(n)-xa(n)
                  resid = (diff**2)*xan(n)/sum1
                  sum = sum + resid
                  write(*,31)xa(n),a(n),diff
   31              format(2x,f5.2,2x,f6.2,2x,f7.2)
              else
                  write(*,32)p(n),a(n)
   32              format(2x,f4.0,2x,f6.2)
              endif
    1 continue
```

```
  if(ians .eq. 1)then
  var(i) = sum/(np-1)
  if(var(i) .lt. varmax)then
      varmax = var(i)
      besth = xh*1.e-9
      varbest = var(i)
  endif
  write(*,33)var(i),varbest
33 format(2x,'variance for this set=',f8.2,/,2x,'varbest=',f8.2,/)
  sum = 0.
  endif
 2 continue
  print *,'hardness = ',besth,' GPa'
  print *,'the variance was ',varbest
  stop
  end
```

```
      Program PLCL
C+ This program determines a value for PL, the indent load at which
C+ the lateral cracking influence becomes important, based on the
C+ input data of radial crack size vs. indent load.  PL is determined
C+ by iterative manipulation of equations 5 and 6 in Cook, et. al.,
C+ J.Am.Ceram.Soc. 73 [7], 1873-78 (1990).
      real cl(100),pl(100),var(100),p(10),xco(10),co(10),xnco(10),pllow,
     +     plhi,plstep
      integer q,qq,np,i,ncl,npl,n,ians
      open(37,file='pl.dat')
      rewind 37
      print *,'how many indent loads did you measure cracks for?'
      read *,np
      print *,'do you want to run the whole program (1),'
      print *,'or do you just want the final results (2)?'
      read *,ians
      sum1 = 0.
      do 10 i = 1,np
          print *,'enter indent load in N'
          read *,p(i)
          if(ians .eq. 1)then
      print *,'enter average crack length measured for that P (in um)'
          read *,xco(i)
          print *,'how many cracks were measured for that P?'
          read *,xnco(i)
          sum1 = sum1 + xnco(i)
          endif
   10 continue
      print *,'enter Xo'
      read *,xo
   50 print *,'enter minimum PL'
      read *,pllow
      print *,'enter max PL'
      read *,plhi
      print *,'enter PL step size'
      read *,plstep
      Q = (plhi-pllow)/plstep
      if(q .ge. 100)then
          print *,'Too many PLs -- redefine limits and/or'
          print *,'step size so that there are no more than 100 PLs'
          go to 50
      endif
   51 print *,'enter minimum CL (in um) [CL is the crack length'
      print *,'produced by indent of load PL, in absence of'
      print *,'lateral cracking influence.]'
      read *,cllow
      print *,'enter max CL'
      read *,clhi
```

```
      print *,'enter CL step size'
      read *,clstep
      QQ = (clhi-cllow)/clstep
      if(qq .ge. 100)then
          print *,'Too many CLs -- redefine CL limits and/or '
          print *,'step size so that there are no more than 100 CLs'
          go to 51
      endif
      varmax = 10000000.
      varbest = 10000000.
      sum = 0.
      do 3 xpl = pllow,plhi,plstep
          if(xpl .eq. pllow)then
              npl = 1
          else
              npl = npl + 1
          endif
          pl(npl) = xpl
          print *,'----------------------------------PL=',xpl,'----'
          do 2 xcl = cllow, clhi, clstep
              if(xcl .eq. cllow)then
                  ncl = 1
              else
                  ncl = ncl + 1
              endif
              cl(ncl) = xcl*1.e-6
              do 1 n = 1,np
              term1 = p(n)/pl(npl)
              co(n) = cl(ncl)*(term1/(1. + term1))**(2./3.)
              co(n) = co(n)*1.e6
              if(ians .eq. 1)then
                  diff = co(n)-xco(n)
                  resid = (diff**2)*xnco(n)/sum1
                  sum = sum + resid
                  if(n .lt. np)then
                      varnce = sum/(np-1)
                      if(varnce .gt. varbest)go to 100
                  endif
                  x = xco(n)
                  y = co(n)
                  write(*,31)x,y,diff
31                 format(2x,f6.1,2x,f6.1,2x,f7.2)
              else
                  write(*,33)p(n),co(n)
                  write(37,33)p(n),co(n)
33                 format(2x,f4.0,2x,f6.1)
              endif
1             continue
```

```
      if(ians .eq. 1)then
          var(ncl) = sum/(np-1)
          if(var(ncl) .lt. varmax)then
              varmax=var(ncl)
              bestcl = xcl
              bestpl = xpl
              varbest = var(ncl)
          endif
          write(*,32)var(ncl),varbest
32    format(2x,'variance for this set =',f8.2,/,'varbest =',f8.2,/)
      endif
100 if(n .lt. np)then
      write(*,34)varnce,varbest
34     format(2x,'variance(',f7.2,') already greater than varbest
     +    (',F7.2,')',/)
      print *,'loop terminated after',n,'increments'
    endif
      sum = 0.
2     continue
3 continue
    print *,'best CL = ',bestcl
    print *,'best PL = ',bestpl
    print *,'the variance was ',varbest
    write(37,*)'best CL = ',bestcl
    write(37,*)'best PL = ',bestpl
    bestcl = bestcl*1.e-6
    t = xo*bestpl/(bestcl)**1.5
    t=t*1.e-6
    print *,'this combination of PL & CL predicts T = ',t,' MPa/m'
    write(37,*)'this combo of PL & CL predicts T = ',t,' MPa/m'
    stop
    end
```

```
      Program Tcurve10
C+ LINEAR STRIPS OF CONSTANT CLOSURE PRESSURE.
C+ This program allows the user to enter up to twenty experimentally
C+ measured strength-indent load pairs, and then will calculate T(c)
C+ curves, use these to calculate strength values, and then compare the
C+ calculated and the measured strengths. The program contains six do
C+ loops. The inner one increments crack size (logarithmically), calc-
C+ ulates a trial T-curve, calculates stress-crack size, and labels the
C+ maximum s-c value as the strength. The second loop increments indent
C+ load, so that you get a strength calculated for each indent load
C+ for which you entered an experimentally measured value. This loop
C+ also keeps track of the sum of the squares of the differences
C+ between calculated and measured strengths. The next loop increments
C+ To. Also,this loop calculates the variance for each set of strength-
C+ indent load values, determines the minimum variance, and then
C+ labels the best values for To, closure pressure, & closure pressure
C+ depth. The variance calculation is weighted towards indent loads
C+ which have the most data. The next loop increments closure pressure.
C+ The next loop increments closure pressure depth. The outermost loop
C+ increments steady state crack size. This program allows the user to
C+ specify the increment size for each do loop. The user will be asked
C+ to input a PL value, which is used to modify the X term to account
C+ for lateral cracking. The user may choose the program's output. The
C+ choices are:(1) a table of measured and calculated strengths, the
C+ difference between them, and the variance for the set, for EACH set
C+ of adjustable parameters, (printed to the screen) and at the end, a
C+ printout of the minimum variance, best To, b, cp, and c*; (2) just
C+ the final results of the program, i.e., the best fit parameters, and
C+ a table of calculated strengths and critical crack sizes determined
C+ by those best fit parameters. Also, the user decides whether to
C+ write a data file containing c, c**1/2, Km, T(c), and stress(c), for
C+ each indent load. This data file should only be created when the
C+ adjustable parameters are entered as CONSTANTS, or else the data
C+ file will be really HUGE. The program can take a while to run
C+ (depends on step sizes).
      real s(115),c(115),to,p(20),x,psi,smax(20),cf(20),cc,term1,
     + term2,xx,cp,b,d,km(115),tc(115),kmcf,tccf,sigp(20),sum,var(150),
     + minvar,sum1,sigps(20),cstar,cstarlo,cstarhi,cstars,cs,pl
      integer ns,ii,ntt,nip,np
C+ Definition of Variables:
C+  s = stress; there is one stress value calculated for each
C+      crack size increment.
C+  c = crack size; incremented in steps of 0.05 power of ten
C+  to = base line toughness value, in Pa*sqrt(m)
C+  xo = constant in the residual stress intensity field, incorporating
C+     the hardness and Young's modulus, but no lateral crack influence
C+  p = indentation load, in N
C+  psi = geometry constant in the applied K field
```

```
C+  smax = maximum calculated stress value, identified as the strength
C+  cf = crack size corresponding to smax
C+  cc = do loop dummy variable used to increment crack size
C+  term1 = part of the microstructural K field term
C+  term2 = another part of the microstructural K field term
C+  xx = dummy variable used in incrementing crack size
C+  cp = constant closure pressure in the microstructural K term
C+  b = depth at which the closure pressure becomes activated
C+  cstar = steady state crack size
C+  d = length of crack wake over which cp acts(=c-b)
C+  km = microstructural stress intensity field
C+  tc = the toughness curve, T(c) = To - Km(c)
C+  ns = used to convert cc into an integer, which is then used
C+       as the term number of the array variables [s(ns), tc(ns),
C+       and km(ns)]
C+  sigp = experimentally measured strength
C+  sigps = number of experimentally measured strengths for given P
C+  sum = sum of squares of calculated - measured strength
C+  sum1 = total number of strengths measured, for all P
C+  var(ntt)= variance for present strength-indent load set = sum/(np-1)
C+  np = number of strength-indent load pairs
C+  minvar = minimum variance
C+  cplow, cphi = low and high range for closure pressure
C+  tolow, tohi = low and high range for To
C+  cstarlo, cstarhi = low and high range for cstar
C+  blow,bhi = low and high range for closure pressure depth
C+  cpstep,bstep,tostep = step sizes for do loops
C+  PL = indent load at which lateral crack influence becomes important
C+--------------------------------------------------------------------
      open(37,file='tc10.dat')
      rewind 37
      write(5,*)'how many measured strengths are there?'
      read *,np
      sum1 = 0.
      do 10 ii = 1,np
         write(5,*)'indent load = (N)?'
         read *,p(ii)
         write(6,*)'indent load = ',p(ii)
         write(5,*)'measured strength for that P = (in MPa)?'
         read *,sigp(ii)
         write(6,*)'average measured strength was ',sigp(ii)
         write(5,*)'# of samples tested for that P = ?'
         read *,sigps(ii)
         write(6,*)'# of samples for that P = ',sigps(ii)
         sum1 = sum1 + sigps(ii)
   10 continue
      write(5,*)'input parameters -- Xo = ?'
      read *,xo
```

```
      write(6,*)'Xo = ',xo
      print *,'enter psi'
      read *,psi
      write(5,*)' minumum To = (in MPa*sqrt(m)) ?'
      read *,tolow
      write(6,*)'min To = ',tolow
      write(5,*)'maximum To = ?'
      read *,tohi
      write(6,*)'max To = ',tohi
      write(5,*)'increment size for To = (in MPa*sqrt(m))?'
      read *,tostep
      write(6,*)'To step size = ',tostep
      write(5,*)'minimum constant closure pressure = (in MPa) ?'
      read *,cplow
      write(6,*)'minimum constant closure pressure = ',cplow
      write(5,*)'maximum closure pressure = ?'
      read *,cphi
      write(6,*)'max cp = ',cphi
      write(5,*)'CP step size = (in MPa)?'
      read *,cpstep
      write(6,*)'cp step size = ',cpstep
      write(5,*)'minimum closure pressure depth = (in microns) ?'
      read *,blow
      write(6,*)'min closure pressure depth = ',blow
      write(5,*)'max closure pressure depth = ?'
      read *,bhi
      write(5,*)'max closure pressure depth = ?',bhi
      write(5,*)'cp depth step size = (in microns)?'
      read *,bstep
      write(6,*)'b step size = ',bstep
      write(5,*)'enter PL  =  (in N)'
      read *,pl
      print *,'enter minimum steady state crack size, in um'
      read *,cstarlo
      print *,'enter max steady state crack size'
      read *,cstarhi
      print *,'enter steady state crack size step size, in um'
      read *,cstars
C+ Define constant terms:
      print *,'want to enter a minvar from a previous run?(1=Y,2=N)'
      read *,ians
      if(ians .eq. 1)then
          print *,'enter minvar'
          read *,minvar
      else
          minvar = 1000000.
      endif
      print *,'want to see all values (1), or just end results(2)?'
```

```
      read *,iprint
      print *,'Want to create data file tc10dat.all, containing ALL'
      print *,' values of c, sqrt(c), kms, tc, and stress ?1-Y,2-N'
      read *,idata
      if(idata .eq. 1)then
        open(70,file='tc10dat.all')
        rewind 70
      endif
      write(*,31)
   31 Format(2x,' measured ',2x,'calculated',2x,'difference')
      do 7 cs = cstarlo, cstarhi, cstars
          print *,'============>CSTAR = ',CS
          cstar = cs*1.e-6
C++++++++++++++++++++++++++++++++++++++++++++++++++++++++++++++++++++++++++++++
C+ Closure pressure depth loop:
C++++++++++++++++++++++++++++++++++++++++++++++++++++++++++++++++++++++++++++++
      do 5 bb = blow, bhi, bstep
          write(6,32)bb
   32      format(2x,50('-'),'b= ',f4.0,10('-'))
          b = bb*1.e-6
C+  ------------------------------------------------------------------
C+ Closure pressure loop:
C+  ------------------------------------------------------------------
      do 4 ccp = cplow,cphi,cpstep
          if(iprint .eq. 1)then
            write(6,33)ccp
   33       format(2x,35('-'),'cp= ',f4.0,10('-'))
          else
            print *,'+'
          endif
          cp = ccp*1.e6
          if(ccp .eq. cplow)then
              ncp = 1
          else
              ncp = ncp + 1
          endif
C+ ..................................................................
C+ To loop:
C+ ..................................................................
      do 3 tt = tolow,tohi,tostep
          to = tt*1.e6
          if(tt .eq. tolow)then
              ntt = 1
          else
              ntt = ntt + 1
          endif
C+ - - - - - - - - - - - - - - - - - - - - - - - - - - - - - - - - - -
C+ Indentation load loop:
```

```
C+ - - - - - - - - - - - - - - - - - - - - - - - - - - - - - - - - - - - - - -
      do 2 nip = 1,np
         x = xo/(1.+p(nip)/pl)
         co = ((x*p(nip))/to)**(2./3.)
         co = co*1.e6
         co = log10(co)
         smaxi=-1.e7
C+ ********************************************************************
C+ Inner loop for stress, T-curve calculations:
C+ ********************************************************************
      do 1 cc = co,3.45, 0.025
         if(cc .eq. co)then
            ns = 1
         else
            ns = ns + 1
         endif
         xx = 10.**cc
         c(ns) = (1.e-6)*xx
         d = c(ns) - b
         if(c(ns) .le. b)then
            km(ns) = 0.
         elseif(c(ns) .gt. b .and. c(ns) .lt. cstar)then
            term1 = 2.*((b/c(ns)) + (d/c(ns)))**(1./2.)
            term2 = -2.*(b/c(ns))**(1./2.) - (d/c(ns))
            km(ns) = -psi*cp*sqrt(c(ns))*(term1+term2)
         else
            km(ns) = -psi*cp*sqrt(cstar)*(1.-2.*(b/cstar)**(1./2.)
     +                  +(b/cstar))
         endif
         tc(ns) = to - km(ns)
         s(ns) = (tc(ns)-x*p(nip)/c(ns)**1.5)/(psi*sqrt(c(ns)))
         if(idata .eq. 1)then
           write(70,40)p(nip),c(ns)*1.e6,sqrt(c(ns)*1.e6),km(ns)
     +              *1.e-6,tc(ns)*1.e-6,s(ns)*1.e-6
   40      format(2x,f4.0,2x,f6.1,2x,f6.2,2(2x,f6.3),2x,f7.2)
         endif
         if(s(ns) .gt. smaxi)then
            smaxi=s(ns)
            smax(nip) = s(ns)*1.e-6
            cf(nip) = c(ns)*1.e6
            kmcf = km(ns)
            tccf = tc(ns)
         endif
    1 continue
C+ ********************************************************************
      resid = (smax(nip) - sigp(nip))
      if(iprint .eq. 1)then
        write(6,34) sigp(nip), smax(nip), resid
```

```
 34    Format(2x,e10.4,2x,e10.4,2x,e10.4)
       endif
       if(nip .eq. 1)then
           sum = ((smax(1) - sigp(1))**2)*sigps(1)/sum1
       else
           sum = sum + ((smax(nip) - sigp(nip))**2)*sigps(nip)/sum1
       endif
       if(nip .lt. np)then
           varnce = sum/(np-1)
           if(varnce .gt. minvar)go to 100
       endif
    2 continue
C+ - - - - - - - - - - - - - - - - - - - - - - - - - - - - - - - - - - - - -
       var(ntt) = sum/(np-1)
       if(var(ntt) .lt. minvar)then
           minvar = var(ntt)
           tobest = to*1.e-6
           cpbest = cp*1.e-6
           bestb = b*1.e6
           bestcs = cstar*1.e6
       endif
       if(iprint .eq. 1)then
         write(6,35)var(ntt),minvar
   35    format(2x,'variance for this set = ',f7.2,/,2x,'minvar= ',
     +   f7.2,/)
       endif
  100 if(nip .lt. np)then
         if(iprint .eq. 1)then
           write(6,36)varnce,minvar,nip
   36 format(2x,'variance( ',f6.2,') already greater than minvar( ',
     +f6.2,')',/,2x,'loop terminated after ',i2,' increments',/)
         endif
       endif
    3 continue
    4 continue
    5 continue
    7 continue
       do 8 j=1,np
         write(6,41)p(j),smax(j),cf(j)
         write(37,41)p(j),smax(j),cf(j)
   41    format(2x,f5.0,2x,f8.2,2x,f8.2)
    8 continue
       write(6,*)'best b = ',bestb
       write(6,*)'best To = ',tobest
       write(6,*)'best cp = ',cpbest
       write(6,*)'best cstar = ',bestcs
       write(6,*)'with a minimum variance of ', minvar
       write(37,*)'best b = ',bestb
```

```
write(37,*)'best To = ',tobest
write(37,*)'best cp = ',cpbest
write(37,*)'best cstar = ',bestcs
write(37,*)'minvar = ',minvar
stop
end
```

```
      Program Tcurve9
c+ This program is designed for trilayer composites.  It uses the same
C+ basic stress intensity factor solution for Kin as the previous 8
c+ programs, but now I define several different crack size domains, for
c+ which the actual form of Kin is slightly different, reflecting the
c+ different materials the crack is sampling.  For this program, the
c+ user inputs the best fit parameters found from Tcurve10 for the two
c+ base materials - i.e., To, CP,  b, and c*.
C+-------------------------------------------------------------------
      real s(115),c(115),to,p(20),x,psi,sigmax(20),cf(20),cc,term1,
     + term2,xx,cp,b,d,km(115),tc(115),kmcf,tccf,sigp(20),sum,var(150),
     + sum1,sigps(20),kms(115),kmb(115),cstars,cstarb,minvar
      integer ns,ii,nip,np,nth
C+-------------------------------------------------------------------
      open(38,file='tc9.d')
      rewind 38
      write(5,*)'how many measured strengths are there?'
      read *,np
      sum1 = 0.
      do 10 ii = 1,np
          write(5,*)'indent load = (N)?'
          read *,p(ii)
          write(6,*)'indent load = ',p(ii)
          write(5,*)'measured strength for that P = (in MPa)?'
          read *,sigp(ii)
          write(6,*)'average measured strength was ',sigp(ii)
          write(5,*)'# of samples tested for that P = ?'
          read *,sigps(ii)
          write(6,*)'# of samples for that P = ',sigps(ii)
          sum1 = sum1 + sigps(ii)
   10 continue
      write(5,*)'input parameters -- Xo = ?'
      read *,xo
      write(6,*)'Xo = ',xo
      print *,'enter psi'
      read *,psi
      write(5,*)' surface To = (in MPa*sqrt(m)) ?'
      read *,tos
      write(6,*)'surface To = ',tos
      write(5,*)'bulk To = ?'
      read *,tob
      write(6,*)'bulk To = ',tob
      write(5,*)'surface constant closure pressure = (in MPa) ?'
      read *,cps
      write(6,*)'surface constant closure pressure = ',cps
      write(5,*)'bulk closure pressure = ?'
      read *,cpb
      write(6,*)'bulk cp = ',cpb
```

```
      write(5,*)'surface closure pressure depth = (in microns) ?'
      read *,bs
      write(6,*)'surface closure pressure depth = ',bs
      write(5,*)'bulk closure pressure depth = ?'
      read *,bb
      write(5,*)'bulk closure pressure depth = ?',bb
      write(5,*)'enter PL  =  (in N)'
      read *,pl
      write(5,*)'surf. material steady state crack size = (um)'
      read *,cstars
      print *,'enter bulk cstar in microns'
      read *,cstarb
      write(5,*)'enter minimum surface layer thickness in microns --'
      write(5,*)'DO NOT ENTER A thickness LESS THAN bs !!'
      read *,thlow
      write(5,*)'enter max surface layer thickness in microns'
      read *,thhi
      write(5,*)'enter thickness step size, in microns'
      read *,thstep
      print *,'want to create data file tc9dat.all, containing all '
      print *,'p, c, c**1/2, km, tc, stress values? It will be a '
      print *,' HUGE, HUGE file unless you are only computing a '
      print *,' few thicknesses.  1=yes, 2=no'
      read *,nans
      if(nans .eq. 1)then
        open(37,file='tc9dat.all')
        rewind 37
      endif
C+ Define constant terms:
      minvar = 1000000.
      tos = tos*1.e6
      tob = tob*1.e6
      cps = cps*1.e6
      cpb = cpb*1.e6
      bs = bs*1.e-6
      bb = bb*1.e-6
      cstars = cstars*1.e-6
      cstarb = cstarb*1.e-6
      write(*,31)
 31   Format(2x,'  P  ',2x,'calculated',2x,'  Cf')
      do 111 th = thlow, thhi, thstep
        if(th .eq. thlow)then
          nth = 1
        else
          nth = nth + 1
        endif
        t = th
        t = t*1.e-6
```

```
      if(bs .ge. t)then
          bb=bb+t
          cstarb=cstarb+t
          go to 100
      endif
      print *,'---------- t = ',th,' ----------'
      write(38,301)th
  301 format(1x,'---------- t = ',f4.0,' ----------')
C+ - - - - - - - - - - - - - - - - - - - - - - - - - - - - - - - - - -
C+ Indentation load loop:
C+ - - - - - - - - - - - - - - - - - - - - - - - - - - - - - - - - - -
      sum = 0.
      do 2 nip = 1,np
          x = xo/(1.+p(nip)/pl)
          co = ((x*p(nip))/tos)**(2./3.)
          co = co*1.e6
          co = log10(co)
          smax = -1.e7
C+ ************************************************************************
C+ Inner loop for stress, T-curve calculations:
C+ ************************************************************************
      do 1 cc = co,3.45, 0.025
          if(cc .eq. co)then
              ns = 1
          else
              ns = ns + 1
          endif
          xx = 10.**cc
          c(ns) = (1.e-6)*xx
          ds = c(ns) - bs
          if(c(ns) .lt. bs)then
              kms(ns)=0.
              kmb(ns)=0.
              km(ns) = 0.
          elseif(c(ns) .ge. bs .and. c(ns) .le. t)then
              term1 = 2.*((bs/c(ns)) + (ds/c(ns)))**(1./2.)
              term2 = -2.*(bs/c(ns))**(1./2.) - (ds/c(ns))
              kms(ns) = -psi*cps*sqrt(c(ns))*(term1+term2)
              kmb(ns)=0.
              km(ns)=kms(ns)+kmb(ns)
          elseif(c(ns) .gt. t .and. c(ns) .le. (t+bb))then
              term1 = 2.*(t/c(ns))**(1./2.) - (t/c(ns))
              term2 = -2.*(bs/c(ns))**(1./2.) +(bs/c(ns))
              kms(ns) = -psi*cps*sqrt(c(ns))*(term1 +term2)
              kmb(ns)=0.
              km(ns) = kms(ns)+kmb(ns)
          elseif(c(ns) .gt. (t+bb) .and. c(ns) .le. cstars)then
              term1 = 2.*(t/c(ns))**(1./2.) - (t/c(ns))
```

```
            term2 = -2.*(bs/c(ns))**(1./2.) + (bs/c(ns))
            kms(ns) = -psi*cps*sqrt(c(ns))*(term1+term2)
            term1b = 1.-2.*((t+bb)/c(ns))**(1./2.)
            term2b = (t+bb)/c(ns)
            kmb(ns) = -psi*cpb*sqrt(c(ns))*(term1b+term2b)
            km(ns) = kms(ns) +kmb(ns)
          elseif(c(ns) .gt. cstars .and. c(ns) .le. (t+cstarb))then
            term1 = 2.*(t/cstars)**(1./2.)-(t/cstars)
            term2 = -2.*(bs/cstars)**(1./2.)+(bs/cstars)
            kms(ns) = -psi*cps*sqrt(cstars)*(term1+term2)
            kmsstar= kms(ns)
            term1b = 1.-2.*((t+bb)/c(ns))**(1./2.)
            term2b = (t+bb)/c(ns)
            kmb(ns) = -psi*cpb*sqrt(c(ns))*(term1b+term2b)
            km(ns) = kms(ns) + kmb(ns)
          elseif(c(ns) .gt. (t+cstarb))then
            term1b= 1.-2.*((t+bb)/(t+cstarb))**(1./2.)
            term2b= (t+bb)/(t+cstarb)
            kmb(ns)= -psi*cpb*sqrt((t+cstarb))*(term1b+term2b)
            kms(ns)=kms(ns-1)
            km(ns) = kmsstar +kmb(ns)
          endif
          if(c(ns) .lt. t)then
            to = tos
          else
            to = tob
          endif
          tc(ns) = to - km(ns)
          s(ns) = (tc(ns)-x*p(nip)/c(ns)**1.5)/(psi*sqrt(c(ns)))
          if(nans .eq. 1)then
          write(37,43)p(nip),c(ns)*1.e6,sqrt(c(ns)*1.e6),-kms(ns)
     +              *1.e-6,-kmb(ns)*1.e-6,tc(ns)*1.e-6,s(ns)*1.e-6
    43     format(2x,f4.0,2x,f6.1,2x,f6.2,3(2x,f8.5),2x,f6.2)
          endif
          if(s(ns) .gt. smax)then
            smax = s(ns)
            sigmax(nip) = smax*1.e-6
            cf(nip) = c(ns)*1.e6
            kmcf = km(ns)
            tccf = tc(ns)
          endif
     1 continue
C+ ********************************************************************
      resid = (sigmax(nip) - sigp(nip))
      write(6,34) p(nip), sigmax(nip), cf(nip)
      write(38,34) p(nip), sigmax(nip), cf(nip)
     34 Format(2x,f4.0,2x,f7.2,2x,f5.0)
      if(nip .eq. 1)then
```

```
          sum = ((sigmax(1) - sigp(1))**2)*sigps(1)/sum1
      else
          sum = sum + ((sigmax(nip) - sigp(nip))**2)*sigps(nip)/sum1
      endif
    2 continue
C+ - - - - - - - - - - - - - - - - - - - - - - - - - - - - - - - - - - - -
      var(nth) = sum/(np-1)
      if(var(nth) .lt. minvar)then
        minvar = var(nth)
        thbest = t*1.e6
      endif
      write(6,35)var(nth),minvar,thbest
   35 format(2x,'variance for this set = ',f7.2,/,2x,'minvar=',f7.2,/,
     +2x,'best t = ',f5.1)
      print *,'-------------------------------------------------'
      write(38,*)'-------------------------------------------------'
  111 continue
  100 if(bs .ge. t)then
          do 22 nip = 1,np
              x = xo/(1+p(nip)/pl)
              co=((x*p(nip))/tos)**(2./3.)
              co=co*1.e6
              co = log10(co)
              smax = -1.e7
          do 11 cc = co,3.45,0.025
              if(cc .eq. co)then
                  ns = 1
              else
                  ns = ns+1
              endif
              xx=10.**cc
              c(ns)=(1.e-6)*xx
              kms(ns)=0.
              if(c(ns) .le. bb)then
                  kmb(ns)=0.
              elseif(c(ns) .gt. bb .and. c(ns) .le. cstarb)then
                  kmb(ns)=-psi*cpb*sqrt(c(ns))*(1.-2.*(bb/c(ns))
     +                    **(1./2.)+(bb/c(ns)))
              elseif(c(ns) .gt. cstarb)then
                  kmb(ns)=-psi*cpb*sqrt(cstarb)*(1.-2.*(bb/cstarb)
     +                 **(1./2.)+(bb/cstarb))
              endif
              km(ns)=kmb(ns)
              tc(ns)=tob-km(ns)
              s(ns)=(tc(ns)-x*p(nip)/c(ns)**1.5)/(psi*sqrt(c(ns)))
              if(nans .eq. 1)then
             write(37,43)p(nip),c(ns)*1.e6,sqrt(c(ns)*1.e6),kms(ns)
     +              *1.e-6,kmb(ns)*1.e-6,tc(ns)*1.e-6,s(ns)*1.e-6
```

```
            endif
            if(s(ns) .gt. smax)then
                smax = s(ns)
                sigmax(nip)=smax*1.e-6
                cf(nip)=c(ns)*1.e6
            endif
11 continue
        write(6,39)p(nip),sigmax(nip),cf(nip)
        write(38,39)p(nip),sigmax(nip),cf(nip)
39 format(2x,f4.0,2x,f6.2,2x,f6.0)
22 continue
   endif
   stop
   end
```

```
      Program Karcnew2
c+ This program uses solution 24.4 from the Stress Analysis of Cracks
c+ Handbook (Tada,Paris,Irwin,1985), which solves for an embedded penny
c+ shaped crack, subjected to a constant line force acting on an arc of
c+ radius b, and half-angle alpha.  As this program is intended for use
C+ with monoliths, alpha is set to a constant value of pi/2.
C+ This program allows the user to enter up to 20 experimentally
C+ measured strength-indent load pairs, and then will calculate T(c)
C+ curves, and use these to calculate strength values.  The program
C+ prints out the calculated strengths, and crack size at failure.  Or,
c+ the user may ask to see all values of stress, Km, and crack size.
C+--------------------------------------------------------------------
      real s(115),c(115),to,p(20),x,psi,smax(20),cf(20),cc,Tinf,
     +xx,cp,b,d,km(115),tc(115),sum,sigps(20),sum1,varnce,
     +pi,delta,var(150),sigp(20),minvar,pressure,pl
      integer ns,ii,nip,np
C+
C+ Definition of Variables:
C+
C+  s = stress; there is one stress value calculated for each
C+      crack size increment.
C+  c = crack size; incremented in steps of 0.025 power of ten
C+  to = base line toughness value, in Pa*sqrt(m)
C+  xo = constant in the residual stress intensity field, incorporating
C+     the hardness and Young's modulus, but no lateral crack influence
C+  p = indentation load, in N
C+  psi = geometry constant in the applied K field
C+  smax = maximum calculated stress value, identified as the strength
C+  cf = crack size corresponding to smax
C+  cc = do loop dummy variable used to increment crack size
C+  xx = dummy variable used in incrementing crack size
C+  cp = constant closure line force in the microstructural K term
C+  b = depth from surf. at which line force is applied
C+  delta=distance behind crack tip at which line force is applied
C+  km = microstructural stress intensity field
C+  tc = the toughness curve, T(c) = To - Km(c)
C+  ns = used to convert cc into an integer, which is then used
C+       as the term number of the array variables [s(ns), tc(ns),
C+       and km(ns)]
C+  i = used to determine which results to print
C+  sigp = experimentally measured strength
C+  sum = sum of squares of calculated - measured strength
C+  np = number of strength-indent load pairs
C+  PL = indent load at which lateral crack influence becomes import.nt
c+  alpha= pressurized arc half-angle (in radians), for bulk material
c+  t = surface layer thickness
C+--------------------------------------------------------------------
      write(5,*)'how many measured strengths are there?'
```

```
      read *,np
      sum=0.
      do 10 ii = 1,np
          write(5,*)'indent load = (N)?'
          read *,p(ii)
          print *,'average strength for that P = (MPa)?'
          read *,sigp(ii)
          print *,'number of samples broken for that P?'
          read *,sigps(ii)
          sum = sum + sigps(ii)
   10 continue
      write(5,*)'input parameters -- Xo = ?'
      read *,xo
      write(6,*)'Xo = ',xo
      print *,'enter psi'
      read *,psi
      write(5,*)' enter minimum To = (in MPa*sqrt(m)) ?'
      read *,tomin
      print *,'enter max To'
      read *,tomax
      print *,'enter To step size'
      read *,tostep
      write(5,*)'enter min constant closure line force = (KN/m) ?'
      read *,cpmin
      print *,'enter max constant closure line force'
      read *,cpmax
      print *,'enter cp step size'
      read *,cpstep
      write(5,*)'enter min c.p. lag distance (microns)'
      read *,dmin
      print *,'enter max closure pressure lag distance'
      read *,dmax
      print *,'enter cp lag distance step size'
      read *,dstep
      write(5,*)'enter PL  =  (in N)'
      read *,pl
      pi=acos(-1.)
      print *,'write ALL values to data file?(1=y, 2=n)'
      read *,ians
      if(ians .eq. 1)then
        open(37,file='karcnew-2dat.all')
        rewind 37
        open(38,file='karcnew-2.dat')
        rewind 38
      endif
      print *,'want to see all p,strength,resid values?(1=y,2=n)'
      read *,iprint
      print *,'want to enter a minvar from previous run? (1=y;2=n)'
```

```
      read *,iwell
      if(iwell .eq. 1)then
        print *,'enter minvar'
        read *,minvar
      else
        minvar = 10000000.
      endif
          do 5 dd=dmin,dmax,dstep
            delta = dd*1.e-6
            do 4 ccp = cpmin,cpmax,cpstep
              cp=ccp*1.e3
              do 3 tt = tomin,tomax,tostep
                if(tt .eq. tomin)then
                  ntt=1
                  else
                  ntt=ntt+1
                endif
                  to = tt*1.e6
C+ - - - - - - - - - - - - - - - - - - - - - - - - - - - - - - - - - - - -
C+ Indentation load loop:
C+ - - - - - - - - - - - - - - - - - - - - - - - - - - - - - - - - - - - -
      do 2 nip = 1,np
          x = xo/(1.+p(nip)/pl)
          co = ((x*p(nip))/to)**(2./3.)
          co = co*1.e6
          co = log10(co)
          smaxi=-1.e7
C+ ************************************************************************
C+ Inner loop for stress, T-curve calculations:
C+ ************************************************************************
      do 1 cc = co,3.45, 0.025
          if(cc .eq. co)then
              ns = 1
          else
              ns = ns + 1
          endif
          xx = 10.**cc
          c(ns) = (1.e-6)*xx
          c1=c(ns)
          b=c1-delta
          if(c(ns) .le. delta .or. cp .eq. 0.)then
              km(ns) = 0.
          elseif(c(ns) .gt. delta)then
            km(ns) = -4.*cp*b*(atan((2.*c1-delta)/delta))/
     +                (pi**(1.5)*sqrt(c1*delta*(2.*c1-delta)))
          endif
          tc(ns) = to - km(ns)
          s(ns) = (tc(ns)-x*p(nip)/c(ns)**1.5)/(psi*sqrt(c(ns)))
```

```
        if(s(ns) .gt. smaxi)then
            smaxi=s(ns)
            smax(nip) = s(ns)*1.e-6
            cf(nip) = c(ns)*1.e6
        endif
      if(ians .eq. 1)write(37,40)c(ns)*1.e6,-km(ns)*1.e-6,tc(ns)*
     +              1.e-6, s(ns)*1.e-6
   40 format(2x,f6.1,2x,f9.6,2x,f9.6,2x,f8.2)
    1 continue
C+ ********************************************************************
      if(ians .eq. 1)then
      write(38,31)
   31  format(2x,'P',2x,'strength',2x,'Co',4x,'Cf')
      write(38,34) p(nip), smax(nip), c(1)*1.e6, cf(nip)
   34 Format(2x,f5.0,2x,f6.1,2x,f6.1,2x,f6.1,/)
      endif
      resid=smax(nip)-sigp(nip)
      if(nip .eq. 1)then
        sum1 = ((smax(1) -sigp(1))**2)*sigps(1)/sum
        else
          sum1=sum1+((smax(nip)-sigp(nip))**2)*sigps(nip)/sum
        endif
        if(nip .lt. np)then
          varnce=sum1/(np-1)
          if(varnce .gt. minvar)go to 100
        endif
        if(iprint .eq. 1)then
          write(6,41)sigp(nip),smax(nip),resid
   41      format(2x,f7.2,2x,f7.2,2x,f7.3)
        endif
    2 continue
C+ - - - - - - - - - - - - - - - - - - - - - - - - - - - - - - - - - -
      var(ntt) = sum1/(np-1)
      if(var(ntt) .lt. minvar)then
        minvar = var(ntt)
        tobest = to*1.e-6
        cpbest = cp*1.e-3
        dbest = delta*1.e6
      endif
      if(iprint .eq. 1)then
        print *,'variance for this set =',var(ntt)
        print *,'-------------------------------------'
      endif
  100  if(nip .lt. np)then
      endif
    3   continue
    4   continue
      print *,'complete through delta = ',dd
```

```
5    continue
     print *,'best To =', tobest
     print *,'best cp =', cpbest,' KN/m'
     print *,'best delta =',dbest
     print *,'minvar = ',minvar
     pressure=cpbest*1.e3/(dbest*1.e-6)
     Tinf = 1.e-6*(sqrt(2.)*cpbest*1.e3/(sqrt(pi*dbest*1.e-6)))
     print *,'this gives steady state toughness =',Tinf,'MPa*sqrt(m)'
     print *,'and P/delta = ',pressure*1.e-6,'MPa'
     if(ians .eq. 1)then
       do 7 j = 1,np
         write(6,42)p(j),smax(j),cf(j)
42         format(2x,f5.0,2x,f8.2,2x,f7.1)
7      continue
     endif
     stop
     end
```

```
      Program Karcnew3c
c+  This program corrects some simplification problems with Karcnew3
c+ and karcnew3b.  Here, the arc line forces are allowed to extend to
c+ the interface, as in karcnew3b.  However, this program solves for Km
c+ for each arc element, all at the SAME point, the crack depth (i.e.,
C+ the deepest point beneath the surface).  Again, this program is for
c+ trilayers, using best fit parameters from the base materials, det.
c+ by karcnew2.  [Program karcnew3d will solve for the Km's at the
c+ surface].
C+--------------------------------------------------------------------
      real s(115),c(115),to,p(20),x,psi,smax(20),cf(20),cc,km(115),
     +xx,cp,b,d,kms(115),kmb(115),tc(115),sum,sigps(20),sum1,varnce,
     +pi,delta,var(150),sigp(20),minvar,pl
      integer ns,ii,nip,np
C+
C+ Definition of Variables:
C+
C+  s = stress; there is one stress value calculated for each
C+      crack size increment.
C+  c = crack size; incremented in steps of 0.05 power of ten
C+  to = base line toughness value, in Pa*sqrt(m)
C+  xo = constant in the residual stress intensity field, incorporating
C+     the hardness and Young's modulus, but no lateral crack influence
C+  p = indentation load, in N
C+  psi = geometry constant in the applied K field
C+  smax = maximum calculated stress value, identified as the strength
C+  cf = crack size corresponding to smax
C+  cc = do loop dummy variable used to increment crack size
C+  xx = dummy variable used in incrementing crack size
C+  cp = constant closure line force in the microstructural K term
C+  b = depth from surf. at which the closure force becomes activated
c+  delta=distance behind crack tip at which closure force is applied
C+  km = microstructural stress intensity field
C+  tc = the toughness curve, T(c) = To - Km(c)
C+  ns = used to convert cc into an integer, which is then used
C+       as the term number of the array variables [s(ns), tc(ns),
C+       and km(ns)]
C+  i = used to determine which results to print
C+  sigp = experimentally measured strength
C+  sum = sum of squares of calculated - measured strength
C+  np = number of strength-indent load pairs
C+  PL = indent load at which lateral crack influence becomes important
c+  alpha= arc angle (in radians), from crack depth to interface
c+  alphas = FULL arc angle for surface material line force
c+  alphab = HALF arc angle for bulk material line force
c+  Theta= arc angle between line force arc midpoint and the crack
c+       depth; for bulk material, Theta=0; for surface material,
c+       Theta is alphas/2 + alphab - epsilon
```

```
c+  epsilon = [alphas-pi/2 + alpha] This is the arc angle which
c+        represents the extra arc segment needed to extend the
c+        surface material line force all the way to the material
c+        interface, rather than being cut off while still in the
c+        surface layer (as in karcnew3 program)
c+  t = surface layer thickness
C+-------------------------------------------------------------------
      f(cp,c1,d,y) = 4.*cp*(c1-d)*atan(y*(c1-d)/d)/
     +              (sqrt((pi**3)*c1*d*(2.*c1-d)))
      f2(cp,c1,d,Theta,A) = (2.*cp*(c1-d)/sqrt((pi**3)*c1*d*(2.*c1-d)))
     + *(atan((2.*c1-d)*tan((Theta+A)/2.)/d)-atan((2.*c1-d)*tan
     +  ((Theta-A)/2.)/d))
      open(37,file='karcnew-3c.dat')
      rewind 37
      write(5,*)'how many measured strengths are there?'
      read *,np
      sum=0.
      do 10 ii = 1,np
          write(5,*)'indent load = (N)?'
          read *,p(ii)
          print *,'average strength for that P = (MPa)?'
          read *,sigp(ii)
          print *,'number of samples broken for that P?'
          read *,sigps(ii)
          sum = sum + sigps(ii)
   10 continue
      write(5,*)'input parameters -- Xo = ?'
      read *,xo
      write(6,*)'Xo = ',xo
      print *,'enter psi'
      read *,psi
      write(5,*)' enter  To = (in MPa*sqrt(m)) ?'
      read *,to
      write(5,*)'enter surf. constant closure line force = (KN/m) ?'
      read *,cpsurf
      print *,'enter bulk constant closure line force'
      read *,cpbulk
      write(5,*)'enter surface c.p. lag distance (microns)'
      read *,dsurf
      print *,'enter bulk closure pressure lag distance'
      read *,dbulk
      write(5,*)'enter PL  =  (in N)'
      read *,pl
      print *,'enter surface layer thickness, in microns'
      read *,t
      t=t*1.e-6
      pi=acos(-1.)
      print *,'write ALL values to data file?(1=y, 2=n)'
```

```
      read *,ians
      if(ians .eq. 1)then
        open(38,file='karcnew3cdat.all')
        rewind 38
      endif
      print *,'want to see all p,strength,resid values; or'
      print *,'just final strengths and Cfs? (1=all; 2=just)'
      read *,iprint
      print *,'want to enter a minvar from previous run? (1=y;2=n)'
      read *,iwell
      if(iwell .eq. 1)then
        print *,'enter minvar'
        read *,minvar
      else
        minvar = 10000000.
      endif
            deltas = dsurf*1.e-6
            deltab = dbulk*1.e-6
            cpb=cpbulk*1.e3
            cps = cpsurf*1.e3
            to = to*1.e6
C+ - - - - - - - - - - - - - - - - - - - - - - - - - - - - - - - - - -
C+ Indentation load loop:
C+ - - - - - - - - - - - - - - - - - - - - - - - - - - - - - - - - - -
      do 2 nip = 1,np
          x = xo/(1.+p(nip)/pl)
          co = ((x*p(nip))/to)**(2./3.)
          co = co*1.e6
          co = log10(co)
          smaxi=-1.e7
C+ ************************************************************************
C+ Inner loop for stress, T-curve calculations:
C+ ************************************************************************
      do 1 cc = co,3.45, 0.025
          if(cc .eq. co)then
              ns = 1
          else
              ns = ns + 1
          endif
          xx = 10.**cc
          c(ns) = (1.e-6)*xx
          c1=c(ns)
          bs=c1-deltas
          bb=c1-deltab
          alpha = acos(t/c1)
          if(c(ns) .le. deltas)then
              kms(ns) = 0.
          elseif(c(ns) .gt. deltas .and. c(ns) .le.
```

```
     +                                (t+deltas))then
            d=deltas
            cp=cps
            alpha=pi/2.
            y=tan(alpha/2.)
            kms(ns) = -f(cp,c1,d,y)
          elseif(c(ns) .gt. (t+deltas))then
            alpha=acos(t/c1)
            alphas=pi/2.-(atan((c1*sin(alpha)-(deltas/
     +                  sin(alpha)))/t))
            epsilon = alpha - atan((c1*sin(alpha)-(deltas/
     +                                  sin(alpha)))/t)
            Theta = alphas/2. - epsilon + alpha
            d=deltas
            cp=cps
            A=alphas/2.
            kms(ns) = -2.*f2(cp,c1,d,Theta,A)
          endif
          if(c1 .le. deltab .or. c1 .lt. t .or. (c1-deltab)
     +                                  .le. t)then
            kmb(ns) = 0.
          elseif(c1 .gt. deltab)then
            alpha=acos(t/c1)
            alphab= atan((c1*sin(alpha)-(deltab/sin(alpha)))/t)
            y=tan(alphab/2.)
            d=deltab
            cp=cpb
            kmb(ns) = -f(cp,c1,d,y)
          endif
          km(ns) = kms(ns) + kmb(ns)
          tc(ns) = to - km(ns)
          s(ns) = (tc(ns)-x*p(nip)/c(ns)**1.5)/(psi*sqrt(c(ns)))
          if(s(ns) .gt. smaxi)then
              smaxi=s(ns)
              smax(nip) = s(ns)*1.e-6
              cf(nip) = c(ns)*1.e6
          endif
        if(ians .eq. 1)write(38,40)c(ns)*1.e6,-kms(ns)*1.e-6,-kmb(ns)*
     +          1.e-6,-km(ns)*1.e-6,tc(ns)*1.e-6,s(ns)*1.e-6
       40 format(2x,f6.1,4(2x,f9.6),2x,f8.2)
        1 continue
C+ ********************************************************************
        if(iprint .eq. 2)then
        write(37,34) p(nip), smax(nip), c(1)*1.e6, cf(nip)
       34 Format(2x,f5.0,2x,f6.1,2x,f6.1,2x,f6.1,/)
        endif
        resid=smax(nip)-sigp(nip)
        if(nip .eq. 1)then
```

```
      sum1 = ((smax(1) -sigp(1))**2)*sigps(1)/sum
      else
        sum1=sum1+((smax(nip)-sigp(nip))**2)*sigps(nip)/sum
      endif
      if(nip .lt. np)then
        varnce=sum1/(np-1)
        if(varnce .gt. minvar)go to 100
      endif
      if(iprint .eq. 1)then
        write(6,41)sigp(nip),smax(nip),resid
41       format(2x,f7.2,2x,f7.2,2x,f7.3)
      endif
   2 continue
C+ - - - - - - - - - - - - - - - - - - - - - - - - - - - - - - - - - - - -
    var(ntt) = sum1/(np-1)
    if(var(ntt) .lt. minvar)then
      minvar = var(ntt)
      tobest = to*1.e-6
      cpbest = cp*1.e-3
      dbest = delta*1.e6
      csbest = cstar*1.e6
    endif
    if(iprint .eq. 1)then
      print *,'variance for this set =',var(ntt)
      print *,'----------------------------------------'
    endif
100  if(nip .lt. np)then
    endif
3    continue
4    continue
    print *,'complete through delta = ',dd
5    continue
    print *,'through cstar=', cs,' , minvar = ',minvar
6    continue
    print *,'best To =', tobest
    print *,'best cp =', cpbest,' KN/m'
    print *,'best delta =',dbest
    print *,'best cstar = ',csbest
    print *,'minvar = ',minvar
    stop
    end
```

APPENDIX III. EQUIPMENT AND SUPPLIER INFORMATION

1. Tape Caster: TAM Ceramics Inc., San Marcos, CA. Model 164 Slurry Caster, with Model 165 Dryer.
2. Mylar casting film: supplied by Dr. Yang-Haw Hu of E. I. duPont de Nemours
3. Glass casting plates: McGrory Glass Inc., Chester, PA. Plates were tempered glass, and had dimensions of 12X72X0.25 in. ± 0.063 in. over total length.
4. Ball Milling Media: U. S. Stoneware, Corp., Mahwah, NJ. 99.5% alumina rods, 0.5X0.5 in.
5. Plastic bottles, for slurries: Fisher Scientific, King of Prussia, PA. Wide-mouth, HDPE.
6. Binder solution: Metoramic Sciences, Inc., Carlsbad, CA. Grade B73181
7. Binder modifier/ surfactant: Metoramic Sciences, Inc., Carlsbad, CA. Grade M1114
8. Static charge elimination device: X-Static, Westsard Electronics, Inc., Aurora, CO.
9. Warm press: Fred S. Carver, Inc., Menomonee Falls, WI. #2089 Model M Hydraulic Laboratory Press, with a set of 2108-1 9X9 in. steel heating platens.
10. Warm pressing dies: Buehler, Ltd., Lake Bluff, IL.
11. Alumina refractory dishes: Morgan Refractories Inc., Canon City, CO. (99.8% pure). Also, McDanel Refractory Co., Beaver Falls, PA. (99.8% pure)
12. Binder burnout/ calcination furnace: L&L Special Furnace Co., Inc., Aston, PA. Model HD9 Electric Furnace, with Honeywell UDC3000 digital program control.
13. Sintering furnace: CM Furnaces, Inc., Bloomfield, NJ. Model 1700SA Rapid Temperature Lab Furnace, with Eurotherm 821 Temperature Control System. (max temp of 1700 C)
14. Isopress: Fluitron Inc., Ivyland, PA. Model CP3-12-60 Cold Isostatic Press. Internal dimensions of pressure vessel - 3X12 in.; max pressure of 60 ksi (~420MPa).
15. Rubber isopressing bags: Klein Rubber Co., Ravenna, OH. 1.6 in. diameter latex bags, with 13 mil wall thickness (~0.3mm).

16. Microhardness machines: Leco Corp., M-400FT Hardness Tester ($P \leq 10N$), and model V-100A Hardness Tester ($P \geq 10N$).

17. Silicone oil: Dow Corning, 704 diffusion pump oil.

18. Strength testing: Instron, Canton, MA. Model 1350

19. Digital storage oscilloscope: Nicolet Instrument Corp., Madison, WI. Model NIC-310.

20. Optical microscopes: Olympus, and Nikon

21. Digital image analysis pad: DonSanto Corp.,Natick, MA. MicroPlanII Image Analysis System.

22. SEMs: (a) ETEC Autoscan Corporation, Hayward, CA. (b) JEOL, Tokyo, Japan(US office- Peabody, MA). Models 840F, and 6300F (both FEG).

23. Computers: Zenith

    Gateway 486/33C

    IBM RISC System/6000 7012-320H Workstations

24. Software: FORTRAN program development, editing, and debugging primarily accomplished using WATFOR-77, which was much easier to learn and use than anything available on the IBM Workstations or the mainframe computers.

25. Chesapeake Bay Crabs: Sea Pride Crab House, Baltimore, MD.

REFERENCES

Aksay, I. A., in Advances in Ceramics Vol. 9: Forming of Ceramics, Am.Ceram.Soc., Columbus, OH, 1984.

Aksay, I. A.; Lange, F. F.; & Davis, B. I., *J. Am. Ceram. Soc.* 66 [10] C-190-92, 1983.

Alford, N. McN; Birchall, J. D., & Kendall, K., *Nature*, Vol. 330, p. 51, 1987

Anstis, G. R.; Chantikul, P.; Marshall, D. B.; & Lawn, B.R., *J. Am. Ceram. Soc.* 64 [9], 533-38, 1981.

Atkins, A. G., & Mai, Y-W; Elastic and Plastic Fracture: Metals, Polymers, Ceramics, Composites, Biological Materials, Halsted Press, NY, 1985.

Bayer, G., *Proc. Brit. Ceram. Soc.* 22, p.39, 1973.

Bennison, S. J.; Padture, N. P.; Runyan, J. L., & Lawn, B. R., *Philosophical Magazine Letters*, 1991, Vol. 64, No. 4, 191-195.

Bennison, S. J.; & Lawn, B. R., *Acta Metall.* 37 [10], 2659-71, 1989.

Blendell, J. E.; & Coble, R. L., *J. Am. Ceram. Soc.*, 65 [3] 174-78, 1982.

Braun, L. M.; Bennison, S. J.; & Lawn, B. R., *J. Am. Ceram. Soc.* 75 [11] 3049-57, 1992.

Chantikul, P.; Bennison, S. J.; & Lawn, B. R., *J. Am. Ceram. Soc.*, 73 [8], 2419-27, 1990.

Chantikul, P.; Anstis, G. R.; Lawn, B. R.; & Marshall, D. B., *J. Am. Ceram. Soc.* 64 [9], 539-43, 1981.

Clegg, W. J.; Kendall, K.; Alford, N. McN.; Button, T. W.; & Birchall, J. D., *Nature*, Vol.347, 4 Oct. 1990, p. 455-7.

Coble, R. L; & Cannon, R. M., in Processing of Crystalline Ceramics, Plenum Press, NY, 1978.

Cook, R. F.; & Clarke, D. R., *Acta Metall. 36* [3] 555-62, 1988.

Cook, R. F.; Pascucci, M. R.; & Rhodes, W. H., *J. Am. Ceram. Soc.* 73 [7] 1873-78, 1990.

Cook, R. F., Mechanical Properties of Ceramics, in Materials Science and Technology, Ed. by R. Cahn, et. al., VCH Publishers, Weinheim, Germany, in press.

Cook, R. F.; Fairbanks, C. J.; Lawn, B. R.; & Mai, Y-W, *J. Mater. Res.* 2 (3), 345 - 356, 1987.

Cook, R. F.; & Pharr, G. M., *J. Am. Ceram. Soc.* 73 [4], 787-817, 1990.

Cutler, R. A.; Bright, J. D.; Virkar, A. V.; Shetty, D. K., *J. Am. Ceram. Soc.*, 70 [10] 714-18, 1987.

de With, G.; & Wagemans, H. H. M., *J. Am. Ceram. Soc.*, 72 [8], 1538-41, 1989.

Faber, K. T.; Iwagoshi, T.; Ghosh, A., J. Am. Ceram. Soc., 71 [9] C399-401, 1988.

Faber, K. T., & Evans, A. G., *Acta Metall.* 31 [4], p.565 (part I); p.577 (part II), 1983.

French, J. D.; Chan, H. M.; Harmer, M. P.; & Miller, G. A., J. Am. Ceram. Soc., 75 [2] 418-23, 1992.

Garvie, R. C.; Hannink, R. H. J., & Pascoe, R. T., *Nature*, Vol. 258, p. 703, 1975.

Green, D. J.; Hannink, R. H. J.; & Swain, M. V., Transformation Toughening of Ceramics, CRC Press, FL, 1988.

Green, D. J., *J. Am. Ceram. Soc.* 66 [10] C-178-79, 1983.

Green, D. J., *J. Am. Ceram. Soc.* 66 [11] 807-10, 1983.

Gruninger, M. F.; Lawn, B. R.; Farabaugh, E. N; & Wachtman, J. B., *J. Am. Ceram. Soc.*, 70 [5], 344-48, 1987.

Gruszka; Mistler; & Runk, *Am. Ceram. Soc. Bull.*, 49 [6] 575-79, 1970.

Gutshall, P. L.; and Gross, G. E., *Engineering Fracture Mechanics*, Vol. 1, 463-71, 1969.

Gutshall, P. L.; and Gross, G. E., *Ceramic Age*, Vol. 84, No. 9, 22-24, 1968.

Hansen, J. J.; Cutler, R. A.; Shetty, D. K.; & Virkar, A. V., *J. Am. Ceram. Soc.*, 71 [12] C501-505, 1988.

Hertzberg, R. W., Deformation and Fracture Mechanics of Engineering Materials, Wiley, 1989.

Heuer, A. H.; Ready, M. J.; Steinbrech, R., *Materials Science and Engineering*, A105/106, p.83-89, 1988.

Heussner, K-H; & Claussen, N., *J. Europ. Ceram. Soc.* 5, p. 193-200, 1989.

Kato, E.; Daimon, K; & Takahashi, J., *J. Am. Ceram. Soc.*, 63 [5-6] 355-56, 1980.

Kendall, K.; Alford, N. McN.; Clegg, W. J.; & Birchall, J. D., *Nature*, Vol. 339, p.130, 1989.

Kingery, W. D.; Bowen, H. K.; & Uhlmann, D. R., Introduction to Ceramics, John Wiley & Sons,Inc., NY, 1976.

Kirchner, H. P.; Gruver, R. M.; & Walker, R. E., *J. Appl. Phys.*, 40 [9] 3445 - 52, 1969.

Kirchner, H. P.; Walker, R. E.; & Plats, D. R., *J. Appl. Phys.* 42 [10] 3685-92, 1971.

Kirchner, H. P.; Gruver, R. M.; & Walker, R. E., *J. Am. Ceram. Soc.*, 51 [5], 251-55, 1968.

Kirchner, H. P.; Gruver, R. M.; & Walker, R. E., *Am. Ceram. Soc. Bull.*, 47 [9] 798 - 802, 1968.

Kirchner, H. P.; Gruver, R. M.; & Walker, R. E., *J. Am. Ceram. Soc.*, 50 [4], 169-73, 1967.

Kirchner, H. P.; & Gruver, R. M., *J. Am. Ceram. Soc.*, 49 [6], 330-33, 1966.

Kirchner, H. P., Strengthening of Ceramics, Marcel Dekker, Inc., NY, NY, 1979.

Kirchner; Gruver; & Walker, *Trans. J. Brit. Ceram. Soc.*, 70 [6] 215-19, 1971.

Kistler, S. S., *J. Am. Ceram. Soc.*, 45 [2] 59-68, 1962.

Knehans, R.; & Steinbrech, R., *J. Meter. Sci. Lett.* 1, p. 327, 1982.

Lange, F. F., *J. Am. Ceram. Soc.* 72, p.3, 1989.

Lange, F. F., J. Mater. Sci. 17, 247-54, 1982.

Lange, F. F.; Metcalf, M.; Davis, B. I.; & Aksay, I. A., *J. Am. Ceram. Soc.* 66 [6], parts I-Iii, p.396, 399, 407; 1983.

Lawn, B. R., *J. Europ. Ceram. Soc.* 7, p.17, 1991.

Lawn, B. R.; Evans, A. G.; & Marshall, D. B., *J. Am. Ceram. Soc.* 63 [9-10] 574 -81, 1980.

Lawn, B. R., Fracture of Brittle Solids, Cambridge University Press, 1993.

Lawn, B. R.; & Fuller, E. R., *J. Mater. Sci.* 19, 4061-4067, 1984.

Lee, E. H.; Rogers, T. G.; & Woo, T. C., *J. Am. Ceram. Soc.*, 48 [9] 480-87, 1965.

Lutz, E. H.; & Swain, M. V., *J. Am. Ceram. Soc.* 74 [11], 2859-68, 1991.

Magley, D. J.; Faber, K. T., Ceram. Eng. Sci. Proc., 10 [9-10] 1350, 1989.

Mai, Y-W; & Lawn, B. R., *J. Am. Ceram. Soc.*, 70 [4], 289-94, 1987.

Mai, Y-W.; & Lawn, B. R., *Ann. Rev. Mater. Sci.* 16, p.415, 1986.

Marshall, D. B., *J. Am. Ceram. Soc.*, 69 [3], 173-80, 1986.

Marshall, D. B.; & Lawn, B. R., *J. Am. Ceram. Soc* 60 [1-2], 86-87, 1977.

Marshall, D. B.; & Evans, A. G., *J. Am. Ceram. Soc.* 68 [5] 225-31, 1985.

McMeeking, R. M.; & Evans, A. G., *J. Am. Ceram. Soc.*, 65 [5], 242-6, 1982.

Mistler, R. E., US Patent No. 3652378, Mar. 28, 1972.

Mistler, R. E., *Am. Ceram. Soc. Bull.* 52 [11], 850-54, 1973.

Mysels, K. J., Introduction to Colloid Chemistry, Interscience Publishers, Inc., NY, 1959.

Olcott, J. S., *Science*, 140 [3572] 1189-93, 1963.

Padture, N. P., & Chan, H. M., *J. Am. Ceram. Soc.* 75 [7] 1870-75, 1992.

Padture, N. P., Ph.D. Dissertation, Lehigh University, 1991.

Paris, P. C., 'Stress-Intensity Factors by Dimensional Analysis', Lehigh University, Inst. of Research Report, 1961.

Paris, P. C.; & Sih, G., 'Stress Analysis of Cracks', in Fracture Toughness Testing and its Applications, ASTM STP 381, p.30-81, 1965.

Prewo & Brennan, *J. Mater. Sci.* 17 [8], 2371-2383, 1982.

Ready, M. J.; Heuer, A. H.; & Steinbrech, R., *J. Am. Ceram. Soc.*, 71 [1] C2-6, 1988.

Reed, J. S., Introduction to the Principles of Ceramic Processing, Wiley, 1988.

Richerson, D. W., Modern Ceramic Engineering, Marcel Dekker, Inc., NY,NY, 1982; 1992.

Roark, R. J., Formulas for Stress and Strain, McGraw Hill, NY, 1954.

Ruhle, M.; Claussen, N.; Heuer, A. H., J. Am. Ceram. Soc., 69 [3] 195-97, 1986.

Runyan, J. L.; & Bennison, S. J., *J. Europ. Ceram. Soc.* 7, p. 93, 1991.

Russo, C. J.; Harmer, M. P.; Chan, H. M.; & Miller, G. A., *J. Am. Ceram. Soc.* 75 [12] 3396-400, 1992.

Sathyamoorthy, R.; Virkar, A. V.; & Cutler, R. A., *J. Am. Ceram. Soc.*, 75 [5] 1136-41, 1992.

Sato, T.; & Ruch, R., Stabilization of Colloidal Dispersions by Polymer Adsorption, Marcel Dekker, 1980.

Selsing, J., *J. Am. Ceram. Soc.* 44, p. 419, 1961.

Stuart, M. D., M.S. Thesis, Lehigh University, 1991.

Subbarao, E. C., in Science and Technology of Zirconia, Vol. I, The Am.Ceram.Soc., Columbus OH, 1981.

Swain, M. V., *J. Mater. Sci. Lett.* 5, p.1313, 1986.

Swain, M. V.; & Rose, L. R. F., *J. Am. Ceram. Soc.*, 69 [7], 511-18, 1986.

Swain, M. V., *Acta Metall.*, 33 [11], 2083-91, 1985.

Swain, M. V., pp.45-67 in Advanced Ceramics, Ed. by S. Somiya, Elsevier Applied Science, 1986.

Swain, M.V., *J. Mater. Sci. Lett.* 15[6], 1577-79, 1980.

Swanson, P.L.; Fairbanks, C. J.; Lawn, B. R.; Mai, Y-W; & Hockey, B. J., *J. Am. Ceram. Soc.* 70 [4], 279-89, 1987.

Tada, H.; Paris, P.; & Irwin, G., The Stress Analysis of Cracks Handbook, Del Research Corp., St. Louis, MO, 1985.

Tadros, Th. F., in Surfactants, Academic Press, Inc., London, 1984.

Tandon, R.; Green, D. J.; & Cook, R. F., *J. Am. Ceram. Soc.* 73 [9] 2619-27, 1990.

Thomas, H. A. J.; & Stevens, R., *Brit. Ceram. Soc. Trans. J.* 88, parts I & II, p.144, p.184, 1989.

Tomey, E. S.; Pober, R. L.; Bowen, H. K.; & Calvert, P. D., in Advances in Ceramics Vol. 9: Forming of Ceramics, Am.Ceram.Soc., Columbus, OH, 1984.

Tsukuma, K; Ueda, K; Matsushita, K.; & Shimada, M., *J. Am. Ceram. Soc.* 68 [2] C56-58, 1985.

Tsukuma, K.; & Shimada, M., *Am. Ceram. Soc. Bull.*, 64 [2] 310-13, 1985.

Vekinis, G.; Ashby, M. F.; & Beaumont, P. W. R., *Acta Metall. Mater.* 38, p.1151, 1990.

Velazquez, M., & Danforth, S. C., in Advances in Ceramics Vol. 9: Forming of Ceramics, Am.Ceram.Soc., Columbus, OH, 1984.

Virkar, A. V.; Huang, J. L.; & Cutler, R. A., *J. Am. Ceram. Soc.*, 70 [3] 164-70, 1987.

Warshaw, S. I., *Am. Ceram. Soc. Bull.*, 36 [1], 28-30, 1957.

Yu, C-S; & Shetty, D. K., *J. Am. Ceram. Soc.*, 72 [6] 921-28, 1989.

Zok, F.; Sbaizero, O.; Hom, C. L.; & Evans, A. G., *J. Am. Ceram. Soc.*, 74 [1] 187-93, 1991.

ABOUT THE AUTHOR

Charles J. Russo was born on August 29, 1965, in Alexandria, Va., to Philip and Joanne Russo. He attended grade school in Arlington, Va., and high school in Millville, N.J., where he graduated valedictorian in 1983. He entered the College of Engineering at Lehigh University in the fall of '83, then competed for and won an Army ROTC scholarship at Fort Knox, Ky., in the summer of '84. In the spring of 1987, he earned a B.S. in Metallurgy and Materials Engineering, and was named a Distinguished Military Graduate. He was commissioned into the Ordnance Corps as a Regular Army officer in May, 1987. The Army granted an educational delay, allowing him to remain at Lehigh to pursue a graduate degree. On Sept. 22, 1990, Charles married his soulmate, Alysha Ruddiman, who is also a Lehigh graduate (B.A. - Psychology, 1988). Over the course of his six year odyssey through graduate school, Charles presented his work at three conferences, published two papers, and won first prize in the student category for a poster presented at the 17th Annual Conference on Composites and Advanced Materials at Cocoa Beach, Fl., in Jan. 1993. The author served as teaching assistant for a number of courses: Mat. 334 (three times) - Scanning Electron Microscopy and Microanalysis; Mat. 63 - Introduction to Materials; Mat. 192 - Structural Materials; and Mat 427 -Advanced Scanning Electron Microscopy. Upon graduation, 1LT Russo will be sent to Fort Hood, Texas, for his initial duty assignment with the U.S. Army.

3. PUBLICATIONS AND PRESENTATIONS

3. PUBLICATIONS AND PRESENTATIONS

3a. Publications

N. P. Padture, S. J. Bennison, J. L. Runyan, J. Rodel, H. M. Chan, and B. R. Lawn, "Flaw Tolerant Al_2O_3-Al_2TiO_5 Composites", Proc. of Symp. on Composites: Processing, Microstructure and Properties, Orlando, FL (1990).

M. P. Harmer, H. M. Chan, and G. A. Miller, "Unique Opportunities for Microstructural Engineering with Duplex Ceramics", Ceramic Transactions, 22, 617, Am. Ceram. Soc. (1991).

N. P. Padture and H. M. Chan, "Influence of Grain Size and Degree of Crystallization of Intergranular Glassy Phase on the Mechanical Behavior of a Debased Alumina", J. Mats. Sci., 26, 2711 (1991).

N. P. Padture and H. M. Chan, "On the Constrained Crystallization of Synthetic Anorthite ($CaO{\cdot}Al_2O_3{\cdot}2SiO_2$)", J. Mater. Res., 7, 170 (1992).

L. Stearns, J. Zhao, and M. P. Harmer, "Processing and Microstructure Development in Al_2O_3-SiC 'Nanocomposites'", J. Eur. Ceram. Soc., 10, 473 (1992).

C. J. Russo, M. P. Harmer, H. M. Chan, and G. A. Miller, "Design of a Laminated Ceramic Composite for Improved Strength and Toughness", J. Am. Ceram. Soc., 75, 3396 (1992).

J. D. French, H. M. Chan, M. P. Harmer, and G. A. Miller, "Mechanical Properties of Interpenetrating Microstructures: The Al_2O_3:c-ZrO_2 System", J. Am. Ceram. Soc., 75[2], 418 (1992).

M. P. Harmer, H. M. Chan, and G. A. Miller, "Unique Opportunities for Microstructural Engineering with Duplex and Laminar Ceramic Composites", J. Am. Ceram. Soc., 75[7], 1715 (1992).

N. P. Padture and H. M. Chan, "Improved Flaw Tolerance in Alumina-1 vol % Anorthite via Crystallization of the Intergranular Glass", J. Amer. Cer. Soc., 75, 1870 (1992).

J. Zhao, L. Stearns, M. P. Harmer, G. A. Miller, and R. F. Cook, "Mechanical Behavior of Al_2O_3-SiC 'Nanocomposites'", J. Am. Ceram. Soc., 76, 503 (1993).

N. P. Padture, S. J. Bennison, and H. M. Chan, "Flaw-Tolerance and Crack-Resistance Properties of Alumina-Aluminum Titanate Composites with Tailored Microstructures", J. Amer. Cer. Soc., 76, 2312 (1993).

J. D. French, M. P. Harmer, H. M. Chan, and G. A. Miller, "High Temperature Fracture Toughness of Duplex Microstructures", submitted to J. Am. Ceram. Soc. (1994).

C. J. Russo, M. P. Harmer, H. M. Chan, and G. A. Miller, "Mechanical Properties of Laminated Ceramic Composites in Alumina- and Zirconia-Based Systems", Proc. 17th Ann. Conf. on Composite Materials and Structures, 14[9-10], 998 (1993).

J. D. French, J. Zhao, M. P. Harmer, H. M. Chan, and G. A. Miller, "Creep of Duplex Microstructures", J. Am. Ceram. Soc. (1994). In Press.

3b. Presentations

M. P. Harmer, "Opportunities for Microstructural Engineering with Duplex and Laminar Ceramics", Univ. of Illinois, 1991.

H. M. Chan, "Mechanical Properties of Tailored Ceramic Microstructures", Univ. of Michigan, Ann Arbor, October 1991.

H. M. Chan, "Unique Opportunities for Microstructural Engineering with Duplex and Laminar Ceramic Composites", Lehigh Valley Chapter Meeting of ASM, Bethlehem, November 1991.

H. M. Chan and M. P. Harmer, "Novel Processing of Ceramic Composites for High Temperature Structural Applications", Wright-Patterson AFB, Dayton, May 1992.

H. M. Chan and M. P. Harmer, "Ceramic Microstructural Design for Mechanical Reliability", Ford Motor Company, Dearborn, June 1992.

H. M. Chan and M. P. Harmer, "Mechanical Properties of Tailored Ceramic Microstructures", Bolling AFB, Washington, D.C., June 1992.

L. C. Stearns, J. Zhao, and M. P. Harmer, "Processing and Microstructure Evolution in Al_2O_3-SiC Particulate Composites", 94th Annual Meeting of the Am,. Cer. Soc, Minneapolis, April 1992.

J. Zhao, L. Stearns, M. P. Harmer, H. M. Chan, G. A. Miller, and R. F. Cook, "Mechanical Properties of Alumina Containing Sub-micron SiC Particles", 94th Annual Meeting of the Am. Cer. Soc., April 1992.

J. D. French, J. Zhao, M. P. Harmer, H. M. Chan, and G. A. Miller, "Tensile Creep of Duplex Ceramic Microstructures", World Congress on Ceramics, Symposium on Multiphase and Interpenetrating Phase Ceramics", San Francisco, November 1992.

H. M. Chan and M. P. Harmer, "Microstructural Design with Duplex Ceramics", Gordon Research Conference on Ceramics, New Hampshire, August 1992.

H. M. Chan, "Tailoring of Ceramic Microstructures for Improved Mechanical Properties", Ford North Penn Electronics Facility, Lansdale, PA, February 1993.

H. M. Chan, "Mechanical Properties of Tailored Ceramic Microstructures", Center for Ceramic Research, Rutgers Univ., Piscataway, NJ, March 1993.

J. French and H. M. Chan, "Indentation Creep of Duplex Microstructures", Int. Symp. on Fracture, Am. Ceram. Soc. Ann. Mtg., Cincinnati, April 1993.

A. M. Thompson, J. C. Fran, I. A. Chou, H. M. Chan, and M. P. Harmer, "Fracture Behavior of Alumina Containing Sub-Micron SiC Particles", Int. Symp. on Novel materials, Am. Ceram. Soc. Ann. Mtg., Cincinnati, April 1993.

M. P. Harmer, "Recent Developments in Structural Ceramics", Lehigh University, Retired Faculty Club, April 1993.

M. P. Harmer, "Microstructural Design of Multiphase Ceramic Composites for Optimum Mechanical Performance", Ann. Mtg. of the Brazilian Ceram. Soc., Curitiba, Brazil, May 1993 (Invited).

H. M. Chan, "Tailoring of Multi-Phase Ceramic Composites for Optimum Mechanical Properties", Meet 'N' 93 (First SES-ASME-ASCE Joint Mtg.), Univ. of VA, Charlottesville, VA, June 1993.

H. M. Chan, "Application of SEM to the Study of Multi-Phase Ceramic Composites", 51st Ann. MSA Meeting, Cincinnati, August 1993.

M. P. Harmer, "Microstructure and Processing of Ceramic Nanocomposites", Penn State University, September 1993.

M. P. Harmer, "Microstructural Design of Multiphase Ceramic Composites", Materials '93 Conference in Porto, Portugal, October 1993 (Invited).

M. P. Harmer, "Mechanical Behavior of Ceramics", University of Oporto, Portugal, October 1993.

J. D. French, J. Zhao, M. P. Harmer, H. M. Chan, and G. A. Miller, "Tensile Creep of Duplex Ceramic Microstructures", World Congress on Ceramics, Symposium on Multiphase and Interpenetrating Phase Ceramics", San Francisco, November 1992.

H. M. Chan and M. P. Harmer, "Microstructural Design with Duplex Ceramics", Gordon Research Conference on Ceramics, New Hampshire, August 1992.

H. M. Chan, "Tailoring of Ceramic Microstructures for Improved Mechanical Properties", Ford North Penn Electronics Facility, Lansdale, PA, February 1993.

H. M. Chan, "Mechanical Properties of Tailored Ceramic Microstructures", Center for Ceramic Research, Rutgers Univ., Piscataway, NJ, March 1993.

J. French and H. M. Chan, "Indentation Creep of Duplex Microstructures", Int. Symp. on Fracture, Am. Ceram. Soc. Ann. Mtg., Cincinnati, April 1993.

A. M. Thompson, J. C. Fran, I. A. Chou, H. M. Chan, and M. P. Harmer, "Fracture Behavior of Alumina Containing Sub-Micron SiC Particles", Int. Symp. on Novel materials, Am. Ceram. Soc. Ann. Mtg., Cincinnati, April 1993.

M. P. Harmer, "Recent Developments in Structural Ceramics", Lehigh University, Retired Faculty Club, April 1993.

M. P. Harmer, "Microstructural Design of Multiphase Ceramic Composites for Optimum Mechanical Performance", Ann. Mtg. of the Brazilian Ceram. Soc., Curitiba, Brazil, May 1993 (Invited).

H. M. Chan, "Tailoring of Multi-Phase Ceramic Composites for Optimum Mechanical Properties", Meet 'N' 93 (First SES-ASME-ASCE Joint Mtg.), Univ. of VA, Charlottesville, VA, June 1993.

H. M. Chan, "Application of SEM to the Study of Multi-Phase Ceramic Composites", 51st Ann. MSA Meeting, Cincinnati, August 1993.

M. P. Harmer, "Microstructure and Processing of Ceramic Nanocomposites", Penn State University, September 1993.

M. P. Harmer, "Microstructural Design of Multiphase Ceramic Composites", Materials '93 Conference in Porto, Portugal, October 1993 (Invited).

M. P. Harmer, "Mechanical Behavior of Ceramics", University of Oporto, Portugal, October 1993.

A. Khan, H. M. Chan, and M. P. Harmer, "Flaw Tolerant Alumina-Mullite Ceramics", 96th Annual Meeting of the American Ceramic Society, Indianapolis, April 1994.

4. AWARDS, ACCOMPLISHMENTS, AND PATENTS

4. AWARDS, ACCOMPLISHMENTS, AND PATENTS

Awards and Accomplishments

Dr. Helen M. Chan has received the ASM International 1992 Bradley Stoughton Award for Young Teachers.

Dr. Helen M. Chan appointed "Class of 1961" Professor (1992).

Dr. Martin P. Harmer was named to be elected as a Fellow of the American Ceramic Society (1993).

Dr. Martin P. Harmer was appointed the Alcoa Foundation Professor of Materials Science and Engineering (1993).

S. Dill, J. D. French, H. M. Chan, and M. P. Harmer received the Rowland B. Snow Award from the American Ceramic Society for the best poster entitled, "Coarsening of a Duplex Microstructure: Effect of a Liquid Phase", Annual Meeting of the American Ceramic Society, Minneapolis (May 1992).

C. J. Russo, M. P. Harmer, H. M. Chan, and G. A. Miller received first place at the 17th Annual Conference on Composites and Advanced Ceramic Materials for the best poster entitled, "Design of a Laminated Ceramic Composite for Improved Strength and Toughness", Cocoa Beach, FL (Jan. 1993).

A. M. Thompson, D. B. Williams, H. M. Chan, M. P. Harmer, K. K. Soni, R. Levi-Setti, J. M. Chabala, and J. Lie, received 2nd place in the ceramographic contest for their poster entitled, "SIM/SIMS of Yttrium Segregation in Creep-Resistant Alumina", Annual Meeting of American Ceramic Society, Indianapolis (April 1994).

Patents

United States Patent Application 230,388, Yttrium-doped Aluminum Oxide

5. DEGREES AWARDED

5. DEGREES AWARDED

M. D. Stuart, "Characterization and Mechanical Behavior of Alumina-Mullite Ceramics", M.S. Thesis, 1991.

J. D. French, "High Temperature Deformation and Fracture Toughness of Duplex Ceramic Microstructures, Ph.D. Thesis, 1993.

C. J. Russo, "Tensile Strength, Flaw Tolerance and T-Curve Behavior of Trilayer Ceramic Composite", Ph.D. Thesis, 1993.

6. PERSONNEL

6. PERSONNEL

Prof. Martin P. Harmer, Principal Investigator
Prof. Helen M. Chan, Co-Principal Investigator
Dr. Gary A. Miller, Co-Principal Investigator

Research Assistants/Associates

Dr. A. M. Thompson
Dr. J. Zhao
Dr. J. C. Fang
J. D. French
A. Khan
C. J. Russo